Investigations into heart failure:

Cardiac and renal pathophysiology in a rodent model for HFpEF

under treatment with a soluble guanylyl cyclase stimulator

Inaugural-Dissertation

to obtain the academic degree

Doctor rerum naturalium (Dr. rer. nat.)

submitted to the Department of Biology, Chemistry, Pharmacy

of Freie Universität Berlin

by

Sarah Michelle Kedziora

(from Berlin, Germany)

2023

The dissertation was prepared in the group of Prof. Dr. Dominik N. Müller and Prof. Dr. Ralf Dechend at the Experimental and Clinical Research Centre, a joint cooperation of the Max Delbrück Center for Molecular Medicine (MDC) and Charité – Universitätsmedizin Berlin supervised by PD Dr. Florian Herse and Dr. Nadine Haase from October 2019 to February 2023.

1st Reviewer: PD Dr. Florian Herse

2nd Reviewer: Prof. Dr. Simone Spuler

Date of defence: 18.10.2023

Acknowledgement

First, I would like to thank Florian Herse for supervising this work and for supporting me as a doctoral student. I would especially like to highlight the trust you have placed in me. Through the freedom and guidance in the background, I not only learned a lot, but also felt safe.

In addition, I would like to thank Prof. Simone Spuler for the professional support as my second university reviewer. The thesis advisory committee meetings were always constructive and have advanced my work.

I would sincerely like to thank Prof. Dr. Peter Sandner from Bayer Pharmaceuticals (Wuppertal, DE) for the fruitful collaborative work on the projects and our interesting discussions among other at the cGMP congress in Augsburg. It has been a pleasure working with you.

I would like to express my heartfelt gratitude to Nadine Haase, who not only supervised my work in the lab, but always had a sympathetic ear for me. I am very grateful for our honest, friendly, collegial relationship and have also found a good friend in you. I appreciate not only the freedom, but also the structure you gave my work over the last few years. The regular conventional and unconventional supervision meetings brought me through tough lock-down times. You managed to make me feel on the right track and found the perfect words when I doubted myself. It is valuable as a doctoral student to have someone by your side for whom mental health plays an important role. You were also the best "post-doctoral assistant" I could have imagined!

My gratitude goes to Dominik Müller and Ralf Dechend for enabling me to spend my doctoral thesis time in their working group. In the last few years, I have learned a lot, grown beyond myself, and found myself in a positive working environment. Not only have you supported me to work independently and coordinate projects, but you have also taught me to work scientifically and gave me the opportunity for inspiring discussions.

A special thank you goes to Jutta and Astrid. You had so much patience with me in the beginning and included me so kindly. Your support is irreplaceable! You have supported this project and me on 47 weekends - yes, I have counted them.

In addition, I would like to thank all technical and scientific staff from the preclinical research centre at the MDC for their professional work and assistance on this project.

Declaration of Independence

Hereby I certify that I have written my dissertation independently and have not used any sources or aids other than those indicated by me. The dissertation has not been accepted or rejected in any previous doctoral process.

Hierdurch versichere ich, dass ich meine Dissertation selbstständig verfasst und keine anderen als die von mir angegeben Quellen und Hilfsmittel verwendet habe. Die Dissertation ist in keinem früheren Promotionsverfahren angenommen oder abgelehnt worden.

Berlin, ...

Content

6

Summary

Heart failure is a clinical syndrome associated with cardiovascular and non-cardiovascular diseases such as hypertension, myocardial infarction, diabetes mellitus, obesity, or chronic kidney disease. Despite similarities in clinical symptoms, heart failure with reduced and preserved ejection fraction (HFrEF and HFpEF) can be distinguished with diminished EF of ≤ 40% or preserved EF ≥ 50%, respectively. Diastolic dysfunction, increased left ventricular (LV) filing pressure and remodelling are characteristic in HFpEF. A rising number of heart failure patients is diagnosed with HFpEF, due to the aging population, increasing prevalence of comorbidities and higher clinical awareness. The two main myocardial hallmarks of HFpEF are increased passive stiffness and impaired active relaxation. Systemic inflammation in patients promotes microvascular endothelial dysfunction that is characterized by impaired nitric oxide (NO) signaling and elevated oxidative stress. Most pharmaceutical interventions that have been shown to be reliable therapeutic options for HFrEF patients, failed in treatment of HFpEF. Although substantial progress has been made in understanding the pathophysiology of HFpEF in recent years, there are no generally accepted therapies that improve the clinical course of HFpEF. Furthermore, the lack of effective interventions causes high mortality and morbidity in HFpEF patients. Vericiguat (BAY 1021189) was developed to stimulate the soluble guanylyl cyclase (sGC) independent of NO and has been approved for treatment in HFrEF. The potential positive effects of sGC stimulation and their mechanisms have not yet been sufficiently investigated. Therefore, the overall goal of this study was to elucidate cardio- and renoprotective effects by sGC stimulation through vericiguat treatment. Here the focus lies on blood pressure (BP) dependent and independent properties of vericiguat to gain insights into molecular pathophysiologic mechanisms, including cardiac remodelling, metabolism, and the effect on the microvascular system. Male double-transgenic rats (dTGR) heterozygous for both genes, human angiotensinogen, and renin, were included in this study. The dTGR show cardiac remodelling with preserved systolic function, cardiac hypertrophy, fibrosis and increased left ventricular end-diastolic pressure, as well as proteinuria, and present endothelial dysfunction with increased oxidative stress. The main finding of this study is that vericiguat had the most pronounced protective effects on cardiac and renal physiologic structure and function at the BP lowering dose (3 mg/kg/d), while the 0.3 and 1 mg/kg/d doses were less affective. The 3 mg/kg/d dose improved survival, body weight and ameliorated cardiac pressure, global and regional strain. Additionally, cardiac marker for remodelling (*Anp, Bnp, Myh7*) and extracellular matrix

deposition (*Ctgf*) improved, which was in line with diminished fibrosis and inflammation. vericiguat was not capable to improve *in vitro* metabolism. Interestingly, in this model for HFpEF cardiomyocytes presented diminished mitochondrial respiration, while cardiac fibroblasts seemed to be oppositely directed with elevated mitochondrial respiration and increased glycolysis. The 3 mg/kg/d vericiguat dose was renoprotective with improved endothelial damage, oxidative stress, tubular injury, fibrosis, and inflammation. The data suggests that vericiguat cannot rescue the HFpEF phenotype but might bear benefits that could complement therapies in cardiovascular diseases. HFpEF in general maintains a burden of human health because the pathophysiologic complexity is incompletely understood.

Zusammenfassung

Herzinsuffizienz ist ein klinisches Syndrom, das mit kardiovaskulären und nicht-kardiovaskulären Erkrankungen wie Bluthochdruck, Herzinfarkt, Diabetes mellitus, Fettleibigkeit oder chronischen Nierenerkrankungen einhergeht. Trotz ähnlicher klinischer Symptome können Herzinsuffizienz mit reduzierter und erhaltener Auswurffraktion (HFrEF bzw. HFpEF) mit einer verminderten EF von ≤ 40% bei HFrEF beziehungsweise ≥ 50% bei HFpEF unterschieden werden. Diastolische Dysfunktion, erhöhte linksventrikulärer Füllungsdruck und kardiale Umstrukturierung sind charakteristisch für HFpEF. Eine steigende Zahl an Herzinsuffizienz Patienten wird mit HFpEF diagnostiziert, welches durch die alternde Gesellschaft, steigende Prävalenz von Begleiterkrankungen und ein höheres klinisches Bewusstsein beeinflusst wird. Die zwei myokardialen Hauptmerkmale von HFpEF sind die erhöhte passive Steifheit und beeinträchtigte aktive Entspannung. Systemische Entzündung in Patienten fördert mikrovaskuläre endotheliale Funktionsstörung, die durch beeinträchtigte Stickstoffmonoxid (NO) Signalgebung mit erhöhtem oxidativem Stress charakterisiert ist. Die meisten pharmazeutische Interventionen, welche sich als zuverlässige Therapieoptionen für HFrEF Patienten erwiesen haben, waren nicht erfolgreich in der Behandlung von HFpEF Patienten. Obwohl erhebliche Fortschritte zum Verständnis der Pathophysiologie von HFpEF in den letzten Jahren gemacht wurden, gibt es bisher keine allgemein anerkannte Therapie, die den klinischen Verlauf von HFpEF verbessert. Darüber hinaus führt der Mangel an wirksamen Interventionen zu einer hohen Mortalität und Morbidität bei HFpEF. Vericiguat (BAY 1021189) wurde entwickelt, um die lösliche Guanylylzyklase (sGC) unabhängig von NO zu stimulieren und wurde bereits für die Behandlung von HFrEF zugelassen. Mögliche positive Effekte durch die sGC-Stimulation und deren Mechanismen bislang unzureichend untersucht. Daher ist das übergeordnete Ziel dieser Studie die kardialen und renalen protektiven Auswirkungen der sGC-Stimulation durch die Vericiguat Behandlung aufzuklären. Hier liegt der Focus auf den Blutdruckabhängigen und -unabhängigen Eigenschaften von Vericiguat, um einen Einblick in die molekularen pathophysiologischen Mechanismen, einschließlich der kardialen Umstrukturierung, des Metabolismus und des Effekts auf das mikrovaskuläre System, zu erhalten. Männliche doppelt transgene Ratten (dTGR), welche heterozygot für die humanen Gene Angiotensinogen und Renin sind, wurden in die Studie eingeschlossen. In den dTGR kommt es zu kardialer Umstrukturierung mit erhaltener systolischer Funktion, kardialer Hypertrophie, Fibrose und erhöhtem linksventrikulärem enddiastolischem Druck, sowie Proteinurie und präsentieren endotheliale Funktionsstörung

mit erhöhtem oxidativen Stress. Das Hauptergebnis dieser Studie ist, dass Vericiguat den ausgeprägtesten protektiven Effekt auf die kardiale und renale physiologische Struktur und Funktion bei der Blutdrucksenkende Dosis (3 mg/kg/d) aufwies, während die Dosen 0,3 und 1 mg/kg/d weniger effektiv waren. Die 3 mg/kg/d Dosis verbesserte das Überleben, Körpergewicht und senkte den kardialen Druck und die globale sowie regionalen Deformation des Herzens. Zusätzlich waren kardiale Marker für die Umstrukturierung (*Anp, Bnp, Myh7*) und extrazellulärer Ablagerung (*Ctgf*) verbessert, im Einklang mit verringerte Fibrose und Entzündung. Vericiguat war nicht fähig den Metabolismus *in vitro* zu verbessern. Interessanterweise zeigten in diesem Model Kardiomyozyten eine verringerte mitochondriale Respiration, während kardiale Fibroblasten entgegengesetzt gerichtet zu sein schienen mit erhöhter mitochondrialer Respiration und erhöhter Glykolyse. Die 3 mg/kg/d Vericiguat Dosis hatte eine Nierenschützende Wirkung mit verbessertem Endothelschaden, oxidativem Stress, tubulärer Schädigung, Fibrose und Entzündung. Diese Daten zeigen, dass Vericiguat zwar den HFpEF Phänotypen nicht verhindern, aber möglicherweise Vorteile mit sich bringt, die die Therapie von Herzkreislauferkrankungen unterstützen könnte. Im Allgemeinen stellt HFpEF weiterhin eine Belastung der Gesundheit des Menschen dar, weil die pathophysiologische Komplexität der Erkrankung nur unzureichend verstanden ist.

Abbreviations

Abbreviation	Explanation
18S	18S ribosomal RNA, gene
36B4	Acidic ribosomal phosphoprotein P0, gene
µM	Micro molar
ACE-I	Angiotensin-converting enzyme inhibitor
AHA/ACC/HFSA	American Heart Association/ American College of Cardiology/ Heart Failure Society of America
ANGII	Angiotensin 2
ANP	Atrial natriuretic peptide
ARNI	Angiotensin receptor-neprilysin inhibitor
ATP	Adenosine triphosphate
AT1R	Angiotensin 2 subtype 1 receptor
AT2R	Angiotensin 2 subtype 2 receptor
BH_4	Tetrahydrobiopterin
BNP	Brain natriuretic peptide
Bpm	Beats per minute
BSA	Bovine serum albumin
CD lipids	Chemically derived lipids
cDNA	Complementary desoxyribonucleic acid
cGMP	Cyclic guanylate monophosphate
CI	Cardiac index
CO	Cardiac output
Col-1α-1	Collagen type 1 alpha 1 chain, gene
Col-3α-1	Collagen type 3 alpha 1 chain, gene
Ctgf	Connective tissue growth factor, gene
Cyb-α	Cytochrome b-245, alpha chain polypeptide, gene
Cyb-β	Cytochrome b-245, beta chain polypeptide, gene
d	Day
Dahl/SS	Dahl salt-sensitive rat
DOCA	Deoxycorticosterone acetate
dP/dt	Ratio of pressure change in left ventricle
dTGR	Double-transgenic rat
Ea	Arterial elastance
E/A	Ratio of peak velocity from early (LV relaxation) to late diastole (atrial contraction)
ECAR	Extracellular acidification rate
EF	Ejection fraction
ESC	European society for cardiology
Et-1	Endothelin 1, gene
Ex/em	Excitation/emission
FAC	Fractional area change
FAD	Flavin adenine nucleotides
FBS	Fetal bovine serum
Fe^{2+}/ Fe^{3+}	Iron oxidation states, ferrous cation/ferric cation
Fn	Fibronectin, gene

FOV	Field of view
FS	Fractional shortening
GTP	Guanosine triphosphate
Glut4 (Slc2a4)	Soluble carrier family 2 (facilitated glucose transporter), member 4, gene
GMP	Guanosine monophosphate
Gucy1α2	Guanylate cyclase 1 soluble subunit alpha 2, gene
Gucy1α3	Guanylate cyclase 1 soluble subunit alpha 1, gene
Gucy1β2	Guanylate cyclase 1 soluble subunit beta 2, gene
Gucy1β3	Guanylate cyclase 1 soluble subunit beta 1, gene
HFmrEF	Heart failure with mildly reduced ejection fraction
HFpEF	Heart failure with preserved ejection fraction
HFrEF	Heart failure with reduced ejection fraction
HR	Heart rate
Icam1	Intercellular adhesion molecule 1, gene
IL1R	Interleukin 1 receptor
ITS	Insulin-transferrin-selenium
kg	Kilogram
Kim-1 (Havcr1)	Kidney injury molecule 1, gene
L-Name	N[w]-nitro-l-arginine methyl ester
LV	Left ventricle
LVEDD	Left ventricular end-diastolic diameter
LVEDP	Left ventricular end-diastolic pressure
LVEDV	Left ventricular end-diastolic volume
LVESD	Left ventricular end-systolic diameter
LVESP	Left ventricular end-systolic pressure
LVESV	Left ventricular end-systolic volume
MAP	Mean arterial pressure
Mcp-1(Ccl2)	Monocyte chemoattractant protein 1, gene
mg	Milligram
min	Minute
mmHg	Millimetre mercury
mM	Millimolar
MRA	Mineral corticoid receptor antagonists
Myh6	Myosin heavy chain 6, gene
Myh7	Myosin heavy chain 7, gene
MYPT1	Myosin phosphatase
NADPH	Nicotinamide adenine dinucleotide phosphate
Ncf-1	Neutrophil cytosolic factor 1, gene
Ncf-4	Neutrophil cytosolic factor 4, gene
Nd1	NADH dehydrogenase subunit 1, mitochondrial gene
Ngal	Neutrophil gelatinase associated lipocalin 2, gene
NDS	Normal donkey serum
NO	Nitric oxide
NOS, (e-, i-, n-)	Nitric oxide synthase (endothelial-, inducible-, neuronal-), proteins
Nos1, 2, -3	Nitric oxide synthase 1, 2, 3, genes
NOX	NADPH oxidase

Nox-4	NADPH oxidase 4, gene
NT-proBNP	N-terminal pro-brain natriuretic peptide
OCR	Oxygen consumption rate
$ONOO^-$	Peroxynitrite
Opn (Spp1)	Osteopontin (secreted phosphoprotein 1), gene
P/S	Penicillin/Streptomycin
Pai1 (Serpine1)	Serpin family E member 1, gene
PBS	Phosphate-buffered saline
PDE	Phosphodiesterase
Pdk4	Pyruvate dehydrogenase kinase 4, gene
PKG	Protein kinase G
P_{max}	Maximal pressure during loop
P_{mean}	Mean pressure during loop
P_{min}	Minimal pressure during loop
RAAS	Renin-angiotensin-aldosterone system
RNA	Ribonucleic acid
ROS	reactive oxygen species
RT	Room temperature
RT-qPCR	Real-time quantitative polymerase chain reaction
SD	Standard deviation
SD rats	Sprague Dawley rats
Sdha	Succinate dehydrogenase complex flavoprotein subunit A, gene
Sell	Selectin L, gene
sGC	soluble guanylyl cyclase
SGLT2	Sodium-glucose co-transporter 2
STE	Speckle tracking echocardiography
SV	Stroke volume
SW	Stroke work
Tgf-β1	transforming growth factor beta 1, gene
Timp1	TIMP metallopeptidase inhibitor 1, gene
TNF- α	Tumor necrosis factor alpha
TPR	Total peripheral resistance
VASP	Vasodilator-stimulated phosphoprotein
Vegf-α	Vascular endothelial growth factor alpha, gene
Vcam1	Vascular cell adhesion molecule 1, gene
WT	Wild-type
τ	Isovolumetric relaxation constant (tau)

List of Tables

List of Figures

I. <u>Introduction</u>

1.1 <u>Heart failure pathology, types, and prevalence</u>

Pathology

Heart failure is a condition that combines multiple symptoms and comorbidities. Patients with heart failure typically present symptoms of reduced exercise tolerance with short breath, cough, lung oedema, fatigue, cardiac arrhythmias, peripheral edema, and overall impaired life quality (Figure 1) [1,2]. Heart failure is associated with cardiovascular diseases such as arterial hypertension (> 140 mmHg systolic and > 90 mmHg diastolic), atrial fibrillation, myocardial infarction, and coronary heart disease. Non-cardiovascular diseases like diabetes mellitus, obesity, adiposity or chronic kidney disease are common among patients with heart failure [2,3]. In addition, smoking, unhealthy diet, physical inactivity, sex, and age are associated with the development of heart failure (Figure 1). Despite similarities in clinical symptoms, there is evidence that supports the distinction between three major mechanistically different pathophysiologic heart failure types: heart failure with reduced ejection fraction (HFrEF), heart failure with mildly reduced ejection fraction (HFmrEF) and heart failure with preserved ejection fraction (HFpEF) [4,5]. Different functional parameters have been used to classify heart failure types in the past and according to the European Society of Cardiology (ESC) 2021 Guidelines and American Heart Association (AHA) 2022 Guidelines the current definition is based on the ejection fraction, which defines the proportion of blood that is pumped from the left ventricle into the circulation [2] [6]. HFrEF is defined as ≤ 40% left ventricular ejection fraction and HFpEF with left ventricular ejection fraction ≥ 50% (Figure 1). The intermediate HFmrEF includes patients with left ventricular ejection fraction between 41% and 49%. In HFrEF, patients suffer from impaired systolic cardiac function, with eccentric hypertrophy, increased left ventricular volume and contraction force, because the contractility of the myocardium is diminished whereby reducing the blood fraction ejected from the heart [2,7]. It has been shown that similar therapies as for patients with HFrEF may be beneficial for patients with HFmrEF, the intermediate type of heart failure [8,9]. The diagnostic distinction of HFmrEF can be supported by structural alterations such as size, hypertrophic status and filling of the left atrium and ventricle [2]. For diagnosis of HFpEF not only the preserved left ventricular ejection fraction ≥ 50% is considered. Criteria for HFpEF include structural cardiac alterations and functional abnormalities with left ventricular diastolic dysfunction relevant for increased left ventricular filing pressure, reduced end-diastolic volume, left ventricular remodelling and elevated release of natriuretic peptides (Figure 1) [2]. HFpEF displays cardiac structural

alterations with thickened ventricular wall, passive stiffness in the ventricular myocardium and impaired active relaxation on a functional level, both considerably affecting the filling of the left ventricle negatively [10]. Besides classic cardiologic parameters, global longitudinal strain has been described to be a useful and sensitive marker to identify HFpEF with relevance to outcome prognosis [11]. In addition, HFpEF patients suffer from physical capability, which has been attributed to impaired cardiac function but also to mitochondrial abnormalities in the skeletal muscle [12].

The clinical syndrome HFpEF is highly heterogeneous. The heterogeneity of HFpEF relies on the complexity of pathophysiologic mechanisms that contribute to the disease. Sex is a risk factor and elderly women have a higher prevalence for HFpEF [13]. However, the HFpEF-associated comorbidities largely influence the diverse presentation of the disease. The cardiometabolic HFpEF phenotype includes patients associated with diseases of disturbed metabolism like obesity, metabolic syndrome or diabetes type 2 [3,14,15]. These metabolic alterations promote a pro-inflammatory state in HFpEF, which leads to altered myocardial energy supply with impaired mitochondrial function [3]. The cardiorenal dysfunction describes the combined phenotype of chronic kidney disease and heart failure that share overlapping pathologies such as renin-angiotensin-aldosterone system (RAAS) activation, systemic inflammation, and endothelial dysfunction [16]. Understanding the connection of cardiac and renal pathophysiology is essential because nearly half of the HFpEF patients have been additionally diagnosed for chronic kidney disease [17]. In models for cardiorenal syndrome, fibrosis and defects in microvasculature have been observed to be impaired in the kidney and heart [18]. The immunometabolic HFpEF phenotype is related to systemic inflammation and investigations have highlighted the role of immune cells in cardiac protection and mediation of injury [19]. Immunometabolism is targeting the interaction between immunology and metabolism is getting increasing attention and potential as therapy.

The distinction of multiple pathologic variations within the clinical syndrome of HFpEF is in line with the observation that effective treatments for HFrEF are mostly unsuccessful to improve clinical outcomes in HFpEF patients [20] (see 1.3). With the exception of sodium-glucose cotransporter 2 (sGLT2) inhibitors that could improve the combined endpoint of cardiovascular death and heart failure admission in HFpEF [21,22]. Although different variations might exist, complete separation is unfeasible because cardio-metabolism, immune-metabolism and the cardiorenal axis are tightly intertwined.
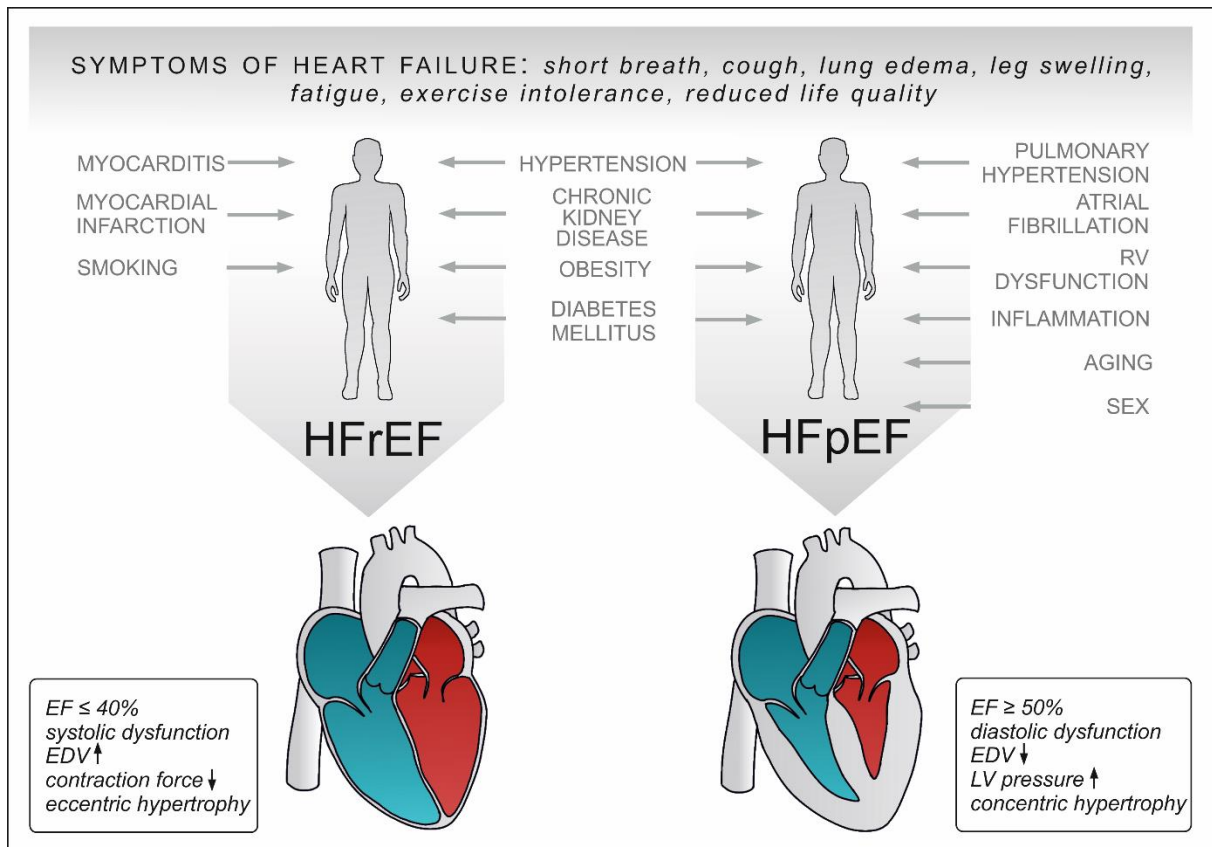
Figure 1. Comparison of symptoms, comorbidities, and characteristics in HFrEF and HFpEF.
Symptoms of heart failure are shared between heart failure with reserved ejection fraction (HFrEF) and heart failure with preserved ejection fraction (HFpEF). Frequent comorbidities include cardiovascular and non-cardiovascular diseases, both increasing the risk for the development of heart failure. HFrEF and HFpEF can be distinguished mainly by ejection fraction (EF), but also present either systolic or diastolic dysfunction with impaired end-diastolic volume (EDV), left ventricular (LV) pressure and hypertrophy. Images in this figure were sketched using ArtFlow and the scheme was assembled using CorelDraw.

Prevalence

The prevalence of heart failure in industrialized countries worldwide ranges between 1 and 3% and is constantly rising [23]. The Heart Failure Association ATLAS project reported a median heart failure prevalence of 17 per 1000 persons [24]. Across European countries heart failure prevalence varies with between 1.5-1.6% (2002-2014) in the UK [25] and 6.8% (2004-2005) in Spain [26], with 4.0% (2009-2013) in Germany [27]. Among heart failure patients over 50% present with HFpEF (data from developed countries) [17]. Importantly, prevalence and incidence have been developing differently over the past decade in HFpEF and HFrEF. While HFrEF seems to have a more stable prevalence due to good therapeutic options, HFpEF prevalence is constantly increasing [17]. Factors for rising proportion of HFpEF could be demographic changes like the aging population, increasing appearance of cardiac-dependent and -independent comorbidities (diabetes, obesity, hypertension) as well

as higher clinical awareness and recording of HFpEF [28]. The general emerging prevalence of heart failure may be attributed to raising numbers of HFpEF cases within the diagnostics of heart failure [4].

The incidence, meaning the rate of new onset heart failure cases per year in Europe and northern America lies between two to three cases per 1000 person-years and mostly stable or decreasing in HFrEF while less stable in HFpEF [23]. A lower socioeconomic status is associated with the risk of incident heart failure of 43% to 87% [29]. Both, prevalence and incidence have been reported to be markedly higher in older patients [25–27].

1.2 Molecular pathogenesis of HFpEF - Disbalance of cellular processes

The following section aims to explain the molecular disbalance in the pathology of HFpEF and draws comparisons to the healthy heart under physiologic conditions.

Two physiologic relevant cardiac hallmarks of HFpEF are 1) the increased myocardial passive stiffness and 2) the impaired active cardiomyocyte relaxation [10]. The myocardial passive stiffness results from the sum of extracellular matrix deposition (fibrosis and collagenization), increased calcium sensitivity of myofilaments and hypophosphorylation of titin. The active relaxation is based on an imbalanced ion homeostasis with higher cytosolic calcium levels in cardiomyocytes [7]. Comorbidities of HFpEF drive systemic inflammation that activate pathology relevant pathways through upregulation of factors such as tumor necrosis factor alpha (*Tnf-α*) or interleukin1 receptor (*Il1-R*). Inflammation promotes microvascular endothelial dysfunction that is characterized by reduced nitric oxide (NO) bioavailability, thereby increasing oxidative stress and production of reactive oxygen species (ROS) in cardiomyocytes (also see section 1.4) [30]. Increased ROS and mitochondrial damage lead to mismatch of energy production and demand. In a multi-omics approach Zhang et al. identified inflammation, cardiac muscle contraction and mitochondrial integrity pathways to be associated with HFpEF phenotype in Dahl salt-sensitive (SS) rats [31]. Based on the findings they suggest that damaged mitochondria accumulate due to dysregulation of mitochondrial genes, therefore promoting ROS production and cardiac remodeling. Mitochondrial ROS production is supported by an overflow of electrons from the respiratory chain, resulting in further formation of ROS from NO [32]. Upstream factors that influence oxygen availability for the physiologic function of mitochondrial respiratory chain need to be considered when measuring mitochondrial oxidative capacity. Such factors include oxygen transport with regards to microvascular rarefaction in the myocardium of HFpEF [33]. Interestingly*, in vitro*

studies have shown that angiotensin II (ANGII), which is elevated in hypertension and a mediator of blood pressure (BP), can directly induce ROS production through promotion of mitochondrial dysfunction [34]. As a result cyclic guanosine monophosphate (cGMP) levels are low and diminished protein kinase G activity leads to vasoconstriction and left ventricular remodeling [30]. There are multiple methods available to investigate mitochondrial function in cardiomyocytes with oxygen consumption rate being one valuable tool to measure mitochondrial activity [35].

Under physiologic conditions, the healthy myocardium depends on the generation and breakdown of adenosine triphosphate (ATP), most of which is generated by mitochondrial oxidative phosphorylation through mitochondrial F_0F_1-ATPase [36]. Hydrolysis of ATP by myosin ATPase is predominantly required for relaxation and less for contraction [37]. The healthy heart mainly uses fatty acids to generate energy via the mitochondrial oxidative phosphorylation [38]. Energy metabolic changes in the failing heart are diverse, but glycolysis and mitochondrial oxidative phosphorylation play a central role. Most abundant energy sources are fatty acids, glucose, lactate, ketones and branch-chain amino acids [38]. Under stress conditions the heart shifts energy metabolism towards glucose oxidation and glycolysis. Although much is known about the cardiac metabolism in HFrEF that presents a state of reduced fatty acid and increased glucose utilization, the metabolism in HFpEF is less clear. In a mouse model for progressive heart failure (abdominal aortic constriction), cardiac hypertrophy has been linked to energy deficiency with a reduction of glucose metabolism and mitochondrial oxidation under insulin resistance [39]. The metabolic dysregulation plays a crucial role in heart failure. As the heart demands increased energy, the metabolic switch to an alternative substrate is inevitable. Increased glycolysis (glycolytic uncoupling) and reduced oxidative capacity (mitochondrial remodeling) further increase oxidative stress [7]. There has been evidence that ketone metabolism plays a role in the energy metabolism of HFpEF [40] as well as glycolysis [41].

Taken together, the complex molecular pathology in HFpEF involves microvascular endothelial dysfunction, impaired NO signaling with ROS production driven amongst others by mitochondrial dysfunction and impaired bioenergetic metabolism due to an imbalance of energy availability and demand.
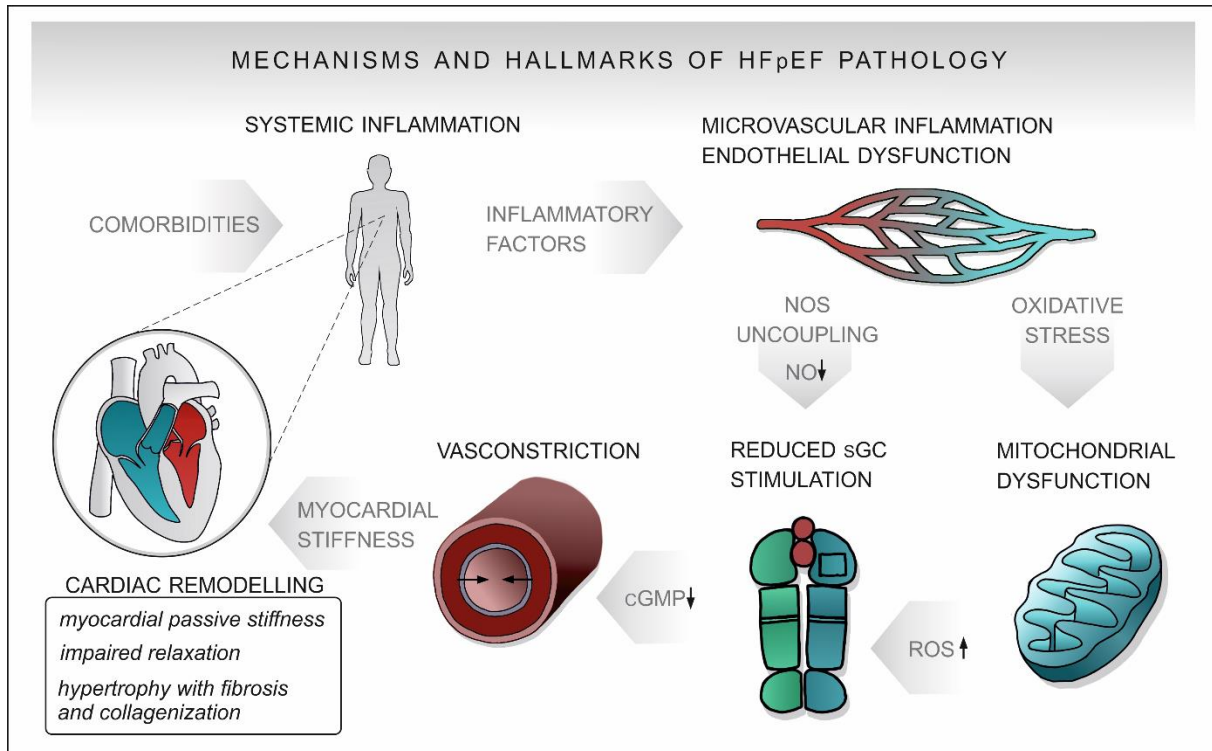
Figure 2. Mechanisms and hallmarks of HFpEF pathology.
Comorbidities associated to heart failure with preserved ejection fraction (HFpEF) drive systemic inflammation, leading to elevation of inflammatory factors. That further triggers microvascular inflammation and endothelial dysfunction, leading on the one hand to reduced levels of nitric oxide (NO) through uncoupling of nitric oxide synthase (NOS). On the other hand, oxidative stress drives mitochondrial dysfunction with altered energy generation and production of reactive oxygen species (ROS). Both lead to a reduced stimulation of soluble guanylyl cyclase (sGC) and reduced cyclic guanosine monophosphate (cGMP). As a result, vasoconstriction and myocardial stiffness occur, impairing cardiac remodelling with myocardial passive stiffness through altered titin phosphorylation, impaired relaxation due to ion imbalance and hypertrophy with fibrosis and collagenization. The scheme is inspired by images in D'Amario et al 2019 and Heinzel et al. 2020 [7,30]. Images in this figure were sketched using ArtFlow and the scheme was assembled using CorelDraw.

1.3 Therapeutic options in heart failure

The above-described heart failure types d different treatment strategies due to their complexity and individual pathophysiology. In general, pharmacologic treatment aims to reduced mortality, prevent (re-)hospitalization, and improve functional capacity and quality of life. Guidelines for heart failure treatment are regularly reported by the European Society of Cardiology (ESC) and the American Heart Association/ American College of Cardiology/Heart Failure Society of America (AHA/ACC/HFSA) giving guidance for clinical practice [2,6]. In recent ESC guidelines, four pharmaceutical drug groups targeting the RAAS and sympathetic nervous system have been recommended for treatment of HFrEF patients: angiotensin-converting enzyme inhibitor (ACE-I) or angiotensin receptor-neprilysin inhibitor (ARNI), beta-blocker and mineral corticoid receptor antagonists (MRA) should be supplemented with sodium-glucose co-transporter 2 (SGLT2) inhibitor, which have recently been added [2,42].

According to ESC guidelines, additional pharmaceuticals can be considered for HFrEF treatment include diuretics for decongestion to improve symptoms. However, pharmaceutic treatment that has proven to be a reliable intervention for HFrEF patients was ineffective in HFpEF [43]. Substances, which are routinely used in HFrEF treatment could not significantly improve the primary outcome of hospitalization and death from cardiovascular causes in HFpEF patients [44–47]. Strikingly, SGLT2 inhibitor improved outcome of worsening heart failure or cardiovascular death in HFpEF patients, giving a new perspective for HFpEF treatment [21,22]. Although substantial progress has been made in understanding the pathophysiology of HFpEF in recent years, there are no generally accepted therapies that improve the clinical course of HFpEF. There are multiple sites affected in the pathogenesis of HFpEF that offer targets for new therapeutic substances in the failing heart, such as abnormal cardiac mechanistic affecting sarcomere function and calcium homeostasis, cardiometabolic alterations including mitochondrial energetics, left atrial pressure overload, right ventricular dysfunction with pulmonary hypertension and microvascular dysfunction [48].

1.4 NO-sGC-cGMP pathway and endothelial dysfunction.

The discovery of nitric oxide (NO) as a signalling molecule was awarded with the Nobel Prize in 1998 [49]. Robert F. Furchgott discovered that endothelial cells are mandatory for acetylcholine-induced relaxation of vessels and identified the "endothelium-dependent relaxing factor", which today is known as NO [50]. NO has been identified to be released by vasodilating compounds and found that endothelium-dependent relaxation is mediated through protein phosphorylation by cyclic guanosine monophosphate (cGMP) by Ferid Murad [51]. Louis J. Ignarro largely contributed to the understanding of the endothelium-dependent NO-cGMP cascade [52].

NO is a small gaseous signalling molecule with the ability to freely diffuse between tissues due to its water and lipid solubility but can therefore not be regulated by storage, release or degradation [53]. Its remarkable activity results from an unpaired electron. Three NO synthase (NOS) isoforms can generate NO by oxidation of L-arginine and further conversion to L-citrulline and NO [54]. The neuronal nNOS is constitutively expressed in the brain and neurons by *Nos1* (nitric oxide synthase 1) gene. The *Nos2* (nitric oxide synthase 2) gene expression can be induced in inflammatory cells, macrophages, fibroblasts, and others, transcribing for the inducible iNOS. The third isoform is mainly expressed by *Nos3* (nitric oxide synthase 3) in endothelial cells (eNOS) [53,54]. eNOS and nNOS are calcium- and calmodulin-dependent.

Shear stress, acetylcholine and bradykinin mediated receptor activation promote calcium-release that stimulates calmodulin binding to eNOS [55]. eNOS is a homodimer with reductase and oxygenase domains. The co-factors oxygen, nicotinamide adenine dinucleotide phosphate (NADPH), tetrahydrobiopterin (BH$_4$) and flavin adenine nucleotides (FAD) are essential for the transfer of electrons from NADPH to the haem-bound oxygen and L-arginine at the oxygenase site of eNOS [56]. In line with this, the bioavailability of NO depends on the expression of eNOS, its activity and integrity.

Endothelial dysfunction includes the pathophysiologic NOS uncoupling. In detail, eNOS produces superoxide O_2^- in the uncoupled state, which increases vascular oxidative stress. Cardiovascular risk factors such as hypertension, diabetes mellitus or chronic smoking stimulate the production of reactive oxygen species (ROS) in the vascular wall by increasing expression and activity of NADPH oxidases (NOX). NOX is expressed in endothelial cells by *Nox2* and *Nox4* genes [57]. In the failing heart and kidney damage NOX4 and NOX2 activity plays a critical role in generation of oxidative stress [57,58]. Superoxide O_2^- forms peroxynitrite (ONOO$^-$) together with vascular NO that is derived from upregulated eNOS activity in cardiovascular disease. The eNOS haem-group itself and the cofactor BH$_4$ are sensitive to oxidation by ONOO$^-$ [56]. Thus, diminished levels of BH$_4$ and oxidized eNOS haem-group contribute to superoxide production. The contribution of eNOS uncoupling to oxidative stress opposite of the intrinsic protective enzymatic function has been observed in animal models of cardiovascular diseases and patients presenting cardiovascular risk factors [59–61].

The ubiquitous expressed receptor of NO is the enzyme NO-sensitive soluble guanylyl cyclase (sGC) that catalyses the transition of guanosine triphosphate (GTP) to cyclic guanosine- 3'5'-monophosphate (cGMP). A structurally different receptor is the plasma membrane-bound guanylyl cyclase, that regulates BP through generation of cGMP upon binding of the ligands atrial- or brain natriuretic peptide (ANP, BNP) [62]. The NO-sensitive sGC is a physiologic relevant heterodimeric enzyme. Four sGC subunits exist: α1, α2, β1 and β2 are encoded by guanylyl cyclase 1 soluble subunit alpha 1 (*Gucy1α3*), alpha 2 (*Gucy1α2*), beta 1 (*Gucy1β3*) and beta 2 (*Gucy1β1*), respectively [63]. The enzyme occurs in two catalytically active isoforms that are composed of one β1-subunits and either one α1- or α2-subunit [64,65]. The haem-dependency of sGC activation has been discovered by Craven and DeRubertis [66]. The β1-subunit carries a conserved prosthetic haem group with a central ferrous atom (Fe^{2+}) and upon NO binding, the haem domain undergoes a conformational change substantially increasing sGC activity [63]. Importantly, in

cardiovascular diseases that are associated with oxidative stress the binding of NO is partially impaired. However, in a physiologic situation, NO-binding results in cGMP production, which has three main targets: the cGMP-dependent protein kinase G (PKG), cGMP-gated ion channels and cyclic nucleotide phosphodiesterase (PDE) [67]. The cGMP binding to protein kinase G (PKG) results in phosphorylation of proteins relevant in multiple cellular pathways, such as regulatory myosin phosphatase (MYPT1), vasodilator-stimulated phosphoprotein (VASP) and titin [68,69]. NO via cGMP-PKG signalling largely contributes to relaxation and constriction of smooth muscle cells by regulating calcium concentrations and cell hyperpolarization that modify actin-myosin dynamics but also influence platelet aggregation, cell proliferation and differentiation, thrombosis and inflammation [67].
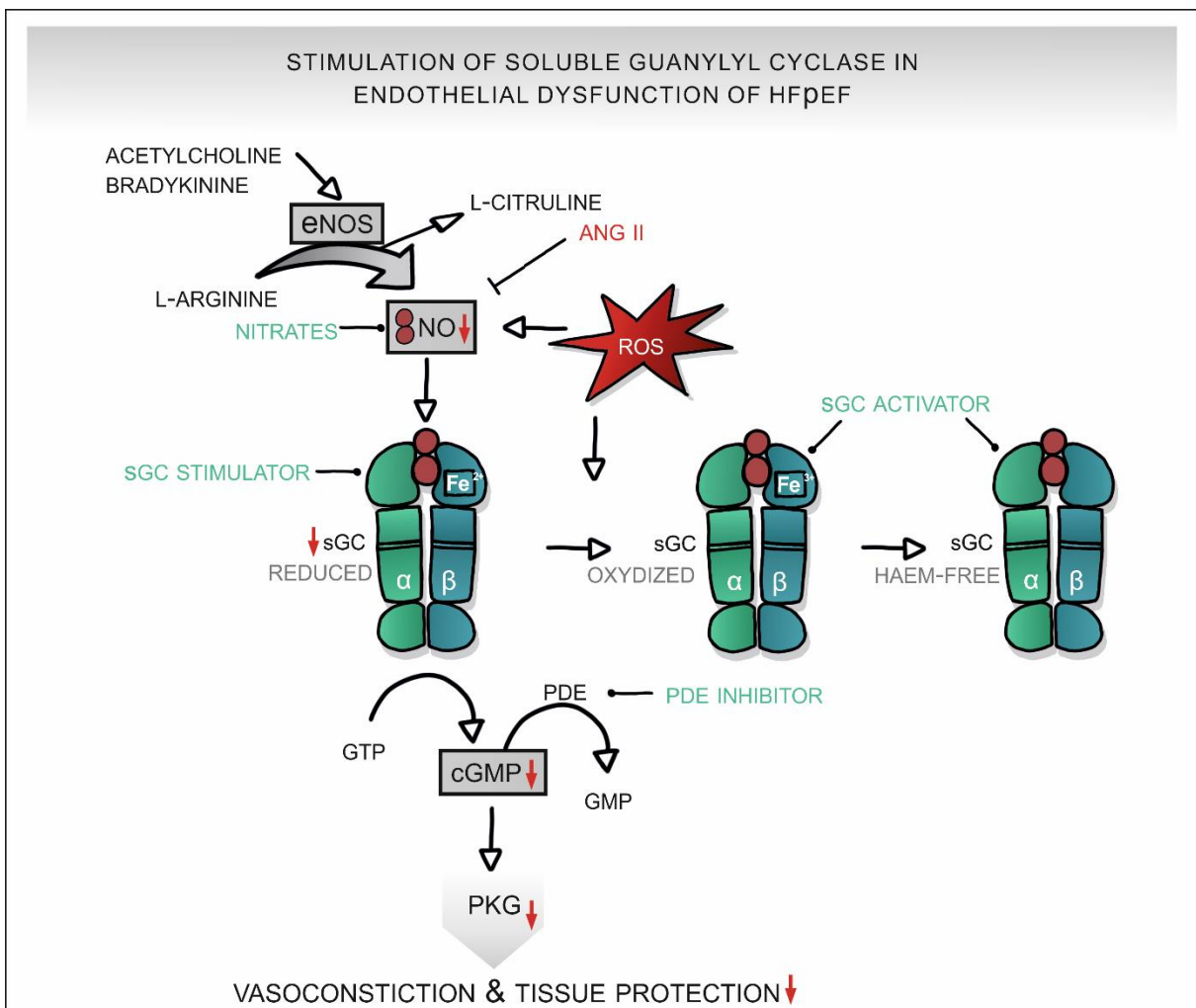
Figure 3. Stimulation of soluble guanylyl cyclase in endothelial dysfunction of HFpEF.
The endothelial nitric oxide synthase (eNOS) is stimulated by acetylcholine, bradykinin and generates nitric oxide (NO) from L-arginine, with L-citrulline as a by-product. NO stimulates the reduced (Fe^{3+}) form of the soluble guanylyl cyclase (sGC), which converts guanosine triphosphate (GTP) into cyclic guanosine monophosphate (cGMP). cGMP is responsible for protein kinase G (PKG) activity that leads to vasoconstriction and thus tissue protection. Angiotensin II (ANGII) inhibits NO, which is in addition reduced by production of reactive oxygen species (ROS). Reduced NO reduces sGC activity, thereby affecting cGMP and PKG levels ending in reduced

tissue protection (red arrows). ROS also directly oxidizes sGC (Fe^{2+}) that can result in haem-loss. Pharmacologic therapeutics (green font) interact at various sites of the pathway. Nitrates can directly increase NO levels, sGC stimulators increase sGC affinity to NO and directly stimulate the reduced enzyme. On the opposite, sGC activators can activate oxidized and haem-free sGC. Inhibitors of the phosphodiesterase (PDE) prevent the degradation of cGMP to guanosine triphosphate by PDE. Images in this figure were sketched using ArtFlow and the scheme was assembled using CorelDraw.

Taken together, endothelial dysfunction captures the imbalance of endothelium-mediated and NO-cGMP induced pathways. Endothelial dysfunction is driven by cardiovascular risk factors like hypertension, obesity, aging, diabetes, smoking and elevated cholesterol [70]. It is characterized by a reduction of NO bioavailability and eNOS activity because of eNOS uncoupling, besides deleterious high levels of ROS, increased leukocyte adhesion, inflammation, and platelet aggregation. The endothelial dysfunction and impaired NO-sGC-cGMP pathway is subject to pharmacologic therapy strategies in heart failure.

1.5 Substances enhancing NO-sGC-cGMP signalling.

Organic nitrates are classic therapeutics in cardiovascular diseases, which aim to increase NO bioavailability within tissue to activate sGC independent of the endothelium. Therapy with organic nitrates reduces preload and end-diastolic pressure therefore improving myocardial perfusion. However, limitations of organic nitrates have been presented in clinical studies with varying degrees of therapeutic efficacy, limited nitrate tolerance, enhanced endothelial dysfunction, reduced physical activity and patients suffering from nitrate head ache [48,71,72].

Further downstream the sGC signalling cascade, the prevention of cGMP degradation has been targeted [73]. In a phase III clinical trial of phosphodiesterase inhibition (PDE5 inhibition with sildenafil), HFpEF patients showed no improvement of exercise capacity [74]. A meta-analysis clarified the ineffectiveness of PDE inhibitors in HFpEF that was reflected in no improvement of left ventricular function, exercise tolerance or pulmonary hypertension but beneficial effects on right ventricular function [75].

Further substances have been identified to modulate the NO-sGC-cGMP pathway in a beneficial way, namely sGC stimulators and activators. sGC stimulators act in two ways, firstly by direct stimulating the cGMP production through binding to the α-subunit of haem-bound sGC independent of NO and secondly by stabilization NO binding to the heme-domain of the sGC [76]. Generation of oxidative stress in cardiovascular diseases creates ROS that can react to peroxynitrite in the presence of NO. Oxidization of the sGC (haem-Fe^{3+}) through peroxynitrite can further result in complete loss of the haem-moiety [77]. Unlike sGC stimulators, sGC activators can bind the haem-free sGC and therefore activate the enzyme in

a NO-mimicking manner [77]. sGC activator cinaciguat (BAY 58-2667) has been described to directly bind to the sGC enzyme with high affinity independent of the haem-group oxidation status [78]. With the potential to activate haem-deficient sGC and thus contributing to cGMP generation independent of NO, sGC activators are valuable pharmacologic substances.

In the development of compounds that would increase NO synthesis by NOS activity, scientist at Bayer discovered sGC stimulators that were capable to directly stimulate sGC whereby enhancing cGMP production [76,79]. Another structurally related compound (benzyl indazole = YC-1) was described to directly stimulate sGC in an NO-independent, haem-dependent manner [80]. Due to low potency of primary identified compounds, further development was required. The substances BAY 41-2272 and BAY 41-8543 were identified and although exhibiting improved sGC stimulation potency (IC_{50} = 0.3 and 0.1 µM, respectively) at low minimal effective concentrations in comparison to initial compounds, they exhibited low oral bioavailability with unsatisfying metabolic stability and interacted with cytochrome p450 enzymes [76,81].

Chemical adjustments of the compound structure led to identification of BAY 63-2521, so called riociguat (BAY 63-2521). Sharkovska et al. observed myocardial and renal (glomerular and interstitial) reduction of fibrosis in two hypertension rat models [82]. It has been shown that riociguat in the transverse aortic constriction (TAC) mouse model for HFrEF has a beneficial effect on cardiac function due to decreased fibrosis, hypertrophy and generally reversed cardiac remodelling [83]. Riociguat was capable to protect right ventricular function and prevent TGF-beta mediated fibrosis in a pressure overload induced murine model for pulmonary arterial hypertension [84]. In addition to sufficient sGC stimulation, riociguat showed good oral bioavailability with improved pharmacokinetics and no negative side interactions. However, riociguat presented short half-life time in humans [85]. Although not successful in the treatment of HFpEF, riociguat interestingly improved right ventricular parameters with reduction of pulmonary arterial pressure in patients with pulmonary hypertension [86]. Riociguat has been extensively studied in clinical trials and has shown substantial improvements in patients with pulmonary hypertension [87,88].

Vericiguat (BAY 1021189) was developed to improve pharmacokinetics, presented a minimal effective concentration of 0.3 µM, showed typical NO-independent sGC stimulation and cGMP production with high oral bioavailability and prolonged half-life due to reduced plasma clearance of 0.3 l/h/kg in rats [76,89]. Follmann et al. reported a daily vericiguat dose to be sufficient in patients [89]. Phase I clinical studies in healthy subjects have been conducted to

guarantee safety and toleration of the compound with regards to pharmacodynamic and -kinetic interactions to other medications [90–92]. In the dose-testing phase II SOCRATES-REDUCED trial, vericiguat could not significantly improve N-terminal pro-brain natriuretic peptide (NT-proBNP) levels, although higher doses were more effective, in patients with worsening HFrEF (NCT01951625) [93]. Vericiguat has been investigated in HFrEF in the phase III clinical trial VICTORIA (NCT02861534). Armstrong et al. observed a reduction of death from cardiovascular causes and heart failure demanding hospitalization, making vericiguat a valuable treatment in HFrEF [94]. Upon these results, vericiguat has been first approved for treatment in chronic heart failure [95]. HFpEF patients that received vericiguat presented an ameliorated quality of life score besides persisting NT-proBNP levels and left atrial volume, the primary endpoints of SOCRATES-PRESERVED (NCT01951638) clinical phase II trial [96]. The phase II clinical trial VITALITY-HFpEF (NCT03547583) has been investigating the efficacy of vericiguat and demonstrated no improvement of physical activity in HFpEF patients [97,98]. According to guidelines for European Society of Cardiology (ESC) sGC stimulator vericiguat can be considered as an additional option to standard therapy for patients with HFrEF [2,99]. Many of the above-mentioned studies did not assess the mechanisms underlying the potential effect achieved by sGC stimulation.

1.6 Animal models to study HFpEF

Mammalian animal models are a crucial research tool to investigate physiologic questions, understand connections within pathways and the complex pathology of diseases. The clinical syndrome of HFpEF is heterogenous in its pathophysiology with a wide spectrum reflecting the diversity of the human population. This issue is represented in diverse preclinical models that are used to decipher the mechanisms of HFpEF [43,100,101]. Rodent models for HFpEF have been achieved by dietary, pharmacological, surgical or genetical approaches with the phenotypes fitting into the heterogeneity of the clinical syndrome with the categories: 1) systemic hypertension models 2) cardiometabolic models including diabetes mellitus and obesity 3) two-hit models and 4) renal pathology models. Below a selection of commonly used rodent models for HFpEF is described.

Spontaneously hypertensive rat (SHR) is a result from selective breeding of animals with a naturally occurring hypertensive phenotype. They accumulated hypertension-related genes that are hereditary, which makes it a suitable research model to understand involvement of genetics to contribution of hypertension [102,103]. The ANGII-infused mouse model utilizes direct

administration of ANGII that leads to cardiac hypertrophy, remodelling, fibrosis and diastolic dysfunction accompanied by hypertension dose-dependently [43,100].

Dahl/SS rats develop a HFpEF-like phenotype when fed a high salt diet with hypertension, left ventricular concentric hypertrophy and stiffness and diastolic dysfunction. At a later time point (> 16 weeks of age) enlarged left ventricular cavity and more normal end-diastolic volume point towards a HFrEF-like phenotype [101,104]. Fillmore et al. have shown with the isolated working heart perfusion methodology in Dahl/SS rats that the decreased diastolic function is accompanied with an increase in cardiac glycolysis rate opposite to a reduced fatty acid oxidation and ATP production [41]. Pharmacologic induction of hypertension by deoxycorticosterone acetate (DOCA) salt in unilateral nephrectomised rats represents another rodent model for HFpEF [105]. DOCA (deoxycorticosterone acetate)-salt hypertensive rats develop diastolic dysfunction, myocardial inflammation and fibrosis [100]. Thoracic aortic constriction is a surgical procedure that induces pressure overload in mice leading to left ventricular hypertrophy [106]. The diastolic dysfunction progresses to HFrEF with systolic dysfunction after four weeks, which limits the use as a HFpEF model [107].

Diabetes mellitus and obesity are risk factors for HFpEF in humans and have been used to generate rodent model organisms. The *ob/ob* mouse (leptin-deficiency) and *db/db* mouse (leptin receptor-deficiency) develop cardiac hypertrophy and fibrosis, diastolic dysfunction with reduced diastolic filling parameter E/A ratio, impaired relaxation and preserved systolic function [108]. With the crossing of Zucker diabetic fatty rats that carry a mutation in the leptin receptor gene with spontaneously hypertensive heart failure rats the diabetic Zucker fatty/spontaneously hypertensive heart failure F1 hybrid (ZSF1) mouse model has been created [107]. Animals present obesity, increased left ventricular end-diastolic pressure, hypertension and renal failure [108,109].

Considered that HFpEF is a complex clinical syndrome, models combining different pathologies in the development of HFpEF bear a great potential. The two-hit mouse model that is created by high fat diet in combination with N[w]-nitro-l-arginine methyl ester (L-NAME) a NOS inhibitor has been used to study the cardiometabolic HFpEF phenotype [108,110]. L-NAME induced hypertension as the mechanical stress and HFD-derived obesity as the metabolic factor induce glucose intolerance, defects in global longitudinal strain and diastolic dysfunction with increased filling pressure [110].

Abnormal renal function is associated with HFpEF in humans. In addition the kidney has an essential role in the progression of the disease as impaired salt and water homeostasis are

harmful factors [111]. Rodent models that reduce renal mass surgically have been established in both rats and mice. The 5/6 nephrectomy uses the contralateral ligation of renal poles in addition to an uninephrectomy mimicking chronic kidney disease in humans [112]. Development of cardiac hypertrophy with preserved systolic function, fibrosis and reduced exercise tolerance have been reported in the 5/6 nephrectomy model with potential to be used as a HFpEF model [107].

Some of these models (Dahl/SS, SHR, TAC, ANGII-infusion, nephrectomy) present preserved ejection fraction to a certain age that further progresses into reduced ejection fraction, which limits the period of use of the model within a study [107].

1.7 Double-transgenic rat (dTGR) model for heart failure

The double-transgenic rat (dTGR) model targets the renin-angiotensin-aldosterone system (RAAS). The classic circulating RAAS is a cascade of hormones that regulate electrolyte homeostasis, water reabsorption and maintain normotensive arterial BP [113]. Renin is an enzyme produced by renal juxtaglomerular cells and in circulation cleaves the liver-derived angiotensinogen to angiotensin I (ANGI) [114]. The angiotensin-converting-enzyme (ACE) further converts ANGI into the key effector peptide Angiotensin II (ANGII). ANGII acts by binding to angiotensin II subtype 1 and 2 receptor (AT1R and AT2R), resulting in systemic vasoconstriction via smooth muscle cell contraction leading to BP elevation [115,116]. Second, ANGII stimulates aldosterone secretion from adrenal glands, which contributes to the maintenance of the sodium-potassium balance [117]. The BP in the circulation is regulated on various levels including multiple feedback loops. Renin is released into the circulation when the BP is low. Release of renin depends on sodium concentration in the urine and is released by renal granular cells upon induction via the tubuloglomerular feedback when sodium is high [118].

On the way of developing the dTGR model, both mouse and human genes have been tested in transgenic approaches [119,120]. The human renin and angiotensin expression in rats were superior to mice genes because human RAAS components show a high species specificity and therefore act independently without interfering with the rat RAAS *in vivo* [121]. In previous experiments, transgenic rodent strains have been established that harbour one component of the RAAS system. Microinjection technology was used to generate transgenic mice that express the human renin gene [122]. Two heterozygous transgenic rat strains were developed to define the contribution of RAAS hormones. The transgenic rat harbouring the human renin

gene (TGR(*hRen*)), that showed most pronounced *hRen* expression in the kidney, lung, intestines and elevated in plasma [121]. The transgenic rat harbouring the human angiotensinogen gene (TGR(*hAgt*)) had highest expression of *hAgt* in liver, kidney, heart and jejunum [121]. Besides elevated plasma levels of human angiotensinogen or renin, hypertension was absent in both transgenic rat lines but could be initiated by application of human renin to TGR(*hAgt*) [121,123,124]. The local vascular effects of human renin have been studied in TGR(*hAgt*). Experiments identified human renin as the pivotal cleaving enzyme for human angiotensinogen that acts in a site-specific-manner within the vascular wall increasing both ANGI and ANGII levels [124]. Although successful overexpression made these models applicable in RAAS research, it presents limitations regarding drug administration in hypertension research. Offspring from crossbreeding of heterozygous transgenic rat TGR(*hRen*) with TGR(*hAgt*) did not develop hypertension [121]. The above-mentioned strains were further bred to homozygosity. Mating of male homozygous TGR(*hAgt*) with female homozygous TGR(*hRen*) resulted in double-transgenic rats heterozygous for both human angiotensinogen and human renin that develop hypertension [125]. ANGII is three- to five-fold elevated in plasma and hearts of dTGR [126]. The dTGR develop hypertension of a moderately severity and present end-organ cardiac and renal damage at the age of seven weeks [127]. The dTGR model has been subject of studies investigating hypertension-related end-organ damage of both heart and kidney [128–130]. In this model, approximately 50% of dTGR exhibit a remarkable phenotypical change towards terminal heart failure with cachexia at the age of seven weeks. Rats with terminal heart failure show diastolic dysfunction with preserved systolic function, pronounced body weight reduction and altered gene expression compared to preterminal non-cachectic dTGR [131]. Due to continuous improvement of laboratory animal regulations, animals had to be sacrificed when presenting signs of cachexia with the end of study at the age of seven weeks. The renal damage is reflected by albuminuria that is preceded by immune cell infiltration and complement activation in the dTGR model, both increasing over time [132].

In previous dTGR studies, the development of cardiac hypertrophy, diastolic ventricular dysfunction with preserved systolic function and proteinuria has been shown in this model [133–135]. Endothelial dysfunction and increased oxidative stress are present in the dTGR [136]. Interestingly, metabolic pathways were affected in the dTGR hearts with an increase in glycolysis and glucose oxidation, a reduction in fatty acid oxidation and functional defects in oxidative phosphorylation and mitochondrial respiratory chain [135]. A previous sGC stimulator candidate, BAY 41-8543, that has been investigated in the dTGR model showed improvement

of survival and dysregulation of genes associated with cardiac fibrosis or inflammation [133]. In addition, dTGR presented ventricular arrythmias and impaired hemodynamic which improved by the treatment.

The previously described dTGR model for hypertension induced HFpEF has been used for the *in vivo* experiments of the present study.

1.8 Research aim

As previously described, diastolic and endothelial dysfunction are predominant in HFpEF, and disturbed cardiac energy metabolism plays a substantial role for cardiac performance. The cardiorenal pathology in HFpEF and its development are insufficiently understood. In addition, HFpEF is characterised by a diverse appearance, a reason why new preclinical studies on the pathogenesis are needed. Strikingly, to date there are insufficient treatment options for HFpEF patients. Stimulation of the sGC by vericiguat in HFpEF has been investigated in preclinical studies only to a limited extent.

The major goal of this work is to understand the sGC involvement in experimental HFpEF. Here, the physiologic protective effects of vericiguat and its potential mode of action should be elucidated. The focus of this work lies on the cardiac function and structure, as well as metabolic alterations and microvascular effects in the heart. In addition, the interorgan cardiorenal damage should be investigated.

More specifically, I hypothesized that:
- vericiguat treatment would improve both cardiac and renal pathophysiology in the dTGR model for HFpEF.
- a shift in energy metabolism of cardiac cells from dTGR hearts could potentially be rescued towards the physiological state by *in vivo* treatment with vericiguat.

Regarding the first hypothesis, I asked which mechanisms contribute to the pathogenesis of HFpEF in a BP-dependent and -independent manner. Further, I questioned which cardiac downstream mechanisms and structural effects are induced by the sGC stimulator vericiguat *in vivo*.

Concerning the second hypothesis, my interest was to find out to what extent the energy metabolism is altered in primary cardiac cells in the failing heart. Simultaneously, I asked whether sGC involvement in cardiac cells can be addressed by vericiguat treatment and is capable to cure the energy homeostasis.

To address the above-mentioned hypotheses and questions, I used the dTGR model for heart failure in an *in vivo* intervention study with vericiguat. The study focuses on cardiac and renal pathology, including cardiac remodelling, metabolism, and effects on the microvascular system. The *in vivo* study approaches the influence of vericiguat treatment on the performance of the heart by echocardiographic and haemodynamic analysis. *In vitro* cardiac and renal transcriptional and histological analysis were performed. The *ex vivo* characterisation of cardiac energy metabolism and mitochondrial performance were conducted using Agilent Seahorse technology.

II. Material and Methods

2.1 Material

2.1.1 Animal housing and experimental procedure

Cremphor EL	238470	Calbiochem by Merck Millipore, DE
Diethylene glycol monoethyl ether (referred to as Transcutol)	8.03127.100	Sigma-Aldrich® by Merck, DE
Isoflurane CP	400806.00.00	CP Pharma mbH, DE
Novaminsulfon-ratiopharm (referred to as Metamizole)	03530394 (PZN)	Ratiopharm
Standard chow	V1324-300	Ssniff Spezialdiäten GmbH, DE
vericiguat	BAY 1021189	provided by Bayer AG Pharmaceuticals, Wuppertal, DE

2.1.2 Cell Culture

(S)-(-)-Blebbistatin (CAS 856925-71-8)	T6038	Targetmol, US
BDM	B0753	Sigma-Aldrich® by Merck, DE
BSA	A7906	Sigma-Aldrich® by Merck, DE
Chemically Defined Lipid Concentrate	11905031	Gibco ™ by Thermo Fisher Scientific Inc., US
DMEM, 1x (w 4.5 g/l glucose, L-glutamine, sodium pyruvate)	10-013-CV	Corning Mediatech, Inc., US
DMSO	D4540	Sigma-Aldrich® by Merck, DE
FBS	P30-3306	PAN-Biotech GmbH, DE
Fuchs-Rosenthal counting chamber, 200 µm depth	7198 05	Brand® GmbH + Co KG, DE
Glutamine (L-)	25030-081	Gibco® by Thermo Fisher Scientific Inc., US
HEPES	H3375-500	Sigma-Aldrich® by Merck, DE
HEPES buffer solution (1M)	15630-056	Gibco® by Thermo Fisher Scientific Inc., US
ITS liquid media supplement (100x), 5ml	I3146	Sigma-Aldrich® by Merck, DE

M199 Medium (w: EBSS, L-Glutamine, 2.2 g/l NaHCO₃)	P04-07050	PAN-Biotech GmbH, DE
Neubauer counting chamber, 100 µm depth	7186 05	Brand® GmbH + Co KG, DE
Dulbecco's Phosphate Buffered Saline (PBS), 1x	D8537	Sigma-Aldrich® by Merck, DE
Penicillin/Streptomycin	P0781	Sigma-Aldrich® by Merck, DE
RPMI Medium	R8758	Sigma-Aldrich® by Merck, DE
Trypan blue (0.5% in PBS)	PK-CA902-1209	PromoCell, US
Trypsin/EDTA (0.05%)	P10-023100	PAN-Biotech GmbH, DE

2.1.3 <u>Primer and Probes for RT-qPCR</u>

Primer and probes were designed exon spanning and species specific for rat using the primer designing tool Primer-BLAST and Primer Express 3.0. All forward (F), reverse (R) primers and probes (P) were purchased from BioTeZ Berlin-Buch GmbH.

Gene	Sequence (5' to 3')	Encoding
18S	F: 5´ ACA TCC AAG GAA GGC AGC AG 3´ R: 5´ TTT TCG TCA CTA CCT CCC CG 3´ P: 5´ CGC GCA AAT TAC CCA CTC CCG AC 3´	18S ribosomal RNA
36b4	F: 5' GCC CAG AGG TGC TGG ACA T 3' R: 5' ATT GCG GAC ACC CTC TAG GA 3' P: 5' ACA GAG CAG GCC CTG CAC ACT CG 3'	acidic ribosomal phosphoprotein P0
Nppa (Anp)	F: 5' GCC CAG AGG TGC TGG ACA T 3' R: 5' ATT GCG GAC ACC CTC TAG GA 3' P: 5' ACA GAG CAG GCC CTG CAC ACT CG 3'	natriuretic peptide A
Nppb (Bnp)	F: 5' CAA GCT GCT TTG GGC AGA AG 3' R: 5' AAA CAA CCT CAG CCC GTC AC 3' P: 5' AGA CCG GAT CGG CGC AGT CAG TCG CTT 3'	natriuretic peptide B
Col-1α-1	F: 5' AGA GCG GAG AGT ACT GGA 3' R: 5' CTG ACC TGT CTC CAT GTT GCA 3' P: 5´ CAA GGC TGC AAC CTG GAT GCC ATC 3'	collagen type 1 alpha 1 chain
Col-3α-1	F: 5' CTG AAA TTC TGC CAC CCT GAA 3' R: 5' CAT CTT GCA GCC TTG GTT AGG 3'	collagen type 3 alpha 1 chain
Ctgf	F: 5´ CGC CAA CCG CAA GAT TG 3´ R: 5´ CAC GGA CCC ACC GAA GAC 3´ P: 5´ CAC TGC CAA AGA TGG TGC ACC CTG 3´	connective tissue growth factor
Cyb-α	F: 5´ CTC TAT TGT TGC AGG AGT GCT CAT 3´ R: 5´ GGT GGA GCC CTT TTT CCT CTT 3´ P: 5´ TGT CTG CTG GAG TAC CCC CGG G 3´	cytochrome b-245, alpha chain polypeptide
Cyb-β	F: 5´ GGA GTG CCC AGT ACC AAA GTT T 3´	cytochrome b-245,

	R: 5´ GAA CAT GGG ACC CAC TAT CCA 3´	beta chain
	P: 5´ CCG GAA ACC CTC CTA TGA CTT GG 3´	polypeptide
Et-1	F: 5' AGG GAA AAC CCT GTC CCA AG 3'	endothelin 1
	R: 5' CAC GGG GCT CTG TAG TCA AT 3'	
Fn	F: 5' GGA CCT GCA CGC CAA TAG CT 3'	fibronectin
	R: 5' TCC CCC ACG ACG TAG GAA 3'	
	P: 5' AGA AAT GTT TTG ATC ACG CTG CTG GGA 3'	
Glut4 (Slc2a4)	F: 5´GCC CGA AAG AGT CTA AAG CG 3´	soluble carrier family 2 (facilitated glucose transporter), member 4
	R: 5´TGG ACG CTC TCT TTC CAA CT 3´	
Gucy1α2	F: 5' ATG CAA AGA GCT TCC TGA GGG T 3'	guanylate cyclase 1 soluble subunit alpha 2
	R: 5'-CCT TGA TCA TTC CCA GCA TTG 3'	
Gucy1α3	F: 5' TCG CTC TTC TGC AAA ACT TTC C 3'	guanylate cyclase 1 soluble subunit alpha 1
	R: 5' CAG CCT TCT GAT GCC ATT ACC 3'	
Gucy1β2	F: 5' GCA TCG GTC CTT TTT GGA AA 3'	guanylate cyclase 1 soluble subunit beta 2
	R: 5' TTC GAC CCA TAG TCT CTC AGG ATA G 3'	
Gucy1β3	F: 5' CAG TTG GTG ACA AGT ATA TGA CAG TGA 3'	guanylate cyclase 1 soluble subunit beta 1
	R: 5' AGC CAG GTG GCA AAT GGA 3'	
Icam1	F: 5' GAT CAT TGC GGG CTT CGT 3'	intercellular adhesion molecule 1
	R: 5' CTG ATC TTC TCT GGC GGT AA 3'	
Kim-1 (Havcr1)	F: 5' ATA ATC ACA CTG TAA GAA TCC CTT TGA G 3'	kidney injury molecule 1
	R: 5' CAA CGG ACA TGC CAA CAT AGA 3'	
	P: 5' CCG CGA AGA AAC CCG ACT AAG GGC 3´	
Mcp-1 (Ccl2)	F: 5' TGC AGT TAA TGC CCC ACT CA 3'	monocyte chemoattractant protein 1
	R: 5' TCT CCA GCC GAC TCA TTG G 3'	
Myh6	F: 5' CGG GAG AAC CAG TCC ATC CT 3'	myosin heavy chain 6
	R: 5' ACA CGC TTC GTG TTG ACA GTC T 3'	
	P: 5' ATC ACT GAG AAT CCG GAG CGG G 3'	
Myh7	F: 5' GCC AAG ACA GTT CGG AAT GAT AA 3'	myosin heavy chain 7
	R: 5' CCT GTT GCC CCA AAA TGG 3'	
	P: 5' TCC TCC CGA TTT GGG AAA TTC ATT CG 3'	
Ncf-1	F: 5´ AGA GAC ATA CCT GAC GGC CAA A 3´	neutrophil cytosolic factor 1
	R: 5´ GGC CCG ATA GGT CTG AAG GA 3´	
	P: 5´ ATG GCA AGA ATA ATG TAG CTG ACA TCA CGG G 3`	
Ncf-4	F: 5´ TGG GTG TCA AAC AAG AGA TTG C 3´	neutrophil cytosolic factor 4
	R: 5´ GGC TCA GGA GGT TCT TCA TGT AG 3´	
	P: 5´ AGA CTC GGA TCC CGG CCC TCA A 3´	
Nd1	F: 5' CGG CTC CTT CTC CCT ACA A 3'	NADH dehydrogenase subunit 1, mitochondrial
	R: 5' ATG GTC CTG CGG CGT ATT 3	
Ngal	F: 5´ TCG TCA GCT TTG CCA AGT C 3'	neutrophil gelatinase associated lipocalin 2
	R: 5´ TTG GTC GGT GGG AAC AGA 3'	
	P: 5´ TGG GCC TCA AGG ATA ACA ACA TCG TTT 3´	
Nos2 (iNos)	F: 5´ CGG TTC ACA GTC TTG GTG AAA G 3´	nitric oxide synthase 2
	R: 5´ ACG CGG GAA GCC ATG AC 3´	

36

	P: 5´ TGT TCT TTG CTT CTG TGC TAA TGC GGA A 3´	
Nos3 (eNos)	F: 5´ CAC CAG GAA GAA GAC TTT TAA GGA A 3´ R: 5´ CAC ACG CTT CGC CAT CAC 3´ P: 5´ TAG CCA ATG CAG TGA AGA TCT CTG CCT CA 3´	nitric oxide synthase 3
Nox-4	F: 5´ GCC TGA TCC TTT TAC CCA TGT G 3´ R: 5´ CCT GCT AGG GAC CTT CTG TGA 3´ P: 5´ CAC AGT CCT GGC TTA CCT TCG CGG 3´	NADPH oxidase 4
Opn (Spp1)	F: 5' TCA CCT CCC GCA TGA AGA G 3' R: 5' CTC AGA CGC TGG GCA ACT G 3'	osteopontin (secreted phosphoprotein 1)
Pai1 (Serpine1)	F: 5' CCA TGA TGG CTC AGA ACA AC 3' R: 5' GTT CCA GGA TGT CGT ACT CGT 3'	serpin family E member 1
Pdk4	F: 5' TCC ACT GCT CCA ACG CCT 3' R: 5' CGG CAA GCC GTA ACC AAA A 3'	pyruvate dehydrogenase kinase 4
Sdha	F: 5´GGC CCA TCG GTG TTG CT 3´ R: 5´ACC GCA GAG ATC GTC CAT ACA 3´	succinate dehydrogenase complex flavoprotein subunit A
Tgf-β1	F: 5' GCC TGA GTG GCT GTC TTT TGA 3' R: 5' CCT GTA TTC CGT CTC CTT GGT T 3' P: 5' CAC TGG AGT TGT CCG GCA GTG GC 3'	transforming growth factor beta 1
Timp1	F: 5' CCG CAG CGA GGA GTT TCT C 3' R: 5' GGC AGT GAT GTG CAA ATT TCC 3'	TIMP metallopeptidase inhibitor 1
Vegf-a	F: 5´ GGG CTG CTG CAA TGA TGA A 3' R: 5´ TCC GCA TGA TCT GCA TAG TGA 3'	vascular endothelial growth factor a
Vcam1	F: 5' TGT GAA TCG AAA ACC GAA GTC 3' R: 5' GGG GAA AAA TAG TCC TTG TTA TTT TC 3'	vascular cell adhesion molecule 1
Sell	F: 5' GGA GCA TCT GGA AAC TGG AC 3' R: 5' CAG ATC CGG TGC TGC TAG A 3'	selectin L

2.1.4 **Chemicals and reagents**

Antimycin A	A8674	Sigma-Aldrich® by Merck, DE
BD FACS Clean	340345	Sigma-Aldrich® by Merck, DE
BD FACS Flow	342003	Sigma-Aldrich® by Merck, DE
BD FACS Rinse	340346	Sigma-Aldrich® by Merck, DE
BD FACS Sheath solution	336911	Sigma-Aldrich® by Merck, DE
BD FACS Shutdown solution	334224	Sigma-Aldrich® by Merck, DE
Citrate buffer [10x] pH 6.0	MKCD2290	Sigma-Aldrich® by Merck, DE
Chloroform	102445	Merck KGaA, DE
Carbonyl cyanide 4-(trifluoromethoxy)phenylhydrazone (FCCP)	C2920	Sigma-Aldrich® by Merck, DE

Collagenase Type 2 [> 125 units/mg]	LS004176 (Lot # 41A20883, 320 U/mg)	Worthington Biochemical Corporation, US
Collagenase Type 4 [> 160 units/mg]	LS004188 (Lot # 49A19027, 305 U/mg)	Worthington Biochemical Corporation, US
DNA Digest Buffer RDD	1011132	Qiagen GmbH, Hilden, DE
DNase I, RNase-free	1010395	Qiagen GmbH, DE
DNase I, RNase-free	04716728001	Roche Diagnostics GmbH, DE
Ethylenediaminetetraacetic acid, EDTA	EDS	Sigma-Aldrich® by Merck, DE
Fast SYBR Green Master Mix	4385614	Thermo Fisher Scientific, US
Glucose (D-(+)-)	G-7021	Sigma-Aldrich® by Merck, DE
Heparin 25.000 I.E., 10x5ml	2147217	B. Braun SE, DE
Magnesium chloride, $MgCl_2$	M8266	Sigma-Aldrich® by Merck, DE
Microfil Yellow	MV-122	Flow Tech Inc., US
Oligomycin A	75351	Sigma-Aldrich® by Merck, DE
Potassium chloride, KCl	4936.1000	Merck, US
Protease from Streptomyces griseus [> 3.5 units/mg]	P5147 (Lot #: SLCB2134)	Sigma-Aldrich® by Merck KGaA, US
QIAzol Lysis Reagent	79306	Qiagen GmbH, DE
Rotenone	R8875	Sigma-Aldrich® by Merck, DE
Sodium chloride, NaCl	9265.1	Carl Roth GmbH + Co. KG, DE
Sodium dihydrogen phosphate monohydrate, NaH_2PO_4	1.06346.	Sigma-Aldrich® by Merck, DE
Taurin	T8691	Sigma-Aldrich® by Merck, DE
TaqMan Fast Universal PCR Master Mix [2x]	4367846	Thermo Fisher Scientific, US
XF Calibrant	100840-000	Agilent Technologies, US
XF DMEM Medium, pH 7.4	103575-100	Agilent Technologies, US

2.1.5 Kits

Anti-APC MicroBeads	130-090-855	Miltenyi Biotech, DE

cDNA Reverse Transcription Kit	4368813	Thermo Fisher Scientific, US
RNeasy Mini Kit	74106	Qiagen GmbH, DE
Seahorse XFe96 FluxPak	102416-100	Agilent Technologies, US
eBioscience Fixation/Perm diluent	00-5223-56	Invitrogen™ by Thermo Fisher, US
Permeabilization Buffer 10x	00-8333-56	
Fixation/Permeabilization concentrate	00-5123-43	

2.1.6 <u>Antibodies and staining dyes for immunohistochemistry and histology</u>

Acetic acid [100%]	1.00063	Merck KGaA, DE
Donkey anti-goat IgG | Cy3-conjugated	705-165-003	Jackson ImmunoResearch Europe Ltd., UK
Donkey anti-mouse IgG | Cy3-conjugated	715-165-151	Jackson ImmunoResearch Europe Ltd., UK
Donkey anti-rabbit IgG | Cy3-conjugated	711-165-152	Jackson ImmunoResearch Europe Ltd., UK
Eosin Y solution 0.5% in water	X883.2	Carl Roth GmbH + Co. KG, DE
Ethanol 99.8% denatured	K928.4	Carl Roth, Karlsruhe, DE
Eukitt Quick hardening mounting medium	3989	Sigma-Aldrich® by Merck, DE
F(ab')2-Goat anti-Rabbit IgG (H+L) Cross-Adsorbed Secondary Antibody, Alexa Fluor™ 488	A11070	Invitrogen™ by Thermo Fisher, US
Formalin	1.00496.5000	Sigma-Aldrich® by Merck, DE
Goat anti-rat CD31 antibody	AF3628	R&D systems, US
Goat anti-rat type I collagen antibody	1310-01	Southern Biotech, US
Goldner's stain I, II, III	3469.1; 3470.1; 3473.1	Carl Roth GmbH + Co. KG, DE
Haemalaun solution acid acc. to Mayer	T865.2	Carl Roth GmbH + Co. KG, DE
Haematoxylin solution A and B acc. to Weigert	X906.1; X907.1	Carl Roth GmbH + Co. KG, DE

Mouse anti-rat Actin antibody	M0851	Agilent Dako, US
Mouse anti-rat CD68 antibody | Clone ED1	MCA341R	Bio-Rad AbD Serotec GmbH, DE
Mouse anti-rat Myosin antibody	50967	Abcam, UK
Mouse anti-rat Vimentin antibody	Sc-6260	Santa Cruz Biotechnology, US
Normal donkey serum (NDS)	017-000-121	Dianova GmbH, Hamburg, DE
Paraffin Paraplast Plus	39602004	Leica by Carl Roth GmbH, US
Paraformaldehyde [4 %] pH 7.2	11762.025	Morphisto GmbH, DE
Periodic acid	P0430	Sigma-Aldrich® by Merck, US
Phosphate buffered Saline [10x]	70011-036	Life Technologies, UK
Rabbit anti-rat Fibronectin antibody	Ab23751	Abcam, UK
Rabbit anti-rat PDGFRα antibody	Ab203491	Abcam, UK
Rabbit anti-rat Troponin T antibody	45932	Abcam, UK
Schiff's reagent	1.09033	Merck KGaA, Darmstadt, DE
Trypsin from porcine pancreas (diluted in 1 ml H2O)	T7168	Sigma-Aldrich® by Merck, DE
Vectashield Hard Set Antifade Mounting Medium with DAPI	H-1500	Vector Laboratories Inc., US
Wheat Germ Agglutinin, Fluorescein	FL-1021	Vector Laboratories Inc., US
Xylene	4436	Carl Roth GmbH + Co. KG, DE

2.1.7 Antibodies and probes for flow cytometry

anti-rat CD31 Antibody, APC conjugated, REAfinity	130-119-131	Miltenyi biotec KG, DE
anti-human/mouse/rat Vimentin antibody, PE-conjugated	IC2105P	R&D systems, US
Anti-mouse CD45, VioBlue conjugated	130-110-802	Miltenyi biotec KG, DE
anti-human/mouse/rat cardiac Troponin T, APC conjugated, REAfinity	130-120-543	Miltenyi biotec KG, DE
Hoechst - bisBenzimide H 33342 trihydrochloride	B2261	Sigma-Aldrich® by Merck, DE
LIVE/DEAD™ Fixable Aqua Dead Cell	L34966	Invitrogen™ by Thermo Fisher, US

Stain Kit for 405 nm excitation		
Sytox Green Dead Cell Stain	S34860	Invitrogen™ by Thermo Fisher, US

2.1.8 <u>Consumables</u>

96-fast PCR plates	721981202	Sarstedt AG & Co. KG, DE
MicroAmp Optical 384-well Reaction Plate	4309849	Applied biosystems by Thermo Fisher Scientific, US
6-well plate	83.3920	Sarstedt AG & Co. KG, DE
24-well plate	662160	Greiner bio-one GmbH, DE
Cotton tips	44303010	Glaswarenfabrik Karl Hecht GmbH, DE
Compresses	TZ-1942	neoLab Migge GmbH, DE
centrifugation tubes 15 ml (sterile)	352096	BD Falcon, US
centrifugation falcon tubes 50 ml (sterile)	352070	BD Falcon, US
Discofix C-3, blau	16494C	B. Braun
Flow cytometer tubes, 5 ml	55.1579	Sarstedt AG & Co. KG, DE
Filter tips 0.1-10 µl	70.1130.210	Sarstedt AG & Co. KG, DE
Filter tips 2-200 µl	70.762.211	Sarstedt AG & Co. KG, DE
Filter tips 100-1000 µl	70.760.211	Sarstedt AG & Co. KG, DE
Folded Filters, ø 210 mm	1201-125	Whatman, UK
filter mesh, polyester monolen, 200 µm	24063	neoLab Migge GmbH, DE
gentleMACS C tubes	130096334	Miltenyi biotec KG, DE
LS Columns	130-042-401	Miltenyi biotec KG, DE
Microcentrifuge tubes 1.5 ml	72.706.400	Sarstedt AG & Co. KG, DE
Microcentrifuge tubes 2.0 ml	72.695.400	Sarstedt AG & Co. KG, DE
Microtubes 0.5 ml	72.699	Sarstedt AG & Co. KG, DE
Microtubes 0.2 ml for qPCR	710900	Biozym Diagnostik GmbH, DE
Microscope slides, superfrost Plus	630-0950	Menzel by Thermo Fisher Scientific, DE
Microtome Blades, Type S35	207500000	PFM Medical, UK
Menzel Microscope Covers slips, 24x50 mm	11911998	Menzel by Thermo Fisher Scientific, DE
needles - Sterican® Gr. 16 23G	4657667	B. Braun SE, DE
Optical adhesive film (for qPCR)	G060/UC-RT	Kisker Biotech GmbH & Co. KG

Precellys-ceramic-beads, ø 2.8 mm	432-0357	Bertin technology by VWR, DE
Rotilabo Embedding Casettes, 40x28x6.8 mm	K113.1	Carl Roth GmbH + Co. KG, DE
Sterile cell culture petri dish, 5 cm	2026-05-31	Sarstedt AG & Co. KG, DE
Sterile cell culture plate, 96-well, F-bottom	83.3924	Sarstedt AG & Co. KG, DE
Sterile cell scraper	83.1832	Sarstedt AG & Co. KG, DE
Sterile filter	PTF205013	Jet Biofil, ES
Sterile serological pipette 5ml	86.1253.001	Sarstedt AG & Co. KG, DE
Sterile serological pipette 10ml	86.1254.001	Sarstedt AG & Co. KG, DE
Sterile serological pipette 25ml	86.1685.001	Sarstedt AG & Co. KG, DE
Syringes - Inject® 5 ml, 10 ml	4606051V, 4606108V	B. Braun SE, DE
Silk suture (1.5, 4/0)	8151516	SMI, BE
tissueTUBE TT05	520071	Covaris, Ltd., US
tissueTUBE TT05 Plug	520082	Covaris, Ltd., US
Tubing LMT-55 2Stop ID 2.79MM	HIRS95222725	Hirschmann Laborgeräte GmbH, DE
Vasofix Safety 1,10 x 33 mm G 20 rosa	4268113S-01	B. Braun

2.1.9 Devices and Equipment

Centrifuge 5424; 5810R	Eppendorf AG, DE
Cooling Device Microm Cool-Cut	Thermo Fisher Scientific, US
Compact Paraffin Tissue Embedder EG1160	Leica Mikrosysteme Vertrieb GmbH, DE
CP02 Automated Dry Pulveriser	Covaris, Ltd.,US
Centrifuge 5424 Centrifuge 5430R Centrifuge 5810R	Eppendorf AG, DE
Centrifuge Sigma 4K10	Thermo Fisher Scientific, US
CO_2 incubator CB 210	Binder
CODA system rodent holder	Kent Scientific Cooperation; Torrington, US
DNA Thermal Cycler	Perkin-Elmer GmbH, Neuried, DE

Dissection tools Graefe forceps (curved), 11051-10 Graefe forceps (straight), 11050-10 Lexer-baby scissors (straight), 14078-10 Fine scissors (sharp-blunt), 14028-10 Clamp Hartman Hemostat (curved), 13003-10	Fine Science Tools GmbH, DE
Flow cytometer BD FACSCanto II	BD Biosciences
Flow cytometer BD Fortessa	BD Biosciences
Guillotine	TSE Systems, DE
gentleMACS™ Dissociator	Miltenyi Biotec
High throughput flow cytometry Sampler (HTS) for FACSCanto II	BD Biosciences
High throughput flow cytometry Sampler (HTS) for LSRFortessa	BD Biosciences
Heat mat, Santias SHK 18, 100 W	Beurer GmbH, DE
Peristaltic perfusion pump	Ismatec, DE
Metabolic cages	Tecniplast, IT
Micro fine scale	Satorius, DE
Microm HM 340E, electronic rotary microtome	Thermo Fisher Scientific, US
Microm STP 120, automatic tissue embedding	Thermo Fisher Scientific, US
Microscope Axio Imager.M2 AxioCam HRc HXP 120 C light source objective plan-apochromat 63x/1.4 Oil DIC Power supply 232	Carl Zeiss AG, DE
NanoDrop 1000 Spectrophotometer	Peqlab Biotechnologie GmbH, DE
Non-CO_2 incubator Incu-line 112 Prime	VWR International GmbH, DE
Precellys Control Device, Lysis & Homogenization	Bertin technologies SAS, FR
pH meter	Beckman Coulther, DE
quadroMACS™ Separator	Miltenyi Biotec
QuantStudio 3 & 5 Real-Time PCR System	Applied biosystems by Thermo Fisher Scientific, US

Section Transfer System STS	Thermo Fisher Scientific, US
Seahorse XFe96 Analyzer	Agilent Technologies, US
Telemetric transmitter (PA-C10)	Data Sciences International (DSI) a division of Harvard Bioscience, Inc., US
Telemetric receiver plate	Data Sciences International (DSI) a division of Harvard Bioscience, Inc., US
Vevo 2100 / Vevo 3100	Visual Sonics Inc., Canada
Vita cuisine Steamer	Tefal, UK
Vortex mixer	Scientific Industries, Inc., New York, US
Whole Slide Scanner Panoramic MIDI BF/FL objective plan-apochromat 20x/0.8x	3DHistech Ltd., HU Carl Zeiss AG, DE
Water bath	Gesellschaft für Labortechnik, DE
Micro-CT scanner SkyScan 1276	Bruker, BE

2.1.10 Software

ArtFlow v2.8.124	ArtFlow Studio
Case Viewer 2.2	3D Histech Ltd., HU
CorelDRAW Graphics Suite 2018	Corel GmbH, DE
Flowjo V10.0.7	Tree Star by BD Biosciences
Image J 1.52a	National Institute of Health, US
LabChart Software v8.1.13	AD Instruments, AU
MaxQuant v1.6.3.4	Max Planck Institute of Biochemistry
Prism Version 6 and 7	GraphPad Software, US
Primer-BLAST	National Centre for Biotechnology Information, US
Primer Express version 3.0	Applied Biosystems™ by Thermo Fisher Scientific
QuantStudio Design & Analysis Software V1.4	Thermo Fisher Scientific Germany BV & Co. KG, DE
R 3.6.3 and R studio 1.1.453	R Core Team, US
Vevo LAB 5.5.1	FUJIFILM Visualsonics Inc., CA
Vevo Strain 2100	FUJIFILM Visualsonics Inc., CA

Wave 2.6.1	Agilent Technologies, US
Word, Excel	Microsoft 365, US
µCT software	Bruker, BE
vendor software v1.4.0.0 for image aquisition	
NRecon v.1.7.3.1 for image reconstruction	
CTAn v.1.20.3.0 for image analysis	

2.2 Methods

2.2.1 Animal study and experimental procedures

The animal study was registered at the *Landesamt für Gesundheit und Soziales Berlin* (G0036/20), carried out and performed by members of the working group from Prof. Dominik N. Müller and Prof. Ralf Dechend at the Experimental and Clinical Research Centre and Max Delbrück Center for Molecular Medicine, Berlin. The study was funded by Bayer Pharmaceutics, Wuppertal, Germany for the investigation of the sGC stimulator vericiguat in a rodent model for heart failure. The study was conducted using the model organism *Rattus norvegicus* and the strain Sprague Dawley (SD).

Female SD rats homozygous transgenic for renin (SD-Tg(hREN)L10J) were mated with male SD rats homozygous transgenic for angiotensinogen (SD-Tg(hAGT)L1623) [121]. Their offspring are dTGR expressing both human renin and angiotensinogen whereby they develop a heart failure phenotype with renal insufficiency. Animals entered the study at the age of four weeks. Age-matched male dTGR and non-transgenic wild-type SD control rats (WT) were included into the study.

2.2.1.1 Breeding and Housing

All dTGR and WT breeding was conducted at the animal facility of Max Delbrück Center in Berlin. Animals were kept in under standard conditions including a controlled temperature of 22 ± 2°C, humidity of 55 ± 10% and a 12/12 h light/dark cycle. Animals were housed in small groups of two to five animals per cage, with exception of single-housing in the metabolic cage and during telemetry admission. Water and standard chow (Sniff V1324-300) were provided ad libitum throughout the experiment except for urine sampling when animals were kept in the metabolic cage without food for 12 hours.

2.2.1.2 Treatment Groups

In this study three different treatment doses of vericiguat were tested. dTGR received either 0.3 mg/kg, 1 mg/kg, or 3 mg/kg of vericiguat daily by oral gavage. Two control groups were used, untreated dTGR and healthy WT controls received the vehicle solution (10% transcutol/ 20% cremophor/ 70% water) daily by oral gavage. Animals were randomly distributed according to their mother and body weight.

The treatment groups were subject of cohort I-IV (see Figure 4). In cohort I BP was measured with the tail cuff method and the animals were single housed for 12 h in a metabolic cage (MC) for urine collection in week 5, 6 and 7. The echocardiography was performed at the end of week 6, rats were sacrificed, and organs harvested at the beginning of week 7. In cohort II the haemodynamic performance of the heart was assessed in week 6 using a Millar tip catheter. In cohort III the heart and kidney were perfused with Microfil in week 7 for *ex vivo, post-mortem* micro-computer tomography (µCT). In Cohort IV a telemetry transmitter was implanted before start of treatment in week 3 and animals were sacrificed for cell isolation in week 7.
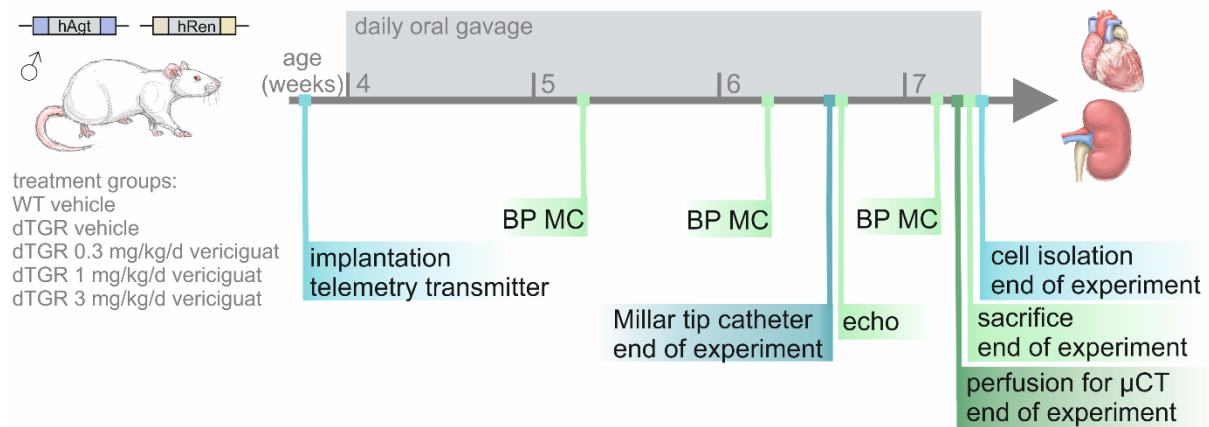
Figure 4 Experimental design of vericiguat treatment in the dTGR model.
Rats, double-transgenic for human angiotensinogen and human renin were included at the age of four weeks. They were randomly assigned to the treatment groups: WT vehicle, dTGR vehicle, dTGR 0.3 mg/kg/d, 1 mg/kg/d or 3 mg/kg/d vericiguat. The substance was applied by daily oral gavage over a period of three weeks. In cohort I blood pressure (BP) measurement and metabolic cage (MC) for urine collection were conducted in week 5, 6 and 7. The echocardiography was performed at the end of week 6 and rats sacrificed at the beginning of week 7. In cohort II the haemodynamic performance of the heart was assessed in week 6. In cohort III the heart and kidney were perfused for micro-CT (µCT) in week 7. In Cohort IV a telemetry transmitter was implanted in week 3 and animals were sacrificed for cell isolation in week 7.

2.2.1.3 Vericiguat solution for treatment

The vehicle solution contained the dissolvent (10% v/v transcutol/20% v/v cremophor/70% v/v water) only. Vericiguat was dissolved using vehicle solution at a concentration of 1.5

mg/ml for the 3 mg/kg/d dose. In detail, Vericiguat was dissolved in transcutol at 37°C. Further, cremophor was added, and the solution was incubated for 15-30 min at 37°C. Water was added to the solution shortly before gavage. For the 1 mg/kg/d dose the 1.5mg/ml vericiguat stock solution was 1:3 diluted in vehicle solution to gain a concentration of 0.5 mg/ml vericiguat. For the 0.3 mg/kg/d dose the 1.5 mg/ml stock solution was diluted 1:10 in vehicle solution to gain a concentration of 0.15 mg/ml vericiguat. All solutions were prepared freshly on the day of use. A volume of 150 to 600 µl was gavaged according to the bodyweight to reach the desired dose. For example, an animal with a body weight of 101-105 g would get 206 µl of the respective solution.

2.2.1.4 Sacrifice

At the end of experiment, rats were sacrificed under 3-4% isoflurane anaesthesia as required by the Regulation for the Protection of Animals Used for Experimental and Other Scientific Purposes ("*Tierschutz-Versuchstierverordnung*"). If not stated otherwise, blood was collected after decapitation, organs harvested, snap frozen in liquid nitrogen and stored at -70°C until further used. Rat hearts from cohort 1 (echocardiography) were dissected in longitudinal orientation. The left ventricle was prepared according to the six regions (posterior base, posterior mid, posterior apex, anterior apex, septal/anterior mid, septal/anterior base) used in echocardiography analysis (see Speckle-Tracking Echocardiography). The renal capsule, fat pad and adrenal glands were removed, kidneys were transversely cut in half for further analysis.

2.2.1.5 Echocardiography

Transthoracic echocardiography measurements were conducted by professional scientific staff of the Preclinical Research Centre (PRC) at the Max Delbrück Center in Berlin. Rats were weighted, initially anesthetized with 3-4% isoflurane and positioned on a 37°C heat pad where body temperature was controlled throughout the measurement. Anaesthesia was maintained through a breathing mask with minimum (1-2.5%) isoflurane. The heart rate and echocardiogram (ECG) were monitored. Hair was removed from the chest and ultrasound gel was applied. Echocardiography scans were recorded in parasternal long and short axis view using the high-resolution ultrasound system Vevo 3100 (Fujifilm, VisualSonics Inc.) with a 30 MHz ultrasound transducer (MX250). The echocardiography data was provided for

analysis by the scientific staff at the PRC, and parameters calculated as described in the following paragraphs.

The B-Mode (brightness modulation) displays the echo amplitude in grey scale. B-Mode analysis were used in short and long parasternal axis for global systolic and diastolic cardiac functional parameters of the left ventricle. Stroke volume (SV), Ejection fraction (EF), heart rate (HR), base-apex distance and cardiac output (CO), calculated with [SV*HR/1000] were measured. In addition, the B-Mode data was used for speckle-tracking echocardiography (see 2.2.1.6).

The M-Mode (motion mode) traces the motion over time at a desired location. M-Mode analysis in short and long axis view were used to gain conventional two-dimensional parameters on cardiac function. Left ventricular end-diastolic diameter (LVEDD) and end-systolic diameter (LVESD), left ventricular posterior wall in diastole (LVPWd) and in systole (LVPWsys), left ventricular anterior wall in diastole (LVAWd) and systole (LVAWsys) were measured. Fractional shortening (FS) [100*((LVEDD-LVESD)/LVEDD)], corrected LV mass [(1.053*((LVEDD+LVPWd+IVSd)^3 - LVEDD^3))*0.8] [137,138] and relative wall thickness [(2*LVPWd)/LVEDD] were calculated with the respective formula.

Pulse-wave (PW)-Doppler sonography measurements were used for diastolic left ventricular function. PW-Doppler measures the blood flow at the mitral valve including the duration of the E-wave (E), a parameter for early diastolic filling, the duration of the A-wave (A), a parameter for late atrial diastolic filling, isovolumetric relaxation time (IVRT) and mitral valve deceleration time (MV decel). The E-wave to A-wave ratio (E/A) was calculated.

Tissue doppler imaging (TDI) visualizes the vessel wall velocity at the mitral annulus. Parameters from TDI are the velocity of the mitral annulus during early passive diastolic LV filling (E') and late atrial contraction (A'), diastolic dysfunction ratio of E' to A' (E'/A') and filling index (E/E').

All echocardiography parameters were calculated according to the standard protocol (Vevo 770® Standard Measurements and Calculations, Rev 1.2; Visual Sonics) using the Vevo LAB Software. The scans were stored in raw data format for further analysis. Transthoracic echocardiography was performed in cohort 1 for complete cardiac characterization, and cohort 3 for calculation of the left ventricular mass.

2.2.1.6 Speckle-Tracking Echocardiography

Speckle-tracking echocardiography (STE) is a diagnostic tool that allows the reproducible, precise assessment of the myocardial function in a two-dimensional, non-invasive manner [139,140]. The STE-derived parameter *strain* reflects myocardial tissue deformation. More precisely, a grey-scale image derived from echocardiography B-Mode is the result of the ultrasound beam scattered by the cardiac tissue. The resulting bright speckles can be traced by the STE software while the underlying algorithm calculates the change in length of the myocardium (in percentage) over a period of time [141].

In humans, STE-derived parameters reflect tissue deformation and can be used as a prognostic factor for early cardiac dysfunction [142]. Global longitudinal peak systolic strain was included in guidelines to detect changes in ventricular (systolic) function [143]. Longitudinal movement of the left ventricle is mainly the result of contraction of subendocardial fibres [144]. Parameters from STE are a valuable readout to assess myocardial function in mice and rats [145].

The provided echocardiography B-Mode loops were filtered according to their quality regarding image acquisition artefacts and differentiability of endo- and epicardium. The parasternal long axis view was used to measure the shortening of the myocardium as global and regional longitudinal strain (Figure 5a). The visibility of aortic and mitral valve served for orientation. The parasternal short axis view was used to measure the global and regional circumferential reduction and radial thickening of LV wall as circumferential and radial strain, respectively (Figure 5b). The papillary muscles at the mid-cavity segment served as orientation. The endocardium was manually traced during the end-diastolic phase, while the epicardium was automatically captured by the software and only corrected when necessary. The mean was calculated from three independent measurements of three consecutive cardiac cycles. The global strain is calculated from the total myocardial movement with 48 speckles equally distributed along the endocardium. The regional strain was calculated for six segments each defined by eight speckles. The cardiac regions are defined according to standardized myocardial segmentation [146]. In the long axis regions are posterior base (1), posterior mid (2), posterior apex(3), anterior septal apex (4), anterior septal mid (5), anterior septal base (6) and in the short axis the regions are anterior free wall (1), lateral wall (2), posterior wall (3), interior free wall (4), posterior septal wall (5), anterior septum (6) (scheme of Figure 5a, b). For strain analysis 18% of long axis images (12/67) and 34% (23/67) of short axis images did not pass quality criteria (Figure 5c).
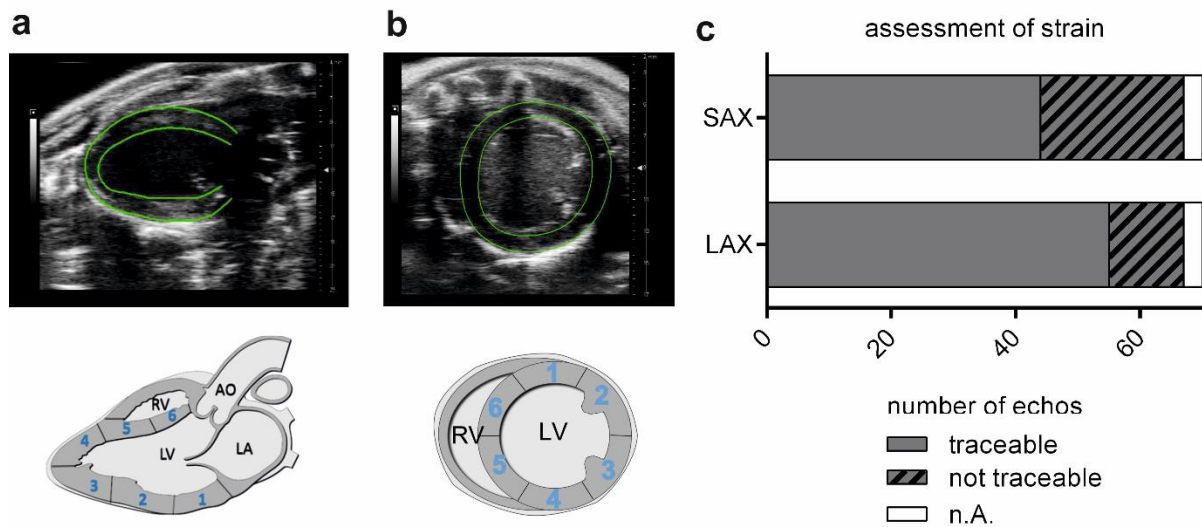
Figure 5 STE tracing of long axis, short axis, and assessment of strain.
a Longitudinal strain tracing in long axis (LAX), b circumferential and radial strain tracing in short axis (SAX) with schematic illustration of myocardial segments 1-6 underneath each image, respectively. c Number of animals used for assessment of strain in echocardiography in short and long axis.

2.2.1.7 Haemodynamic measurement via Millar tip catheter

Haemodynamic measurement was carried out and values calculated by professional scientific staff of the PRC at the Max Delbrück Center in Berlin. The provided data were statistically tested and interpreted by me (Sarah M. Kedziora). Animals received carprofen (5 mg/kg BW; *s.c.*) 30 min prior to the initial anaesthesia with 3-4% isoflurane. Narcosis was maintained with 1-2% isoflurane, hair was removed, and skin disinfected. The animals were intubated and kept on a heating plate at 37°C throughout the experiment. The Millar tip catheter was inserted through the right carotid artery into the left ventricle. Echocardiography and pressure-volume-values were used to control the correct placement of the catheter. To measure volume-independent parameters using occlusion the diaphragm and *vena cava* were dissected. The *v. cava* was occluded multiple times for approx. 3 sec following a 2 min break. The animals were decapitated under final narcosis and organs and blood harvested. Haemodynamic parameters were determined using LabChart software (v8.1.13; AD Instruments). This includes the following pressure measurements, mean arterial pressure (MAP), left ventricular end-systolic and end-diastolic pressure (LVESP, LVEDP), and left ventricular maximal, minimal, and average pressure during a loop (LV P_{max}, LV P_{min}, LV P_{mean}). These measures of left ventricular end-systolic and end-diastolic volume (LVESV, LVEDV) were taken. The stroke volume (SV = [LVEDV-LVESV]), cardiac output (CO = [SV*HR]), cardiac index (CI = [CO/BW]), arterial elastance (Ea = [LVESP/(V_{max}-V_{min})]) and total peripheral

resistance (TPR = [MAP/CO]) were calculated. The maximal and minimal rate of rise of left ventricular pressure (dP/dt max, dP/dt min), stroke work (SW = [MAP*SV]) and isovolumetric relaxation constant (τ) were measured.

2.2.1.8 BP measurement *in vivo* via Telemetry and Tail Cuff

Measurements of BP were performed by professional scientific and technical staff of the PRC at the Max Delbrück Center, Berlin.

In cohort III the BP was non-invasively measured with the Tail Cuff Method at single timepoints at five, six and seven weeks of age. Therefore, the animal was placed in the rodent holder (CODA system), the tail cuff was attached to the tail and BP measured after 5-10 min adaptation.

In cohort IV, invasive BP measurement was conducted using a telemetric system (DSI). The telemetric transmitter (PA-C10; DSI) was implanted and the sensor located infrarenal in the abdominal aorta at the age of three weeks. The transmitter was sewed to the peritoneum and the abdomen closed with surgical clips. Pain management was conducted using the analgetic metamizole one day pre-surgery and three days post-surgery (400 mg/kg/24h). For BP detection animals were housed separately, each cage placed on its respective transmitter detection plate. The invasive telemetry technology allows continuous measurement of BP throughout the period of treatment. Animals from the telemetry cohort were sacrificed at the age of seven weeks with 3-4% isoflurane anaesthesia and decapitation with subsequent isolation of cardiac cells (Chapter 2.2.3).

2.2.1.9 Urine and blood analysis

The urine was collected at week five, six and seven weeks for 12 h in a metabolic cage, centrifuged (2700 x g, 10 min, 4°C), aliquoted and stored at -80°C for further analysis. Albumin and creatinine were detected with ELISA technology according to the manufactures' instructions at Bayer Pharmaceuticals as previously described [147].

2.2.2 Organ perfusion and micro-computer tomography

After an initial isoflurane inhalation narcosis (5%) and following isoflurane overdose (10%), a Y-shaped laparotomy was performed to expose the organs and the thymus carefully removed. In short, the organs were rinsed and casted in a protocol-based order. The organ

casting required several occlusions, incisions, and cannulas. The vessels were sealed with suture thread. In the first step, the left subclavian artery, left common carotid artery, brachiocephalic artery, left brachiocephalic vein, *superior* and *inferior vena cava* were sealed with suture. Next, a cannula (20G, B.Braun) was introduced into the aorta proximal to the renal arteries and fixed with a clamp. The *inferior vena cava* was cut to drain the blood from the heart using PBS-Heparin (B.Braun; 25 IU / 5 ml in 500 ml 1x PBS). An appropriate volume of Microfil (Flow Tech, Inc.) was freshly prepared at a ratio of 0.1/1/1 curing agent / pigmented solution / diluent for a suited viscosity to fill microvasculature. Microfil was applied to the heart at a constant speed (14 ml/min) via a peristaltic perfusion pump. The *inferior vena cava* and ascending aorta were sealed near the heart as soon as Microfil appeared consistently at the incision and coronary arteries were visibly filled. The Microfil was cured for two hours at room temperature. The organs were harvested and stored in 4% PFA at 4°C until scanned with µCT (Figure 6 a).

The micro-computer tomography (CT) scanning and data integration were conducted by professional scientific staff of the PRC at the Max Delbrück Center in Berlin. The statistical analysis and interpretation were done by me (Sarah M. Kedziora). The aim was to calculate the volume of the vascular tree and diameter of vessels. Samples were wrapped in foil and scanned with a micro-CT scanner (SkyScan 1276, Bruker, BE) using the Vendor's software for image acquisition. A 360°C acquisition step and shoot mode with source current of 55 µA was used. The flat field correction was applied, and images reconstructed with NRecon software (beam-hardening correction: 42%; ring-artefact correction: 5%). A 3D visualization of the cardiac vasculature was prepared using CTVox. The cut-off value was defined to 0.4 mm regarding existing literature [33,148]. Figure 6 b) shows three viewing angles of micro-CT scanned vasculature of hearts perfused with Microfil contrast agent.
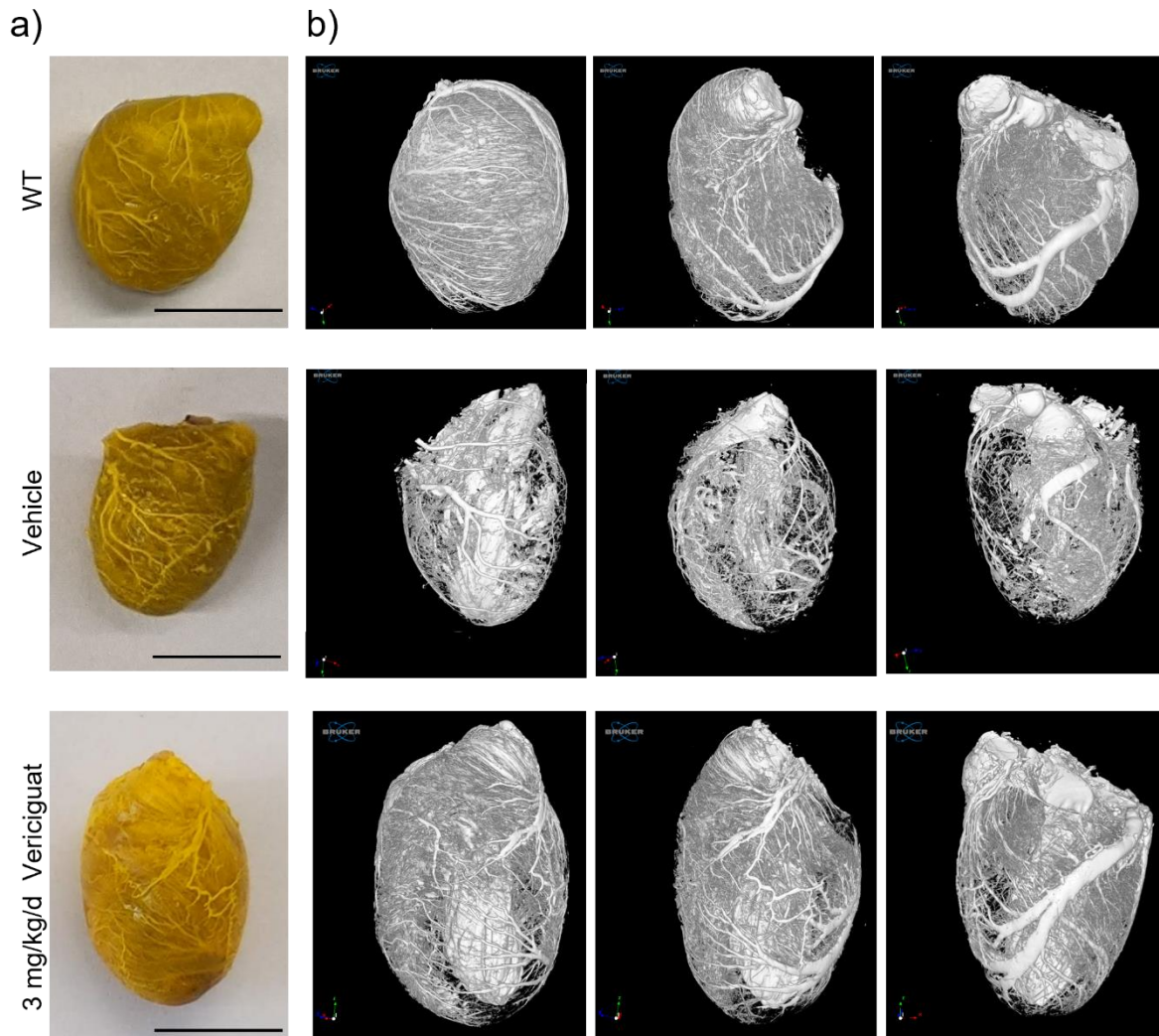
Figure 6. Microfil perfusion and micro-CT.
*a Hearts were perfused with Microfil yellow, coronary arteries are visible. Scalebar 1 cm. **b** Microfil perfused organs were scanned with the micro-CT scanner and three angles of 3D reconstructed vascular tree in each heart is displayed for wild-type, vehicle, and 3 mg vericiguat dose.*

2.2.3 Cell culture methods

2.2.3.1 Isolation of primary cardiac cells

The isolation of cardiac cells from the ventricles was adapted for rats, based on the Langendorff-free method [149]. Adjustments to the use of blebbistatin as a contraction inhibitor instead of 2,3-butanedione monoxime (BDM) were done [150]. Blebbistatin is superior over BDM as it does not inhibit the mitochondrial respiration [151]. Advantage of blebbistatin over BDM in isolated primary rat cardiomyocytes is shown in the results section 3.5.1.

In addition non-cardiomyocytes were isolated in a simultaneous approach based on the protocol of Gündüz et al. [152]. The combination of both methods allowed the isolation of viable

cardiomyocytes, cardiac fibroblasts, and cardiac endothelial cells from a single rat heart. The protocols combine direct needle perfusion through the left ventricle *ex vivo*, enzymatic digestion, gravity settling, feature-driven plating and column-based separation via antibody labelling and magnetic beads.

All buffers and solutions (Table 1, Table 2) were prepared with distilled, autoclaved water, sterile filtered, aliquoted, and stored at 4°C or -20°C. Prior to use the contraction inhibitor blebbistatin was added freshly, the pH was adjusted to 7.6 and solutions pre-warmed to 37°C for isolation. The contraction inhibitor blebbistatin [MW 292.33 g/mol] was dissolved in DMSO at a stock concentration of 25 mmol/l. An appropriate volume of blebbistatin was added to buffer and media directly before use to gain a final concentration of 10 µM.

For isolation of primary cardiac cells from the rat heart, the animal was anaesthetized with 3-5% isoflurane for 3 min. and decapitation followed. For dissection of the heart, the thorax and abdomen were disinfected, opened and fat tissue carefully removed. The apex was punctured with the EDTA syringe needle into the left ventricle. Vena cava inferior and aorta descendants were cut open and the heart immediately flushed with EDTA buffer (10 ml, 1-2 min). EDTA buffer served to remove blood, inhibit contraction and coagulation. Next, vena cava superior, aorta ascendants and pulmonary trunk were clamped close to guarantee perfusion via the coronary vasculature. The heart was transferred to a 6-well petri dish containing fresh EDTA buffer. Digestion was carried out by sequential injection of 10 ml EDTA buffer, 5 ml PB buffer and repetitive injection of recycled collagenase buffer for a maximum of 20 min. The perfusion buffer was used to remove EDTA and remaining blood from the tissue. Signs of successful tissue digestion included softening of tissue, white edges, and cloudiness of collagenase buffer. Remaining vessels and atria were discarded, heart tissue quartered in 3 ml fresh collagenase and gently pulled into 1 mm pieces using forceps for maximum of 20 min. The digestion was terminated using 5 ml FBS containing stop buffer. The cell suspension was filtered through a 100 µm filter mesh, washed with another 5 ml stop buffer and equally transferred to two 15 ml falcons. Remaining tissue from the filter was used to isolate primary cardiac fibroblasts and endothelial cells.

For primary cardiac myocytes, a gravity settling series was conducted. A first 30 min settling was followed by using 4 ml of the three calcium reintroduction buffers (CR) gradually restoring physiological calcium levels. Between CR-buffers, the cell pellet was enriched with viable cardiomyocytes and dead cells removed with the supernatant. The final pellet was resuspended in 1 ml plating medium and cells counted with a Fuchs-Rosenthal counting

chamber. For cardiomyocytes 96-well plates were pre-coated with 50 µl of Matrigel (1:50 diluted in DMEM) per well and washed with 1x PBS before seeding. Cells were seeded to the pre-coated plate at an appropriate density in plating medium. After 1 hour at 37°C and 5% CO_2 the medium was changed to culture medium.

Table 1 Buffer and solutions for cardiomyocyte isolation with Langendorff-free methodology.
[+] Blebbistatin stock solution [25 mM] was added directly before use to gain a concentration of 10 µM, pH 7.6.

Substance	Molecular weight (g/mol)	Final concentration (mmol/l)	Required mass (g/l)
EDTA buffer[+]			
NaCl	58.44	130	7.5972
KCl	74.55	5	0.37275
NaH_2PO_4	119.98	0.5	0.05999
HEPES	238.3	10	2.383
Glucose	180.16	10	1.8016
Taurin	125.15	10	1.2515
EDTA	292.24	5	1.4612
Perfusion buffer[+]			
NaCl	58.44	130	7.5972
KCl	74.55	5	0.37275
NaH_2PO_4	119.98	0.5	0.05999
HEPES	238.3	10	2.383
Glucose	180.16	10	1.8016
Taurin	125.15	10	1.2515
$MgCl_2$	95.5	1	0.095

Table 2. Buffer, media, and solutions used for isolation and culture of primary cardiac myocytes.
[+] Blebbistatin stock solution [25 mM] was added directly before use to gain a concentration of 10 µM, pH 7.6.
[#]including 10 µM blebbistatin

Substance	Final concentration (% v/v)	Required volume (ml)
Culture medium[+] (total volume)		100
M199 medium	96	96
BSA [5% w/v in 1x PBS]	2	2
Insulin-Transferrin-Selenium [100x]	1	1

CD lipids	1	1
Penicillin/Streptomycin	1	1
Plating medium[+] (total volume)		100
M199 medium	94	94
FBS	5	5
Penicillin/Streptomycin	1	1
Stopp buffer		10
Perfusion buffer[#]	95	9.5
FBS	5	0.5
Calcium Reintroduction Solutions	Culture media[#] : perfusion buffer[#]	
Calcium Reintroduction Solution I	1 : 3	
Calcium Reintroduction Solution II	1 : 1	
Calcium Reintroduction Solution III	3 : 1	
Collagenase buffer	Final concentration (U/ml)	
Collagenase II	525	
Collagenase IV	450	
Protease XIV	2	
Dissolved in total volume of PB buffer [#]	13 ml	

For cardiac fibroblast isolation, 0.0625 g BSA, 0.0025 g Collagenase II and Protease, 120 µl of 2.5% Trypsin stock solution and 188 µl of 0.1 M $CaCl_2$ stock solution were added freshly to 25 ml of Disco buffer (Table 3). The remaining tissue from cardiomyocyte isolation were mixed with 5 ml Disco buffer, inverted 2-3x and incubated (15 min, 37°C). After repeated inverting (2-3x), the supernatant was transferred to a new tube, centrifuged (300 x g, 5 min, 4°C) and the pellet resuspended with 10-20 ml fibroblast medium. The fibroblast medium consisted of DMEM supplemented with 10% FBS, 1% P/S and 1% HEPES. Fibroblasts were cultured at 37°C, 5% CO_2 and medium refreshed every 48 hours without washing. The remaining tissue and supernatant were used to isolate cardiac endothelial cells.

Table 3. Buffer and solutions used for fibroblast isolation.

Substance	Molecular weight	Final concentration	Required mass or volume per 1l
Dispase/Collagenase (Disco) buffer			

	Molecular weight	final concentration	Required mass
DNase I (Roche)	10 000 unit/l	0.1 unit/l	10 µl
NaCl	58.44 g/mol	136.9 mmol/l	8.0 g
KCl	74.55 g/mol	4.96 mmol/l	0.37 g
Na$_2$HPO$_4$	119.98 g/mol	0.83 mmol/l	0.1 g
Hepes	238.3 g/mol	25.18 mmol/l	6 g
Glucose	180.16 g/mol	11.1 mmol/l	2 g
	Molecular weight	**final concentration**	**Required mass (g per 10 ml)**
CaCl stock solution	110.98 g/mol	0.1 mmol/l	1.1099
Trypsin stock solution	23.4 kDa	2.5%	0.25

Cardiac endothelial cells were isolated using the anti-APC micro beads and anti-rat CD31 APC-conjugated antibody according to the manufactures protocol. Remaining tissue was transferred to a gentleMACS C tube and dissociated with the heart_02 program on the gentleMACS dissociator. The suspension was filtered through a 30 µM filter and washed with GGG. After centrifugation (300 x g, 10 min, 4°C) the pellet was resuspended in 100 µl GGG and 2 µl anti-CD31 antibody (1:50) per 10^7 cells and incubated (10 min, 4°C). Washing with 1-2 ml GGG and centrifugation (300 x g, 10 min, 4°C) was repeated twice. Cells were resuspended in 80 µl GGG plus 20 µl anti-APC micro beads per 10^7 cells, incubated (15 min, 4°C) and washed as described before. The cells were resuspended in 500 µl GGG and applied to a LS column placed in the gentleMACS separator. After washing (3x 3ml) the column was removed from the magnetic field and CD31 positive cells eluted with 5 ml GGG using the plunger. The column-based separation was repeated twice, cells counted and cultured in endothelial cell medium at 37°C, 5% CO$_2$. Endothelial cells were seeded to Matrigel pre-coated plates (see cardiomyocyte section) at an appropriate density. For endothelial cell medium RPMI was supplemented with 20% FBS and 1% P/S. GGG buffer consists of 1x PBS with 0.5% BSA (5 g/l) and 2 mM EDTA (20 ml [100 mM EDTA stock]/l).

2.2.3.2 Energetic profile analysis with Seahorse Assay

The energetic profile of isolated primary cardiac cells was detected using the Seahorse Assay technology (Agilent). Mitochondrial oxidative phosphorylation and glycolysis are the main cellular pathways to generate energy. Adaptation to environmental changes can lead to a switch between these two pathways. With the Agilent Seahorse XF Cell Mito Stress Test

(User Guide Kit 103015-100) the oxygen consumption rate (OCR), a key parameter of mitochondrial oxidative phosphorylation can be recorded (Figure 7A). The Agilent Seahorse XF Glycolysis Stress Test (User Guide Kit 103020-100) directly measures the extracellular acidification rate (ECAR), a readout for glycolysis (Figure 7B). The combination of both plate-based live cell assays can be conducted for metabolic measurements in real time.

The Seahorse cartridge contains two biosensor fluorophores at the bottom of the cartridge sleeve. One is quenched by oxygen, while the other is sensitive to protons. A sensor with optic fibres is lowered into the cartridge sleeve and emits light to excite these fluorophores. Alterations in oxygen and pH levels are detected by the sensor as changes in fluorescence emission. The sensor cartridge was hydrated according to the protocol (Agilent, protocol 103536-400). In summary, the ports of the 96-well utility plate were filled with sterile water and sensor cartridge lowered onto the utility plate. An aliquot of Seahorse XF Calibrant and the cartridge were incubated in a non-CO_2 incubator at 37°C overnight. On the day of the assay, sterile water was replaced by 200 µl pre-warmed XF Calibrant and cartridge incubated before filling of the ports (37°C, no CO_2, 45-60 min).

For the Seahorse Assay cells were seeded into the cell culture plate on the day of isolation after 1 h culture (5% CO_2, 37°C) at a density of $1x10^3$ cardiomyocytes/well and $6x10^4$ endothelial cells/well. Fibroblasts were measured on day 7 of culture (5% CO_2, 37°C) and seeded to the Seahorse Plate on day 6 with a density of $4x10^4$ fibroblasts/well.

During the assay, the mitochondrial respiration and glycolysis are manipulated using different chemical substances (Figure 7). When cells are previously starved, glucose directly stimulates glycolysis and thereby increases ECAR, giving the opportunity to calculate basal glycolysis by subtracting non-glycolytic acidification. Oligomycin inhibits the mitochondrial F0F1-ATP synthase (complex V), thus decreasing OCR resulting in lower mitochondrial respiration that is linked to ATP production. At the same time oligomycin forces the cell to produce energy by glycolysis detected as an increase in ECAR, namely maximal glycolytic capacity. The uncoupling agent carbonyl cyanide-4 (trifluoromethoxy) phenylhydrazone (FCCP) uncouples the proton gradient and therefore lowers the mitochondrial membrane potential. As a result, the electron transport chain is disrupted, increasing the oxygen consumption of complex IV. This can be measured as increase in OCR representing maximal mitochondrial respiration and spare respiratory capacity. Rotenone and antimycin A block the electron transport chain by inhibition of complex I and III, respectively which results in decrease of OCR and detection of non-mitochondrial respiration. During method

establishment, the concentrations of substances and chemicals were titrated to identify the suitable concentration for each cardiac cell type.
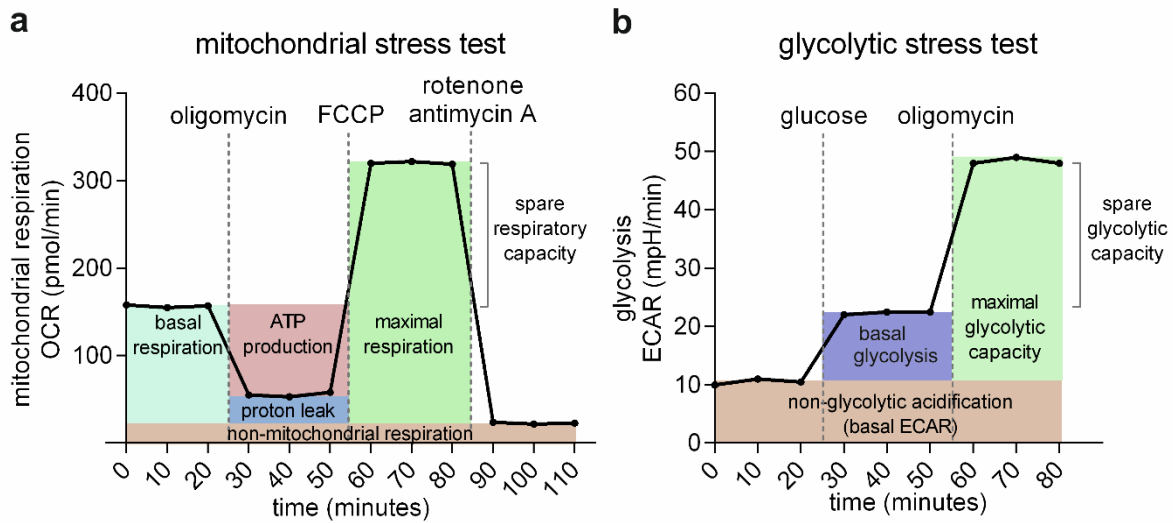
Figure 7. Schematic overview of mitochondrial and glycolytic stress test.
a Mitochondrial stress test measures mitochondrial respiration as oxygen consumption rate (OCR in pmol/min) over time. Due to sequential injection of oligomycin, carbonyl cyanide-4 (trifluoromethoxy) phenylhydrazone (FCCP), rotenone and antimycin A the basal and maximal and non-mitochondrial respiration, ATP production, proton leak and spare respiratory capacity can be detected. b Glycolytic stress test measures glycolysis as extracellular acidification rate (ECAR in mpH/min) over time with injection of glucose and oligomycin. Basal glycolysis, maximal glycolytic capacity, non-mitochondrial acidification, and spare glycolytic capacity can be calculated when cells are starved without glucose before experimental testing. The scheme was constructed with GraphPad Prism and the layout edited with CorelDraw.

Agilent Seahorse XF Base Medium pH 7.4 was supplemented with 0.68 mM glutamine [200 mM stock] with or without 5.55 mM glucose [1M stock]. Port solutions were prepared 10X concentrated just prior to assay using the pre-treatment medium and 2.5 mM stocks of chemicals. The stimulation was carried out with glucose – oligomycin – FCCP – rotenone/antimycin A at a final well concentration of 5.55 mM – 10 µM – 10 µM – 1 µM/1 µM for cardiomyocytes or 5.55 mM – 2 µM – 1 µM – 1 µM/1 µM for fibroblasts and endothelial cells. The concentrations were previously titrated for each cell type.

The four ports of the cartridge were filled with injection solutions (A = 20 µl, B = 22 µl, C = 25 µl, D = 27 µl). Four injection strategies were carried along the experiment for each animal as listed in Table 4 with six technical replicates for cardiomyocytes and fibroblasts and three for endothelial cells. The controls were used to judge the viability, activity, and integrity of the cells. The starved-strategy was used to assess ECAR and the not-starved-strategy to measure OCR. Prior to the assay, the plate was centrifuged (300 x g, 5 min), medium removed and cells washed with 180 µl Seahorse medium per well. The step was repeated

and a final volume of 180 µl per well added for pre-treatment and incubation at 37°C in the non-CO_2 incubator (45-60 min).

Table 4. Injection strategies for Seahorse Assay.

Strategy	Pre-treatment	Port A	Port B	Port C	Port D
Starved	Only glutamine	glucose	oligomycin	FCCP	rotenone/ antimycin A
Not starved	glutamine + glucose	Medium as in pre-treatment	oligomycin	FCCP	rotenone/ antimycin A
glucose Boost control	glutamine + glucose	glucose	glucose	glucose	glucose
Viability/Activity control	glutamine + glucose	Medium as in pre-treatment	Medium as in pre-treatment	Medium as in pre-treatment	Medium as in pre-treatment

A baseline (three cycles) was recorded before stimulation of the cells. After injection of solutions from port A, B and C, five cycles were recorded, three cycles were recorded after injecting solution from port D. One cycle in the consists of 3 min. mixing, 3 min. waiting and 3 min. measuring for fibroblasts and adaptation to 1 min mixing for cardiomyocytes and endothelial cells due to high sensitivity of cardiomyocytes to currents. OCR (pmol/min) and ECAR (mpH/min) values were normalized to flow cytometric measured cell number or cell quantity related Hoechst intensity (see Hoechst assay 2.2.6.1). Replicates with technical issues were excluded. Values are reported relative to basal OCR or ECAR for better visualisation. For method establishment purposes, the length and number of cycles, injection port solutions and concentrations, cell number and utilized contraction inhibitor were adapted and modified as indicated, respectively.

2.2.4 Molecular biological methods

2.2.4.1 Gene expression analysis

The expression of marker genes was measured with the two-step, reverse-transcription quantitative polymerase chain reaction. Therefore, ribonucleic acid (RNA) was isolated from heart or kidney tissue and reverse transcribed into complementary desoxyribonucleic acid (cDNA) for stability reasons. The quantity of the target gene sequence in the cDNA was

determined by with either TaqMan chemistry that utilizes the primer-probe detection method or the Sybr Green Dye detection method.

2.2.4.2 RNA isolation

The RNA was isolated from rat kidney tissue or from posterior mid segment two of rat heart tissue with the RNeasy Mini Kit. According to the manufacture protocol, a small piece of tissue was homogenized with 1 ml Qiazol Lysis Reagent and precellys ceramic beads for two cycles (15 sec, 5500 rpm) in a tissue homogenizer.

The RNA from primary cardiomyocytes seeded at a density of $2x10^4$ cells/well (24-well plate) was isolated after overnight culture (37°C, 5% CO_2, 5.55 mM glucose in M199). Quiazol was directly added (500 µl/well) and cells lysed by pipetting up and down. The cardiomyocyte sample was stored at -70°C until protocol was proceeded.

The homogenate was incubated (5 min, RT), supplemented with 200 µl chloroform and inverted (5x). After incubation (2-3 min, RT), centrifugation (15 min, 12000 x g, 4°C) 100 µl of the RNA containing upper phase were combined with 70% ethanol (1:1) mixed and added to the RNAse Mini Column. The incubation (1 min) was followed by centrifugation (30 sec, 8000 x g), discard of flow through and washing with RW1-buffer. DNA that remained on the column was digested (15 min, RT) using DNase I 1:8 diluted in RDD-buffer. The bound RNA was cleaned with several washing steps (1x RW1-buffer, 2x RPE-buffer) alternating with centrifugation (30 sec, 8600 x g) and a dry centrifugation step (1 min, 12900 x g). To elute the RNA from the column, it was incubated with 30 µl RNAse free water (5 min, RT) before final centrifugation (1 min, 12900 x g). The samples were stored at -80°C.

2.2.4.3 cDNA transcription

The RNA concentration was determined at 260 nm wavelength with a Nanodrop Spectrophotometer ND-1000 (PeqLab). The absorbance ratios 260/280 and 260/230 served as quality controls as they indicate a contamination with proteins and phenol, respectively. One microlitre was added to the device for measurement, RNase free water served as blank. RNA yields > 2 µg/µl were diluted 1:1 in RNase free water. RNA samples were diluted in water to a final concentration of 2 µg/µl in 10 µl. For the synthesis of single-stranded cDNA from RNA templates the high-capacity cDNA reverse transcription kit (Thermo Fisher Scientific) was used according to manufactures protocol.

The oligonucleotide primers in the kit have a high binding probability as they are designed of six randomly assigned base pairs. After 1:1 dilution with 2x reverse transcription master mix (see Table 5), transferred into thermal cycler using the cDNA synthesis program (10 min, 25°C – 120 min, 37°C – 5 min, 85°C, final 4°C). cDNA samples were 1:10 diluted in ddH$_2$O and stored at 4°C for direct use in RT-qPCR or -20°C for extended storage.

Table 5. Reverse transcription master mix (2x)

Substance	Volume [µl]/reaction
10x Reverse Transcription Buffer	2.0
10x Reverse Transcription Random Primers	2.0
25x dNTP Mix [100 mM]	0.8
MultiScribe Reverse Transcriptase [50 U/µl]	1.0
Nuclease-free H$_2$O	4.2
Total volume	10.0

2.2.4.4 Real-time quantitative polymerase chain reaction (RT-qPCR)

The primer and probes were designed exon spanning with Primer Express 3.0 and ordered from BioTez GmbH Berlin-Buch, DE. The primer concentration of 10 mM and probe concentration of 5 mM were obtained by dilution in ddH$_2$O and stored at -20°C. RT-qPCR is used to quantify the amplification of the target gene in real-time to determine the starting concentration in the sample. Both TaqMan and Sybr Green methodology use carboxy-X-rhodamine (ROX) as a passive reference dye not affected by the reaction. For TaqMan a reporter dye (6-carboxyfluorescin [FAM]) is bound to the 5' end and a non-fluorescent quencher dye (tetramethylrhodamine [TAMRA]) at 3' end of the oligonucleotide probe. Quenching of the reporter dye occurs when the oligonucleotide probe is intact and excitation energy transferred from the reporter (max. excitation 543 nm) to the quencher (max emission 517 nm) due to local proximity, called fluorescence resonance energy transfer [FRET]. After annealing of the probe to the complementary DNA strand the reporter is released upon 5' end cleavage by the DNA polymerase. Separation of the reporter from the quencher dye results in detectable fluorescence from the reporter dye. The Sybr Green dye creates a fluorescence signal when bound to double-stranded DNA. In both methods the fluorescence intensity is proportional to the amount of PCR product resulting from amplification cycles.

The master mix was prepared according to Table 6 and supplemented with 0.4 µl sample cDNA [10 ng/µl]. A standard series was created from a standard mix containing 5 µl of each cDNA sample that was diluted to 20, 10, 5, 2.5, 1.25 ng/µl. A no template control (NTC) containing water was carried along. The samples and standards were analysed in triplicates in a 96-well or 384-well plate. The plates were centrifuged (5 min, 2200 rpm) prior amplification in the QuantStudio 3 or 5 RT-qPCR System. The program consisted of step 1 (20 sec, 95°C) – step 2 (1 sec, 95°C) – step 3 (20 sec, 60°C) – step 4 (1 sec, 95°C) – step 5 (20 sec, 60°C) – step 6 (1 sec, 95°C) for TaqMan, and only step 1-3 for Sybr.

Table 6. Master mix for RT-qPCR

Component	Volume [µl]/reaction
TaqMan Fast Universal PCR Master Mix [2x] or Fast SYBR Green Master Mix [2x]	2.5
Forward primer [10 mM]	0.15
Reverse primer [10 mM]	0.15
Probe [5 mM] or ddH$_2$O	0.15
ddH2O	1.65
Total volume	4.6

The relative standard curve method was used for quantification. Gene expression was normalized to expression levels of the ribosomal gene *36b4* in heart and *18S* in kidney. In heart tissue *36b4* (also known as *Rplp0*) was used as a housekeeping gene because it is stable and recommended in rodent heart failure models [153,154].

2.2.4.5 DNA isolation and estimation of mitochondrial content

The protocol for DNA isolation from cardiac segment four was adapted from Quiros et al. [155]. DNA concentration was measured with Nanodrop Spectrophotometer ND-1000 (PeqLab) at 260 nm wavelength and adjusted to 10 ng/µl. The gene for mitochondrial NADH dehydrogenase 1 (mt-*Nd1*), part of complex I in the electron transport chain and *18S* were measured with RT-qPCR. The mt-*Nd1/18S* ratio serves as a measure for mitochondrial content.

2.2.5   Staining methods

2.2.5.1 Tissue histology

Heart and kidney tissues were fixed in 4% buffered formalin solution for a minimum of 48 hours. Formaldehyde binds to the amino group of proteins, thereby conserving the primary structure of the tissue. After dehydration, organs were embedded in paraffin with the automated tissue embedder and the following program: 60 min – 70% ethanol, 60 min – 80% ethanol, 120 min – 96% ethanol, 120 min – isopropanol, 180 min – xylol, 60 min – paraffin 62°C. The organs were embedded in paraffin blocs. Immediate cooling prevented air inclusions. The hearts were cut longitudinally and kidneys transversely, both at 2 µm thickness with an electronic rotary microtome. The tissue sections were transferred to the object slides with the help of a 40-42°C water bath. Paraffin was removed with xylol (3x 5 min) before staining and a descending alcohol series (100, 90, 80, 70, 50, 30% ethanol) was used to rehydrate the slices. Fixation of the staining with an ascending alcohol series (96%, 2x 100% ethanol, 2x xylol) was conducted before mounting unless stated otherwise. For one histological method, the respective samples were simultaneously stained and scanned with the Slide Scanner Panoramic MIDI (objective plan-apochromat 20x/0.8x; Zeiss) shortly after to ensure comparability.

For all immunofluorescence staining, antigen unmasking was carried out by boiling samples (20 min) in citrate buffer, cooling to room temperature (RT) and washing with distilled water (5 min). Protein digestion was achieved using 3% hydrogen peroxide (15 min, RT) for heart and trypsin (15 min at 37°C and 15 min at RT) for kidney tissue. Unmasking and digestion were not carried out for WGA staining. Further, 10% NDS (in 1x PBS) was used for blocking (60 min, exception: 10 min for collagen type 1) to prevent unspecific antibody binding. The primary antibody or reagent was diluted in 10% NDS and applied to the section with a concentration shown in Table 7. After incubation in a humidity chamber overnight (4°C), excess antibody was removed with 1x PBS. The appropriate secondary antibody was diluted in 1x PBS, incubated in a humidity chamber (120 min at RT) and excess antibody washed off with 1x PBS. Slides were mounted using Vectashield/Dapi medium. A negative control without secondary antibody was carried along. Immediate scanning was conducted to prevent fluorescence bleaching. Exposure times for Dapi (4',6-diamidino-2-phenylindole, 350/470 nm, ex/em), Cy3 (554/568 nm, ex/em), Fluorescein (495/515 nm, ex/em) were adjusted to the staining intensity.

Table 7. Concentrations for immunofluorescence staining in tissue.

Staining	Primary antibody/reagent, concentration	Secondary antibody, concentration
Collagen type 1	Anti-type I collagen, 1:20	Cy3-conjugated anti-goat IgG, 1:300
Fibronectin	Anti-fibronectin, 1:75	Cy3-conjugated anti-rabbit IgG, 1:300
Cd31	Anti-Cd31, 1:50	Cy3-conjugated anti-goat IgG, 1:100
Cd68, heart	Anti-Cd68 (ED1), 1:50	Cy3-conjugated anti-mouse IgG, 1:100
Cd68, kidney	Anti-Cd68 (ED1), 1:100	Cy3-conjugated anti-mouse IgG, 1:300
Podocin	Anti-podocin, 1:100	Cy3-conjugated anti-rabbit IgG, 1:300

The overview staining with haemalaun-eosin (HE) served to assess the glomerular size. HE staining was conducted following manufactures protocol (T865, Carl Roth GmbH + Co. KG). Shortly, slides were incubated with haemalaun solution (8 min). Acidic structures like DNA in the nucleus appear blue due to the alkaline property of haemalaun. The slides were rinsed (15 min) with tap water to obtain blue colour by pH increasing. Counterstaining was done with eosin G-solution (3 min). Alkaline structures like collagen, proteins, cytoplasm, and mitochondria are stained pink by the synthetic, acidic eosin. The slides were rinsed with distilled water before fixation and mounting.

Tissue components that are rich in carbohydrates can be stained with Periodic-acid-Schiff (PAS) staining. Free hydroxyl groups of glycogen and glycoproteins are oxidized by periodic acid to aldehydes that bind to fuchsin present in the Schiff's reagent. For PAS staining slides were incubated with 0.5% periodic acid (5 min) and cleaned with distilled water (3x 3 min). Schiff's reagent was incubated in a dark wet chamber and rinsed off after 10 min. Counterstaining with haemalaun (5 min) and immersing the slide in acid alcohol were each followed by cleaning off leftovers with distilled water. Final tap water rinsing (10 min) was done to obtain the blue colour.

Masson-Goldner-Trichrome (MGT) staining was conducted according to the manufactures protocol (3459, Carl Roth GmbH + Co. KG). Connective tissue appears green when visualized with MGT. In short, nuclei were stained with Weigert's iron haematoxylin solution A and B (ratio 1:1, 3 min). Incubation with Goldner's stain I (8 min), Goldner's stain II (3 min) and Goldner's stain III (5 min) was done. Slides were quickly washed out with acetic acid.

2.2.5.2 Histologic analysis

The collagen type-1 staining was used to detect perivascular fibrosis in heart tissue. Area (a) of the fibrotic area, media and lumen were encircled for all intact vessels of a cardiac section in Case Viewer. The perivascular fibrotic area was calculated as follows: [(a of connective tissue – a of vessel area)/ (a of connective tissue – a of lumen)].

The proportion of interstitial fibrosis in the heart was visualised by fibronectin staining. Five representative field of view (FOV) images were taken in Case Viewer (20x magnification), compared using Image J settings (8-bit conversion, threshold 15-255, measure particles 0-infinity) and reported as percentage of fibrotic area per FOV.

Immunofluorescence staining of endothelial cell marker Cd31 was used to detect capillary density. Five representative images were taken with Case Viewer. The Image J settings (8-bit conversion, threshold 20-255 [Black Background], analyse particles, summary count) were used to count capillaries per FOV.

The anti-Cd68 (ED1) antibody recognizes a protein on the lysosomal membrane [156]. In cardiac tissue, the Cd68-positive cells were counted in ten fields of view (20x magnification) using Case Viewer software and the Counter Dongle application. Colocalization of Dapi-positive nucleus helped to identify positive cells. In renal tissue, number of Cd68-positive cells and the percent of stained area were measured in ten representative FOV taken with Case Viewer (20x magnification) and compared using Image J (8-bit conversion, threshold 15-255, measure particles 0-infinity, summary count).

The tubular damage was evaluated with the semi-quantitative tubular injury score as previously described [157]. Ten images per kidney were scored in a blinded manner regarding the percentage of cast formation, degeneration, tubular dilation, brush border loss and necrosis.

Perivascular and interstitial fibrosis were analysed in MGT stained kidney sections. The outline of the vessel surrounding connective tissue, media and lumen was captured for three vessels per kidney using Case Viewer software. The ratio of fibrotic to vessel area was calculated with the formula described for the collagen type 1 staining. The interstitial fibrosis was measured in ten images per kidney recorded with Case Viewer software (20x magnification). Percentage of green stained connective tissue in the image was calculated using Image J. Background subtraction and colour deconvolution for the green signal were done. The images were converted to 8 bit and thresholds set to cover whole

tissue area or collagen area only. The percentage of interstitial fibrosis was calculated by [(collagen area/whole tissue area)*100].

PAS staining of glomeruli visualises glomerulosclerosis, which is a measure of constriction of capillaries and fibrosis in the glomerulus that is responsible for renal filtration. The sclerosis was measured in five images of glomeruli per kidney taken with Case viewer (40x magnification). In Image J the following settings were used: 8-bit conversion, upper thresholds adjusted to cover stained area only, convert to black and white, encircle glomerular area (region of interest), analyse particles size: 0 -infinity, summary of percent-stained area).

2.2.5.3 Immunofluorescence staining of isolated cardiac cells

Isolated primary cardiac cells were added to sterile slides, incubated (37°C, 5% CO_2, 2-3 h). Matrigel-precoated slides were used for cardiomyocytes and cardiac endothelial cells. Medium was removed, slides washed twice with 1x PBS and incubated with ice-cold 100% methanol (20 min). After drying, slides were stored at -20°C.

For immunofluorescence staining of primary cardiac cells, slides were washed with 1x PBS (10 min), proteins unmasked using PBST (0.3% Triton X in 1x PBS, 3x 10 min) and blocked with 10% NDS (30 min). The primary antibody was diluted in 10% NDS as shown in Table 8 and incubated overnight (4°C). Excess antibody was washed off with 1x PBS (3x 10 min) and the slides incubated with the appropriate Cy3- or Alexa 488-conjugated secondary antibody (1:500 in 1x PBS, 2h, RT). Double-stainings were conducted after each other. After washing with 1x PBS (3x 10 min) slides were mounted with Vectashield/Dapi medium. Images were taken with the Microscope Axio Imager.M2 (Zeiss) and objective plan-apochromat 63x/1.4 Oil DIC using the software Axio Vision. Filter sets for Dapi (4',6-diamidino-2-phenylindole, 350/470 nm, ex/em), Cy3 (554/568 nm, ex/em), Alexa 488 (490/525 nm, ex/em) were used, and excitation time adjusted to the fluorescence intensity.

Table 8. Concentrations for immunofluorescence staining in fixed primary cells.

Cell type	Primary antibody, concentration
Cardiomyocytes	Mouse anti-alpha actin, 1:200
	Rabbit anti-troponin T, 1:200
	Mouse anti-myosin, 1:100
Fibroblasts	Mouse anti-vimentin, 1:200

	Rabbit anti-PDGFR-alpha, 1:500
	Rabbit anti-fibronectin, 1:200
Endothelial cells	Goat anti-Cd31, 1:100

2.2.6 Protein chemistry methods

2.2.6.1 Hoechst assay

After seahorse assay, a nuclear staining with Hoechst was performed in isolated primary cardiomyocytes. Hoechst stock solution (2 mg/ml in HBSS [Hanks balanced salt solution, Sigma-Aldrich]) was diluted to 1 µg/ml (1:2000 in 1xPBS). After centrifugation of the plate (300 x g, 5 min, 4°C), supernatant was removed and 200 µl Hoechst [1 µg/ml] applied. After incubation (15 min, RT, dark) the Hoechst intensity was measured with the plate reader Tecan – Infinite Lumi 200 pro and appropriate settings (excitation wavelength λ_{EX}: 350 nm, emission wavelength λ_{EM}: 461 nm, gain: 70, flashes: 10, multiple reads per well: 3x3 (XY-line), 500 µm border).

2.2.6.2 Flow cytometry detection of cardiac cells

After the seahorse assay, isolated primary fibroblasts and endothelial cells were stained, fixed and permeabilized according to manufactures protocol for cell count and proof of cell integrity with flow cytometry. Cardiomyocyte viability was verified in a separate, non-Seahorse plate, where primary isolated cardiomyocytes were cultured at a density of $2x10^4$ cells/well (96-well plate) for 4 hours (37°C, 5% CO_2), according to the time span of the Seahorse Assay. In short, the plate was centrifuged (300 x g, 5 min, 4°C), flipped to remove supernatant and incubated with 100 µl LD405 (Life/Dead Fixable Aqua Dead Cell Stain Kit, Invitrogen, 30 min, 4°C, dark). After washing twice with GGG and centrifugation (300 x g, 5 min, 4°C) in between, 100 µl of fixation/permeabilization concentrate diluted 1:4 with eBioscience fixation/perm diluent was applied (30 min, 4°C, dark). The cells were washed with 1x permeabilization buffer (perm buffer 1:10 in ddH_2O), centrifuged and stored in 1x perm buffer at 4°C. Staining was conducted on the day of measurement. The antibody (see 2.1.7 Antibodies and probes for flow cytometry) was diluted 1:50 (Troponin T) or 1:100 (Vimentin, CD31, CD45) in 1x perm buffer and incubated (30 min, 4°C, dark). After washing twice with perm buffer and centrifugation (300 x g, 5 min, 4°C) in between, 200 µl SytoxGreen (1:10 000 in perm buffer) was added per well for 5 min. Cells number was determined by flow cytometry with the setup including forward scatter (FSC), sideward

scatter (SSC) and filters for FITC, PE, APC, Pacific Blue and AmCyan were used with appropriate voltages.

2.2.7 <u>**Statistics**</u>

Statistical analysis was performed using GraphPad Prism (version 6 and 7) or R (v3.6.3) with R studio (v1.1.453). Data is presented as mean ± SD or boxplot as indicated. The normality of data was tested with D'Agostino-Person or Shapiro-Wilk normality test. Outliers were identified with ROUT outlier test (Q = 1%) and excluded from further analysis. Significance between more than two groups was tested with ordinary one-way ANOVA with Holm-Sidak's multiple comparisons test (for normally distributed data) or Kruskal-Wallis test with Dunn's multiple comparisons test (for not normally distributed data). Ordinary two-way ANOVA with Dunnett's multiple comparisons test was performed when multiple timepoints and more than two groups were analysed. The concrete statistical tests used for analysis are displayed in the respective figure legend. The p-values were reported as $*p < 0.05$, $**p < 0.01$, $***p < 0.001$, $****p < 0.0001$ and are depicted in the figure.

III. Results

3.1 Vericiguat improves survival, body weight and BP.

Treatment with vericiguat improved the survival dose-dependently. All WT and dTGR treated with 3 mg/kg/d vericiguat survived until week 7. While treatment with 1 and 0.3 mg/kg/d vericiguat resulted in 78.6% and 69.2% survival, respectively. Only 61.5% of vehicle treated dTGR survived until week 7 (Figure 8a). At the end of the study animals treated with 3 mg/kg/d vericiguat had higher body weight (256.6 ± 28.7 g, mean ± SD, one-way ANOVA with Dunnett's multiple comparison p < 0.0003) compared to vehicle treated dTGR (202.4 ± 38.5 g, mean ± SD) (Figure 8b). The doses 1 and 0.3 mg/kg/d vericiguat did not improve body weight significantly. Weight gain was stable in all groups in week four and five. Fluctuations and weight loss occurred from week six in vehicle treated, 0.3 and 1 mg/kg/d vericiguat treated dTGR (Figure 8c). Unintentional severe weight loss caused by heart failure in the dTGR was prevented by 3 mg/kg/d vericiguat treatment (Figure 8c).
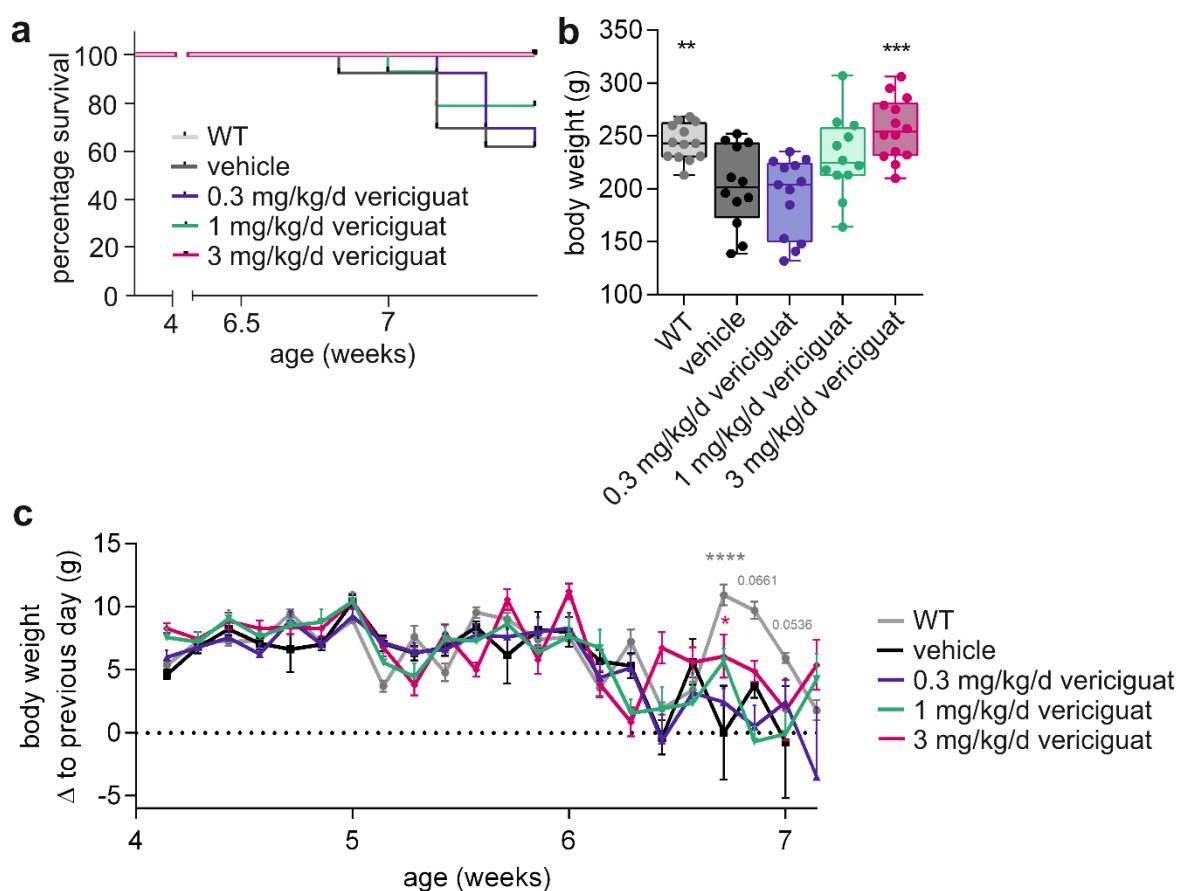
Figure 8. Body weight and survival improve by vericiguat treatment.
a Percentage survival of WT, vehicle treated and vericiguat treated dTGR is display over the study period. b Body weight at week 7, displayed as boxplot. One-way ANOVA in comparison to vehicle treated dTGR. From left to right n = 13/12/13/12/14. c Body weight changes over three weeks of treatment with vericiguat or vehicle. Data

displayed as mean ± SD. Ordinary two-way ANOVA with Dunnett's multiple comparison against vehicle treated dTGR. p-value is indicated as **p < 0.01, ****p < 0.0001.

3.1.1 <u>Vericiguat improves tail-cuff measured BP.</u>

The short-term BP recording was assessed using tail-cuff methodology at three different time points (5, 6, and 7 weeks of age) and is expressed as mean ± SD in this paragraph. The 0.3 mg/kg/d dose did not lower the BP at any time point of treatment. It was used to identify BP independent effects of vericiguat. The 1 mg/kg/d dose had a slight effect on BP, while the 3 mg/kg/d dose was able to reduce BP significantly from week 5 on.

In detail, systolic BP progressively increased in vehicle treated dTGR from 198.0 ± 14.3 mmHg in week 5, 218.0 ± 16.2 mmHg in week 6 to 226.0 ± 7.3 mmHg in week 7 (Figure 9a). In comparison, the systolic BP of WT rats was 146.2 ± 10.4 mmHg in week 7 (p < 0.0001, two-way ANOVA). Treatment with 0.3 mg/kg/d vericiguat did not reduce systolic BP at any timepoint (212.0 ± 11.4 mmHg in week 5, 213.6 ± 13.0 mmHg in week 6, 226.0 ± 18.9 mmHg in week 7). Treatment with 1 mg/kg/d vericiguat improve systolic BP significantly only in week 6 (186.1 ± 17.2 mmHg in week 5, 199.1 ± 13.7 mmHg in week 6, p = 0.0461, 206.2 ± 21.5 mmHg in week 7). Treatment with 3 mg/kg/d vericiguat improved systolic BP significantly to 165.3 ± 23.1 mmHg in week 5, 174.7 ± 12.4 mmHg in week 6 and 182.5 ± 28.8 mmHg in week 7 (p = 0.0001, < 0.0001, < 0.0001 from two-way ANOVA, respectively) (Figure 9a).

Diastolic BP progressively increased in vehicle treated dTGR from 153.2 ± 13.8 mmHg in week 5, 168.9 ± 16.4 mmHg in week 6 to 170.8 ± 6.8 mmHg in week 7 (Figure 9b). The diastolic BP of WT rats was normotensive (90.85 ± 14.4 mmHg in week 5, 94.5 ± 8.9 mmHg in week 6 to 98.4 ± 7.9 mmHg in week 7, p each < 0.0001 from two-way ANOVA in comparison to vehicle). Treatment with 0.3 mg/kg/d vericiguat did not reduce diastolic BP at any timepoint (163.2 ± 12.1 mmHg in week 5, 158.1 ± 14.4 mmHg in week 6, 174.4 ± 22.8 mmHg in week 7). Treatment with 1 mg/kg/d vericiguat improved diastolic BP significantly in week 5 (134.4 ± 14.1 mmHg, p = 0.0176) and 6 (139.3 ± 13.1 mmHg, p = 0.001), but not in week 7 (149.0 ± 22.1 mmHg). Treatment with 3 mg/kg/d vericiguat improved diastolic BP significantly to 116.5 ± 16.5 mmHg in week 5, 117.0 ± 12.5 mmHg in week 6 and 126.0 ± 24.0 mmHg in week 7 (p each < 0.0001 from two-way ANOVA in comparison to vehicle, respectively) (Figure 9b).

Mean BP increased continuously in vehicle treated dTGR from 167.9 ± 13.4 mmHg in week 5, 185.0 ± 16.2 mmHg in week 6 to 189.0 ± 6.5 mmHg in week 7 (Figure 9c). WT rats were

normotensive with mean BP of 102.2 ± 14.8 mmHg in week 5, 106.1 ± 0.1 mmHg in week 6 to 114.0 ± 8.6 mmHg in week 7 (*p* each < 0.0001 from two-way ANOVA in comparison to vehicle, respectively). Treatment with 0.3 mg/kg/d vericiguat did not improve mean BP (179.0 ± 11.7 mmHg in week 5, 176.4 ± 13.8 mmHg in week 6, 191.2 ± 21.4 mmHg in week 7). Treatment with 1 mg/kg/d vericiguat improved mean BP significantly in week 6 (158.9 ± 13.2 mmHg, *p* = 0.001), but not in week 5 (151.4 ± 14.5 mmHg) and week 7 (167.5 ± 21.5 mmHg). The 3 mg/kg/d vericiguat dose was most effective and significantly reduced mean BP to 132.5 ± 18.6 mmHg in week 5, 135.9 ± 12.3 mmHg in week 6 and 144.6 ± 25.3 mmHg in week 7 (*p* each < 0.0001 from two-way ANOVA in comparison to vehicle, respectively) (Figure 9c).
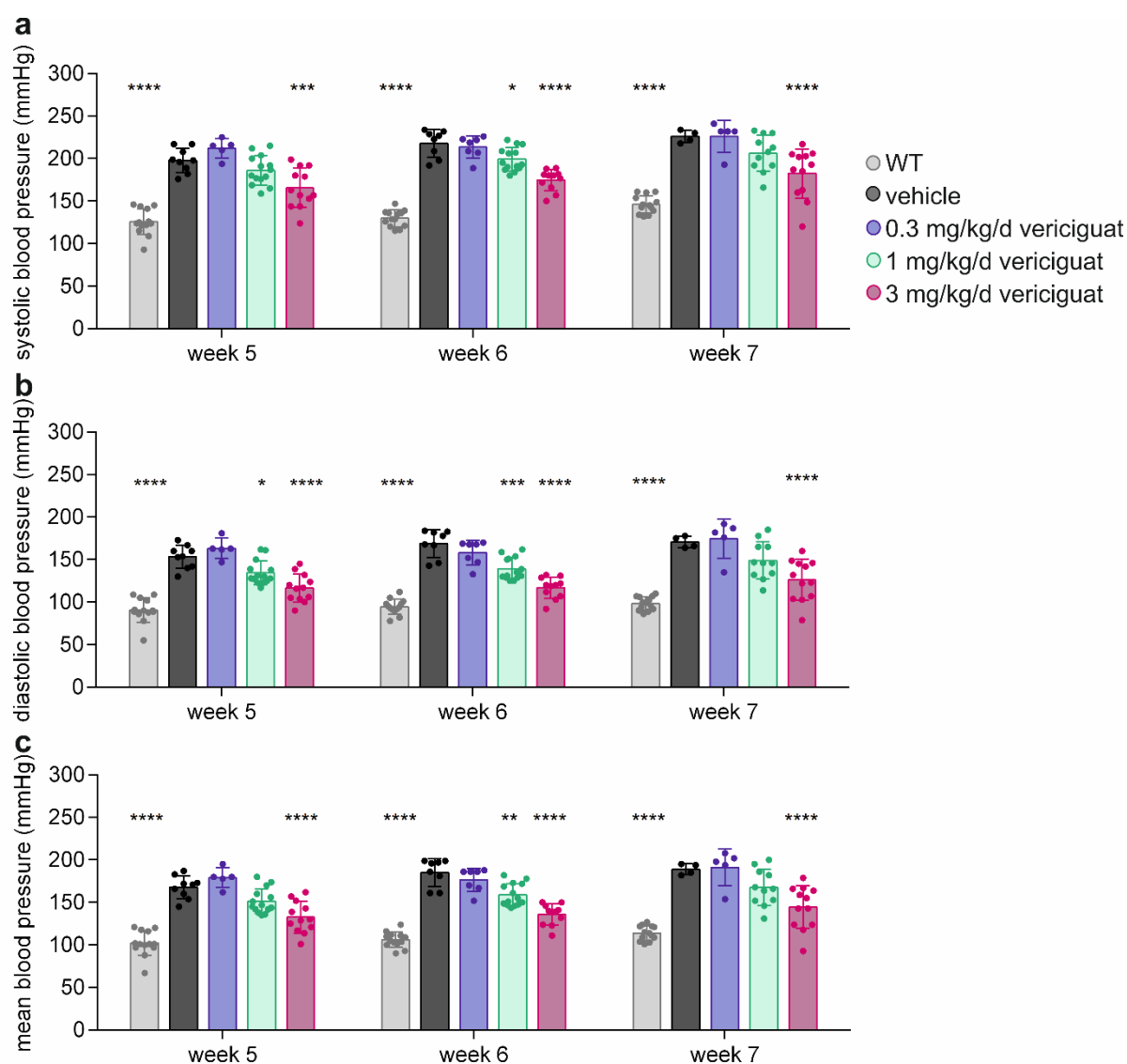
Figure 9 Tail-cuff measured BP at week five to seven of age.

a Systolic *b* diastolic and *c* mean BP are displayed as mean ± SD for WT, vehicle treated, 0.3, 1 and 3 mg/kg/d vericiguat treated dTGR at week five, six and seven. Two-way ANOVA with Dunnett's multiple comparison to respective vehicle. n = 4-14; p-value is indicated as *$p < 0.05$, **$p < 0.01$, ***$p < 0.001$, ****$p < 0.0001$.

3.1.2 Time-dependent reduction of telemetric-measured BP

The results from tail-cuff BP monitoring were reflected by radiometric telemetry mean arterial pressure measurements. The 3 mg/kg/d vericiguat treatment dose-dependently decreased the mean arterial BP over time from week 5 on compared to vehicle treated dTGR and was consistent over the study course whereby most pronounced at week 7 (Figure 10a). The 1 mg/kg/d vericiguat treatment decreased mean arterial BP slightly but not significantly with highest reduction in week 7 (Figure 10a). Unfortunately, the 0.3 mg/kg/d dose of vericiguat could not be evaluated due to transmitter failures.

To assess the BP kinetics over the course of 24 hours after vericiguat administration in week 5, 6 and 7, the radiometric telemetry mean arterial BP is presented as hourly averages on day 7, 14 and 21 of treatment (Figure 10b-d). Reduction of BP was observed approximately one hour after administration of vericiguat and increases again after 10 to 12 hours. In addition, the nocturnal mean BP was only reduced on treatment day 21, resulting in a significant net BP reduction at week 7 (Figure 10d).

Additional to the BP reduction, heart rate of 1 and 3 mg/kg/d vericiguat treated dTGR temporarily increased to 440.5 ± 38.6 bpm and 490.9 ± 42.0 bpm (mean ± SD), respectively in comparison to vehicle treated dTGR (400.0 ± 30.8 bpm, mean ± SD) when measured one to two hours after drug administration. In contrast, the mean daily heart rate measured by telemetry was unaffected during the treatment period.
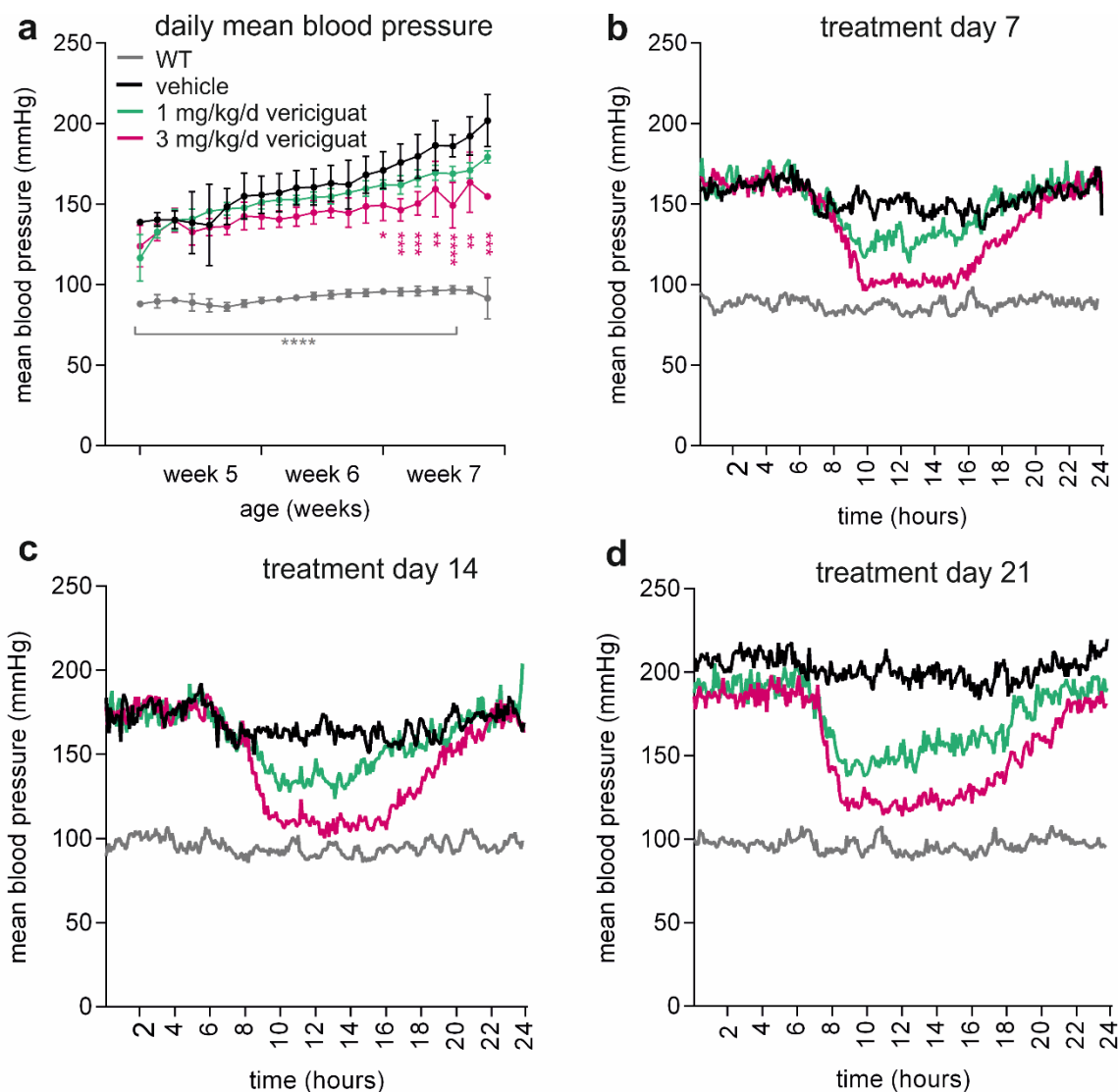
Figure 10. Radiometric telemetry-derived daily mean arterial BP measurement.
a Mean arterial BP over three weeks of treatment for WT (grey), vehicle treated (black), 1 (green) and 3 mg/kg/d (red) vericiguat treated dTGR. Data expressed as daily average mean ± SD, n=3-5. Two-way ANOVA with Dunnett's multiple comparison against vehicle treated dTGR. p-value is indicated as *p < 0.05, **p < 0.01, ***p < 0.001, ****p < 0.0001. b Course of mean arterial BP over 24 hours on day 7, 14 and 21 of treatment. Data expressed as hourly average mean, n=3-5.

The organ weights are represented in relation to tibia length because the heart failure phenotype affects body weight, which can therefore not be used for normalisation. Despite the reduction in BP, vehicle treated and vericiguat treated dTGR had similar cardiac hypertrophy indices (heart-to-tibia ratio mean ± SD of 0.354 ± 0.04, 0.353 ± 0.04, 0.368 ± 0.03 and 0.374 ± 0.02 for vehicle-, 0.3, 1 and 3 mg/kg/d vericiguat treated dTGR, respectively), which were significantly higher compared to WT rats (mean ± SD, 0.277 ± 0.02, p = 0.0008, Kruskal-Wallis test) (Figure 11a). The relative kidney weight (kidney-to-tibia ratio) was significantly lower in WT rats (mean ± SD, 0.312 ± 0.02, p = 0.046, one-way ANOVA) in

comparison to vehicle treated and 0.3, 1 and 3 mg/kg/d vericiguat treated dTGR at the end of the study (mean ± SD, 0.35 ± 0.03, 0.36 ± 0.04, 0.35 ± 0.02, 0.36 ± 0.03, respectively) (Figure 11b).The lung weight can indicate signs of lung congestion. Relative lung weight (lung-to-tibia ratio) was similar in all groups (Figure 11c). Relative spleen weight (spleen-to-tibia ratio) was higher in WT rats compared to vehicle treated dTGR, while vehicle- and vericiguat treated groups displayed similar values (Figure 11d).
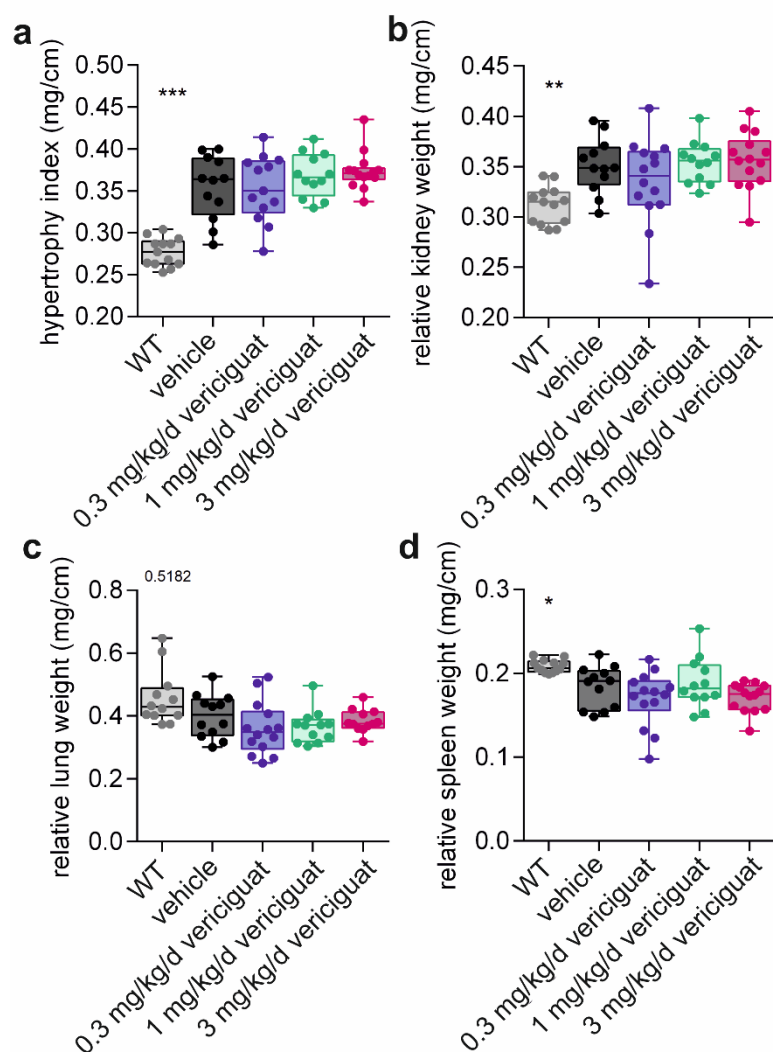
Figure 11. Organ weights indicate cardiac hypertrophy, without lung congestion and increased kidney weight.
*a Hypertrophy index (relative heart weight to tibia length ratio), b relative kidney weight, c relative lung weight, d relative spleen weight of WT, vehicle treated and vericiguat treated dTGR. All relative values are expressed as ratio to tibia length. Data displayed as boxplot, n = 12-14. One-way ANOVA or Kruskal-Wallis test as appropriate with multiple comparison to vehicle. p-value is indicated as *p < 0.05, **p < 0.01, ***p < 0.001.*

3.2 Echocardiographic assessment of cardiac performance

The cardiac performance and structure were examined using echocardiography. The macro-anatomic analysis of the heart showed hypertrophy (Figure 12 and Table 9). An increase in

left ventricular posterior wall thickness during diastole (LVPWd, Figure 12a) was observed in vehicle treated dTGR in comparison to WT rats. Vericiguat treatment did not lead to a reduction of LVPWd (Figure 12a). The relative wall thickness of the left ventricle during diastole was similarly affected (Figure 12b). The calculated left ventricular mass was reduced in WT rats and increased in 1 mg/kg/d vericiguat treated dTGR in comparison to vehicle treated dTGR (Figure 12c). The diastolic left ventricular anterior wall (LVAWd, Figure 12d) was significantly thicker in vehicle treated dTGR compared to WT rats. Vericiguat treatment of 0.3 mg/kg/d and 3 mg/kg/d had no adverse effect, while 1 mg/kg/d led to a further increase in anterior wall thickness in the heart (Figure 12d). Respective images of the left ventricle from echocardiography short axis view demonstrate the wall thickening without improvement by 3 mg/kg/d vericiguat treatment (Figure 12e). The left ventricular end diastolic diameter in diastole was not significantly altered between controls and treatment groups (Table 9). In summary, no improvement of cardiac hypertrophy by vericiguat could be observed but the 1 mg/kg/d vericiguat dose seemed to further increase hypertrophy.
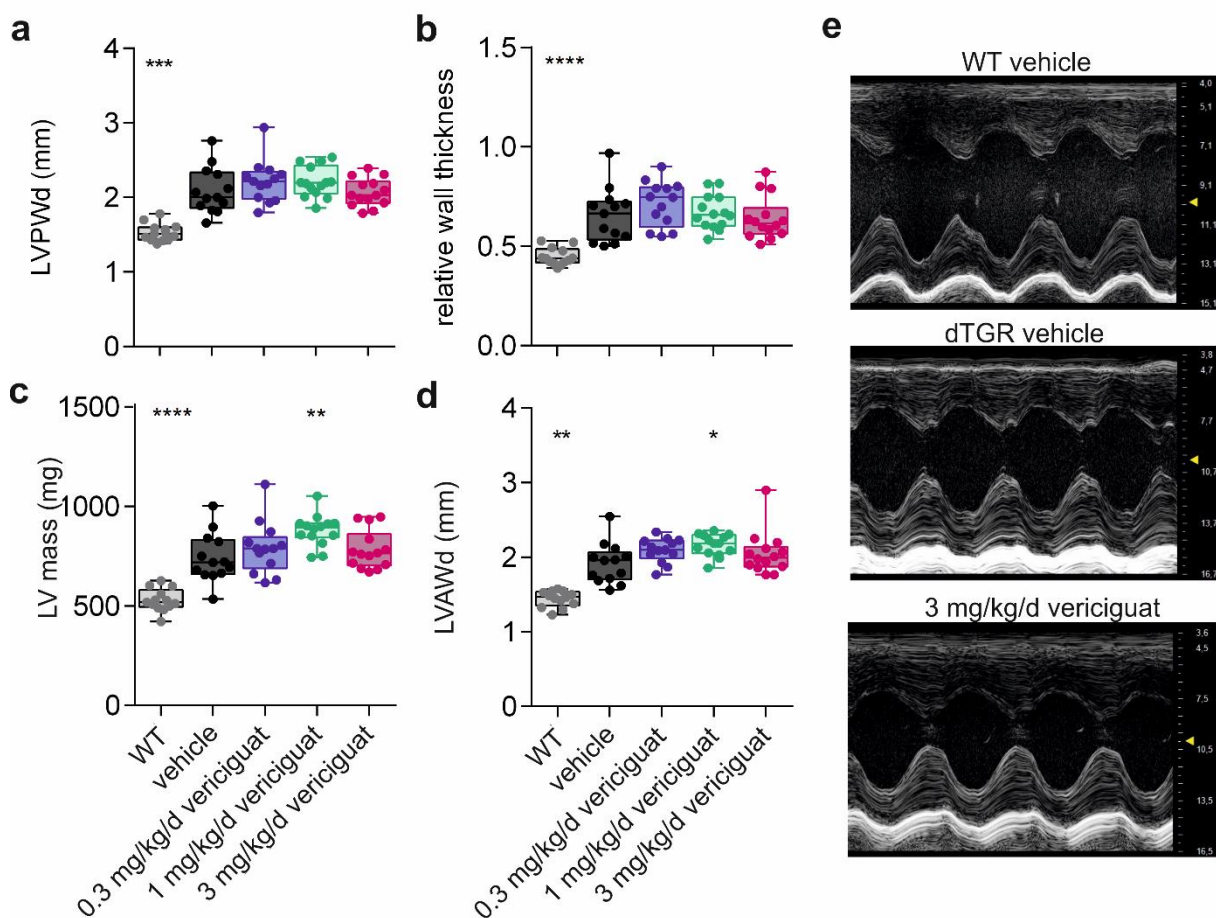
Figure 12. Structural echocardiographic parameter indicate cardiac hypertrophy in vehicle treated and vericiguat treated dTGR.

a Left ventricular posterior wall thickness in diastole (LVPWd), *b* relative wall thickness of the left ventricle (in diastole), *c* LV mass (in diastole), *d* left ventricular anterior wall in diastole (LVAWd) were increased in vehicle treated dTGR compared to WT rats. Vericiguat could not prevent wall thickening. *e* Representative echocardiographic images from left ventricular wall in short axis view displays immutable hypertrophy in 3 mg/kg/d vericiguat treated dTGR. Data from short axis echocardiography is expressed as boxplot, n=12-14. One-way ANOVA or Kruskal-Wallis test as appropriate with multiple comparison to vehicle. p-value is indicated as *p < 0.05, **p < 0.01, ***p < 0.001, ****p < 0.0001. Specialized staff from the preclinical research centre of the Max Delbrück Center performed the echocardiography and analysis. I carried out the calculation and interpretation.

Echocardiographic parameters were recorded to evaluate systolic and diastolic function of the heart in healthy WT rats and vehicle- or vericiguat treated dTGR (Figure 13a and Table 9). Focussing on vehicle treated dTGR in comparison to healthy WT rats, a preserved systolic function could be observed. Ejection fraction (EF) values of the left ventricle remained above 50% (Figure 13b) and fractional shortening (FS) was similar between WT and vehicle treated dTGR (Table 9). Cardiac output (CO, Figure 13c) and stroke volume (SV) were similar in WT rats and vehicle treated dTGR. Vericiguat administration of 1 and 3 mg/kg/d led to an increase in EF, FS, CO and SV compared to vehicle treated dTGR (Figure 13a-c, Table 9), while 0.3 mg/kg/d vericiguat dose had no effect. The heart rate was higher in vehicle treated dTGR than WT rats, while vehicle- and vericiguat treated dTGR had similar heart rates at the timepoint of echocardiography (Table 9). In summary, BP-dependent vericiguat doses additionally improved stable systolic cardiac function in dTGR.
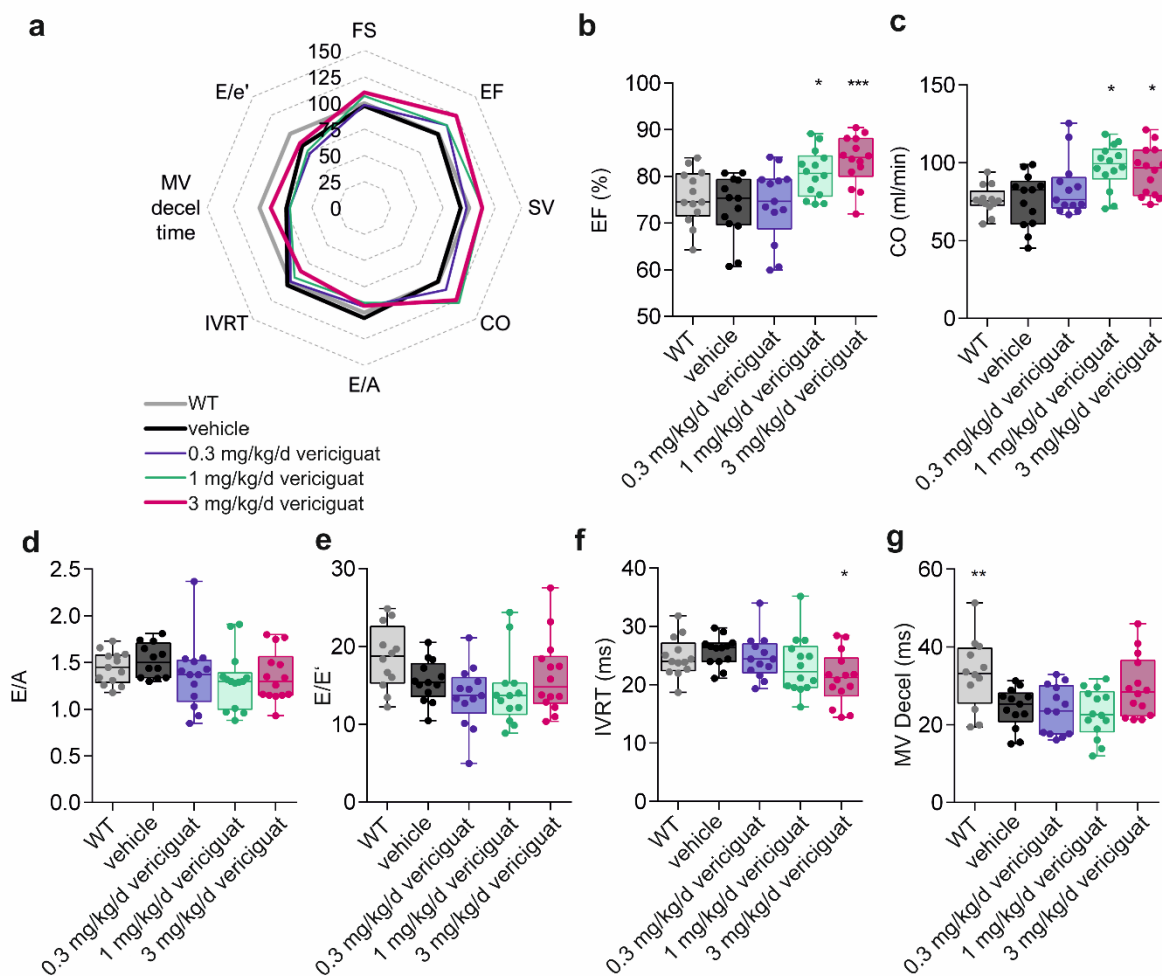
Figure 13. Functional cardiac echocardiographic parameters show diastolic dysfunction and preserved systolic function.
a Echocardiographic data is displayed relative to WT in percentage in a spider plot. b Ejection fraction (EF), c Cardiac output (CO), d E-wave to A-wave ratio E/A, e mitral valve deceleration time (MV Decel), f Isovolumetric relaxation time (IVRT) and g peak early diastolic filling velocity (E) to early mitral valve velocity (E') ratio (E/E') are displayed as boxplots, n=12-14. One-way ANOVA or Kruskal-Wallis test was carried out as appropriate with multiple comparison to vehicle. Fractional shortening (FS). p-value is indicated as *p < 0.05, **p < 0.01, ***p < 0.001. Specialized staff from the preclinical research centre of the Max Delbrück Center performed the echocardiography. I carried out the calculation and interpretation.

Determination of LV diastolic function characterizing mitral flow velocity was assessed using Pulse wave-Doppler. Peak early diastolic filling (E-wave) velocity and atrial filling (A-wave) velocity were similar between WT rats, vehicle- and vericiguat treated dTGR (Table 9). The resulting E-wave to A-wave velocity ratio (E/A, Figure 13d) was not different between groups.

Tissue Doppler imaging was used to measure mitral annulus velocity during early passive (E') and late (A') diastolic LV filling. There were no differences between vehicle treated, vericiguat treated dTGR and WT rats resulting in similar ratios of E'-wave to A'-wave velocity (E'/A', Table 9). The ratio of WT rats, vehicle- and vericiguat treated dTGR showed no difference in

the E/E' filling index, an estimate of LV filling pressure (Figure 13e). Pulse wave Doppler was used to measure the time between aortic closing and mitral valve opening, so called isovolumetric relaxation time (IVRT). IVRT was similar in WT rats compared to vehicle treated dTGR (Figure 13f). Administration of 3 mg/kg/d vericiguat reduced IVRT in comparison to vehicle treated dTGR. The isovolumetric contraction time (IVCT), meaning the period between mitral valve closing to aortic valve opening, was not different between groups (Table 9). A shorter mitral valve deceleration time (MV decel) reflects an elevated filling pressure indicating diastolic dysfunction. The MV deceleration time was reduced in vehicle treated dTGR in comparison to WT rats. Treatment with 3 mg/kg/d vericiguat increased deceleration time without reaching significance (Figure 13g). Taken together, the cardiac performance was characterized by cardiac left ventricular and septal hypertrophy, preserved systolic function with further elevation by administration of 3 mg/kg/d vericiguat and limited diastolic dysfunction.

Table 9. Parameter from echocardiography describe cardiac structure, systolic and diastolic function.
Data is shown as mean ± SD. One-way ANOVA with Dunnett's multiple comparison or Kruskal-Wallis Test with Dunn's multiple comparison to vehicle was performed, adjusted p-values are reported.

Echo parameter	WT (*p*-value)	vehicle	0.3 mg/kg/d vericiguat (*p*-value)	1 mg/kg/d vericiguat (*p*-value)	3 mg/kg/d vericiguat (*p*-value)
Structural parameter					
LVPW sys (mm), short axis	2.60 ± 0.27 (0.0009)	3.18 ± 0.27	3.34 ± 0.42 (0.6579)	3.42 ± 0.51 (0.2957)	3.39 ± 0.34 (0.3941)
LVPWd (mm), short axis	1.53 ± 0.12 (0.0006)	2.22 ± 0.28	2.21 ±2.05 (> 0.9999)	2.07 ± 0.19 (0.7635)	2.07 ± 0.19 (> 0.9999)
LVAWsys (mm), short axis	2.43 ± 0.31 (0.0073)	2.90 ± 0.41	3.149 ± 0.45 (0.2810)	3.41 ± 0.33 (0.0028)	3.31 ± 0.36 (0.0243)
LVAWd (mm), short axis	1.45 ± 0.11 (0.0095)	1.918 ± 0.27	2.09 ±0.16 (0.2802)	2.166 ±0.15 (0.0373)	2.05 ± 0.28 (> 0.9999)
LVEDD (mm)	6.85 ± 0.30 (0.1007)	6.46 ± 0.49	6.26 ± 0.51 (0.6061)	6.64 ± 0.34 (0.7114)	6.53 ± 0.55 (0.9841)
LVESD (mm)	3.73 ± 0.46 (0.5021)	3.53 ± 0.43	3.11 ± 0.74 (0.2499)	3.27 ± 0.60 (0.5021)	2.85 ± 0.77 (0.0264)
Base-apex distance (mm)	11.61 ± 0.51 (0.0061)	12.69 ± 1.15	12.55 ± 0.65 (0.9661)	12.57 ± 0.88 (0.9661)	12.77 ± 0.82 (0.9661)

Systolic function					
EF (%)	75.59 ± 5.79 (0.7794)	73.41 ± 6.69	74.07 ± 7.94 (0.9961)	80.62 ± 5.00 (0.0131)	83.35 ± 5.29 (0.0004)
Fractional shortening (%)	45.69 ± 5.25 (> 0.9999)	45.39 ± 5.86	50.86 ± 8.04 (0.2622)	50.86 ± 7.78 (0.2566)	56.64 ± 10.07 (0.0071)
CO (ml/min)	76.30 ± 8.95 (> 0.9999)	75.73 ± 17.07	83.93 ± 18.35 (> 0.9999)	97.62 ± 14.59 (0.137)	94.66 ± 15.45 (0.0349)
SV (µl)	208.9 ± 25.34 (0.6482)	192.4 ± 46.87	203.8 ± 42.99 (0.8658)	236.4 ± 36.82 (0.0161)	235.5 ± 28.51 (0.0187)
HR (bpm)	366.4 ± 29.56 (0.0262)	395.8 ± 21.48	412.8 ±29.97 (0.3230)	413.9 ±24.51 (0.2605)	402.8 ±29.30 (0.9087)

Diastolic function					
E (mm/s)	1024 ± 153.0 (> 0.9999)	970.8 ± 156.7	914.5 ± 200.4 (> 0.9999)	966.8 ± 156.8 (> 0.9999)	996.0 ± 203.4 (> 0.9999)
A (mm/s)	720.6 ± 149.2 (0.8073)	665.1 ± 118.0	700.3 ± 181.8 (0.9530)	765.7 ± 160.9 (0.3321)	759.9 ± 201.6 (0.3836)
E/A	1.45 ± 0.17 (>0.9999)	1.52 ± 0.18	1.37 ± 0.38 (0.3151)	1.31 ± 0.31 (0.079)	1.35 ± 0.27 (0.2185)
IVRT (ms)	24.77 ± 3.41 (0.9216)	25.74 ± 2.53	24.68 ± 3.78 (0.8973)	23.30 ± 4.89 (0.3157)	21.16 ± 4.51 (0.0130)
MV Decel (ms)	33.11 ± 9.15 (0.0095)	24.29 ± 5.20	23.86 ± 6.12 (0.9997)	22.99 ± 6.22 (0.9687)	29.69 ± 7.88 (0.1556)
E' (mm/s)	57.93 ± 15.45 (> 0.9999)	64.29 ± 15.51	71.50 ± 19.97 (> 0.9999)	71.48 ± 19.97 (> 0.9999)	66.72 ± 23.33 (> 0.9999)
A' (mm/s)	66.85 ± 13.21 (0.4612)	57.35 ± 15.38	61.44 ± 18.97 (0.9344)	62.48 ± 16.96 (0.8662)	71.05 ± 20.89 (0.1414)
E/E'	18.60 ± 4.11 (0.6313)	15.56 ± 2.69	13.61 ± 3.96 (0.7374)	14.26 ± 4.54 (0.6336)	16.19 ± 4.84 (> 0.9999)

Left ventricular posterior wall in systole (LVPWsys) and diastole (LVPWd); left ventricular anterior wall in systole (LVAWsys) and diastole (LVAWd); left ventricular end-systolic diameter (LVESD) and end-diastolic diameter (LVEDD); ejection fraction (EF); cardiac output (CO); stroke volume (SV); heart rate (HR); peak early diastolic filling velocity (E); peak atrial diastolic filling velocity (A); Isovolumetric relaxation time (IVRT); mitral valve deceleration time (MV Decel); early (E') and late atrial (A') mitral valve velocity during LV filling.

Two-dimensional speckle tracking is an echocardiography-based methodology (2D-STE) to assess left ventricular strain, a parameter to further evaluate myocardial performance. The global strain characterizes the total endocardial and epicardial movement in longitudinal, radial, or circumferential direction, while the spatial strain reflects the movement of particular cardiac regions (Figure 14a, d, g). Due to the shortening of the myocardium during a contraction cycle, the GLS and GCS are expressed as negative values (mean ± SD), while the GRS describes the thickening of the myocardium during contraction and is therefore positive.

WT rats displayed a GLS of -21.6 ± 2.0% (mean ± SD, $p < 0.0001$, one-way ANOVA), while vehicle treated dTGR had a mean GLS of -15.5 ± 2.2% (mean ± SD, Figure 14b), indicating reduced myocardial movement along the longitudinal dimension, a typical sign for impaired cardiac relaxation. Vericiguat treatment dose-dependently improved GLS at 1 mg/kg/d (-18.4 ± 2.0%, mean ± SD, $p = 0.004$) and 3 mg/kg/d (-20.3 ± 2.8%, mean ± SD, $p < 0.0001$), while 0.3 mg/kg/d (-16.9 ± 1.2%, mean ± SD, $p = 0.337$) had no effect (Figure 14b) in comparison to vehicle treated dTGR. Analysis of the spatial longitudinal strain in different cardiac regions reveals that the myocardial performance of the posterior apex has been altered the most followed by posterior base and mid, as well as anterior apex and base, whereas anterior mid was not significantly different between WT rats and vehicle treated dTGR (Figure 14c). Vericiguat was able to improve the longitudinal strain in the posterior apex dose-dependently already at 0.3 mg/kg/d. Other anatomic regions (posterior base, mid and anterior mid) of spatial longitudinal strain were improved by 1 or 3 mg/kg/d vericiguat treatment (Figure 14c). The GRS was significantly lower in vehicle treated dTGR (35.0 ± 5.1%, mean ± SD) than in WT rats (52.4 ± 4.6%, mean ± SD, $p < 0.0001$, one-way ANOVA) and could not be improved by vericiguat treatment (35.3 ± 6.7%, 34.7 ± 7.5%, 35.7 ± 3.8% for 0.3, 1 and 3 mg/kg/d, mean ± SD, respectively) (Figure 14e). A similar result was observed in the spatial approach, with a significant difference of spatial radial strain in left ventricular anterior free, lateral, posterior, and interior free wall between WT rats and vericiguat treated dTGR (Figure 14f). The GCS was impaired in vehicle treated dTGR (-25.1 ± 2.6%, mean ± SD) in comparison to WT rats (-30.8 ± 2.2%, mean ± SD, $p = 0.0003$, one-way ANOVA) but could not be improved by vericiguat treatment (-26.9 ± 2.8%, -27.2 ± 2.8%, -27.8 ± 2.2% for 0.3, 1 and 3 mg/kg/d, mean ± SD, respectively) (Figure 14h). The result was reflected in spatial circumferential strain of left ventricular anterior free, lateral, posterior, and interior free wall, with significant differences between WT rats and vericiguat treated dTGR (Figure 14i).
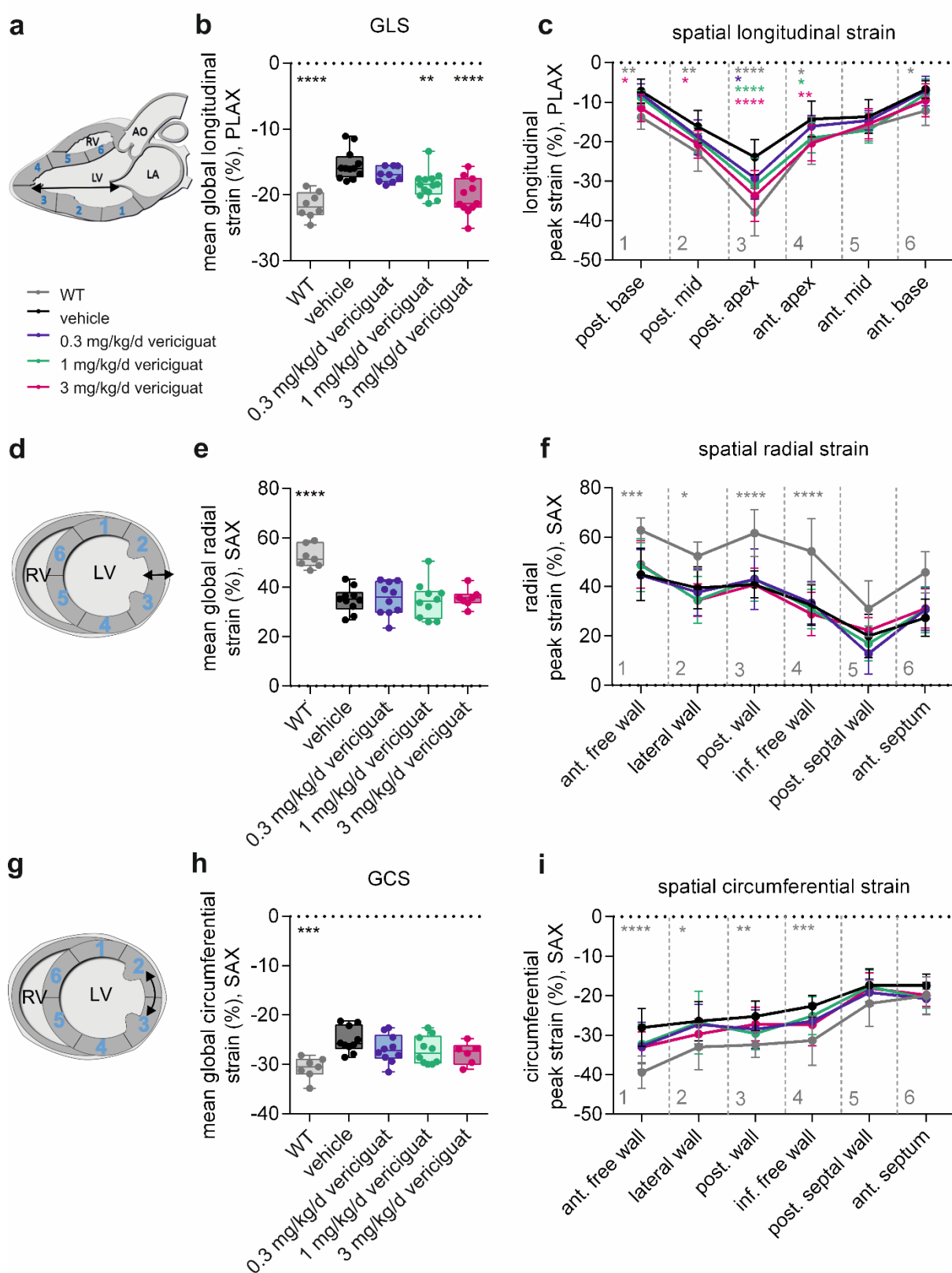
Figure 14. Assessment of global and spatial cardiac strain by speckle tracking echocardiography to evaluate myocardial performance.

a, d, g Scheme of global myocardial strain assessment in longitudinal, radial, and circumferential direction and regional segmentation. *b* Global longitudinal strain (GLS, %) measured in parasternal long axis (PLAX) is improved by vericiguat dose-dependently. *c* Spatial longitudinal strain in six cardiac regions (posterior base, mid, apex and

*anterior base, mid, apex) is improved by vericiguat segment-specifically. **e** Global radial strain (GRS, %) measured in short axis (SAX) is reduced in vehicle- and vericiguat treated dTGR. **f** Spatial radial strain elucidates reduction in left ventricular anterior free wall, lateral wall, posterior wall, and inferior free wall segments. No significant reduction in posterior septal wall and anterior septum. **h** Global circumferential strain (GCS, %) measured in short axis (SAX) is affected in vehicle- and vericiguat treated dTGR. **i** Spatial circumferential strain shows increase in left ventricular anterior free wall, lateral wall, posterior wall, and interior free wall segments but not in posterior septal wall or anterior septum. **b, e, h** Data expressed as boxplot, n=8-13. One-way with Dunnett's multiple comparison. **c, f, i** Data expressed as mean ± SD, n = 8-13. Two-way ANOVA with Dunnett's multiple comparison to vehicle. p-value is indicated as *p < 0.05, **p < 0.01, ***p < 0.001, ****p < 0.0001. Specialized staff from the preclinical research centre of the Max Delbrück Center performed the echocardiography. I carried out the measurement, calculation, and interpretation.*

3.3 Impaired left ventricular and peripheral pressure by cardiac haemodynamic.

To achieve detailed cardiac haemodynamic analysis, cardiac catheterization was performed at the end of week 6. Left ventricular pressure-volume (PV) loops were recorded during catheter investigations from WT rats, vehicle and vericiguat treated dTGR (Figure 15a). Alterations in vehicle treated dTGR were notable in comparison to WT rats and vehicle treated dTGR.

Mean arterial pressure (MAP) measured during haemodynamic assessment was increased in vehicle treated dTGR in comparison to WT rats. Only administration of 3 mg/kg/d vericiguat was capable to reduce MAP (Table 10). General parameter such as heart rate and body weight were not significantly different between groups (Table 10). Haemodynamic measured left ventricular end systolic pressure (LVESP) was elevated to 177.6 ± 19.7 mmHg in vehicle treated dTGR in comparison to 101.3 ± 11.0 mmHg (mean ± SD, one-way ANOVA, $p < 0.0001$) in WT rats (Figure 15b). Application of 3 mg/kg/d vericiguat significantly reduced LVESP to 132.6 ± 27.9 mmHg (mean ± SD, one-way ANOVA, $p = 0.0279$). Left ventricular end diastolic pressure (LVEDP) showed a similar tendency but differences between groups were not significant (Figure 15c Table 10). Along with this observation, the minimum (P_{min}), maximum (P_{max}) and average pressure (P_{mean}) during a PV-loop were higher in vehicle treated dTGR compared to WT rats. Significant reduction of P_{min} was achieved by 3 mg/kg/d vericiguat treatment in comparison to vehicle treated dTGR (Table 10). There were no significant changes recorded in end systolic volume (ESV), end diastolic volume (EDV) or stroke volume between WT rats, vehicle or vericiguat treated dTGR (Table 10). Invasive measured cardiac index (ml/min/BW) was not changes in vehicle treated dTGR compared to WT rats and administration of 1 mg/kg/d vericiguat led to a slight increase compared to vehicle treated dTGR (Table 10).
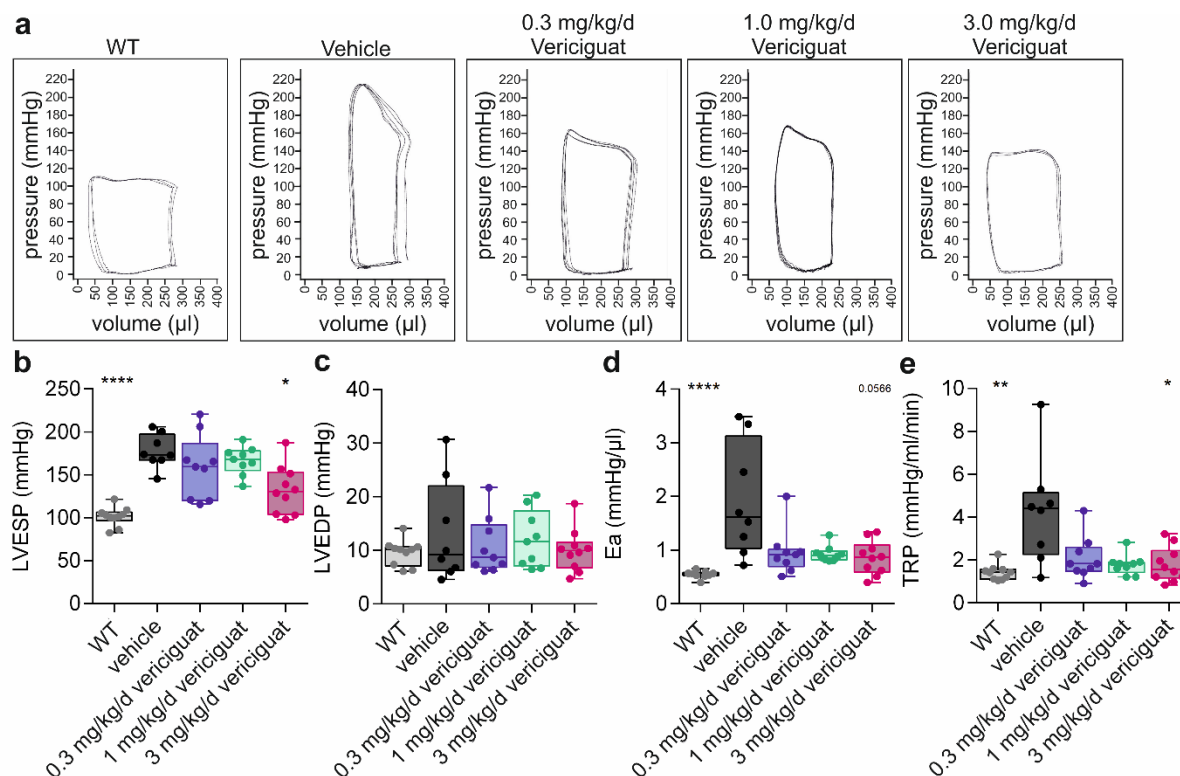
Figure 15. Haemodynamic assessment indicates elevated left ventricular and peripheral pressure.
a Representative pressure-volume loops from haemodynamic analysis with cardiac catheterization for WT, vehicle- and vericiguat treated dTGR. b Left ventricular end-systolic pressure (LVESP) c Left ventricular end-diastolic pressure (LVEDP) d Arterial resistance (Ea) e Total peripheral resistance (TRP) are elevated in vehicle treated dTGR and partially restored with 3 mg/kg/d vericiguat treatment. b-e Data expressed as boxplot, n = 8-10. One-way ANOVA or Kruskal Wallis Test with Dunnett's multiple comparison to vehicle were applied. p-value is indicated as *p < 0.05, **p < 0.01, ***p < 0.001, ****p < 0.0001. Specialized staff from the preclinical research centre of the Max Delbrück Center performed the catheterization and measurement. I carried out the statistical analysis and interpretation of data.

The haemodynamic measurement takes cardiac pressure and volume into account and can be used to calculate and evaluate total peripheral resistance (TPR) and arterial resistance (Ea). Ea reflects the vascular resistance, TPR is the cumulative resistance obtained by the vasculature on circulating blood. Ea and TPR were increased in vehicle treated dTGR compared to WT (Figure 15d, e). Administration of 3 mg/kg/d vericiguat diminished Ea and reduced TPR significantly in comparison to vehicle treated dTGR (Figure 15d, e).

The invasive measured systolic indices: maximum rate of change in pressure over time (dP/dt max) and stroke work (SW) were not changed between WT rats and vehicle treated dTGR. Only 1 mg/kg/d vericiguat increased SW in comparison to vehicle treated dTGR (Table 10). Invasive measured diastolic indices minimum rate of change in pressure over time (-dP/dt min) and the isovolumetric relaxation constant Tau (τ) were similar in WT rats and

vehicle treated dTGR. Administration of 1 mg/kg/d vericiguat reduced both -dP/dt min and Tau (Table 10).

Taken together, the invasive measurement of haemodynamic implies increased left ventricular pressure and elevated peripheral and vascular resistance with partial improvement by vericiguat, while parameters of diastolic dysfunction were not affected.

Table 10. Haemodynamic parameters from Millar tip catheter describing systolic and diastolic function.

haemodynamic parameter	WT (*p-value*)	vehicle	0.3 mg/kg/d vericiguat (*p-value*)	1 mg/kg/d vericiguat (*p-value*)	3 mg/kg/d vericiguat (*p-value*)
General parameter					
MAP (mmHg)	89.54 ± 12.64 (< 0.0001)	160.1 ± 29.68	143.8 ±40.20 (> 0.9999)	137.6 ± 29.85 (0.5952)	113.4 ± 22.36 (0.0258)
Heart rate (bpm)	373.1 ± 24.82 (0.088)	411.3 ± 40.98	425.1 ± 24.06 (> 0.9999)	430.6 ± 31.38 (0.7536)	419.9 ± 27.36 (> 0.9999)
Body weight (g)	220.4 ± 8.20 (0.1064)	200.7 ± 19.94	197.4 ± 16.39 (> 0.9999)	207.9 ± 23.45 (> 0.9999)	213.5 ±34.88 (> 0.9999)
Left ventricular pressure and volume parameter					
LVESP (mmHg)	101.4 ± 11.00 (< 0.0001)	177.6 ± 19.66	159.2 ± 37.00 (0.8376)	166.5 ± 16.35 (> 0.9999)	132.6 ± 27.86 (0.0279)
LVEDP (mmHg)	9.588 ± 2.41 (> 0.9999)	13.28 ± 9.49	10.79 ± 5.27 (> 0.9999)	12.05 ± 5.28 (> 0.9999)	9.99 ± 3.95 (> 0.9999)
LV P_{max} (mmHg)	107.6 ± 10.27 (< 0.0001)	186.8 ± 20.19	172.6 ± 43.12 (> 0.9999)	185.1 ± 22.78 (> 0.9999)	147.8 ± 26.02 (0.1322)
LV P_{min} (mmHg)	2.438 ± 1.97 (0.0622)	6.374 ± 4.67	3.659 ± 2.34 (> 0.9999)	2.683 ± 1.06 (0.3909)	2.248 ±1.87 (0.0328)
LV P_{mean} (mmHg)	52.02 ± 5.99 (0.0005)	86.52 ± 16.28	80.50 ± 22.75 (> 0.9999)	86.56 ± 17.45 (> 0.9999)	68.71 ± 16.19 (0.2196)
LVESV (µl)	102.7 ± 43.39 (> 0.9999)	101.7 ± 50.20	84.76 ± 51.63 (> 0.9999)	68.79 ± 25.81 (0.7529)	68.47 ± 46.83 (0.7175)
LVEDV (µl)	286.1 ± 52.79 (0.3145)	218.6 ± 98.84	260.6 ± 92.11 (> 0.9999)	255.7 ± 46.17 (> 0.9999)	244.0 ± 82.51 (> 0.9999)
SV (µl)	177.3 ± 43.62 (0.1198)	119.1 ± 63.46	178.9 ± 43.62 (0.1189)	183.9 ± 33.42 (0.0915)	170.2 ± 53.72 (0.3118)

CI (ml/min/BW)	301.3 ± 84.43 (> 0.9999)	249.5 ± 132.8	385.4 ± 108.7 (0.0501)	387.0 ± 102.0 (0.0374)	331.6 ± 77.37 (0.4474)
Ea (mmHg/µl)	0.548 ± 0.07 (< 0.0001)	1.933 ± 1.06	0.963 ± 0.48 (0.2011)	0.934 ± 0.15 (0.3154)	0.856 ± 0.31 (0.0566)
TPR (mmHg/ml/min)	1.426 ± 0.36 (0.0013)	4.253 ± 2.47	2.072 ± 0.99 (0.2497)	1.783 ± 0.47 (0.1897)	1.784 ± 0.81 (0.0464)
Systolic indices					
dP/dt max (mmHg/s)	7054 ± 1299 (0.1845)	9031 ± 862.6	9895 ± 2519 (> 0.9999)	10575 ± 1199 (0.2302)	9681 ± 2029 (> 0.9999)
SW (mmHg*µl)	17945 ± 5035 (> 0.9999)	18053 ± 8929	26479 ± 9037 (0.1345)	30049 ± 7617 (0.0138)	22079 ± 6142 (0.6584)
Diastolic indices					
-dP/dt min (mmHg/s)	-7994 ± 1125 (0.3967)	-9475 ± 3847	-12859 ± 3526 (0.3293)	-13616 ± 1436 (0.0447)	-10217 ± 1735 (> 0.9999)
τ (ms)	9.952 ± 0.99 (> 0.9999)	10.23 ± 1.40	8.764 ± 1.35 (0.1455)	8.417 ± 1.53 (0.0334)	8.756 ± 1.73 (0.1246)

Mean arterial pressure (MAP); left ventricular end-systolic and end-diastolic pressure (LVESP, LVEDP); left ventricular maximal, minimal and average pressure during a loop (LV P_{max}, LV P_{min}, LV P_{mean}); left ventricular end-systolic and end-diastolic volume (LVESV, LVEDV); stroke volume (SV); cardiac index (CI); arterial elastance (Ea); total peripheral resistance (TPR); maximal and minimal rate of rise of left ventricular pressure (dP/dt max, dP/dt min); stroke work (SW); isovolumetric relaxation constant (τ).

3.4 Vericiguat enhances cardiac pathophysiology.

3.4.1 Cardiac remodelling improved in vericiguat treated hearts.

Cardiac remodelling is a striking feature of heart failure and characterized by concentric hypertrophy and myocardial stiffness including collagen deposition and fibrosis. Besides lowering BP and in parts improving cardiac performance, vericiguat had a beneficial effect on marker genes expression in cardiac tissue (posterior mid segment). All cardiac mRNA expression data are displayed in Table 11.

The expression of hypertrophy marker atrial natriuretic peptide (*Anp*) and brain natriuretic peptide (*Bnp*) were largely increased in vehicle treated dTGR in comparison to WT rats (Figure 16a, b). Vericiguat administration at 1 mg/kg/d and 3 mg/kg/d reduced the high expression of *Anp* in comparison to vehicle treated dTGR. The high levels of *Bnp* expression could be significantly reduced by all doses of vericiguat (Figure 16a, b; Table 11). Osteopontin (*Opn*) expression, an indicator for cardiac remodelling [158], is increased in vehicle treated dTGR in comparison to WT rats by 10-fold, but no significant reduction was observed

under vericiguat treatment (Figure 16c). The characteristic shift in heart failure from cardiac α-myosin heavy chain (*Myh6*) toward the fetal β-myosin heavy chain (*Myh7*) isoform was observed [159]. *Myh6* was reduced in vehicle treated dTGR (0.997 ± 0.26, mean ± SD) in comparison to WT rats (1.481 ± 0.17, mean ± SD, p=0.0001, one-way ANOVA,) and *Myh7* was elevated in vehicle treated dTGR 0.974 ± 0.40 in comparison to WT rats (0.250 ± 0.10, mean ± SD, p=0.0044, one-way ANOVA, Figure 16d-f). Vericiguat treatment was not able to significantly prevent the shift towards β-myosin heavy chain.
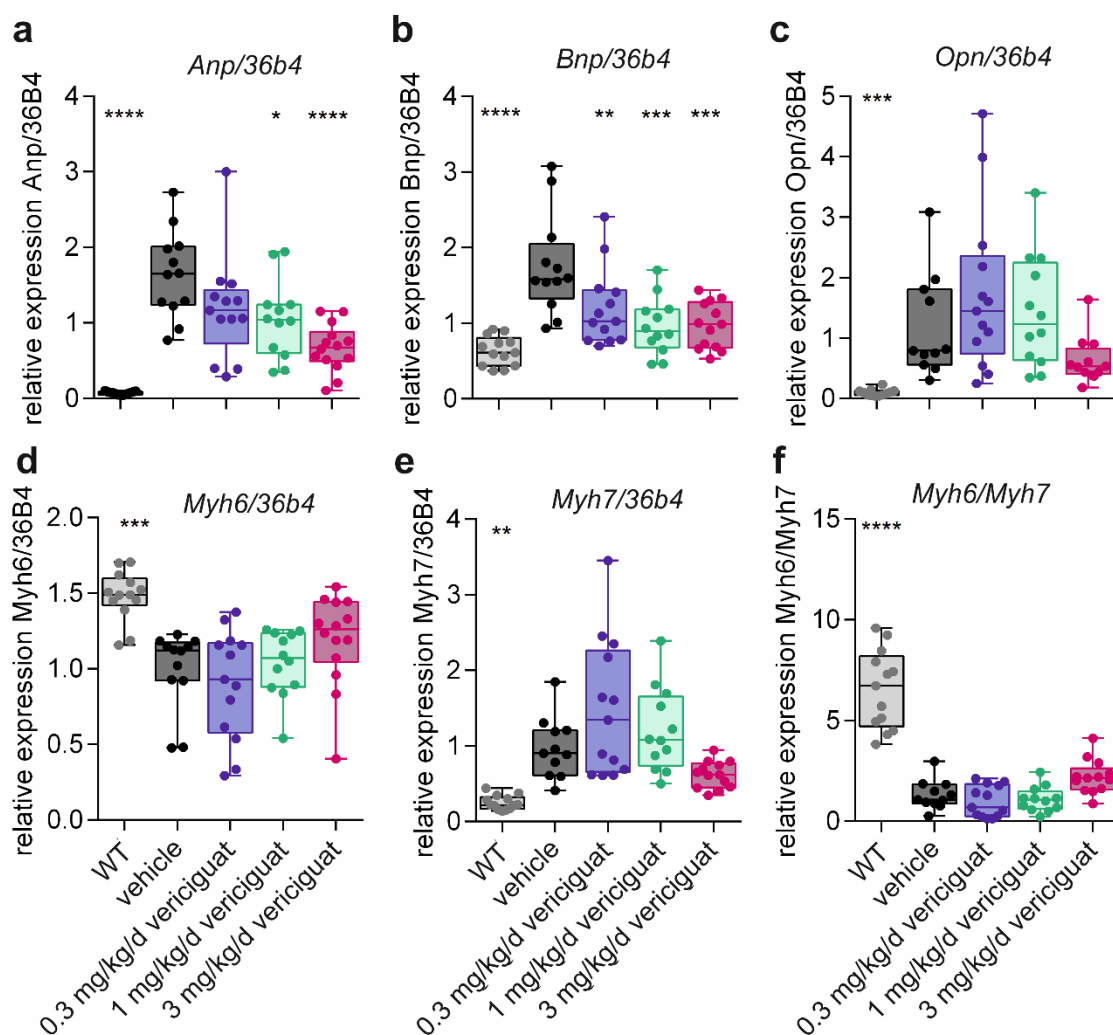
Figure 16. Expression of marker genes relevant for cardiac remodelling partially improve by vericiguat treatment.
*a Atrial natriuretic peptide (Anp), b brain natriuretic peptide (Bnp), c osteopontin (Opn), d α-myosin heavy chain (Myh6) isoform e β-myosin heavy chain (Myh7) isoform mRNA expression. f Myh6/Myh7 mRNA expression ratio. Data is displayed as boxplot, n = 13, 12, 13, 12, 14. One-way ANOVA with Dunnett's multiple comparison or Kruskal-Wallis test with Dunn's multiple comparison to vehicle. p-value is indicated as *p < 0.05, **p < 0.01, ***p < 0.001, ****p < 0.0001.*

Although cardiac remodelling marker gene expression was improved in part by vericiguat treatment, evidence denotes that fibrosis and hypertrophy cannot be completely prevented

by sGC stimulation with vericiguat. The cardiac fibrosis was investigated to identify the pathologic level of vericiguat influence.

Perivascular fibrosis was examined by immunohistological analysis of Collagen 1 (COL1) staining in the heart (Figure 17a, left). The perivascular fibrosis area was analysed relative to vessel media cross-sectional area. Quantification of heart sections showed increased cardiac perivascular matrix deposition in vehicle treated dTGR in comparison to WT rats (Figure 17a, right). Vericiguat treatment could not reduce the perivascular fibrosis. Interstitial fibrosis was evaluated by immunohistology straining of fibronectin (FN) stained heart sections (Figure 17b, left). The cardiac interstitial fibronectin-positive area was measured in percentage per field of view. In vehicle treated dTGR heart sections interstitial matrix deposition was increased three-fold in comparison to WT rats (Figure 17b, right). The 3 mg/kg/d vericiguat treatment was capable to reduce interstitial fibrosis in comparison to vehicle treated dTGR (Figure 17b, right). Connective tissue growth factor (*Ctgf*) expression in cardiac tissue was increased in vehicle treated dTGR compared to WT rats (Figure 17c). Reduction of *Ctgf* expression could be achieved by 1 and 3 mg/kg/d vericiguat in comparison to vehicle treated rats.
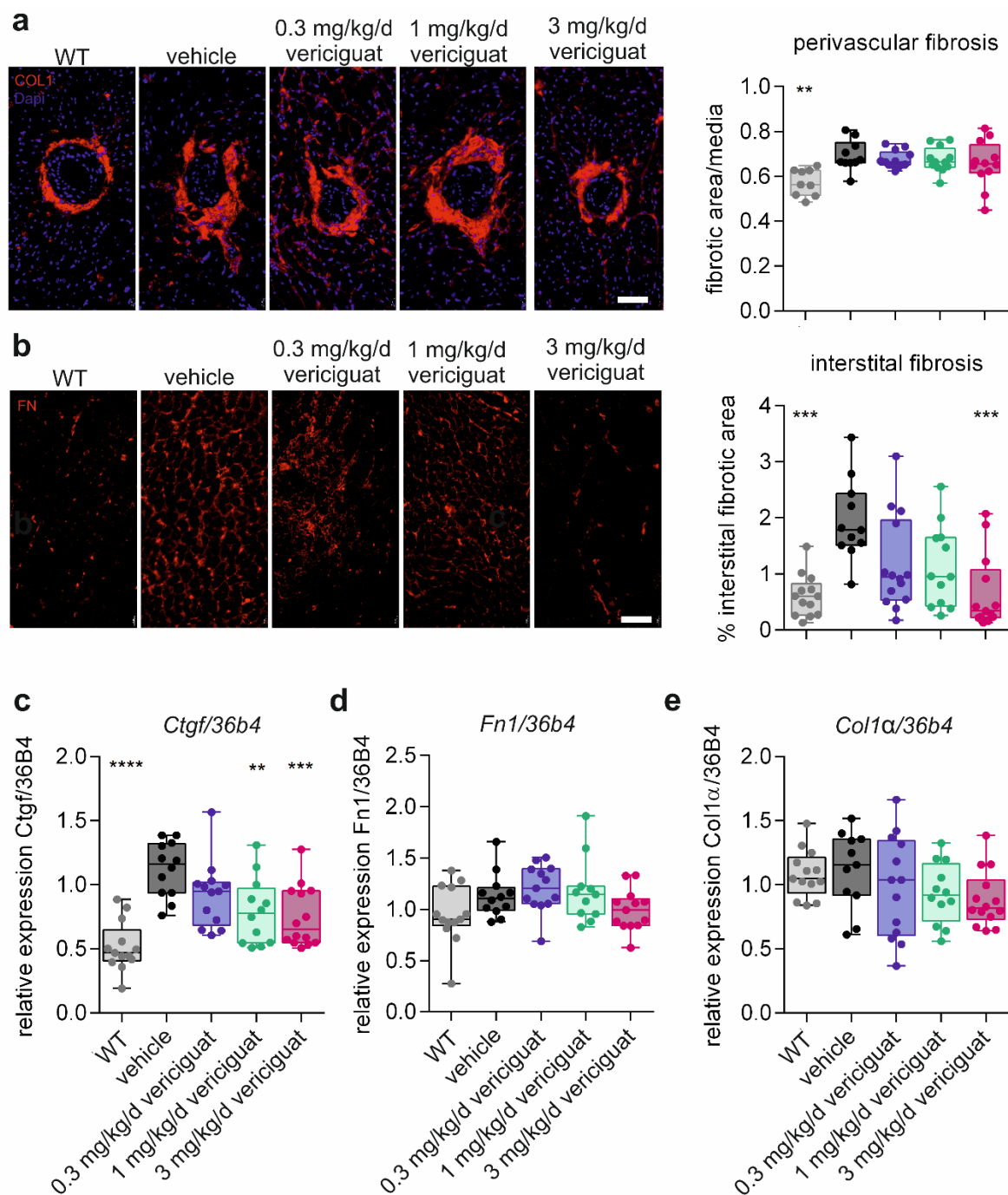
Figure 17. Strong cardiac fibrosis pattern ameliorates under 3 mg/kg/d vericiguat treatment.
*Immunohistochemical **a** COL1-staining of cardiac perivascular fibrosis with DAPI nuclear co-staining and **b** fibronectin-staining (FN) of cardiac interstitial fibrosis in WT rats, vehicle- and vericiguat dTGR with quantification of fibrotic area per media area or field of view to the right. Scalebar 50 μm. Cardiac mRNA expression of **c** Ctgf, **d** Fn1, **e** Col1α normalized to 36B4 expression in left ventricular posterior mid segment. Data is displayed as boxplot, n = 12-14. One-way ANOVA or Kruskal-Wallis test with multiple comparison to vehicle, p-value *p < 0.05, **p < 0.01, ***p < 0.001.*

Expression of cardiac fibrosis marker genes showed significant elevation of tissue inhibitor of metalloproteinase 1 (*Timp1*) in vehicle treated dTGR in comparison to WT rats. Treatment

with vericiguat had no effect on *Timp1* gene expression compared to vehicle treated dTGR (Table 11). The gene expression of fibronectin (*Fn*), collagen type 1 alpha 1 chain (*Col1α*), collagen type 3 alpha 1 chain (*Col3*) and neutrophil gelatinase associated lipocalin 2 (*Ngal*) were not significantly different in vehicle treated dTGR compared to WT rats. Vericiguat had no effect on *Fn1, Col1α, Col3* and *Ngal* gene expression compared to vehicle treated dTGR (Table 11).

Table 11. Cardiac gene expression measured with RT-qPCR in WT rats, vehicle and vericiguat treated dTGR. Data is reported as mean ± SD, sample number per group is indicated. One-way ANOVA with appropriate multiple comparison was performed, p-values are reported.

Gene	WT n=13 (*p*-value)	vehicle n=12	0.3 mg/kg/d vericiguat n=13 (*p*-value)	1 mg/kg/d vericiguat n=12 (*p*-value)	3 mg/kg/d vericiguat n=14 (*p*-value)
Anp	0.074 ± 0.02 (< 0.0001)	1.639 ± 0.58	1.187 ± 0.69 (0.0778)	1.048 ± 0.52 (0.0139)	0.669 ± 0.31 (< 0.0001)
Bnp	0.636 ± 0.19 (< 0.0001)	1.759 ± 0.66	1.203 ± 0.51 (0.0089)	0.963 ± 0.38 (0.0001)	0.971 ± 0.31 (0.0001)
Col1α	1.058 ± 0.19 (0.996)	1.116 ± 0.30	0.982 ± 0.40 (0.583)	0.932 ± 0.24 (0.3279)	0.886 ± 0.22 (0.1363)
Col3	0.964 ± 0.13 (0.979)	0.914 ± 0.24	0.824 ± 0.45 (0.8552)	0.819 ± 0.32 (0.8384)	0.707 ± 0.17 (0.2248)
Ctgf	0.518 ± 0.19 (< 0.0001)	1.123 ± 0.22	0.924 ± 0.26 (0.1210)	0.792 ± 0.26 (0.0037)	0.749 ± 0.24 (0.0006)
Cybα	1.385 ± 0.34 (> 0.9999)	1.279 ± 0.33	1.173 ± 0.38 (0.7908)	1.248 ± 0.36 (> 0.9999)	1.296 ± 0.37 (> 0.9999)
Cybβ	1.182 ± 0.12 (0.4876)	1.049 ±0.37	0.954 ± 0.31 (0.7513)	0.981 ± 0.16 (0.9067)	0.997 ± 0.20 (0.9572)
Et1	0.589 ± 0.135 (0.0019)	0.987 ± 0.35	1.088 ± 0.31 (0.9537)	1.011 ± 0.31 (> 0.9999)	0.971 ± 0.33 (> 0.9999)
Fn1	0.952 ± 0.29 (0.2234)	1.135 ± 0.22	1.206 ± 0.23 (0.8921)	1.178 ± 0.32 (0.9836)	0.994 ± 0.20 (0.4424)
Glut4	0.978 ±0.09 (0.008)	0.822 ± 0.13	0.877 ± 0.11 (0.6281)	0.877 ± 0.11 (0.6548)	0.949 ± 0.151 (0.0362)
Gucy1α2	0.943 ± 0.142	0.827 ± 0.10	0.852 ± 0.15	0.847 ± 0.144	0.848 ± 0.16

	(0.1555)		(0.9794)	(0.9914)	(0.988)
Gucy1α3	0.981 ± 0.146 (0.0119)	0.794 ± 0.07	0.899 ± 0.20 (0.5173)	0.865 ± 0.16 (> 0.9999)	0.764 ± 0.14 (> 0.9999)
Gucy1β3	0.706 ± 0.11 (> 0.9999)	0.798 ± 0.22	0.825 ± 0.27 (> 0.9999)	0.777 ± 0.18 (> 0.9999)	0.779 ± 0.16 (> 0.9999)
Icam	0.765 ± 0.69 (0.1895)	0.935 ± 0.32	0.978 ± 0.24 (0.9677)	0.820 ± 0.22 (0.5304)	0.899 ± 0.19 (0.9839)
Myh6	1.481 ± 0.17 (0.0001)	0.997 ± 0.26	0.900 ± 0.36 (> 0.9999)	1.038 ± 0.22 (> 0.9999)	1.193 ± 0.30 (0.1723)
Myh7	0.250 ± 0.10 (0.0044)	0.974 ± 0.40	1.485 ± 0.90 (0.0643)	1.209 ± 0.555 (0.6540)	0.621 ± 0.177 (0.2880)
Mcp1	0.572 ± 0.20 (0.4334)	0.859 ± 0.48	0.778 ± 0.54 (> 0.9999)	0.491 ± 0.15 (0.1346)	0.796 ± 0.28 (> 0.9999)
Ncf1	0.652 ± 0.09 (0.0191)	0.850 ± 0.21	0.871 ± 0.185 (0.9939)	1.004 ± 9.16 (0.1115)	1.167 ± 1.870 (< 0.0001)
Ncf4	0.896 ± 0.15 (> 0.9999)	0.898 ± 0.25	0.846 ± 0.19 (0.8910)	0.821 ± 0.17 (0.6992)	0.838 ± 1.06 (0.8249)
Ngal	1.107 ± 0.11 (> 0.999)	1.188 ± 0.20	1.112 ± 0.27 (0.8149)	1.063 ± 0.19 (0.6952)	1.106 ± 0.22 (> 0.9999)
Nos2	1.389 ± 0.23 (0.0003)	0.818 ± 0.37	0.781 ± 0.45 (0.9961)	0.798 ± 0.36 (0.9997)	0.983 ± 0.25 (0.5460)
Nos3	1.306 ± 0.14 (0.202)	1.092 ± 0.15	1.198 ± 0.24 (0.4230)	1.103 ± 0.21 (0.9997)	1.111 ± 0.18 (0.9965)
Opn	0.099 ± 0.06 (0.0001)	1.176 ± 0.84	1.741 ± 1.34 (> 0.9999)	1.430 ± 0.94 (> 0.9999)	0.626 ± 0.38 (0.6148)
Pdk4	0.965 ± 0.37 (0.5007)	0.714 ± 0.70	0.853 ± 0.58 (0.8804)	0.901 ± 0.43 (0.7590)	0.406 ± 0.19 (0.3073)
Sdha	0.792 ± 0.09 (0.9846)	0.765 ± 0.18	0.815 ± 0.17 (0.8763)	0.898 ± 0.19 (0.1768)	0.825 ± 0.19 (0.7819)
Sell1	0.931 ± 0.15 (0.2116)	0.800 ± 0.22	0.773 ± 0.18 (0.9872)	0.782 ± 0.21 (0.9974)	0.673 ± 0.13 (0.2199)
Tgfβ	0.997 ± 0.12 (0.2693)	0.902 ± 0.08	0.937 ± 0.14 (0.9206)	0.9034 ± 0.13 (> 0.9999)	0.917 ± 0.18 (0.9963)
Timp1	0.689 ± 0.16	0.966 ± 0.18	0.88 ± 0.11	0.985 ± 0.30	0.912 ± 0.29

	(0.0050)		(> 0.9999)	(> 0.9999)	(0.9313)
Vcam	0.862 ± 0.18 (0.126)	1.324 ± 0.54	1.239 ± 0.32 (0.9505)	1.041 ± 0.41 (0.2158)	1.165 ± 0.38 (0.6679)

3.4.2 Involvement of mitochondrial content and genes of energy metabolism

To better understand the context of cardiac energy metabolism, mitochondrial content (in segment: septal apex) and target gene expression (in segment: posterior mid) were investigated. The ratio of mitochondrial NADH dehydrogenase subunit 1 (mt-*ND1*) to nuclear DNA (*18S*) is a measure for mitochondrial content [155]. The mitochondrial content was not significantly different between WT rats, vehicle and vericiguat treated dTGR (Figure 18a). The expression of soluble carrier family 2 (facilitated glucose transporter) member 4 (*Glut4*) was significantly higher in WT rats than vehicle treated dTGR. Administration of 3 mg/kg/d vericiguat improved *Glut4* expression significantly (Figure 18b). The expression of pyruvate dehydrogenase kinase 4 (*Pdk4*) was not significantly different between vehicle and vericiguat treated dTGR (Figure 18c). Cardiac succinate dehydrogenase complex flavoprotein subunit A (*Sdha*) gene expression showed no difference in all groups (Table 11). *Glut4, Pdk4* and *Sdha* are involved in energy generation and cell metabolism.
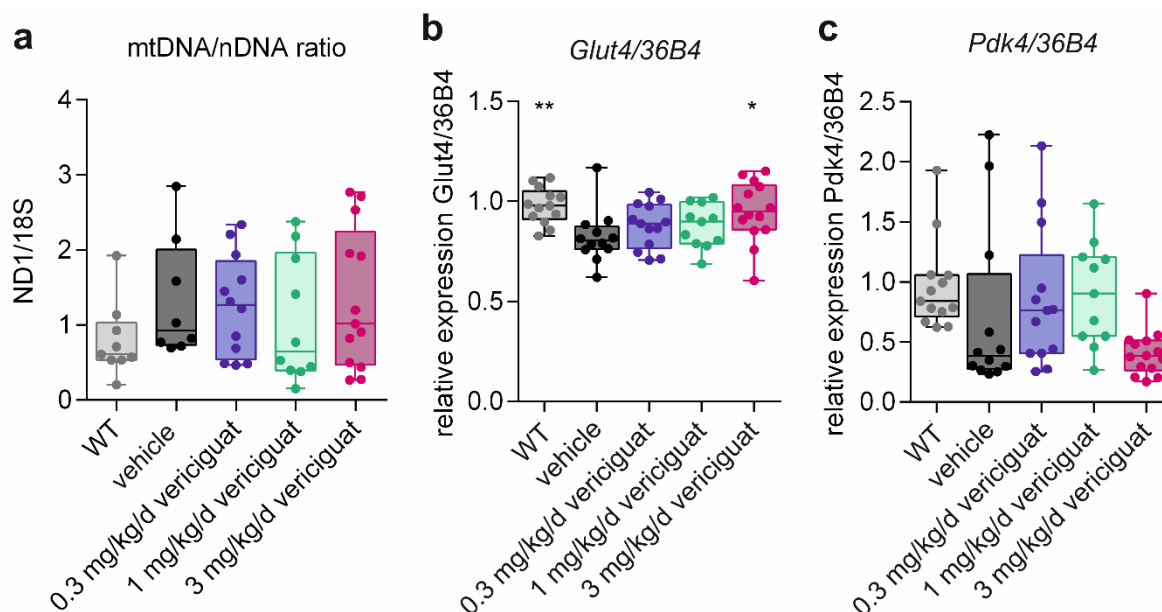
Figure 18. Mitochondrial content and expression of glycolysis associated genes is affected in the dTGR heart.
a Mitochondrial content measured by RT-qPCR of ND1 (mtDNA) relative to 18S (nDNA) in isolated DNA of septal apex segment. b Expression of soluble carrier family 2 (facilitated glucose transporter) member 4 (Glut4) and c pyruvate dehydrogenase kinase 4 (Pdk4) relative to 36B4 in posterior mid segment. Data shown as boxplot, n = 8-14. Ordinary one-way ANOVA with multiple comparison to vehicle. p-value *p < 0.05, **p < 0.01.

3.4.3 Defects in cardiac inflammation, endothelial damage, and microanatomy

Oxidative stress, endothelial damage, immune activation and inflammation drive fibrosis and fibroblast activation [160]. Cardiac remodelling marker gene expression was improved by vericiguat rising the question to which extend alterations occur in these driving factors.

The cardiac mRNA expression of oxidative stress marker was mostly unaffected. Neutrophil cytosolic factor 1 (*Ncf1*) was elevated in vehicle treated dTGR compared to WT rats (Table 11). *Ncf1* gene expression was 2-fold increased in 3 mg/kg/d vericiguat treated dTGR in comparison to vehicle treated dTGR. Cardiac neutrophil cytosolic factor 4 (*Ncf4*), cytochrome b-245 alpha chain polypeptide (*Cybα*) and cytochrome b-245 beta chain polypeptide (*Cybβ*) gene expression were not difference in all groups (Table 11). The cardiac inflammation was assessed by CD68 (ED1)-stained macrophages and monocytes (Figure 19a). The number of CD68-posive cells per field of view was significantly higher in the heart of vehicle treated dTGR compared to WT rats (Figure 19b). Vericiguat reduced cardiac macrophage and monocyte infiltration at the 3 mg/kg/d dose in comparison to vehicle treated dTGR (Figure 19b). The cardiac gene expression of transforming growth factor beta (*Tgfβ*), inflammation regulator and activator [161], and monocyte chemoattractant protein 1 (*Mcp1*) were not significantly changed in WT rats, vehicle or vericiguat treated dTGR (Table 11).
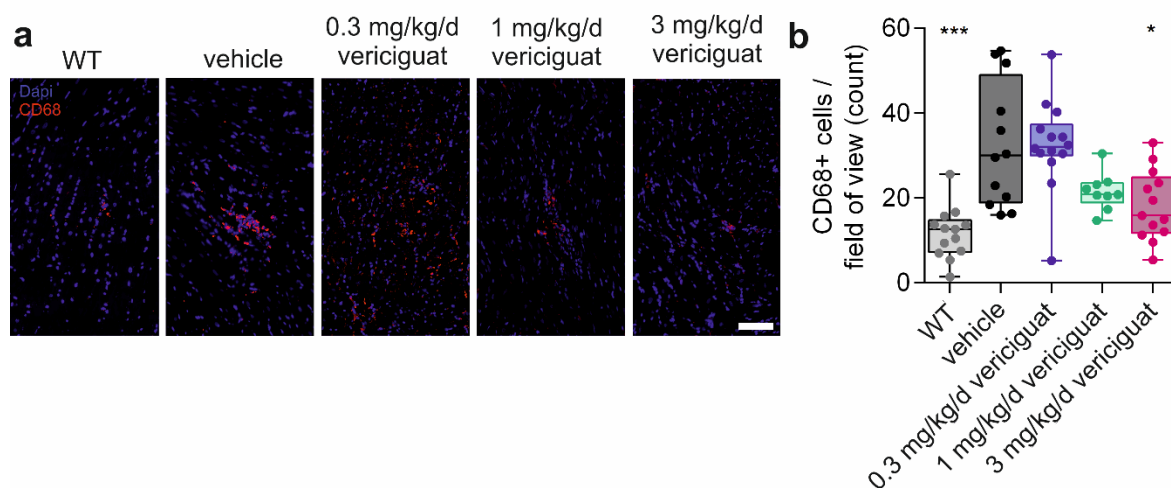
Figure 19. Cardiac inflammation measured by staining of CD68-positive macrophages and monocytes is reduced by vericiguat treatment.
a Representative images of CD68 (ED1)-stained macrophages and monocytes in cardiac tissue. Nuclear co-staining with DAPI is shown. Scalebar 50 µm. b Quantification of CD68+ cells per field of view as count in WT rats, vehicle- and 0.3, 1 or 3 mg/kg/d vericiguat treated dTGR. Data depicted as boxplot, n = 12-14. Kruskal-Wallis test with Dunn's multiple comparison to vehicle, p-value *p < 0.05, ***p < 0.001.

Immunohistochemical CD31-staining of heart tissue was analysed to examine the cardiac capillary density with a size below 50 µm (Figure 20a). The number of CD31-positive capillaries per field of view was similar in WT rats, vehicle- and vericiguat treated dTGR (Figure 20a right). The endothelial damage was assessed by cardiac expression of endothelial relevant marker genes. The expression of nitric oxide synthase 2 (*Nos2*) and (*Nos3*) was lower in vehicle treated dTGR compared to WT rats, indicating diminished synthesis of NO, which is relevant for stimulation of the sGC. No effect on *Nos2* and *Nos3* gene expression was observed in vericiguat treated dTGR compared to vehicle treated dTGR (Figure 20b, c). Furthermore, the expression of the genes transcribing sGC subunits was examined. Soluble guanylate cyclase subunit alpha 1 (*Gucy1α3*) expression was reduced in vehicle treated dTGR compared to WT rats in the heart. Treatment with vericiguat had no effect on *Gucy1α3* gene expression compared to vehicle treated dTGR (Figure 20d). Soluble guanylate cyclase subunit beta 1 (*Gucy1β3*) and soluble guanylate cyclase subunit alpha 2 (*Gucy1α2*) gene expression was similar in hearts of all groups (Table 11). In vehicle treated dTGR, cardiac expression of endothelin 1 (*Et1*) and vascular cell adhesion molecule 1 (*Vcam1*) was increased compared to WT rats (Figure 20e, f). The Et1 and Vcam1 cardiac expression could not be lowered by administration of compared to vehicle treated dTGR (Figure 20e, f). Cardiac expression of intercellular adhesion molecule 1 (*Icam*) and Selectin L (*Sell1*) was similar in all groups (Table 11).
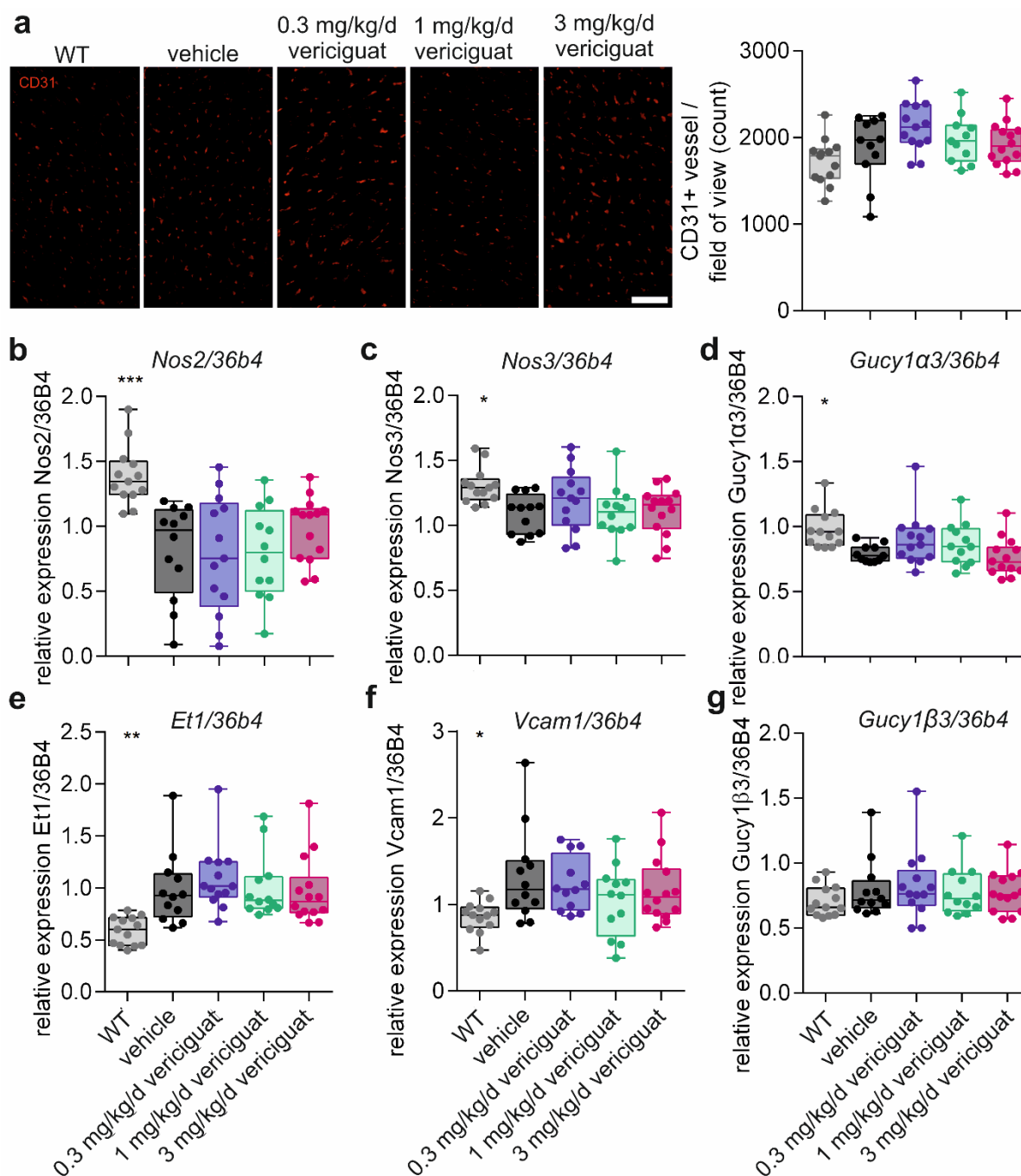
Figure 20. Structure of cardiac capillaries and expression of vascular markers in the heart.
*Cardiac mRNA expression of **a** Nos2, **b** Nos3, **c** Gucy1α3, **d** Et1, **e** Vcam1 normalized to 36B4 expression in left ventricular posterior mid segment. **f** Immunohistochemical CD31-staining of cardiac capillaries in WT rats, vehicle- and vericiguat dTGR with quantification of count of CD31-positive vessels per field of view. Scalebar 50 μm. Data is displayed as boxplot, n = 12-14. One-way ANOVA or Kruskal-Wallis test with multiple comparison to vehicle as appropriate, p-value *p < 0.05, **p < 0.01, ***p < 0.001.*

Investigations into endothelial damage denoted that alterations were exclusively present on transcriptional level in vehicle treated dTGR but could not be diminished by vericiguat administration. Detailed analysis of the cardiac microvascular morphology was done by

micro-computer tomography (CT) to identify potential pathologic modifications in the vasculature. The microvascular structure was investigated by micro-CT scans of Microfil-perfused hearts from WT rats, vehicle- and 3 mg/kg/d vericiguat treated dTGR. The cardiac vessel distribution showed no differences in the volume of vessels with a diameter below 0.7 mm between WT rats, vehicle treated or 3 mg/kg/d vericiguat treated dTGR, encouraging the results from CD31-staining (Figure 21a). A reduction of volume in medium-sized vessels was observed, with significant differences between WT rats compared to vehicle treated dTGR at 0.08 mm (mean ± SD, WT: 0.0045 ± 0.001%, vehicle: 0.0032 ± 0.001%, p = 0.0002, two-way ANOVA) to 0.16 mm (mean ± SD, WT: 0.0020 ± 0.001%, vehicle: 0.0012 ± 0.0002%, p = 0.0231, two-way ANOVA) diameter (Figure 21a, b). The 3 mg/kg/d vericiguat treatment had no significant effect on the volume of cardiac vessel diameter (mean ± SD, 0.0034 ± 0.001% at 0.08 mm, 0.0011 ± 0.0003%, at 0.16 mm).
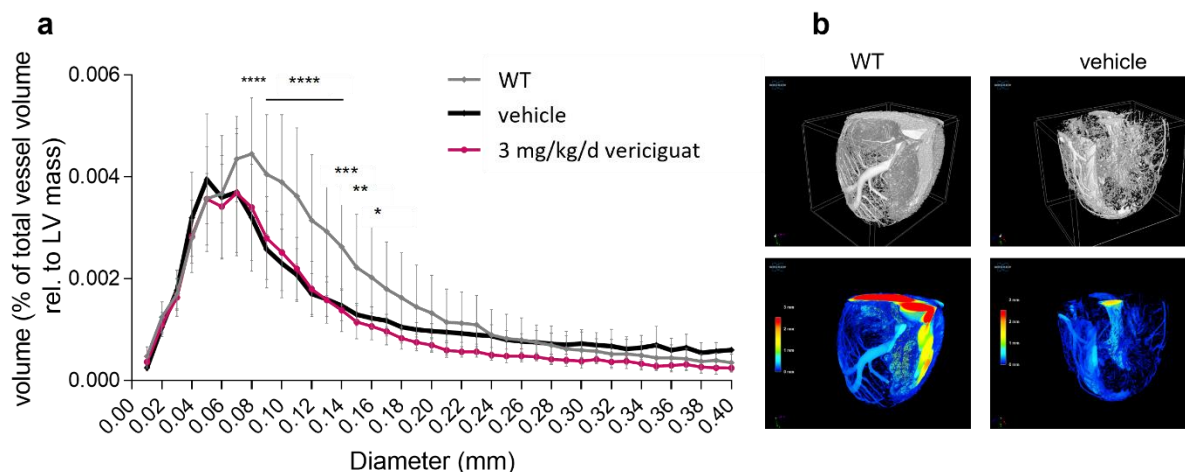
Figure 21. Microvascular profile in WT rats, vehicle and vericiguat treated dTGR hearts.
a The vascular volume to total vessel volume in percent (normalized to left ventricular mass) is shown for 0.02 to 0.4 mm diameter. Mean ± SD is displayed for WT rats, vehicle- and 3 mg/kg/d vericiguat treated dTGR, n = 4, 4, 6, respectively. Two-way ANOVA with Dunnett's multiple comparison to vehicle. p-value *p < 0.05, **p < 0.01, ***p < 0.001, ****p < 0.0001. *b* Representative images of hearts from WT rats and vehicle treated dTGR in grey-scale (upper panel) and pseudo colour (lower panel) with smallest capillaries in blue and largest vessels in red. Professional scientific staff from the preclinical research centre of the Max Delbrück Center performed the micro-CT measurement and imputation. I carried out the perfusion, calculation, and interpretation of data.

3.5 Successful isolation of primary cardiac cells

Primary cardiomyocytes, cardiac fibroblasts and cardiac endothelial cells were simultaneously isolated from ventricles of WT rats, vehicle and 3 mg/kg/d vericiguat treated dTGR with an adapted Langendorff-isolation procedure. Immunohistochemical staining, gene expression and flow cytometry were used for verification of cell identity, integrity, and viability within isolated cardiac cell populations.

Isolated cardiomyocytes from WT rats showed striation and were positive for the cellular marker myosin, actin, and troponin T but did not show fibroblast marker platelet-derived growth factor receptor α (*Pdgfra*) (Figure 22a). Primary cardiomyocytes showed similar expression of atrial and brain natriuretic peptide (*Anp, Bnp*) and soluble carrier family 2 (facilitated glucose transporter) member 1 and 4 (*Glut1, Glut4*) normalized to *36B4* expression after 24 hours culture (37°C, 5% CO_2, 5.55 mM glucose, blebbistatin as contraction inhibitor, $2x10^4$ cells/well in 24-well plate, Figure 22b). The flow cytometric measured population of nucleus-containing (SytoxGreen-positive) live troponin T-positive cells was above 60% in cardiomyocytes from WT rats, vehicle and 3 mg/kg/d vericiguat treated dTGR (Figure 22c, d). There are studies that report differentiation of primary mouse cardiomyocytes already after 24 hours, discouraging culture over several days [149,162]. For this reason, experiments in this study were performed on the day of isolation after a maximum culture of four hours.
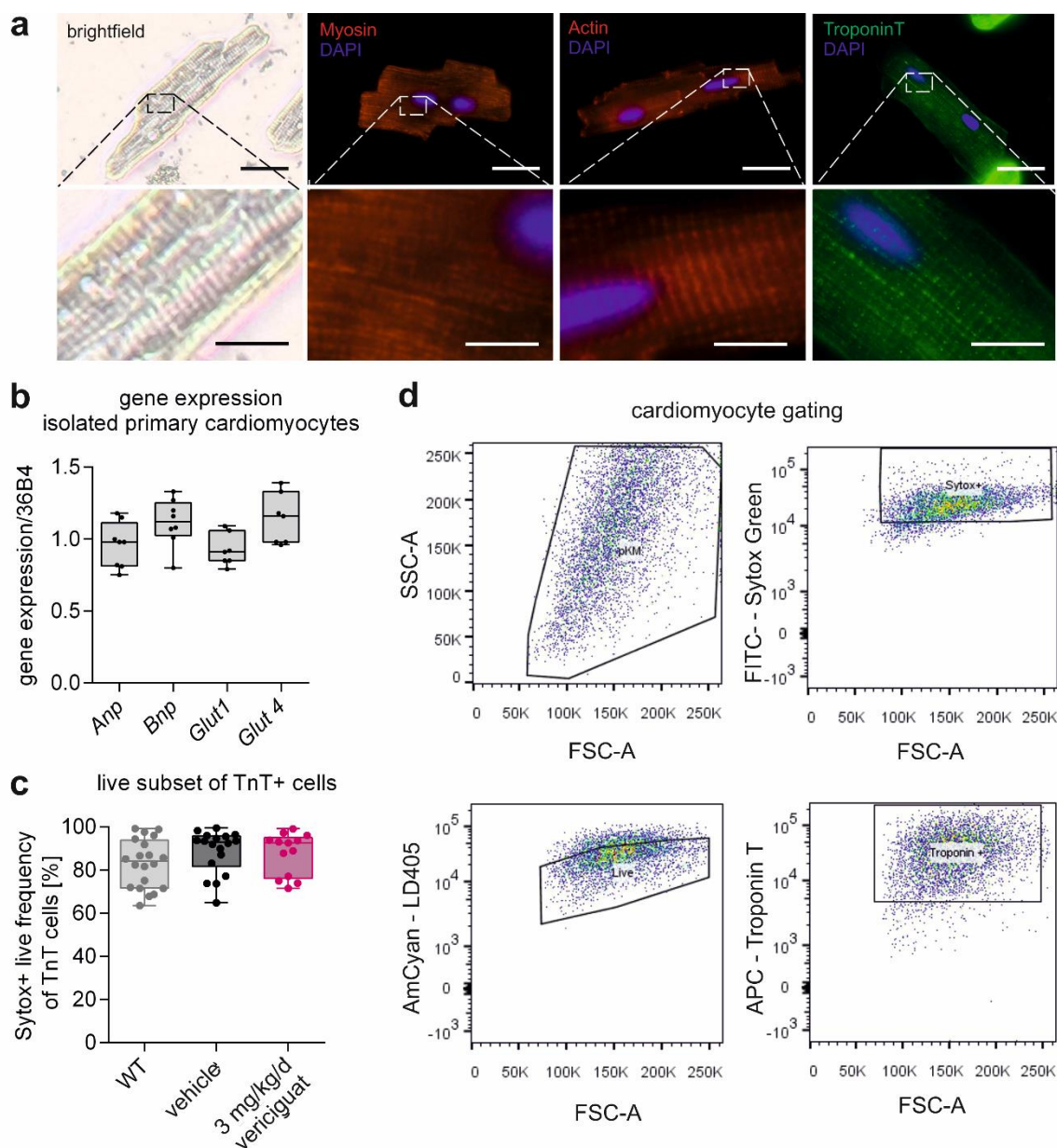
Figure 22. Confirmation of cardiomyocyte identity, integrity, and viability.
a Primary isolated cardiomyocytes from WT rat hearts showed typical striation in brightfield and were positive for myosin, actin, and troponin T staining after 2 h culture (37°C, 5% CO_2). Nuclear co-staining with DAPI is shown, zoomed regions are highlighted. Scalebar 30 μm (upper panel), 10μm (lower panel). b Cardiomyocytes cultured for 24 hours (37°C, 5% CO_2, 5.55 mM glucose, blebbistatin as contraction inhibitor, $2x10^4$ cells/well in 24-well plate) showed expression of atrial and brain natriuretic peptide (Anp, Bnp) and soluble carrier family 2 (facilitated glucose transporter) member 1 and 4 (Glut1, Glut4). Expression is reported relative to housekeeper gene 36B4 as boxplot, n = 3 independent experiments. c SytoxGreen-positive (nuclear staining), live subset of troponin T-positive cells was measured with flow cytometry of cardiomyocytes from WT rats, vehicle- and vericiguat treated dTGR. Data is displayed as boxplot, n = 5, 6, 4. Statistical testing using one-way ANOVA. d Gating strategy used to identify population of interest in isolated primary cardiomyocytes.

Primary isolated cardiac fibroblast from WT rat hearts presented typical morphology in brightfield and were positive for staining of cellular marker PDGFRα, fibronectin, and vimentin after 7 days culture (37°C, 5% CO_2, Figure 23c). The fibroblast population was characterized

with flow cytometry (Figure 23b, c). The vimentin-positive population of live cells was above 50% in cells isolated from WT rats or vehicle treated dTGR (Figure 23b). Primary cardiac fibroblasts from two animals in the 3 mg/kg/d vericiguat treated dTGR group showed reduced viability and were therefore excluded from further analysis. The CD31-positive and CD45-positive subset of live fibroblasts were used to identify the amount of other cell types (endothelial and immune cells) in the population. Both showed presence below 20% in the fibroblast population, with one exception in the 3 mg/kg/d vericiguat group, which was excluded as mentioned above.
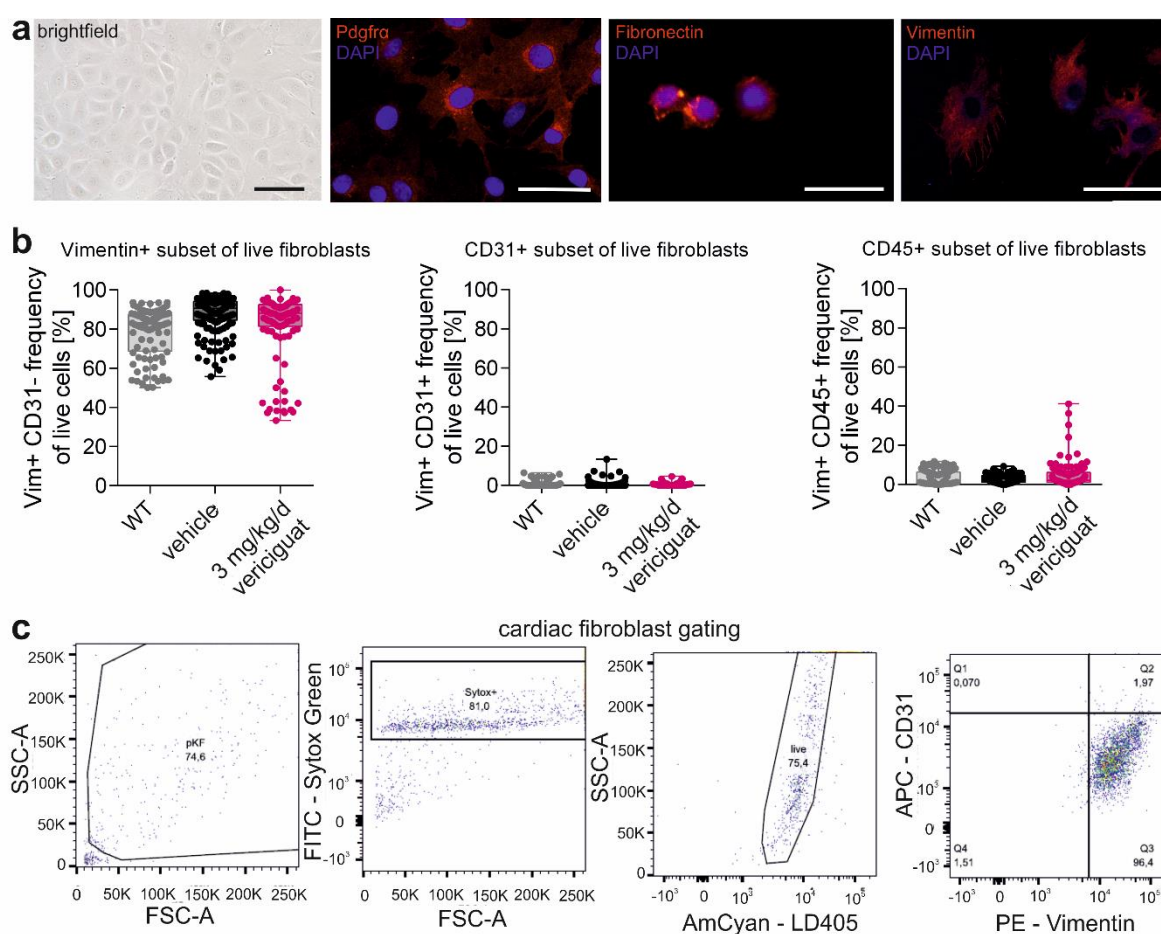
Figure 23. Confirmation of cardiac fibroblast identity, integrity, and viability.
a Primary isolated cardiac fibroblast from WT rat hearts showed typical morphology in brightfield and were positive for Pdgfrα, fibronectin, and vimentin staining after 7 days culture (37°C, 5% CO_2). Nuclear co-staining with DAPI is shown. Scalebar 50 µm. b Flow cytometric measured vimentin-positive subset, CD31-positive subset and CD45-positive subset of live fibroblasts are shown as boxplot, replicates from n = 5, 6, 4. Statistical testing using one-way ANOVA. c Gating strategy to identify population of interest in flow cytometry data of isolated primary cardiac fibroblast.

The isolated primary cardiac endothelial cells from WT rats were identified with the endothelial cell-specific marker CD31 (Figure 24a). With flow cytometric characterization of

endothelial cells, a CD31-positive/CD45-negative live cell population above 70% was identified (Figure 24b, c). Cells from one 3 mg/kg/d vericiguat treated heart were below 70% viability and excluded from further analysis. The double positive (CD31 and CD45-positive) as well as CD31-negative/CD45-positive subsets of live cells were below 10% (Figure 24b).
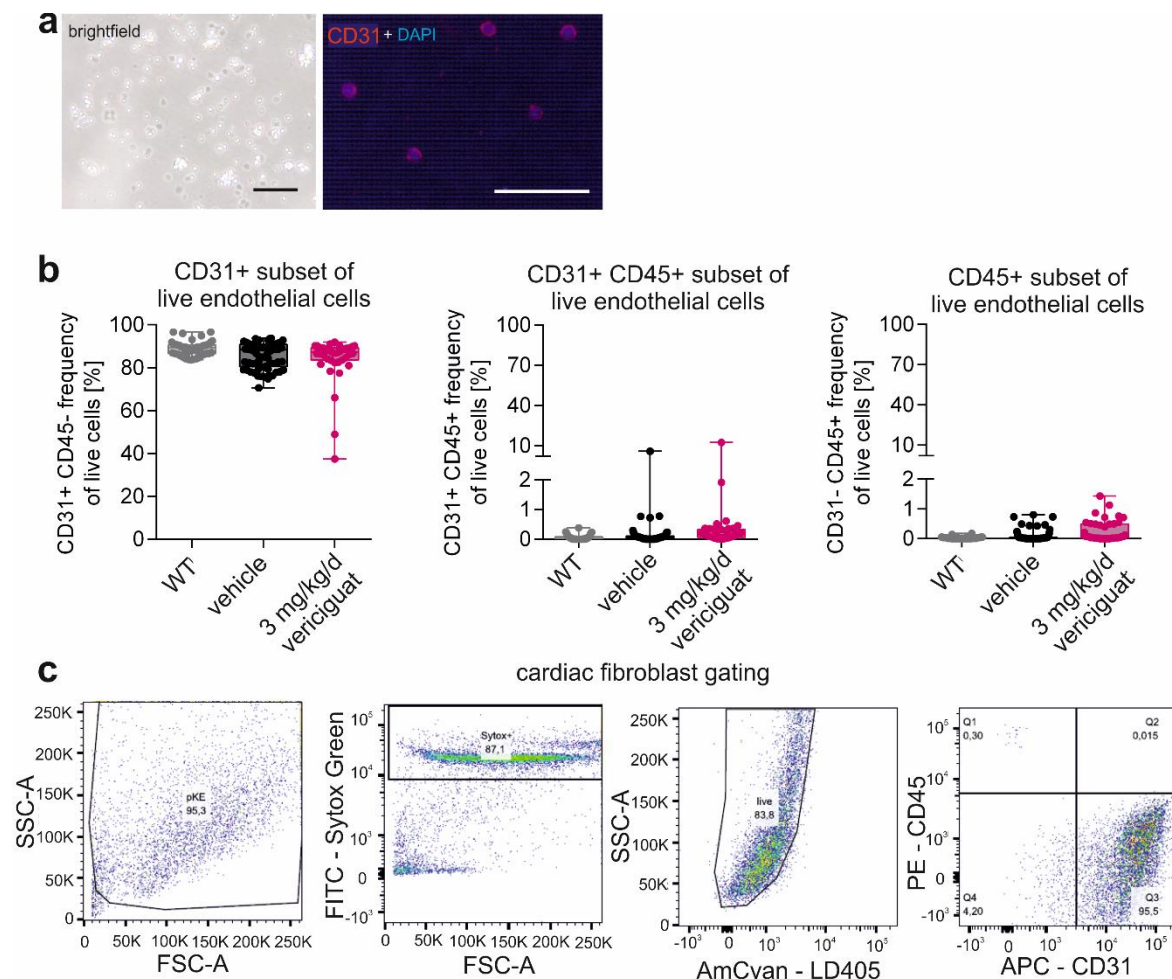
Figure 24. Confirmation of cardiac endothelial cell identity, integrity, and viability.
a Primary isolated cardiac endothelial cells from WT rat hearts showed typical morphology in brightfield and were positive for CD31 staining after 2 hours of culture (37°C, 5% CO$_2$). Nuclear co-staining with DAPI is shown. Scalebar 50 µm. b CD31-positive/CD45-negative subset, CD31-/CD45-positive subset and CD31-negative/CD45-positive subset of live endothelial cells from flow cytometry are shown as boxplot, replicates from n = 4, 5, 3. Statistical testing with one-way ANOVA. c Gating strategy for flow cytometry data to identify population of interest in isolated primary cardiac endothelial cells.

3.5.1 Importance of contraction inhibitor and cell type for bioenergetic records

The inhibition of contraction is crucial to measure cardiomyocytes *in vitro*. The physiologic feedback to contraction is lacking in cell cultures of isolated primary cardiomyocyte and beating requires extensive amount of energy. Therefore, adult primary cardiomyocytes would

die within a short period without inhibition of contraction. A commonly used contraction inhibitor is 2,3-butanedione 2-monoxime (BDM), a non-selective myosin ATPase inhibitor. It has been reported that BDM in addition inhibits the mitochondrial ATP-synthase (complex V) and blebbistatin would be a superior inhibitor for *in vitro* experiments [151]. The effect on mitochondrial respiration of BDM and blebbistatin has been studied in non-contracting adult rat primary cardiac fibroblasts and naturally contracting cardiomyocytes from WT rats in three independent experiments (Figure 25). The values in this paragraph are indicated as mean ± SD. The contraction inhibitor test shows reduction of OCR by BDM (41.43 ± 1.13 pmol/min) similar to oligomycin (46.41 ± 1.10 pmol/min) in cardiac fibroblasts, while blebbistatin (78.60 ± 1.75 pmol/min) does not cause an OCR reduction compared to medium (85.26 ± 0.95 pmol/min) (Figure 25a). In addition, oligomycin is then not capable to further inhibit mitochondrial respiration and the effect of proton-gradient uncoupler FCCP is largely diminished (101.6 ± 26.58 pmol/min) in comparison to blebbistatin (222.6 ± 33.47 pmol/min) or medium (248 ± 26.58 pmol/min) injection (Figure 25a). A similar effect was observed in primary cardiomyocytes, where BDM reduced OCR (23.33 ± 1.5 pmol/min), while blebbistatin did not affect OCR (52.76 ± 0.6 pmol/min) in the reported period compared to medium (41.56 ± 1.6 pmol/min) (Figure 25b). Due to these observations, blebbistatin was used for future cardiac cell isolation.
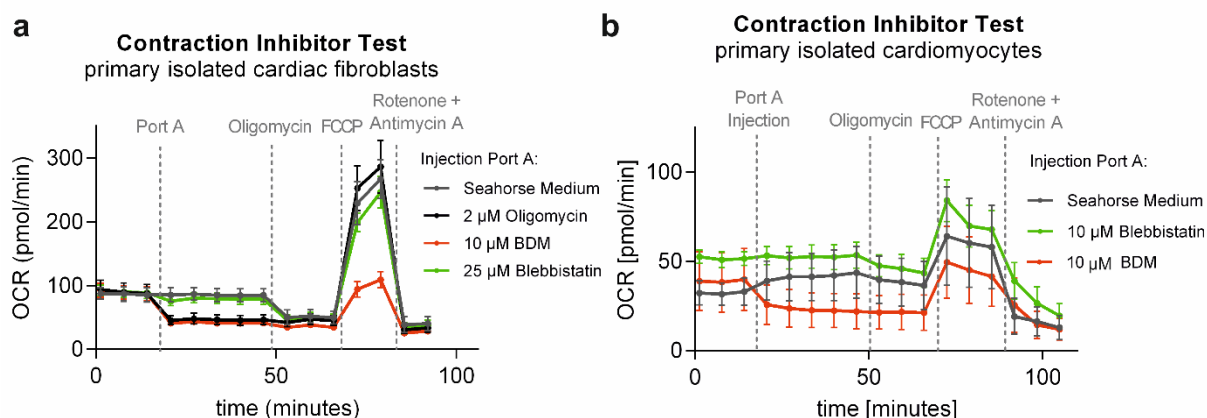
*Figure 25. Contraction inhibitor test for application of BDM or blebbistatin during primary cardiac cell isolation. Oxygen consumption rate (OCR, in pmol/min) from contraction inhibitor test with Agilent seahorse assay technology in **a** isolated cardiac fibroblasts and **b** isolated cardiomyocytes. Seahorse medium, oligomycin, BDM or blebbistatin were injected from Port A. Number of cycles were adapted accordingly. Curve from one representative experiment. Values indicates as mean ± SEM. Cardiac fibroblasts: 2 µM oligomycin, 1 µM FCCP, 1 µM rotenone/antimycin A. Cardiomyocytes: 4 µM oligomycin, 2 µM FCCP, 1 µM rotenone/antimycin A.*

The basal oxygen consumption is largely different in cardiomyocytes, cardiac fibroblasts, and cardiac endothelial cells. Isolated cardiomyocytes from WT rats show extremely high OCR

values. Therefore, a similar OCR level could be achieved with only $1x10^3$ cardiomyocytes per well (81.25 ± 36.13 pmol/min, mean ± SD) in comparison to $4x10^4$ cardiac fibroblasts (90.55 ± 55.86 pmol/min, mean ± SD) per well. Cardiac endothelial cells showed least basal OCR levels (15.13 ± 8.6 pmol/min, mean ± SD), even with increased cell numbers of $6x10^4$ cells per well. The total number of isolated cardiac endothelial cells was the limiting factor for density used.
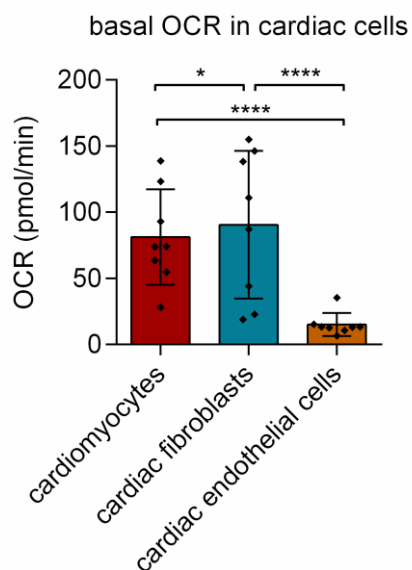
Figure 26. Difference of basal oxygen consumption rate (OCR) in isolated cardiac cells.
The basal oxygen consumption rate (OCR) differs in $1x10^3$ cardiomyocytes, $4x10^4$ cardiac fibroblasts and $6x10^4$ cardiac endothelial cells per well isolated from WT rats. Data is displayed as mean ± SD, n=9. Statistical testing using ordinary two-way ANOVA with Tukey correction for multiple comparison. p-value is reported as *p < 0.05, ****p < 0.0001.

3.6 Energy profile of isolated primary cardiac cells

The mitochondrial oxidative phosphorylation and glycolysis were measured using seahorse life-cell energy flux assays (seahorse technology Agilent). The mitochondrial stress test, a measure for the mitochondrial respiration of a cell and the glycolytic stress test, a readout for cellular glycolysis were performed in isolated primary cardiac cells. Cardiomyocytes, cardiac fibroblasts, and cardiac endothelial cells were isolated in a simultaneous approach from healthy control (WT), vehicle treated and 3 mg/kg/d vericiguat treated dTGR.

3.6.1 Cardiomyocytes indicated reduced mitochondrial energy metabolism.

Isolated primary cardio myocytes from WT showed a characteristic energy profile in the mitochondrial stress test (Figure 27a). Oligomycin reduced OCR, while FCCP increased OCR to its maximum and rotenone and antimycin suppressed oxidative phosphorylation to measure non-mitochondrial respiration. Vehicle and 3 mg/kg/d vericiguat treated dTGR showed a different pattern with higher values after oligomycin injection and lower values after

stimulation with FCCP. Quantification of parameters from the mitochondrial stress test showed no difference in basal mitochondrial respiration in WT, vehicle and 3 mg/kg/d vericiguat treated dTGR (Figure 27b). The maximal mitochondrial respiration was lower in cardiomyocytes from vehicle treated dTGR (95.76 ± 61.62 pmol/min/Hoechst, mean ± SD) in comparison to cardiomyocytes from WT rats (136.3 ± 96.23 pmol/min/Hoechst, mean ± SD, p = 0.0486, one-way ANOVA with Dunnett's multiple comparison). The maximal mitochondrial respiration was not improved in cardiomyocytes from 3 mg/kg/d vericiguat treated dTGR (103.4 ± 49.95, mean ± SD, p = 0.8902, one-way ANOVA with Dunnett's multiple comparison) compared to vehicle treated dTGR (Figure 27c). ATP production (Figure 27d), non-mitochondrial respiration (Figure 27e) and proton leak (Figure 27f), were not significantly different between the three groups.
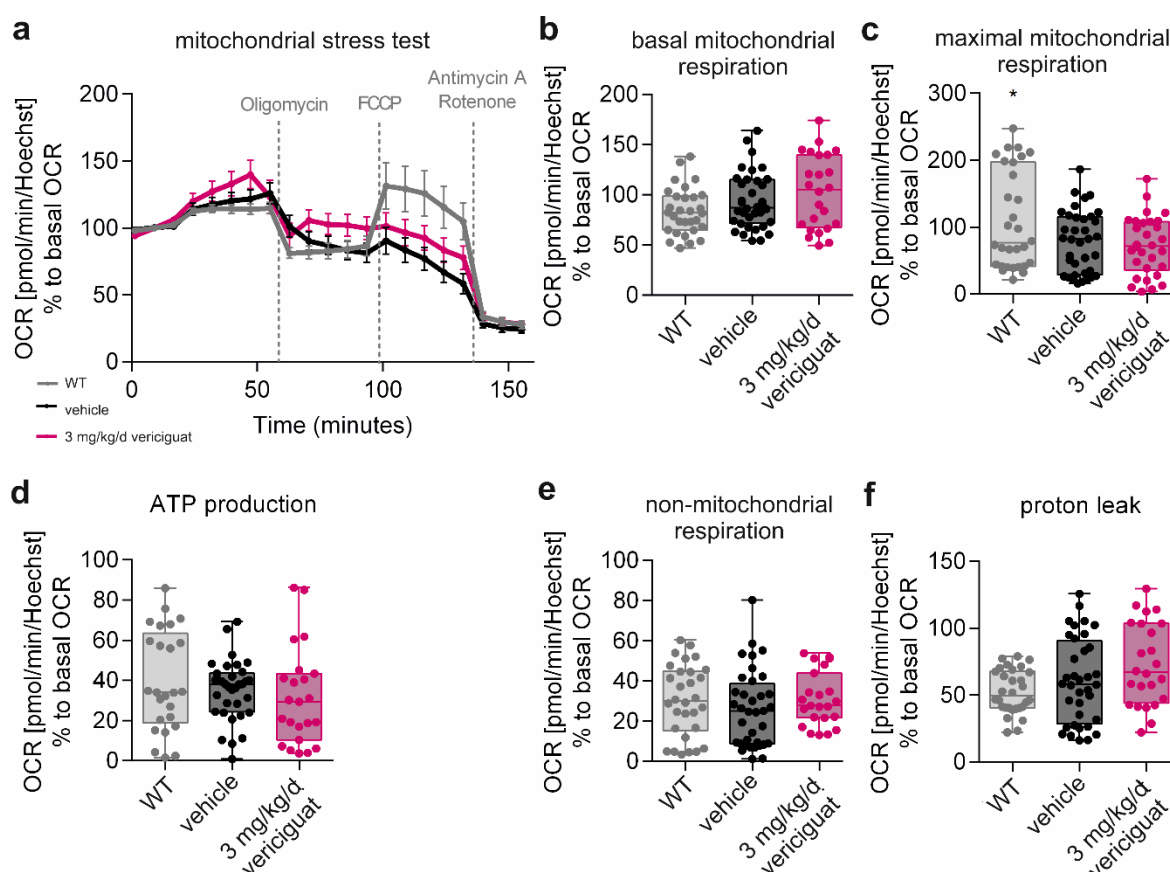
Figure 27. Mitochondrial energy metabolism is reduced in isolated primary cardiomyocytes from vehicle treated and 3 mg/kg/d vericiguat treated dTGR.
*a Mitochondrial stress test in isolated primary rat cardiomyocytes as oxygen consumption rate (OCR) normalised to nuclear Hoechst staining-derived intensity in % to respective basal OCR values over the assay time. Data is displayed as mean ± SEM. Quantification of **b** basal mitochondrial respiration **c** maximal mitochondrial respiration **d** proton leak **e** ATP production and **f** non-mitochondrial respiration from mitochondrial stress test. Data is shown as boxplot. Replicates originate from n = 5 WT rats, n = 6 vehicle treated dTGR and n = 4 vericiguat treated dTGR (3 mg/kg/d). Ordinary one-way ANOVA with Dunnett's multiple comparison to vehicle. p-value reported as *p < 0.05.*

The glycolytic stress test in isolated primary cardiomyocytes from WT rats, vehicle and 3 mg/kg/d vericiguat treated dTGR showed an increase of extracellular acidification rate (ECAR) after stimulation with glucose, meaning an increase in glycolysis. It was most pronounced in cells from vericiguat treated dTGR hearts (Figure 28a). Oligomycin did not further increase ECAR. Quantification of the glycolytic stress test showed no difference in basal glycolysis between cardiomyocytes from WT rats (111.8 ± 63.6 mpH/min/Hoechst, mean ± SD) and vehicle treated dTGR (138.1 ± 78.6 mpH/min/Hoechst, mean ± SD). A mild but not significant increase of basal glycolysis in cardiomyocytes from 3 mg/kg/d vericiguat treated dTGR (181.8 ± 115.1 mpH/min/Hoechst, mean ± SD) in comparison to vehicle treated dTGR was observed (Figure 28b). The maximal glycolytic capacity was not significantly different the groups (WT: 175.7 ± 148.3 mpH/min/Hoechst, vehicle: 97.4 ± 65.7 mpH/min/Hoechst, 3 mg/kg/d vericiguat: 155.3 ± 149.4 mpH/min/Hoechst, all mean ± SD, Figure 28c).

Figure 28. Glycolytic stress test measured in isolated primary cardiomyocytes from vehicle- and 3 mg/kg/d vericiguat treated dTGR.
a Glycolytic stress test in isolated primary rat cardiomyocytes measured as extracellular acidification rate (ECAR) normalised to nuclear Hoechst staining-derived intensity in % to basal ECAR values over the assay time. Data is displayed as mean ± SEM. Quantification of b basal glycolysis and c maximal glycolytic capacity from glycolytic stress test. Data is shown as boxplot. Replicates originate from n = 5 WT rats, n = 6 vehicle treated dTGR and n = 4 vericiguat treated dTGR (3 mg/kg/d). Ordinary one-way ANOVA with Dunnett's multiple comparison to vehicle.

3.6.2 Cardiac fibroblasts shifted towards mitochondrial energy generation.

Analysis of mitochondrial respiration and glycolysis was performed in isolated primary cardiac fibroblasts after seven days of culture (37°C, 5% CO_2). Cardiac fibroblasts from WT rats showed a characteristic energy profile in the mitochondrial stress test (Seahorse technology Agilent, Figure 29a). OCR was reduced by oligomycin, FCCP led to maximal OCR

while non-mitochondrial respiration could be detected by suppression of oxidative phosphorylation by rotenone and antimycin A. Vehicle and 3 mg/kg/d vericiguat treated dTGR showed higher basal OCR values, less OCR reduction after oligomycin injection and higher OCR values after stimulation with FCCP (Figure 29a). Parameters from the mitochondrial stress test were quantified and are indicated as mean ± SD in this paragraph. OCR values of isolated primary cardiac fibroblasts from vehicle treated dTGR were significantly higher in comparison to isolated primary cardiac fibroblasts from WT for basal mitochondrial respiration (vehicle: 68.30 ± 7.1 pmol/min/Hoechst, WT: 52.67 ± 11.9 pmol/min/Hoechst, Kruskal-Wallis test, $p < 0.0001$) (Figure 29b), maximal mitochondrial respiration (vehicle: 142.6 ± 44.0 pmol/min/Hoechst, WT: 90.03 ± 53.0 pmol/min/Hoechst, Kruskal-Wallis test, $p = 0.0004$) (Figure 29c), ATP production (vehicle: 57.53 ± 5.7 pmol/min/Hoechst, WT: 39.58 ± 11.2 pmol/min/Hoechst, Kruskal-Wallis test, $p < 0.0001$) (Figure 29d) and non-mitochondrial respiration (vehicle: 38.90 ± 13.4 pmol/min/Hoechst, WT: 25.12 ± 6.2 pmol/min/Hoechst, Kruskal-Wallis test, $p = 0.0001$) (Figure 29e). Mitochondrial respiration parameter mentioned above were similar in isolated primary cardiac fibroblasts from 3 mg/kg/d vericiguat treated dTGR (basal: 62.19 ± 4.7 pmol/min/Hoechst, maximal: 150.4 ± 48.7 pmol/min/Hoechst, ATP production: 53.94 ± 4.6 pmol/min/Hoechst, non-mitochondrial: 38.69 ± 6.0 pmol/min/Hoechst) in comparison to isolated primary cardiac fibroblasts from vehicle treated dTGR (Figure 29b-e). Proton leak was similar between isolated primary cardiac fibroblasts from WT rats and vehicle treated dTGR. Isolated primary fibroblasts from hearts of 3 mg/kg/d vericiguat treated dTGR showed a reduction in proton leak (Figure 29f).

Figure 29. Mitochondrial stress test and assessment of mitochondrial energy metabolism in isolated primary cardiac fibroblasts.
a Mitochondrial stress test in isolated primary rat cardiac fibroblasts as oxygen consumption rate (OCR) normalised to cell count in % to basal OCR values over the assay time. Data is displayed as mean ± SEM. Quantification of b basal mitochondrial respiration c maximal mitochondrial respiration d proton leak e ATP production and f non-mitochondrial respiration from mitochondrial stress test. Data is shown as boxplot. Replicates originate from n = 5 WT rats, n = 6 vehicle treated dTGR and n = 4 of 3 mg/kg/d vericiguat treated dTGR. Kruskal-Wallis test with Dunn's correction for multiple comparison to vehicle. p-value reported as *p < 0.05, ***p < 0.001, ****p < 0.0001.

Isolated primary cardiac fibroblasts from WT, vehicle treated and 3 mg/kg/d vericiguat treated dTGR showed an increase of extracellular acidification rate (ECAR) after stimulation with glucose in the glycolytic stress test. It was most pronounced in fibroblasts from vehicle treated dTGR, followed by fibroblasts from 3 mg/kg/d vericiguat treated dTGR (Figure 30a). After oligomycin injection, ECAR increased in fibroblasts from vehicle treated and 3 mg vericiguat but not in those from rats (Figure 30a). Basal glycolysis and maximal glycolytic capacity were quantified from glycolytic stress test (Figure 30b, c). Both were significant lower in fibroblasts from WT rats (basal: 111.5 ± 118.2 mpH/min/1000 cells, maximal: 262.3 ± 126.0 mpH/min/1000 cells, mean ± SD, $p < 0.0001$, Kruskal-Wallis test) compared to fibroblasts from vehicle treated dTGR (basal: 338 ± 162.6 mpH/min/1000 cells, maximal: 530.5 ± 307.6 mpH/min/1000 cells, mean ± SD). In both parameters ECAR values from

isolated primary cardiac fibroblasts from 3 mg/kg/d vericiguat treated dTGR (basal: 232.6 ± 128.1 mpH/min/1000 cells, maximal: 367.8 ± 119.4 mpH/min/1000 cells, mean ± SD) were not significant different to those from vehicle treated dTGR (Figure 30b, c).
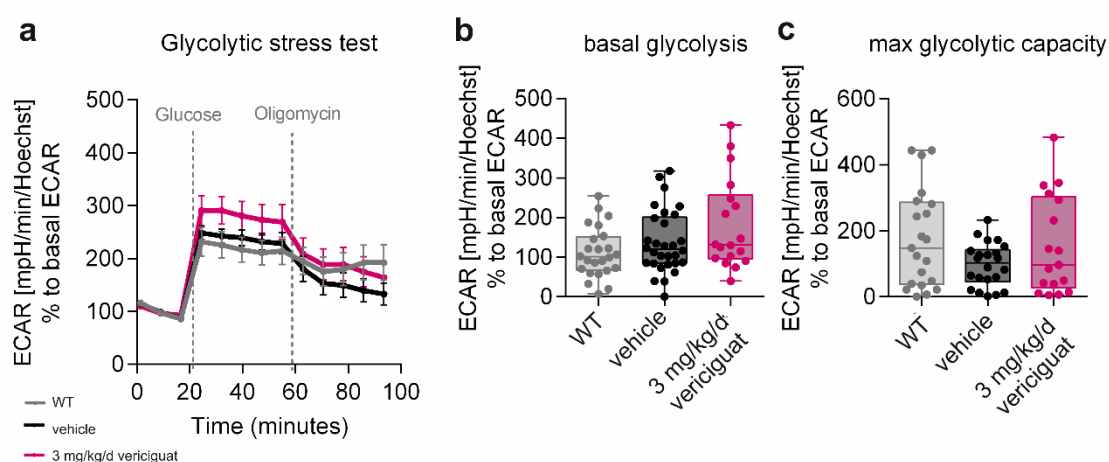

Figure 30. Glycolytic stress test measured in isolated primary cardiac fibroblasts from vehicle- and 3 mg/kg/d vericiguat treated dTGR.
*a Glycolytic stress test in isolated primary rat cardiac fibroblasts measured as extracellular acidification rate (ECAR) normalised to cell count in % to basal ECAR values over the assay time. Data is displayed as mean ± SEM. Quantification of b basal glycolysis and c maximal glycolytic capacity from glycolytic stress test. Data is shown as boxplot. Replicates originate from n = 5 WT rats, n = 6 vehicle treated dTGR and n = 4 vericiguat treated dTGR (3 mg/kg/d). Kruskal-Wallis test with Dunn's multiple comparison to vehicle. p-value reported as ****p < 0.0001.*

3.6.3 <u>Energy profile of cardiac endothelial cells was unaltered.</u>

The mitochondrial respiration of isolated primary cardiac endothelial cells from WT rats, vehicle and 3 mg/kg/d vericiguat treated dTGR was characterized with mitochondrial stress test (Figure 31a). All groups showed a characteristic energy profile in the mitochondrial stress test with limited ability of FCCP to increase OCR. Quantification of mitochondrial stress test showed no differences of mitochondrial respiration in isolated primary cardiac endothelial cells from WT rats, vehicle and 3 mg/kg/d vericiguat treated dTGR (Figure 31b-e). Proton leak was significantly lower in endothelial cells from WT rats (17.57 ± 9.0 pmol/min/1000 cells, mean ± SD, p = 0.0122 Kruskal-Wallis test) in comparison to those from vehicle treated dTGR (29.88 ± 9.4 pmol/min/1000 cells, mean ± SD), while vericiguat had no effect (Figure 31f).
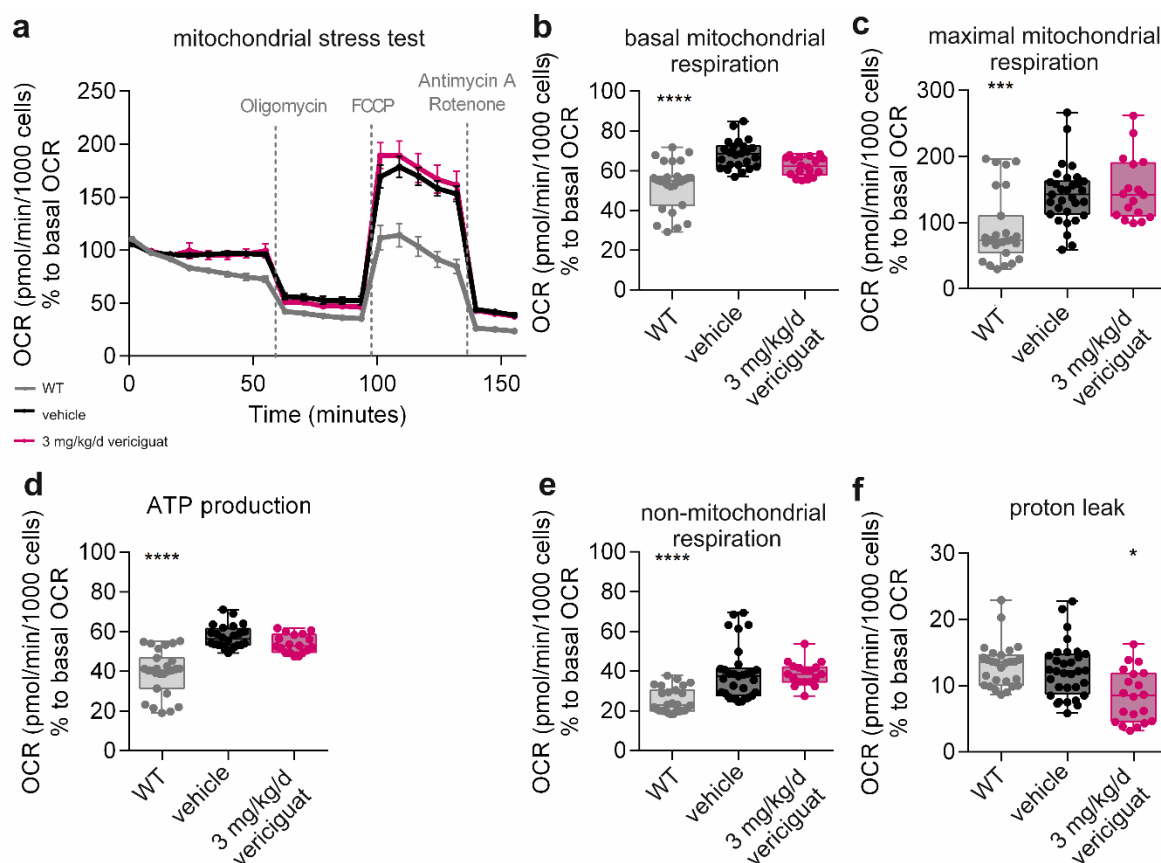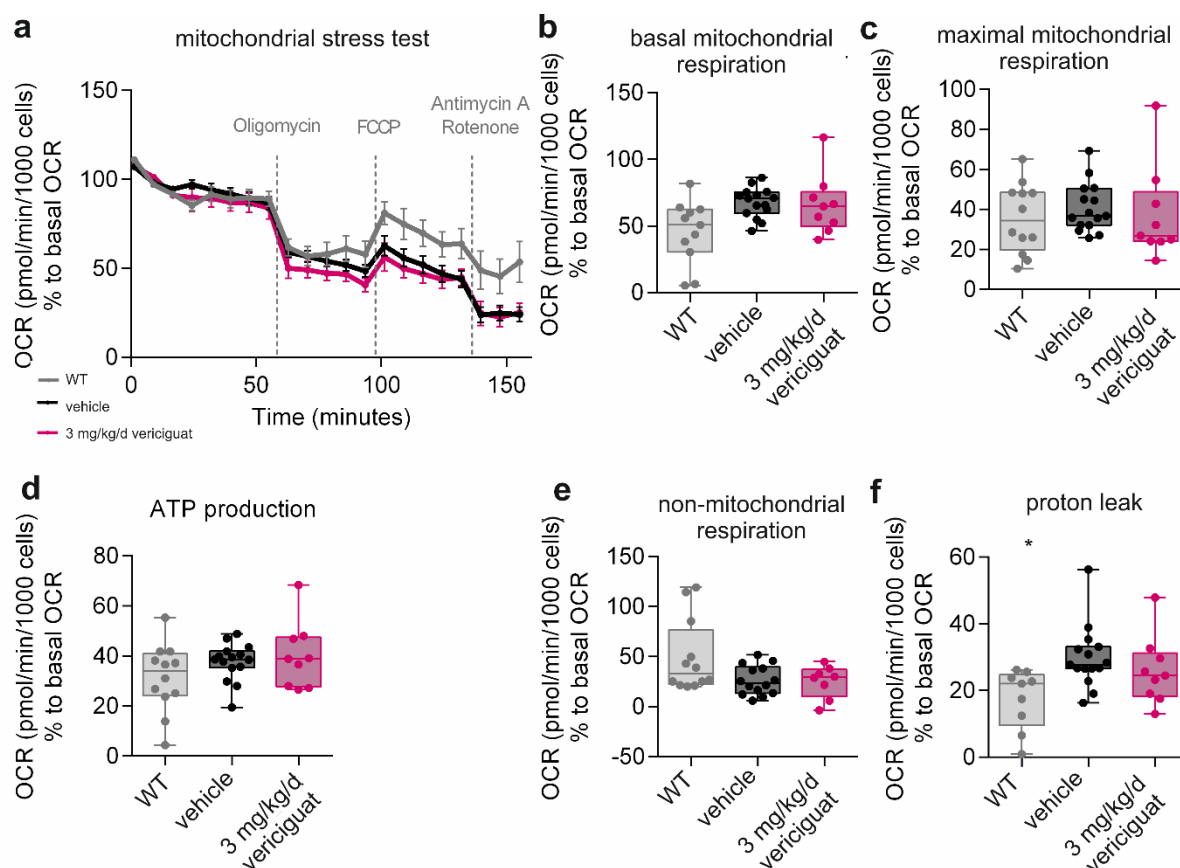
Figure 31. Mitochondrial stress test and assessment of mitochondrial energy metabolism in isolated primary cardiac endothelial cells.
***a** Mitochondrial stress test in isolated primary rat cardiac endothelial cells as oxygen consumption rate (OCR) normalised to cell count in % to respective basal OCR values over the assay time. Data is displayed as mean ± SEM. Quantification of **b** basal mitochondrial respiration **c** maximal mitochondrial respiration **d** proton leak **e** ATP production and **f** non-mitochondrial respiration from mitochondrial stress test. Data is shown as boxplot. Replicates originate from n = 4 WT rats, n = 5 vehicle treated dTGR and n = 3 vericiguat treated dTGR (3 mg/kg/d). Kruskal multiple comparison to vehicle. p-value reported as *p < 0.05.*

Isolated primary cardiac endothelial cells from WT, vehicle and 3 mg/kg/d vericiguat treated dTGR showed a delayed increase of extracellular acidification rate (ECAR) after stimulation with glucose in the glycolytic stress test (Figure 32a). The increase in ECAR was most pronounced in endothelial cells from vehicle treated dTGR. After oligomycin injection ECAR did not increased in isolated primary endothelial. Quantification of the glycolytic stress test showed similar basal glycolysis and maximal glycolytic capacity in endothelial cells from WT rats, vehicle or 3 mg/kg/d vericiguat treated dTGR (Figure 32b, c).
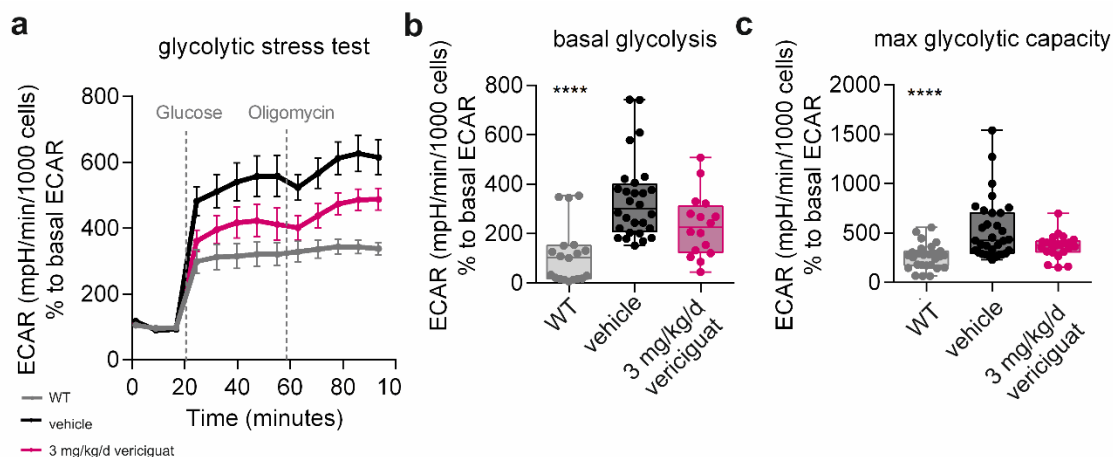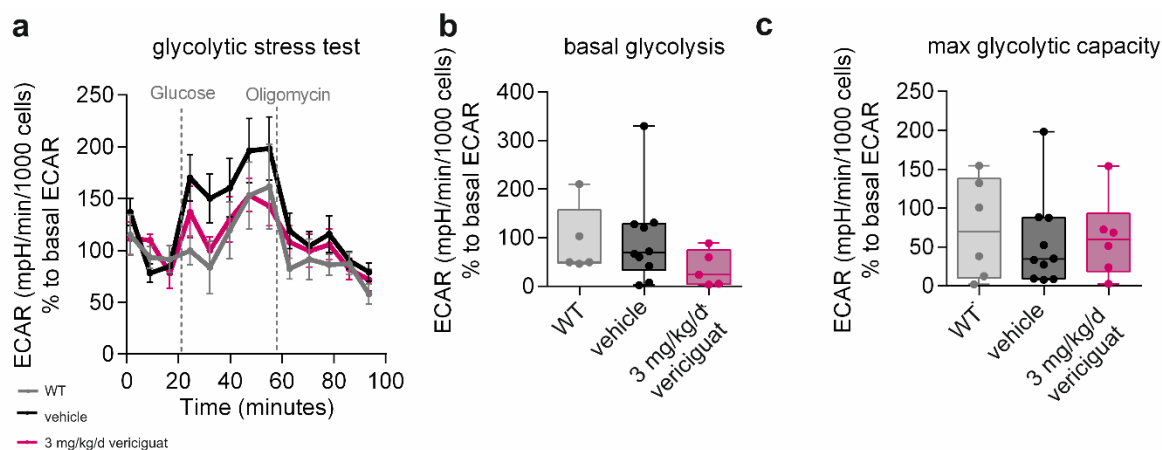
Figure 32. Glycolytic stress test measured in isolated primary cardiac endothelial cells from vehicle- and 3 mg/kg/d vericiguat treated dTGR.
a Glycolytic stress test in isolated primary rat cardiac endothelial cells measured as extracellular acidification rate (ECAR) normalised to cell count in % to basal ECAR values over the assay time. Data is displayed as mean ± SEM. Quantification of b basal glycolysis and c maximal glycolytic capacity from glycolytic stress test. Data is shown as boxplot. Replicates originate from n = 4 WT rats, n = 5 vehicle treated dTGR and n = 3 vericiguat treated dTGR (3 mg/kg/d). Kruskal-Wallis test with Dunn's multiple comparison to vehicle.

Besides the differences in mitochondrial respiration and glycolysis of isolated cardiac cells from WT rats and vehicle treated dTGR, vericiguat had no convincing effect on the energy profile.

3.7 Protective effects of vericiguat on renal damage

3.7.1 Urinary albumin and creatinine indicate improved renal function.

The renal function was evaluated by measurement of urinary albumin, creatinine, and urea, reported as mean ± SD in this paragraph (Figure 33). Urinary albumin excretion progressively rose in vehicle treated dTGR from 1146 ± 799 µg/d in week 5, to 3984 ± 2771 µg/d in week 6 and 10441 ± 8867 µg/d in week 7 indicating albuminuria (Figure 33a). WT rats had significant lower albumin excretion (48 ± 22 µg/d in week 5, 141 ± 89 µg/d in week 6, $p = 0.0005$ and 188 ± 41 µg/d in week 7, $p < 0.0001$, two-way ANOVA in comparison to vehicle, Figure 33a). Administration of 0.3 mg/kg/d vericiguat had no advanced effect on albumin excretion compared to vehicle treated dTGR (1326 ± 916 µg/d in week 5, 2455 ± 1034 µg/d in week 6 and 8843 ± 3857 µg/d at week 7). A significant reduction in albuminuria was not achieved in week 5 with 1 mg/kg/d (485 ± 346 µg/d) but was reduced to 1248 ± 1020 µg/d in week 6 ($p = 0.0134$) and 2668 ± 1847 µg/d in week 7 ($p = 0.0005$) in comparison to vehicle treated dTGR. The 3 mg/kg/d vericiguat treatment reduced albumin excretion compared to vehicle in dTGR (101 ± 66 µg/d in week 5,

357 ± 146 µg/d in week 6, $p < 0.0001$ and 1011 ± 740 µg/d at week 7, $p < 0.0001$, two-way ANOVA) (Figure 33a, b). The albuminuria was most pronounced in vehicle treated dTGR in week 7 and largely improved by 3 mg/kg/d vericiguat at that time point (Figure 33b).

Urinary creatinine level was decreased in vehicle treated dTGR to 1.1 ± 0.3 mmol/l in comparison to WT rats with 3.6 ± 0.8 mmol/l in week 7 (one-way ANOVA, $p < 0.0001$, Figure 33c). Treatment of dTGR with 0.3 or 1 mg/kg/d vericiguat could not ameliorate urinary creatinine compared to vehicle treated dTGR in week 7 (0.3 mg/kg/d: 1.0 ± 0.4; 1 mg/kg/d: 2.0 ± 1.3 mmol/l). With 3 mg/kg/d vericiguat (3.8 ± 1.8 mmol/l in week 7, one-way ANOVA, $p < 0.0001$) urinary creatinine increased significantly in comparison to vehicle treated dTGR (Figure 33c). Similar, urea excretion at week 7 was reduced to 200.3 ± 39.8 mmol/l in vehicle treated dTGR in comparison to WT (572.3 ± 113.2 mmol/l, one-way ANOVA, $p < 0.0001$) and dose-dependently improved by vericiguat treatment (0.3 mg/kg/d: 166.7 ± 51.69 mmol/l, $p = 0.95$; 1 mg/kg/d: 330.9 ± 174.3 mmol/l, $p = 0.14$; 3 mg/kg/d: 534.6 ± 225.7 mmol/l, $p < 0.0001$, one-way ANOVA in comparison to vehicle, Figure 33d).
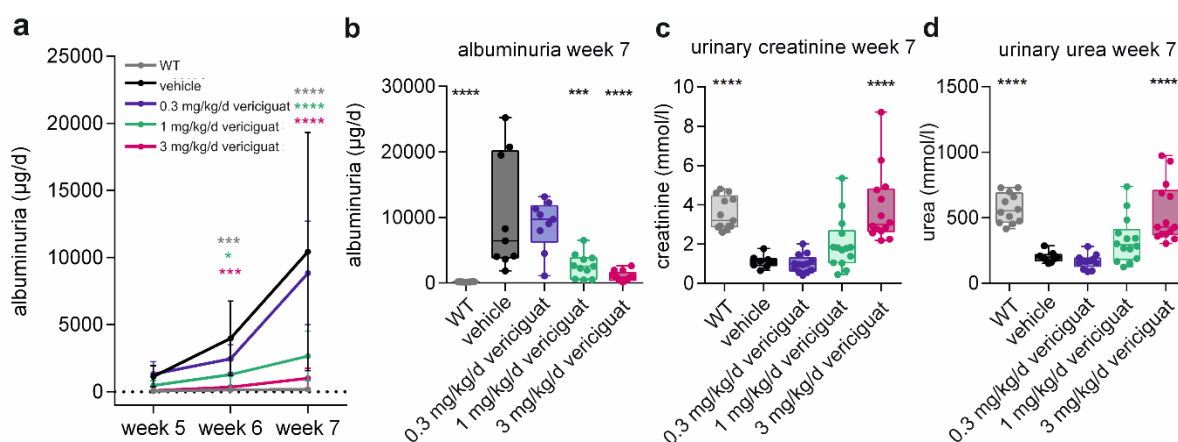
Figure 33. Albuminuria is ameliorated by 1 and 3 mg/kg/d vericiguat.
*a The course of albuminuria is expressed as µg albumin per day in WT rats, vehicle- or 0.3, 1 and 3 mg/kg/d vericiguat treated dTGR at week 5, 6 and 7. Data expressed as mean ± SD, n = 9-14. Two-way ANOVA with Dunnett's correction for multiple comparison. b Albuminuria (µg albumin/day), c urinary creatinine (mmol/l) and d urinary urea are elevated in vehicle treated dTGR and improved by vericiguat. Data shown as boxplot, n = 12-14. Ordinary one-way ANOVA with Dunnett's multiple comparison to vehicle. p-value indicated as ***p < 0.001, ****p < 0.0001.*

3.7.2 <u>Vericiguat improves renal endothelial damage and oxidative stress.</u>

Endothelial damage and oxidative stress were characterized in the kidney by analysis of marker gene expression (Figure 34). Endothelin (*Et1*), vascular endothelial growth factor alpha (*Vegfα*), genes associated with endothelial damage showed increased mRNA expression in the kidney in vehicle treated dTGR compared to WT rats (Figure 34, Table 12).

Only administration of 3 mg/kg/d vericiguat reduced the expression of *Et1* significantly in comparison to vehicle treated dTGR, while *Vegfα* expression did not benefit from any vericiguat dose compared to vehicle treated dTGR. The mRNA expression of *Cybα* and *Cybβ* both oxidative stress marker, was increased in kidneys of vehicle treated dTGR compared to WT rats. Neutrophil cytosolic factor 1 (*Ncf1*) and neutrophil cytosolic factor 4 (*Ncf4*) are not only indicator for oxidative stress but prognostic marker for renal immune infiltration [163]. They were significantly elevated in vehicle treated dTGR in comparison to WT rats. The 3 mg/kg/d vericiguat treated dTGR presented reduction of mRNA expression of *Cybα, Cybβ, Ncf1* and *Ncf4* in comparison to vehicle treated rats (Figure 34, Table 12). NADPH oxidase 4 (*Nox4*) gene expression was similar in all groups (Table 12).
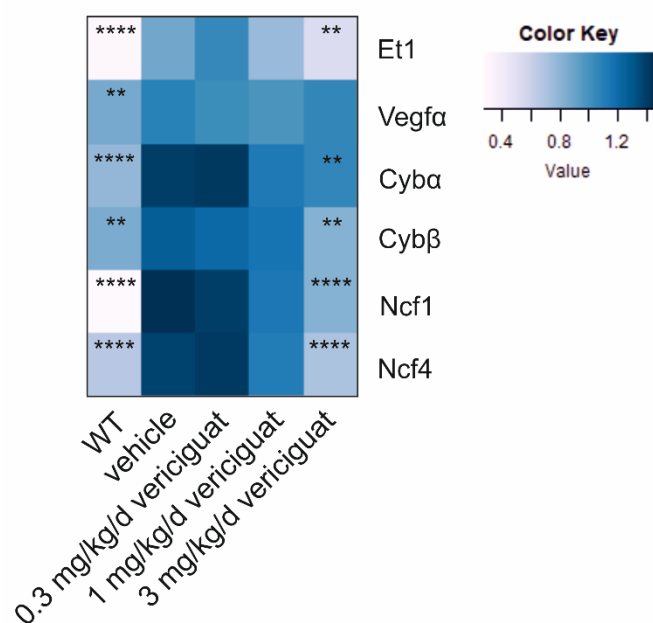
Figure 34. Renal gene expression of endothelial damage and oxidative stress marker.
Hypothesis-driven heatmap shows expression of endothelial damage and oxidative stress marker genes in the kidney relative to 18S expression, measured with RT-qPCR. Endothelin (Et1), vascular endothelial growth factor α (Vegfα), Cytochrome b-245 alpha and beta chain polypeptide (Cybα, Cybβ), neutrophil cytosolic factor 1 and 4 (Ncf1, Ncf4) The colour key represents low values in light colour, high values in dark blue, n = 12-14. Ordinary one-way ANOVA or Kruskal-Wallis test with respective multiple comparison to vehicle was performed. p-value is indicated as *p < 0.05, **p < 0.01, ***p < 0.001, ****p < 0.0001.

Table 12. Renal gene expression measured with RT-qPCR.
Data is reported as mean ± SD, sample number per group is indicated. One-way ANOVA or Kruskal-Wallis test with appropriate multiple comparison were performed, p-values are reported.

Gene	WT	vehicle	0.3 mg/kg/d	1 mg/kg/d	3 mg/kg/d
	n=13	n=12	vericiguat	vericiguat	vericiguat

	(*p*-value)		n=13 (*p*-value)	n=12 (*p*-value)	n=14 (*p*-value)
Kim1	0.012 ± 0.01 (< 0.0001)	1.602 ± 0.81	2.338 ± 1.37 (> 0.9999)	1.417 ± 1.07 (> 0.9999)	0.318 ± 0.26 (0.0161)
Ngal	0.116 ± 0.024 (0.0004)	1.340 ± 0.74	1.939 ± 1.07 (0.1426)	1.396 ± 1.01 (0.9990)	0.244 ± 0.11 (0.0016)
Ctgf	0.763 ± 0.17 (0.0029)	1.096 ± 0.27	1.189 ± 0.33 (0.7170)	0.927 ± 0.19 (0.2438)	0.829 ± 0.18 (0.0191)
Opn	0.093 ± 0.02 (< 0.0001)	1.175 ± 0.47	1.500 ± 0.48 (0.1124)	1.125 ± 0.65 (0.7746)	0.342 ± 0.21 (< 0.0001)
Mcp1	0.445 ± 0.12 (< 0.0001)	1.187 ± 0.54	1.200 ± 0.27 (0.9999)	0.836 ± 0.42 (0.0473)	0.559 ± 0.18 (< 0.0001)
Col3	0.708 ± 0.13 (0.0003)	1.386 ± 0.38	1.267 ± 0.24 (> 0.9999)	1.139 ± 0.57 (0.4190)	0.717 ± 0.31 (0.0002)
Col1α	0.891 ± 0.33 (0.0012)	1.869 ± 0.58	1.816 ± 0.70 (> 0.9999)	1.431 ± 0.71 (0.4869)	0.745 ± 0.39 (< 0.0001)
Timp1	0.199 ± 0.03 (< 0.0001)	1.364 ± 0.425	1.600 ± 0.45 (0.4257)	1.269 ± 0.682 (0.9469)	0.424 ± 0.21 (< 0.0001)
Pai1	0.213 ± 0.06 (< 0.0001)	1.222 ± 0.40	1.438 ± 0.37 (0.2890)	0.965 ± 0.45 (0.1722)	0.473 ± 0.16 (< 0.0001)
Nox4	0.919 ± 0.11 (0.9240)	0.985 ± 0.27	0.966 ± 0.28 (0.9991)	0.944 ± 0.33 (0.9861)	1.243 ± 0.27 (0.0510)
Cybβ	0.857 ± 0.14 (0.0061)	1.267 ± 0.39	1.215 ± 0.36 (0.9813)	1.163 ± 0.39 (0.8386)	0.826 ± 0.19 (0.0023)
Ncf1	0.278 ± 0.07 (< 0.0001)	1.454 ± 0.29	1.402 ± 0.36 (0.9746)	1.144 ± 0.38 (0.0342)	0.828 ± 0.23 (< 0.0001)
Ncf4	0.669 ± 0.13 (< 0.0001)	1.382 ± 0.32	1.416 ± 0.28 (0.9931)	1.115 ± 0.35 (0.0576)	0.710 ± 0.21 (< 0.0001)
Et1	0.307 ± 0.10 (< 0.0001)	0.880 ± 0.28	1.055 ± 0.36 (0.2337)	0.769 ± 0.28 (0.6389)	0.529 ± 0.13 (0.0023)
Vegfα	0.872 ± 0.13 (0.0020)	1.090 ± 0.16	1.032 ± 0.16 (0.7277)	0.993 ± 0.17 (0.3221)	1.063 ± 0.12 (0.9729)
Tgfβ	0.594 ± 0.10 (< 0.0001)	1.312 ± 0.34	1.365 ± 0.23 (0.9594)	1.062 ± 0.37 (0.0670)	0.654 ± 0.17 (< 0.0001)

Cybα	0.782 ± 0.10	1.395 ± 0.26	1.419 ± 0.25	1.136 ± 0.28	1.066 ± 0.30
	(< 0.0001)		(0.9973)	(0.0467)	(0.0053)

3.7.3   Renal tubular integrity largely benefits from vericiguat treatment.

Besides renal function and expression of relevant marker, the tubular injury was analysed in cortical images of Periodic-acid-Schiff (PAS)-stained kidneys (Figure 35a). The semi-quantitative tubular injury score was elevated in the kidney of vehicle treated dTGR (26.75 ± 9.5%/FOV, mean ± SD) compared to WT rats (8.39 ± 2.6%/FOV, mean ± SD, $p < 0.0001$, Kruskal-Wallis test). It was only significantly reduced in 3 mg/kg/d vericiguat treated dTGR in comparison to WT rats (9.71 ± 6.6%/FOV, mean ± SD, $p = 0.0001$, Figure 35a). The renal injury marker kidney injury molecule 1 (*Kim1*), which is mainly present in the proximal tubules, *Ngal* and *Opn* that is expressed in the loops of Henle, showed increased mRNA expression in the kidney of vehicle treated dTGR compared to WT rats (Figure 35b-d, Table 12). Administration of 3 mg/kg/d vericiguat reduced the high expression in dTGR (Figure 35b-d), while 0.3 and 1 mg/kg/d doses had no effect.
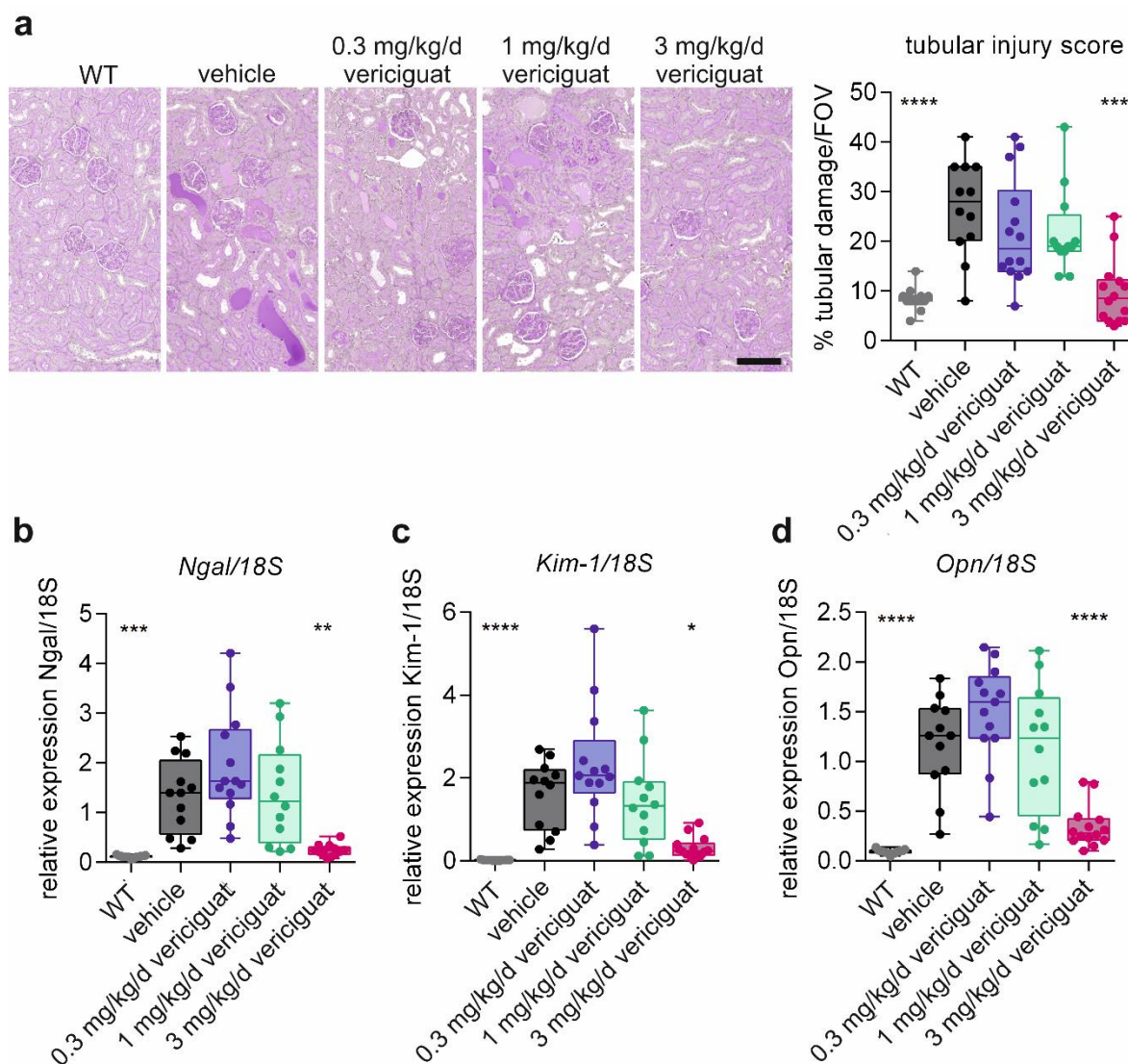
Figure 35. Tubular renal injury largely improved by treatment with 3 mg/kg/d vericiguat.
a Left: Representative image of PAS-stained renal cortex display tubular cast formation, dilation, degeneration, and partial brush border loss in vehicle-, 0.3 and 1 mg/kg/d vericiguat treated dTGR. Scalebar 150 µm. Right: Semi-quantitative analysis of tubular injury score displays increased percentage of tubular damage per field of view (FOV) in vehicle-, 0.3 and 1 mg/kg/d vericiguat treated dTGR with improvement by 3 mg/kg/d vericiguat treatment. Kruskal-Wallis test with Dunn's multiple comparison. Data displayed as boxplot, n = 12-14. Renal gene expression of b Neutrophil gelatinase associated lipocalin 2 (Ngal), c kidney injury molecule 1 (Kim-1) and d Osteopontin (Opn) relative to 18S is shown as boxplot. Ordinary one-way ANOVA with Dunnett's multiple comparison to vehicle. p-value shown as *p < 0.05, **p < 0.01, ***p < 0.001, ****p < 0.0001.

3.7.4 Limited advantage by vericiguat treatment on renal fibrosis.

Investigation of renal fibrosis was conducted on perivascular, interstitial, and glomerular level. The expression of the fibrosis associated genes *Col1α, Col3*, Serpin family E member 1 (*Pai1*) and TIMP metallopeptidase inhibitor 1 (*Timp1*) were increased in kidneys of vehicle treated dTGR compared to WT rats (Figure 36a, Table 12). Vericiguat treatment with 3 mg/kg/d ameliorated the expression of these fibrosis associated genes in comparison to

vehicle treated rats. The 0.3 and 1 mg/kg/d vericiguat doses had no effect on *Col1α, Col3, Pai1* and *Timp1* gene expression compared to vehicle treated dTGR.

Perivascular and interstitial fibrosis were examined by histologic analysis of MGT-stained kidney sections (Figure 36d). Perivascular fibrotic area was normalized to the cross-sectional media area. The renal perivascular matrix deposition was similar between groups (Figure 36b). Interstitial renal fibrosis was estimated as positive area per view field. In kidney sections of vehicle treated dTGR the interstitial fibrosis was elevated to 5.8% in comparison to 0.5% in WT rats. Vericiguat treatment with 3 mg/kg/d could not significantly reduce renal interstitial matrix deposition with remaining interstitial fibrosis of 2.8% (Figure 36c).
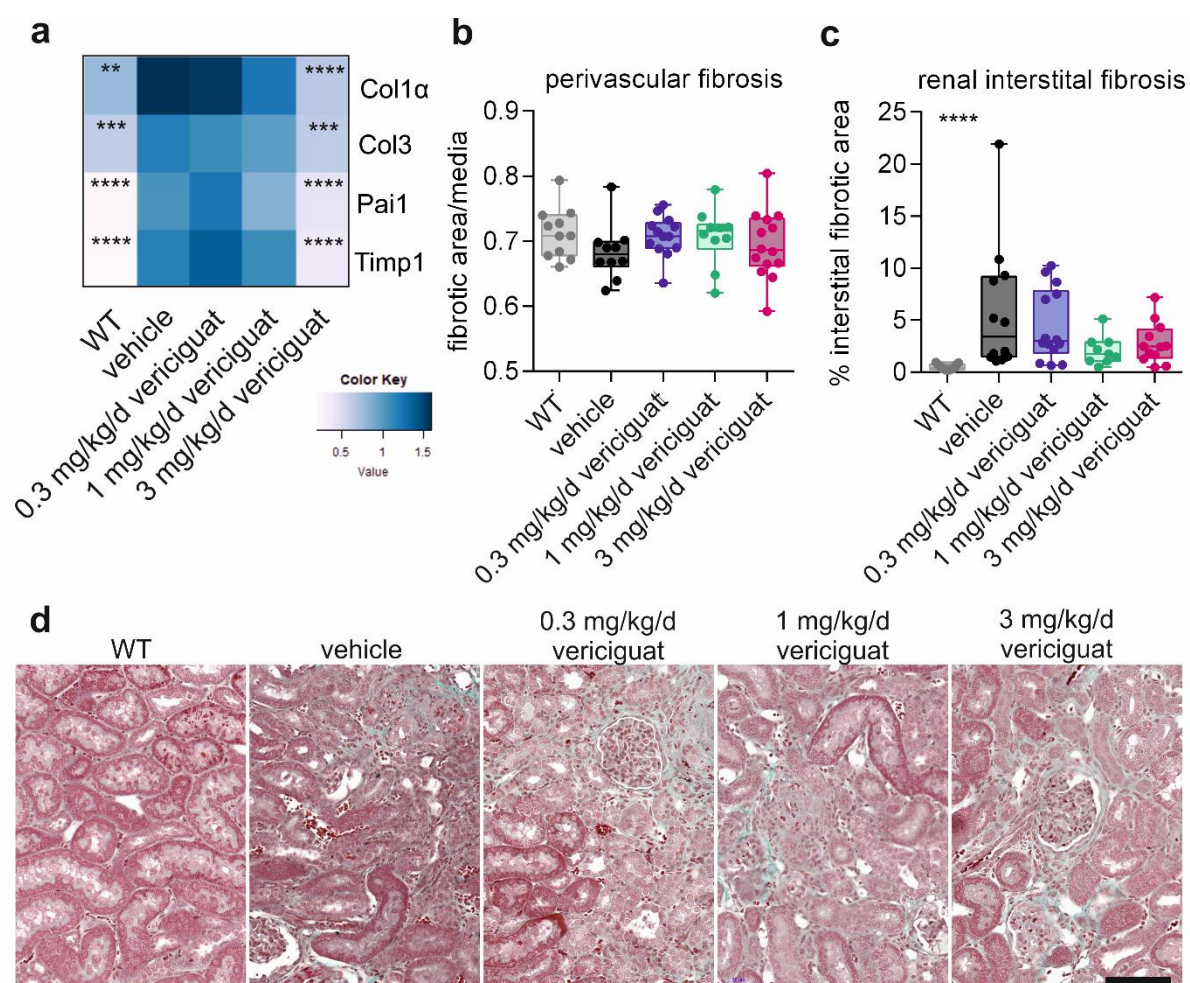
Figure 36. Expression of fibrosis marker improve with vericiguat treatment besides manifestation of renal interstitial fibrosis.
a Hypothesis-driven heatmap represents expression of fibrosis marker genes collagen type 1 and 3 alpha 1 chain (Col1a, Col3), Serpin family E member 1 (Pai1) and TIMP metallopeptidase inhibitor 1 (Timp1) normalized to 18S, measured with RT-qPCR. The colour key represents low values in light, high values in dark blue. b Perivascular fibrosis in Masson-Goldner-Trichrome (MGT)-stained kidney slides was quantified as the fibrotic are relative to media area. c Quantification of renal interstitial fibrosis in MGT-stained kidneys is shown as percentage of interstitial fibrosis area. Data displayed as boxplot. a-c Ordinary one-way ANOVA with Dunnett's multiple comparison or Kruskal-Wallis test with Dunn's multiple comparison, respectively. n = 12-14. p-value is indicated as **p < 0.01, ***p < 0.001, ****p < 0.0001. d Representative image of MGT-stained renal outer medulla displays increased interstitial fibrosis in vehicle- and vericiguat treated dTGR. Scalebar 100 µm.

Besides the observed increase in renal interstitial fibrosis, the glomerulosclerosis was analysed using PAS-stained images of glomeruli. In the kidneys of vehicle treated dTGR (78.2 ± 2.4%, mean ± SD) glomerulosclerosis was pronounced compared to WT rats (66.4 ± 2.5%, mean ± SD, $p < 0.0001$, one-way ANOVA) indicating glomerular injury (Figure 37). Administration of 1 (74.3 ± 3.7%, mean ± SD, $p = 0.0015$) and 3 mg/kg/d vericiguat (74.5 ± 2.2%, mean ± SD, $p = 0.0022$) decreased sclerosis in renal tissue in comparison to vehicle treated dTGR.
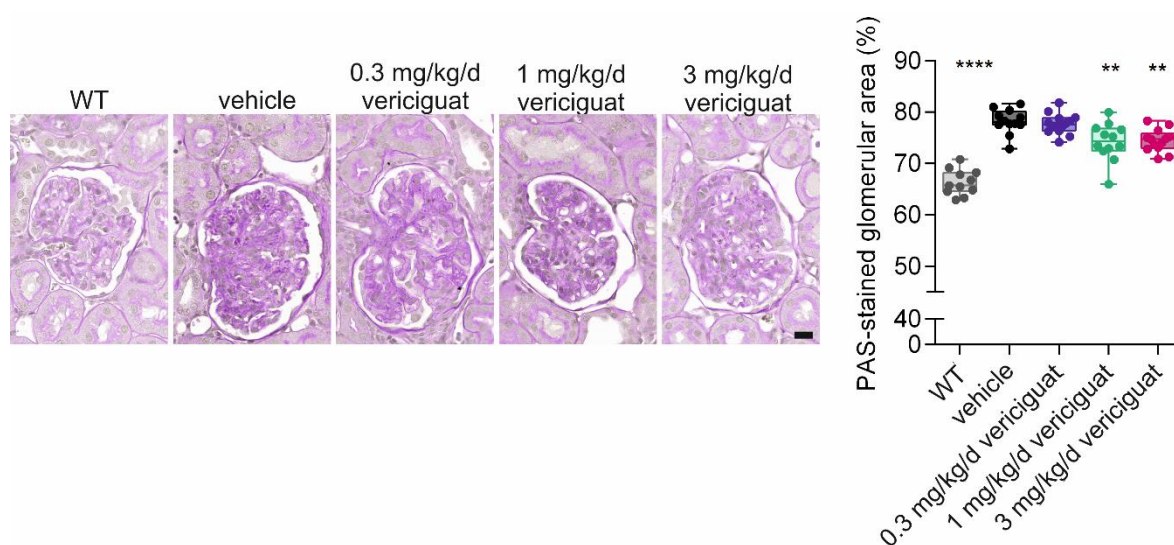
Figure 37. Glomerulosclerosis in renal tissue of WT, vehicle- and vericiguat treated dTGR.
Left: Representative image of PAS-stained glomeruli in WT rats, vehicle, 0.3, 1 and 3 mg/kg/d vericiguat treated dTGR indicated increased sclerosis. Scalebar 20 µm. Right: Quantification of glomerular damage as PAS-stained glomerular area (%) is increased in vehicle treated dTGR and improves with 1 and 3 mg/kg/d vericiguat treated. Ordinary one-way ANOVA with multiple comparison to vehicle. Data displayed as boxplot, n = 12-14. p-value shown as *p < 0.05, **p < 0.01, ***p < 0.001, ****p < 0.0001.

3.7.5 Anti-inflammatory effect of vericiguat in the kidney.

The renal inflammation was obtained with expression analysis of inflammation marker genes and immunohistochemical staining of CD68 (ED1)-staining in kidney slides. The relative expression of renal *Ctgf*, *Mcp1* and *Tgfβ* to *18S* were elevated in vehicle treated dTGR compared to WT rats (Figure 38a, Table 12). Administration of 3 mg/kg/d vericiguat significantly ameliorated mRNA expression of the inflammation related genes in comparison to vehicle treated rats. Treatment with 0.3 mg/kg/d vericiguat had no effect, whereas 1 mg/kg/d vericiguat also significantly reduced *Mcp1* but not *Tgfβ* and *Ctgf* gene expression (Figure 38a). In CD68 (ED1)-stained kidney slides monocytes/macrophage were quantified as the count of CD68-positive cells per field of view (Figure 38b) and the CD68-positive area

within a field of view (Figure 38c). Both showed an increase of monocytes/macrophages in the kidney of vehicle treated dTGR (mean ± SD, 198.7 ± 98.2 count, 0.14 ± 0.07%) in comparison to kidneys from WT rats (mean ± SD, 29.4 ± 10.9 count, *p* < 0.0001, 0.03 ± 0.01% *p* < 0.0001, Kruskal-Wallis test). Compared to vehicle treated dTGR, 3 mg/kg/d vericiguat treated dTGR (mean ± SD, 57.7 ± 30.7 count, *p* = 0.0011, 0.05 ± 0.02%, *p* = 0.0014) had reduced renal macrophages and monocyte infiltration (Figure 38b-d).
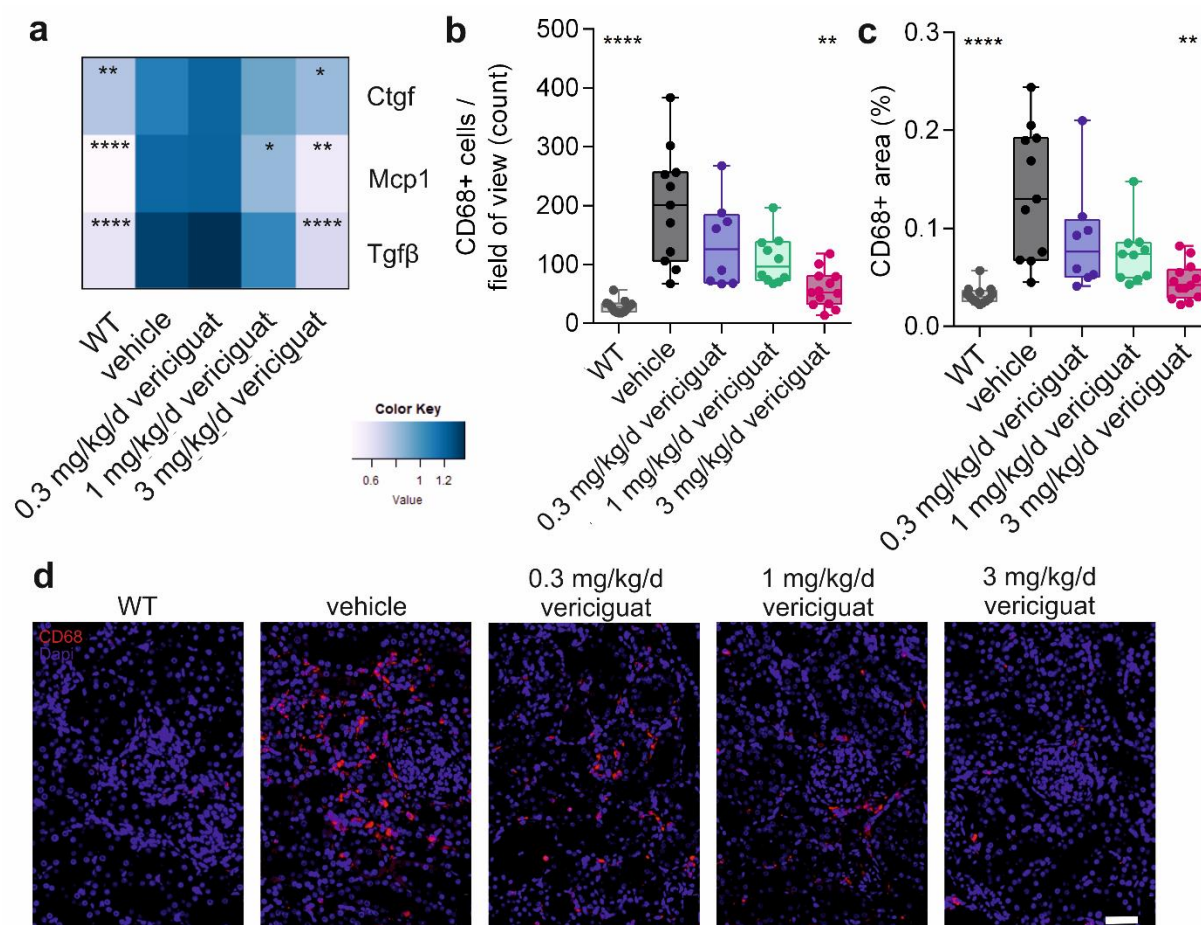
Figure 38. Reduced renal expression of inflammation marker and presence of monocyte/macrophages in 3 mg/kg/d vericiguat treated dTGR.
a Hypothesis-driven heatmap displays expression of inflammation marker genes connective tissue growth factor (Ctgf), monocyte chemoattractant protein 1 (Mcp1), transforming growth factor beta (Tgfβ) relative to 18S, measured with RT-qPCR. The colour key represents low values in light, high values in dark blue. In CD68 (ED1)-stained kidney slices monocytes/macrophage were quantified as b count of CD68-positive cells per field of view and c CD68-positive area (% of total area). Data displayed as boxplot. a-c Kruskal-Wallis test with Dunn's multiple comparison to vehicle, n = 8-13. p-value is indicated as *p < 0.05, **p < 0.01, ***p < 0.001, ****p < 0.0001. d Representative image of CD68 (ED1)-stained renal cortex displays increased macrophage/monocyte infiltration (red) in vehicle treated dTGR. Scalebar 50 µm.

IV. <u>Discussion</u>

This work discusses the intervention with the sGC stimulator vericiguat in an experimental preclinical model for HFpEF. I hypothesized an improved cardiac and renal pathophysiology in the dTGR model for hypertension-induced heart failure. The highlight of this study is the interorgan cardiorenal protective effect achieved by vericiguat administration. In short, the 3 mg/kg/d dose of the sGC stimulator vericiguat rescued survival, improved BP and had pronounced protective effects on cardiac performance, remodelling, fibrosis, and inflammation independent of improvement of hypertrophy or microvascular rarefaction. Strikingly, the 3 mg/kg/d dose of vericiguat was capable to rescue renal physiologic structure and function. The energy metabolism and contribution of the sGC in different cardiac cell types was hypothesized to play a pivotal role. Distinct metabolic roles of cardiomyocytes and cardiac fibroblasts were identified, including a shift from oxidative phosphorylation to glycolysis, thus highlighting the importance of the cardiac metabolism in cardiorenal HFpEF. Further, the doses of 1 and 0.3 mg/kg/d vericiguat were less affective in ameliorating HFpEF-related features.

4.1 <u>Blood pressure contribution to cardiorenal protection by vericiguat</u>

The 3 mg/kg/d dose of vericiguat significantly reduced mean, systolic and diastolic BP at all timepoints and the development of BP throughout the treatment. In addition, it rescued survival and body weight. In the kinetic BP analysis by telemetry, a reduction was caused for 12 hours. Although the effective period was prolonged by 3 over 1 and 0.3 mg/kg/d vericiguat, a 24-hour reduction could not be achieved. The precursor sGC stimulator candidate (BAY-41-8543) showed a similar pharmacokinetic profile in BP reduction [133]. In humans, the fluctuation of BP bears an increased risk for cardiovascular diseases and the prevention of BP fluctuation is a main goal in BP management [164]. The overall goal is to affectively achieve a 24-hour BP control with a dose given once per day. Despite the limited kinetics of vericiguat, protective cardiorenal effects could be observed in this hypertension-induced heart failure model. This suggests that the temporary BP reduction already caused relief for the vasculature and tissue and subsequently could reduce end-organ damage and preserve cardiac and renal function.

The intermediate dose of 1 mg/kg/d vericiguat could only reduce mean, diastolic and systolic BP in the second week of treatment. Thus, the improvements at the end of the study by the 1 mg/kg/d dose can therefore not be attributed to a significant reduction in blood pressure at

that time point but rather seem to be the result of the previous pressure relief in the tissue in week 6. Interestingly, kinetic BP analysis through telemetry revealed limited BP reduction after application of the substance that quickly normalised to the preceding value. In the present study the dose of 1 mg/kg/d vericiguat was not sufficient compared to 3 mg/kg/d vericiguat, which in a previous study was superior to the higher 10 mg/kg/d vericiguat dose in rats [89]. This result highlights the importance of improving half-life time of the substances and simultaneously outlines the limits of pharmaceutics. The lowest dose (0.3 mg/kg/d) of vericiguat did not reduce the mean BP significantly in this model, therefore BP independent mechanisms could be identified.

4.2 Speckle tracing echocardiographic and cardiac performance

The cardiac function was protected by 3 mg/kg/d vericiguat. The EF and CO were similar in healthy WT, vehicle and 0.3 mg/kg/d treated dTGR, while the 1 and 3 mg/kg/d doses further improved EF and CO. Parameters for diastolic dysfunction (E/A and E/E' ratio) showed no significant differences between groups, suggesting pseudonormal dysfunction. Further, MV deceleration time was reduced in vehicle treated dTGR without significant improvement through vericiguat. However, hypertrophy measured by heart weight and echocardiographic assessment of ventricular wall thickness persisted despite vericiguat treatment. In response to overload, the myocardium develops pathologic hypertrophy to lower wall stress in the left ventricle and increase contractility. In contrast to the sGC stimulator vericiguat, the sGC activator cinaciguat could prevent hypertrophy[165].

Another important diagnostic tool to identify HFpEF is the speckle tracking echocardiography assessment of cardiac strain [166]. The 3 mg/kg/d vericiguat dose rescued the global and spatial longitudinal strain to a sufficient degree, while 1 and 0.3 mg/kg/d vericiguat had less impact dose dependently. Strain differences in different anatomical segments existed in the myocardium among which the apex presented the most pronounced alterations in the dTGR model. These results from speckle tracking echocardiography go along with observations by Beyhoff et al. who showed changes in longitudinal strain to be most pronounced in the apex of the subendocardial fibrosis mouse model [167]. In HFpEF patients longitudinal, radial and circumferential strain were impaired on global level and in the six distinct myocardial regions [168]. Interestingly, in the study of Kim et al. the global circumferential strain had a higher prediction strength than the global longitudinal strain. Here, the global and spatial circumferential strain in vehicle treated dTGR were increased without improvement by

vericiguat. Similarly, global and spatial radial strain was reduced in vehicle and vericiguat treated dTGR.

In this study, cardiac haemodynamics revealed an impaired pressure-volume relation. The cardiac pressure measured in the left ventricle and arteries as LVESP, LVEDP, Ea and TRP were increased in the preclinical model and ameliorated only by the 3 mg/kg/d vericiguat dose. These results suggest a pronounce involvement of blood pressure in the protection of cardiac function.

4.3 Microvascular rarefaction and endothelial dysfunction in the preclinical model for HFpEF.

The microvascular rarefaction in the myocardium of Microfil-perfused hearts that were scanned with a micro-CT was observed in this study, while the microvascular density was similar between all groups in histologic staining. Keeping in mind that hypertrophy persisted in vericiguat treated dTGR, this indicated an undersupply of the tissue with oxygen and nutrients from the circulation. It remains elusive whether the number of medium-sized vessels was reduced or constricted. The findings are in line with coronary microvascular rarefaction and decreased microvascular density in HFpEF patients [33]. Andrade et al. found that vascular rarefaction is promoted by specific metabolites, confirming the importance of metabolism in endothelial cell function and maintenance [169]. In the dTGR model vericiguat did not improve microvascular structure but others have reported a positive effect of vericiguat on the microcirculation in a model for acute myocardial ischemic reperfusion injury [170]. In addition another sGC stimulator has been described to support angiogenesis in *in vitro* models [171].

In line with this, the vascular alterations were not improved by vericiguat treatment in the heart. Biomarker relevant for endothelial function were impaired in the model, with reduced expression of *Nos2* and *Nos3* genes that encode the enzymes iNOS and eNOS relevant for NO production [54]. It has been shown that iNOS contributes to HFpEF development through mitochondrial function and oxidative stress [172]. Further, the cardiac expression of *Et1* and *Vcam1* was elevated in the model. These vascular biomarkers were not improved by 3 mg/kg/d vericiguat treatment.

4.4 Renal protection positively affects the heart through interorgan crosstalk

In cardiorenal syndrome, the interorgan crosstalk between the heart and kidney is essential. The kidney contributes to a large extend to BP maintenance and with that can indirectly

protect organs like the heart. Kidney damage is known to negatively affect the heart, while renal protection can have an indirect positive effect on the heart. In cardiorenal HFpEF the contribution of the kidney must be considered. The present preclinical data show a renoprotective effect by the 3 mg/kg/d vericiguat dose with improved albuminuria, expression of endothelial damage and oxidative stress marker, tubular injury, fibrosis, and inflammation. In a model of acute kidney injury, the metabolome analysis linked cardiac oxidative stress and impaired energy generation to development of diastolic dysfunction, highlighting the importance of the kidney to maintain cardiac diastolic function [173]. Interestingly, the renoprotective effects of the 1 mg/kg/d dose included improvement of urinary albumin excretion and glomerulosclerosis, while all other renal alterations persisted despite treatment. In contrast to this, the 0.3 mg/kg/d dose had no protective effect. These results suggest that vericiguat cannot ameliorate the HFpEF phenotype independent of the reduction in BP.

Therefore, the BP lowering effect of vericiguat could be responsible for the improved renal outcome because the kidney is a pressure sensitive organ. Whether this is a direct effect of vericiguat on the sGC-cGMP pathway in the kidney or secondary to BP lowering remains elusive.

4.5 sGC involvement in cardiac remodelling, fibrosis and inflammation

In line with the above-mentioned findings on cardiac function, cardiac marker for remodelling, *Anp, Bnp, Myh7* and *Ctgf* improved by 3 mg/kg/d vericiguat treatment, which was in line with diminished fibrosis and inflammation in histology. Additionally, cardiac expression of *Anp* and *Bnp,* marker for cardiac remodelling and stress were improved by 1 mg/kg/d vericiguat. Interestingly, solely *Bnp* gene expression in the heart was improved by the 0.3 mg/kg/d dose, thereby enhancing its role as an important marker in heart failure. BNP protein, secreted by cardiomyocytes under stress, is not only acting in an endocrine fashion but has been shown to be cardioprotective through paracrine mechanisms that highlight the relevance of myocyte and non-myocyte crosstalk in the heart [174].

Differences in collagen deposition and fibroblast activity have been shown in cultured cells from human biopsies of patients with solely hypertension or hypertension plus HFpEF, highlighting their distinction from HFrEF pathology [175]. Resident cardiac fibroblasts are activated by mechanical stress and profibrotic factors such as ANGII or TGF-beta. In the activated state infiltration and remodelling of the extracellular matrix with collagen and fibronectin deposition takes place. Prolonged signals for activation leads to differentiation of

fibroblasts to myofibroblasts [176]. *Ctgf* expression can be stimulated by ANGII, ET-1 and TGF-beta but importantly both cardiomyocytes and fibroblasts express, synthesize and secrete TGF-beta and CTGF [177]. These factors act in an autocrine and paracrine manner that indicates cell-to-cell crosstalk, which has been demonstrated by *in vitro* experiments [178]. It has been shown that macrophages play a signalling role in activation of fibroblasts in HFpEF [179]. Investigations into the cellular composition of the human heart has not only described the heterogeneity of cardiac cells but defined sub-populations and their complex interaction networks, for example between fibroblasts, cardiomyocytes and macrophages [180]. Here, inflammation, measured as the number of macrophages/monocytes in the heart, was elevated in the vehicle treated dTGR, while 3 mg/kg/d vericiguat was capable to reduce inflammation. Macrophages have been shown to play an essential role in the maintenance of cardiac function and integrity of cardiomyocytes [181]. In an experimental series utilizing healthy mice, researchers have shown that cardiac resident macrophages prevent inflammation and retain cardiomyocyte integrity through removal of vesicles containing abnormal mitochondria. Li et al. investigated the role of cardiac single-cells in hypertrophy in a longitudinal manner utilizing a pressure-overload mouse model. Within the group of cardiomyocytes, ten subtypes were identified, that showed overall high abundance in the hypertrophic state, whereas decreased presence at the HFrEF state. They showed that non-cardiomyocyte play a crucial role in disease development and identified that cardiomyocyte transition was mediated by macrophage crosstalk [182].

4.6 Relevance of cardiometabolic analyses

Although cardiac remodelling was largely improved, hypertrophy measured by heart weight and echocardiographic assessment of ventricular wall thickness persisted despite vericiguat treatment. It has been shown that the metabolic switch from oxidation of fatty acids to glucose supports cardiac hypertrophy through aspartate synthesis. Ritterhoff et al. speculated a competitive energy demand from contraction and hypertrophic growth in cardiomyocytes [183]. In addition, it has been shown that the heart under HFpEF conditions shifts energy generation towards glycolysis instead of mitochondrial oxidative phosphorylation. Though, to date it is not clear which cardiac cell types are responsible for or contribute to the altered energy homeostasis in HFpEF. It could be of interest to identify cardiac cell types that represent a key role in cardiac metabolism and could subsequently be

target for future therapeutic approaches. I proposed a different energy metabolism profile in different cardiac cell types and that vericiguat would improve the metabolic function.

The energy production and demand plays an important role in HF. There are multiple methods available to investigate mitochondrial function in cardiomyocytes with oxygen consumption rate being one valuable tool to measure mitochondrial activity [35]. The Agilent Seahorse technology is a method to address real-time live cell energy metabolism in isolated cells. Some limitations of the method should be acknowledged: stress is caused to the cells during enzymatic isolation procedure and further other sources of cellular oxygen consumption (f.e. ROS production) or proton production has to be considered.

Interestingly, in this model for hypertension-induced heart failure cardiomyocytes, cardiac fibroblasts and endothelial cells played distinguished roles in the energy metabolism. Cardiomyocytes presented diminished maximal mitochondrial respiration only. The reduced maximal mitochondrial respiration could be due to decreased substrate availability, diminished electron transport chain integrity, or decreased mitochondrial mass, which was similar in heart tissue of groups in this study. The relatively high values of non-mitochondrial respiration observed in cardiomyocytes are comparable to observations from other researchers [184]. In comparison the PDK1 knockdown in cardiomyocytes *in vitro* showed a reduction of mitochondrial oxygen consumption rate, indicating an diminished mitochondrial activity and reduced ATP levels relevant for the HFrEF phenotype in the PDK1-deficient murine model [185].

Cardiac fibroblasts had elevated mitochondrial respiration (basal, maximal, non-mitochondrial) and ATP production. An explanation for the elevation of mitochondrial respiration in vehicle treated dTGR could be the increased presence of ROS in cardiac fibroblasts. In a multi-omics approach Zhang et al. identified inflammation, cardiac muscle contraction and mitochondrial integrity pathways to be associated with HFpEF phenotype in Dahl SS rats [31]. Based on these findings they suggest that damaged mitochondria accumulate due to dysregulation of mitochondrial genes, therefore promoting ROS production and cardiac remodelling. In general, high basal mitochondrial respiration could be due to increased ATP production, proton leak or non-mitochondrial respiration, of which only proton leak was not affected itself. The high maximal mitochondrial respiration could be due to increased substrate availability, mitochondrial mass, or improved electron transport chain

integrity. Only proton leak was similar reduced by vericiguat treatment that could result from damage of the membrane or complexes in the electron transport chain.

Strikingly, in the present study glycolysis (basal and maximal) was increased in cardiac fibroblasts but not in cardiomyocytes. Gizak et al. suggested a metabolic crosstalk between cardiomyocytes and cardiac fibroblasts in terms of glycolysis. They observed that a reduced glycolytic capacity in cardiomyocytes was accompanied with increased glucose metabolism in fibroblasts and hypothesized a cardiac energy metabolic profile of cardiomyocytes preferentially utilizing lactate over glucose [186]. In a mouse model for progressive heart failure (abdominal aortic constriction), cardiac hypertrophy has been linked to energy deficiency with a reduction of glucose metabolism and mitochondrial oxidation under insulin resistance [39]. Interestingly, the relevant glucose transport in the heart, *Glut4* was reduced in the vehicle treated dTGR as described in previous studies and improved by vericiguat treatment [131]. Fillmore et al. showed that upregulation of glycolysis and elevated *Glut1* expression preceded reduction of fatty acid oxidation in the heart of the Dahl-SS rat model for HFpEF [187]. They observed that glucose oxidation was not altered indicating an uncoupling of aerobe glycolysis and anaerobe glucose oxidation (oxidation of pyruvate to acetyl-CoA), that through an imbalance of protons and calcium homeostasis negatively affected cardiac contractility. At an advanced HFrEF state in this model, fatty acid oxidation was significantly decreased, highlighting the metabolic differences between heart failure types [187].

Various studies continuously focus on revealing pathways related to HFpEF pathology, which could be targeted in future therapies. Murashige et al. demonstrated that the healthy human heart mainly facilitates fatty acids to generate energy demand, opposite to the skeletal muscle, which mainly consumes glucose. Interestingly, in this study the bioenergetics of the HFrEF patients showed a higher contribution of ketones, lactate and amino acids to ATP production in comparison to HFpEF patients [188]. It has been shown that lipid metabolism plays a central role in cardiometabolic HFpEF with tightly regulated transcription factors (FoxO1 = fork head box protein O1) and genes (*Xbp1s* = spliced form of X-box binding protein 1) that in an dysregulated state promote lipid accumulation in the myocardium [189]. Besides fatty acid oxidation, the oxidation of pyruvate in mitochondria is an essential step in cardiac energy generation. It has been shown that pyruvate and it's transport into mitochondria plays a critical role in heart failure (HFrEF) [190]. McCommis et al. showed that mice deficient for the mitochondrial pyruvate carrier developed cardiac contractile dysfunction and remodelling while through dietary interventions with a high-fat ketogenic diet

could reverse the phenotype. The role of ketones (for example beta-hydroxybutyrate) for energy supply in HFpEF has been shown to be relevant in inflammation and mitochondrial function [191]. It has been observed that ketone oxidation is more pronounced in the failing heart to overcome the energy deficiency that sources from reduced (long-chain) fatty acid (FA) oxidation. Carley et al. showed in a TAC model that not only ketone bodies but also short-chain FA oxidation is elevated in the failing heart to bypass energy deficiency [192], thus presenting a potential new therapeutic field.

In conclusion, although diminished mitochondrial respiration and elevated glycolysis in this model highlighted the relevance of metabolism in HFpEF, vericiguat was not capable to improve *in vitro* metabolism measurements. Interestingly, in this model for HFpEF cardiomyocytes and fibroblasts played distinguished roles in energy metabolism. While cardiomyocytes presented diminished mitochondrial respiration, cardiac fibroblasts seemed to be oppositely directed with elevated mitochondrial respiration and increased glycolysis. Of note, *Glut4* expression but not *Pdk4* expression were diminished in the heart of this model, both involved in glucose transport and oxidation. In summary, the observed cardiac functional improvements did not originate from improved metabolism by vericiguat.

4.7 sGC modulation as a potential therapy option

The NO-sGC-cGMP pathway influences disease progression and pathology in heart failure in various ways. Modulation of the sGC has been shown to be a potential therapeutic target for cardiovascular diseases including heart failure.

Vericiguat (BAY 1021189) has been tested for pharmacokinetic properties and oral bioavailability and tolerance *in vivo* and showed NO-independent sGC stimulation and cGMP production in rats [76,89]. Apart from a vericiguat study by Follmann et al. in L-NAME treated rats transgenic for renin, no pre-clinical studies on vericiguat mode of action and physiologic protective effects in HFpEF are available. Follmann et al. reported BP reduction with both 3 and 10 mg/kg/d vericiguat, while left ventricular hypertrophy and plasma ANP levels decreased [89]. In addition, renal protection presented with reduced proteinuria and the 3 mg/kg/d dose resulted in 70% survival. These results are in line with our observation that vericiguat can maintain cardiac and renal function in a model of hypertension-induced cardiovascular disease.

Opposite to the effect of the sGC stimulator vericiguat in this study, the sGC activator BAY 58-2667 reduced cardiomyocyte hypertrophy [193]. Interestingly, valsartan treatment in a

previous study was capable to ameliorate hypertrophy in the dTGR model [126]. Although ANGII receptor AT1 blockage with valsartan had beneficial effects in the ANGII-induced heart failure model (dTGR), valsartan treatment of patients with HFpEF did not achieve a significant reduction of hospitalization and death in the clinical trial [45]. The reduction of fibrosis in the left ventricular interstitium by vericiguat was in line with observations made with other sGC stimulators. Reduction of fibrosis in myocardial interstitium and surrounding vasculature was mediated through lower *Col1* and *Tgf-β* expression by BAY 41-2272 in ANGII-induced and aortic constriction-induced rat models for hypertension [194]. Interestingly, Bay 41-2272 was capable to inhibit ACE synthesis *in vivo* and *in vitro* in cultured cardiac fibroblasts, thus preventing myofibroblast transition [195]. In the present study lower cardiac *Ctgf* expression was observed at the end of the study, whereas *Col1* and *Tgf-β* remained unaltered, speculating that increased expression of pro-fibrotic genes occurs at an earlier time point of disease progression. Sharkovska et al. observed myocardial and renal (glomerular and interstitial) reduction of fibrosis by riociguat in two hypertension rat models [82]. *In vitro* studies showed that the anti-fibrotic effect of NO in cardiac fibroblasts is mediated by expression of *Tgf-β* [196].

Despite the remarkable results of sGC stimulators *in vivo* and reduction of death from cardiovascular causes and heart failure demanding hospitalization in HFrEF [94], vericiguat could not convince in clinical trials for HFpEF. While NT-proBNP levels, cardiac primary endpoints and physical activity persisted in clinical trials for HFpEF patients [97,98], only the quality of life score was ameliorated [96]. The question is why vericiguat improved pathophysiology in the rodent model but could not achieve the primary endpoint in the clinical trials [96–98]. Patients that were included in these clinical trials investigating the efficacy of vericiguat presented severe HFpEF. One could speculate that reasons for the lack of effectiveness might be either the heterogeneous occurrence of the disease, that the disease was too advanced and treated too late in the patient cohorts or that the dose was too low to reach the primary endpoint. Although clinical trials have been conducted to investigate the effect of vericiguat in HFpEF, the pre-clinical study brings insights into possible positive effects that could not be considered by the selected clinical endpoints in clinical trials [96–98]. Beyond that, there may be molecular aspects that vericiguat can improve and could not be easily studied in humans, such as cardiac tissue, regional differences, and metabolism of the heart. In a model, the molecular effects can be investigated against the pathophysiological background, which also allows the possible deduction of the substance vericiguat for other diseases.

The data suggests that vericiguat cannot rescue the HFpEF phenotype but might bear pharmacologic benefits that could complement therapies in cardiovascular diseases.

4.8 Limitations and advantages of the pre-clinical study

All studies have limitations and strengths that need to be noted. The animal model used in this study has been shown in previous studies to be a suitable model for chronic heart failure [133]. The model expresses both transgenes unrestrictedly and presents preserved ejection fraction and develops terminal heart failure with loss of body weight and cardiac arrhythmias without transition into a HFrEF phenotype [131]. In the present study investigation into cardiac metabolism were performed in intact cells instead of isolated mitochondria, which has the advantage that physiologic conditions can be maintained. In the dTGR model hypertension is driven mainly by elevated ANGII levels, whereas HFpEF is a heterogenous disease often presenting two- or multiple hits in cardiovascular, - metabolic, -renal and - inflammatory diseases. There are other rodent models that follow a multiple-hit strategy to mimic HFpEF in a model, which might be an adverse choice for this disease [110].

In humans, STE-derived parameters reflect tissue deformation and can be used as a prognostic factor for early cardiac dysfunction [142]. The echocardiography of the left ventricle is well established in rodent, but differences between clinical research and basic research results in limited comparability. In rodents a parasternal long axis view is used in comparison to a four-chamber view in patients. Although the complete left ventricle was carefully visualized, segmental differences may be the result of apical foreshortening [197]. Precise segmental strain analysis is challenging and must therefore be acknowledged as an important limitation. In addition, echocardiography was performed under isoflurane narcosis, which has been observed to influence heart rate that might have an impact on the analysis when compared to physiologic states. Histologic sections of mid-region might not fully reflect the cardiac pathology to its full extend. Blood was removed from the heart, though it is likely that blood cells remained in the tissue. This could have affected macrophage/monocyte staining in the cardiac tissue, as both resident and infiltration macrophages occur in the heart [181].

For the isolation of cardiac cells, a short isoflurane narcosis and decapitation were performed. Although the preparation and timeline were precisely controlled (standard operating protocol, consistent experimental performer, tight time measurement) digestion of healthy and failing hearts was quite distinct. One reason is the pronounced stiffness of

cardiac tissue due to fibrosis and extracellular matrix deposition in the failing heart. In addition, one must consider the severe concentric hypertrophy and reduced vasculature that made it more difficult for the digestion solution to reach all endocardial areas similarly. In the isolation procedure, contraction inhibition was necessary because the extreme high energy demand of beating cardiomyocyte could not have been served in cell culture. Although blebbistatin was superior to BDM, it should be considered that this might have affected the metabolic analysis compared with physiologic states. Due to low cell number, fibroblasts were cultured before metabolic analysis, which should be considered as it could have influenced fibroblast expression and energy profile. In addition, specific fibroblast markers are rare but PDGFRα has been described to identify fibroblasts in combination with other genes [180].

One limitation of the dTGR model is that only male animals can be included as they develop the required phenotype. On the contrary, the HFpEF prevalence in humans is higher in women than in men [13]. A possible explanation is the difference in bioenergetics, in an *in vitro* study, mitochondria of cardiomyocyte from female and male mice presented differences, with the latter being less resistant against acute stress [198]. Sex differences in HFpEF may be related to variations in mitochondrial function [199]. Evaluation of HFpEF mouse models with HFpEF scores makes clear that models remain a tool to mimic a human disease without fully covering all pathophysiologic variations or accompanying comorbidities [200].

4.9 Conclusion and outlook

This study showed that vericiguat could improve the HFpEF phenotype at the BP lowering 3 mg/kg/d dose, while the 1 and 0.3 mg/kg/d doses were less affective. The cardiorenal protection highlighted the positive impact on interorgan crosstalk, likely mediated by prevention of renal damage through BP reduction. Further, the cardiac cell metabolism seems to play a pivotal role with distinct tasks for the different cell types. Investigations into cardiac cell metabolism are of great value and have not been sufficiently elucidated to date. Although vericiguat could not successfully rescue all symptoms and mechanisms in HFpEF, it is a potential therapeutic with regards to BP management, cardiorenal protection and fibrosis. In addition, sGC stimulators have been effective in other cardiovascular diseases, therefore presenting a pharmaceutic potential substance group. HFpEF in general remains a burden of human health because this comorbidity-driven heterogeneous condition needs to be further investigated. The importance of multi-level investigations into pathologic improvements

through pharmacologic interventions is substantial in preclinical research. It is especially challenging due to the heterogeneity of HFpEF and the multiple syndromes that are associated with it.

References

1. Paulus, W. J. *et al.* How to diagnose diastolic heart failure: a consensus statement on the diagnosis of heart failure with normal left ventricular ejection fraction by the Heart Failure and Echocardiography Associations of the European Society of Cardiology. *European heart journal* **28,** 2539–2550; 10.1093/eurheartj/ehm037 (2007).

2. McDonagh, T. A. *et al.* 2021 ESC Guidelines for the diagnosis and treatment of acute and chronic heart failure. *European heart journal* **42,** 3599–3726; 10.1093/eurheartj/ehab368 (2021).

3. Schiattarella, G. G. & Hill, J. A. Cardiometabolic HFpEF: Mechanisms and Therapies. *Cardiometab Syndr J* **1,** 117; 10.51789/cmsj.2021.1.e18 (2021).

4. Dunlay, S. M., Roger, V. L. & Redfield, M. M. Epidemiology of heart failure with preserved ejection fraction. *Nature reviews. Cardiology* **14,** 591–602; 10.1038/nrcardio.2017.65 (2017).

5. Borlaug, B. A. & Redfield, M. M. Diastolic and systolic heart failure are distinct phenotypes within the heart failure spectrum. *Circulation* **123,** 2006-13; discussion 2014; 10.1161/CIRCULATIONAHA.110.954388 (2011).

6. Heidenreich, P. A. *et al.* 2022 AHA/ACC/HFSA Guideline for the Management of Heart Failure: A Report of the American College of Cardiology/American Heart Association Joint Committee on Clinical Practice Guidelines. *Circulation* **145,** e895-e1032; 10.1161/CIR.0000000000001063 (2022).

7. Heinzel, F. R. *et al.* Left ventricular dysfunction in heart failure with preserved ejection fraction-molecular mechanisms and impact on right ventricular function. *Cardiovascular diagnosis and therapy* **10,** 1541–1560; 10.21037/cdt-20-477 (2020).

8. Cleland, J. G. F. *et al.* Beta-blockers for heart failure with reduced, mid-range, and preserved ejection fraction: an individual patient-level analysis of double-blind randomized trials. *European heart journal* **39,** 26–35; 10.1093/eurheartj/ehx564 (2018).

9. Lund, L. H. *et al.* Heart failure with mid-range ejection fraction in CHARM: characteristics, outcomes and effect of candesartan across the entire ejection fraction spectrum. *European journal of heart failure* **20,** 1230–1239; 10.1002/ejhf.1149 (2018).

10. Gevaert, A. B., Boen, J. R. A., Segers, V. F. & van Craenenbroeck, E. M. Heart Failure With Preserved Ejection Fraction: A Review of Cardiac and Noncardiac Pathophysiology. *Frontiers in physiology* **10,** 638; 10.3389/fphys.2019.00638 (2019).

11. Tschöpe, C. & Senni, M. Usefulness and clinical relevance of left ventricular global longitudinal systolic strain in patients with heart failure with preserved ejection fraction. *Heart failure reviews* **25,** 67–73; 10.1007/s10741-019-09853-7 (2020).

12. Kumar, A. A., Kelly, D. P. & Chirinos, J. A. Mitochondrial Dysfunction in Heart Failure With Preserved Ejection Fraction. *Circulation* **139,** 1435–1450; 10.1161/CIRCULATIONAHA.118.036259 (2019).

13. Sotomi, Y. *et al.* Sex Differences in Heart Failure With Preserved Ejection Fraction. *Journal of the American Heart Association* **10,** e018574; 10.1161/JAHA.120.018574 (2021).

14. Obokata, M., Reddy, Y. N. V., Pislaru, S. V., Melenovsky, V. & Borlaug, B. A. Evidence Supporting the Existence of a Distinct Obese Phenotype of Heart Failure With Preserved Ejection Fraction. *Circulation* **136,** 6–19; 10.1161/CIRCULATIONAHA.116.026807 (2017).

15. Kitzman, D. W. & Lam, C. S. P. Obese Heart Failure With Preserved Ejection Fraction Phenotype: From Pariah to Central Player. *Circulation* **136,** 20–23; 10.1161/CIRCULATIONAHA.117.028365 (2017).

16. Zannad, F. & Rossignol, P. Cardiorenal Syndrome Revisited. *Circulation* **138,** 929–944; 10.1161/CIRCULATIONAHA.117.028814 (2018).

17. Méndez, A. B., Azancot, M. A., Olivella, A. & Soler, M. J. New aspects in cardiorenal syndrome and HFpEF. *Clinical kidney journal* **15,** 1807–1815; 10.1093/ckj/sfac133 (2022).

18. van Dijk, C. G. M. *et al.* Distinct Endothelial Cell Responses in the Heart and Kidney Microvasculature Characterize the Progression of Heart Failure With Preserved Ejection Fraction in the Obese ZSF1 Rat With Cardiorenal Metabolic Syndrome. *Circulation. Heart failure* **9,** e002760; 10.1161/CIRCHEARTFAILURE.115.002760 (2016).

19. Schiattarella, G. G. *et al.* Immunometabolic Mechanisms of Heart Failure with Preserved Ejection Fraction. *Nature cardiovascular research* **1,** 211–222; 10.1038/s44161-022-00032-w (2022).

20. Figtree, G. A. *et al.* Effects of Canagliflozin on Heart Failure Outcomes Associated With Preserved and Reduced Ejection Fraction in Type 2 Diabetes Mellitus. *Circulation* **139,** 2591–2593; 10.1161/CIRCULATIONAHA.119.040057 (2019).

21. Anker, S. D. *et al.* Empagliflozin in Heart Failure with a Preserved Ejection Fraction. *The New England journal of medicine* **385,** 1451–1461; 10.1056/NEJMoa2107038 (2021).

22. Solomon, S. D. *et al.* Dapagliflozin in Heart Failure with Mildly Reduced or Preserved Ejection Fraction. *The New England journal of medicine* **387,** 1089–1098; 10.1056/NEJMoa2206286 (2022).

23. Savarese, G. *et al.* Global burden of heart failure: A comprehensive and updated review of epidemiology. *Cardiovascular research*; 10.1093/cvr/cvac013 (2022).

24. Seferović, P. M. *et al.* The Heart Failure Association Atlas: Heart Failure Epidemiology and Management Statistics 2019. *European journal of heart failure* **23,** 906–914; 10.1002/ejhf.2143 (2021).

25. Conrad, N. *et al.* Temporal trends and patterns in heart failure incidence: a population-based study of 4 million individuals. *The Lancet* **391,** 572–580; 10.1016/S0140-6736(17)32520-5 (2018).

26. Anguita Sánchez, M. *et al.* Prevalence of Heart Failure in the Spanish General Population Aged Over 45 Years. The PRICE Study. *Revista Española de Cardiología (English Edition)* **61,** 1041–1049; 10.1016/s1885-5857(09)60007-4 (2008).

27. Störk, S. *et al.* Epidemiology of heart failure in Germany: a retrospective database study. *Clinical research in cardiology : official journal of the German Cardiac Society* **106,** 913–922; 10.1007/s00392-017-1137-7 (2017).

28. Oktay, A. A., Rich, J. D. & Shah, S. J. The emerging epidemic of heart failure with preserved ejection fraction. *Current heart failure reports* **10,** 401–410; 10.1007/s11897-013-0155-7 (2013).

29. Potter, E. L., Hopper, I., Sen, J., Salim, A. & Marwick, T. H. Impact of socioeconomic status on incident heart failure and left ventricular dysfunction: systematic review and meta-analysis. *European heart journal. Quality of care & clinical outcomes* **5,** 169–179; 10.1093/ehjqcco/qcy047 (2019).

30. D'Amario, D. *et al.* Microvascular Dysfunction in Heart Failure With Preserved Ejection Fraction. *Frontiers in physiology* **10,** 1347; 10.3389/fphys.2019.01347 (2019).

31. Zhang, W. *et al.* Morphometric, Hemodynamic, and Multi-Omics Analyses in Heart Failure Rats with Preserved Ejection Fraction. *International journal of molecular sciences* **21**; 10.3390/ijms21093362 (2020).

32. Ataei Ataabadi, E. *et al.* Nitric Oxide-cGMP Signaling in Hypertension: Current and Future Options for Pharmacotherapy. *Hypertension (Dallas, Tex. : 1979)* **76,** 1055–1068; 10.1161/HYPERTENSIONAHA.120.15856 (2020).

33. Mohammed, S. F. *et al.* Coronary microvascular rarefaction and myocardial fibrosis in heart failure with preserved ejection fraction. *Circulation* **131,** 550–559; 10.1161/CIRCULATIONAHA.114.009625/ (2015).

34. Doughan, A. K., Harrison, D. G. & Dikalov, S. I. Molecular mechanisms of angiotensin II-mediated mitochondrial dysfunction: linking mitochondrial oxidative damage and vascular endothelial dysfunction. *Circulation research* **102,** 488–496; 10.1161/CIRCRESAHA.107.162800 (2008).

35. Dedkova, E. N. & Blatter, L. A. Measuring mitochondrial function in intact cardiac myocytes. *Journal of molecular and cellular cardiology* **52,** 48–61; 10.1016/j.yjmcc.2011.08.030 (2012).

36. Hong, S. & Pedersen, P. L. ATP synthase and the actions of inhibitors utilized to study its roles in human health, disease, and other scientific areas. *Microbiology and molecular biology reviews : MMBR* **72,** 590-641, Table of Contents; 10.1128/MMBR.00016-08 (2008).

37. Goldman, Y. E. Kinetics of the Actomyosin ATPase in Muscle Fibers. *Annual Review of Physiology* **49,** 637–654; 10.1146/annurev.ph.49.030187.003225 (1987).

38. Lopaschuk, G. D., Karwi, Q. G., Tian, R., Wende, A. R. & Abel, E. D. Cardiac Energy Metabolism in Heart Failure. *Circulation research* **128,** 1487–1513; 10.1161/CIRCRESAHA.121.318241 (2021).

39. Zhang, L. *et al.* Cardiac insulin-resistance and decreased mitochondrial energy production precede the development of systolic heart failure after pressure-overload hypertrophy. *Circulation. Heart failure* **6,** 1039–1048; 10.1161/CIRCHEARTFAILURE.112.000228 (2013).

40. Lopaschuk, G. D., Karwi, Q. G., Ho, K. L., Pherwani, S. & Ketema, E. B. Ketone metabolism in the failing heart. *Biochimica et biophysica acta. Molecular and cell biology of lipids* **1865,** 158813; 10.1016/j.bbalip.2020.158813 (2020).

41. Fillmore, N. *et al.* Uncoupling of glycolysis from glucose oxidation accompanies the development of heart failure with preserved ejection fraction. *Molecular medicine (Cambridge, Mass.)* **24,** 3; 10.1186/s10020-018-0005-x (2018).

42. McMurray, J. J. V. *et al.* Dapagliflozin in Patients with Heart Failure and Reduced Ejection Fraction. *The New England journal of medicine* **381,** 1995–2008; 10.1056/NEJMoa1911303 (2019).

43. Yoon, S. & Eom, G. H. Heart failure with preserved ejection fraction: present status and future directions. *Experimental & molecular medicine* **51,** 1–9; 10.1038/s12276-019-0323-2 (2019).

44. Pitt, B. *et al.* Spironolactone for heart failure with preserved ejection fraction. *The New England journal of medicine* **370,** 1383–1392; 10.1056/NEJMoa1313731 (2014).

45. Solomon, S. D. *et al.* Angiotensin-Neprilysin Inhibition in Heart Failure with Preserved Ejection Fraction. *The New England journal of medicine* **381,** 1609–1620; 10.1056/NEJMoa1908655 (2019).

46. Yusuf, S. *et al.* Effects of candesartan in patients with chronic heart failure and preserved left-ventricular ejection fraction: the CHARM-Preserved Trial. *Lancet (London, England)* **362,** 777–781; 10.1016/S0140-6736(03)14285-7 (2003).

47. Kjeldsen, S. E. *et al.* Medical Therapies for Heart Failure With Preserved Ejection Fraction. *Hypertension (Dallas, Tex. : 1979)* **75,** 23–32; 10.1161/HYPERTENSIONAHA.119.14057 (2020).

48. Patel, R. B. & Shah, S. J. Drug Targets for Heart Failure with Preserved Ejection Fraction: A Mechanistic Approach and Review of Contemporary Clinical Trials. *Annual review of pharmacology and toxicology* **59,** 41–63; 10.1146/annurev-pharmtox-010818-021136 (2019).

49. Smith, O. Nobel Prize for NO research. *Nature medicine* **4,** 1215; 10.1038/3182 (1998).

50. Furchgott, R. F. & Zawadzki, J. V. The obligatory role of endothelial cells in the relaxation of arterial smooth muscle by acetylcholine. *Nature* **288,** 373–376; 10.1038/288373a0 (1980).

51. Rapoport, R. M., Draznin, M. B. & Murad, F. Endothelium-dependent relaxation in rat aorta may be mediated through cyclic GMP-dependent protein phosphorylation. *Nature* **306,** 174–176; 10.1038/306174a0 (1983).

52. Ignarro, L. J. Biosynthesis and metabolism of endothelium-derived nitric oxide. *Annual review of pharmacology and toxicology* **30,** 535–560; 10.1146/annurev.pa.30.040190.002535 (1990).

53. Xu, W. M. & Liu, L. Z. Nitric oxide: from a mysterious labile factor to the molecule of the Nobel Prize. Recent progress in nitric oxide research. *Cell research* **8,** 251–258; 10.1038/cr.1998.25 (1998).

54. Förstermann, U. *et al.* Nitric oxide synthase isozymes. Characterization, purification, molecular cloning, and functions. *Hypertension (Dallas, Tex. : 1979)* **23,** 1121–1131; 10.1161/01.hyp.23.6.1121 (1994).

55. Rafikov, R. *et al.* eNOS activation and NO function: structural motifs responsible for the posttranslational control of endothelial nitric oxide synthase activity. *The Journal of endocrinology* **210,** 271–284; 10.1530/JOE-11-0083 (2011).

56. Förstermann, U. & Münzel, T. Endothelial nitric oxide synthase in vascular disease: from marvel to menace. *Circulation* **113,** 1708–1714; 10.1161/CIRCULATIONAHA.105.602532 (2006).

57. Kuroda, J. *et al.* NADPH oxidase 4 (Nox4) is a major source of oxidative stress in the failing heart. *Proceedings of the National Academy of Sciences of the United States of America* **107,** 15565–15570; 10.1073/pnas.1002178107 (2010).

58. Sedeek, M., Nasrallah, R., Touyz, R. M. & Hébert, R. L. NADPH oxidases, reactive oxygen species, and the kidney: friend and foe. *Journal of the American Society of Nephrology : JASN* **24,** 1512–1518; 10.1681/ASN.2012111112 (2013).

59. Rajagopalan, S. *et al.* Angiotensin II-mediated hypertension in the rat increases vascular superoxide production via membrane NADH/NADPH oxidase activation. Contribution to alterations of vasomotor tone. *The Journal of clinical investigation* **97,** 1916–1923; 10.1172/JCI118623 (1996).

60. Li, H. *et al.* Reversal of endothelial nitric oxide synthase uncoupling and up-regulation of endothelial nitric oxide synthase expression lowers blood pressure in hypertensive rats. *Journal of the American College of Cardiology* **47,** 2536–2544; 10.1016/j.jacc.2006.01.071 (2006).

61. Kawashima, S. & Yokoyama, M. Dysfunction of endothelial nitric oxide synthase and atherosclerosis. *Arteriosclerosis, thrombosis, and vascular biology* **24,** 998–1005; 10.1161/01.ATV.0000125114.88079.96 (2004).

62. Kuhn, M. Molecular Physiology of Membrane Guanylyl Cyclase Receptors. *Physiological reviews* **96,** 751–804; 10.1152/physrev.00022.2015 (2016).

63. Evgenov, O. V. *et al.* NO-independent stimulators and activators of soluble guanylate cyclase: discovery and therapeutic potential. *Nature reviews. Drug discovery* **5,** 755–768; 10.1038/nrd2038 (2006).

64. Denninger, J. W. & Marletta, M. A. Guanylate cyclase and the .NO/cGMP signaling pathway. *Biochimica et biophysica acta* **1411,** 334–350; 10.1016/S0005-2728(99)00024-9 (1999).

65. Koesling, D., Russwurm, M., Mergia, E., Mullershausen, F. & Friebe, A. Nitric oxide-sensitive guanylyl cyclase: structure and regulation. *Neurochemistry international* **45,** 813–819; 10.1016/j.neuint.2004.03.011 (2004).

66. Craven, P. A. & DeRubertis, F. R. Requirement for heme in the activation of purified guanylate cyclase by nitric oxide. *Biochimica et biophysica acta* **745,** 310–321; 10.1016/0167-4838(83)90063-8 (1983).

67. Francis, S. H., Busch, J. L., Corbin, J. D. & Sibley, D. cGMP-dependent protein kinases and cGMP phosphodiesterases in nitric oxide and cGMP action. *Pharmacological reviews* **62,** 525–563; 10.1124/pr.110.002907 (2010).

68. Chen, L. *et al.* Vasodilator-stimulated phosphoprotein regulates proliferation and growth inhibition by nitric oxide in vascular smooth muscle cells. *Arteriosclerosis, thrombosis, and vascular biology* **24,** 1403–1408; 10.1161/01.ATV.0000134705.39654.53 (2004).

69. Krüger, M. *et al.* Protein kinase G modulates human myocardial passive stiffness by phosphorylation of the titin springs. *BMC Pharmacol* **9**; 10.1186/1471-2210-9-S1-P37 (2009).

70. Park, K.-H. & Park, W. J. Endothelial Dysfunction: Clinical Implications in Cardiovascular Disease and Therapeutic Approaches. *Journal of Korean medical science* **30,** 1213–1225; 10.3346/jkms.2015.30.9.1213 (2015).

71. Redfield, M. M. *et al.* Isosorbide Mononitrate in Heart Failure with Preserved Ejection Fraction. *The New England journal of medicine* **373,** 2314–2324; 10.1056/NEJMoa1510774 (2015).

72. Münzel, T., Daiber, A. & Gori, T. Nitrate therapy: new aspects concerning molecular action and tolerance. *Circulation* **123,** 2132–2144; 10.1161/CIRCULATIONAHA.110.981407 (2011).

73. Golshiri, K., Ataei Ataabadi, E., Portilla Fernandez, E. C., Jan Danser, A. H. & Roks, A. J. M. The importance of the nitric oxide-cGMP pathway in age-related cardiovascular disease: Focus on phosphodiesterase-1 and soluble guanylate cyclase. *Basic & clinical pharmacology & toxicology* **127,** 67–80; 10.1111/bcpt.13319 (2020).

74. Redfield, M. M. *et al.* Effect of phosphodiesterase-5 inhibition on exercise capacity and clinical status in heart failure with preserved ejection fraction: a randomized clinical trial. *JAMA* **309,** 1268–1277; 10.1001/jama.2013.2024 (2013).

75. Chen, Z. *et al.* Phosphodiesterase inhibitor for heart failure with preserved ejection fraction: A systematic review and meta-analysis. *Saudi pharmaceutical journal : SPJ : the official publication of the Saudi Pharmaceutical Society* **30,** 1079–1087; 10.1016/j.jsps.2022.05.012 (2022).

76. Sandner, P. From molecules to patients: exploring the therapeutic role of soluble guanylate cyclase stimulators. *Biological chemistry* **399,** 679–690; 10.1515/hsz-2018-0155 (2018).

77. Sandner, P. *et al.* Soluble Guanylate Cyclase Stimulators and Activators. *Handbook of experimental pharmacology* **264,** 355–394; 10.1007/164_2018_197 (2021).

78. Stasch, J.-P. *et al.* NO- and haem-independent activation of soluble guanylyl cyclase: molecular basis and cardiovascular implications of a new pharmacological principle. *British journal of pharmacology* **136,** 773–783; 10.1038/sj.bjp.0704778 (2002).

79. Stasch, J.-P. & Hobbs, A. J. NO-independent, haem-dependent soluble guanylate cyclase stimulators. *Handbook of experimental pharmacology,* 277–308; 10.1007/978-3-540-68964-5_13 (2009).

80. Mülsch, A. *et al.* Effect of YC-1, an NO-independent, superoxide-sensitive stimulator of soluble guanylyl cyclase, on smooth muscle responsiveness to nitrovasodilators. *British journal of pharmacology* **120,** 681–689; 10.1038/sj.bjp.0700982 (1997).

81. Boerrigter, G. & Burnett, J. C. Nitric oxide-independent stimulation of soluble guanylate cyclase with BAY 41-2272 in cardiovascular disease. *Cardiovascular drug reviews* **25,** 30–45; 10.1111/j.1527-3466.2007.00003.x (2007).

82. Sharkovska, Y. *et al.* Nitric oxide-independent stimulation of soluble guanylate cyclase reduces organ damage in experimental low-renin and high-renin models. *Journal of hypertension* **28,** 1666–1675; 10.1097/HJH.0b013e32833b558c (2010).

83. Rüdebusch, J. *et al.* Stimulation of soluble guanylyl cyclase (sGC) by riociguat attenuates heart failure and pathological cardiac remodelling. *British journal of pharmacology* **179,** 2430–2442; 10.1111/bph.15333 (2022).

84. Rai, N. *et al.* Effect of Riociguat and Sildenafil on Right Heart Remodeling and Function in Pressure Overload Induced Model of Pulmonary Arterial Banding. *BioMed research international* **2018,** 3293584; 10.1155/2018/3293584 (2018).

85. Frey, R. *et al.* Clinical Pharmacokinetic and Pharmacodynamic Profile of Riociguat. *Clinical pharmacokinetics* **57,** 647–661; 10.1007/s40262-017-0604-7 (2018).

86. Murata, M. *et al.* Clinical Significance of Guanylate Cyclase Stimulator, Riociguat, on Right Ventricular Functional Improvement in Patients with Pulmonary Hypertension. *Cardiology* **146,** 130–136; 10.1159/000510860 (2021).

87. Ghofrani, H.-A. *et al.* Riociguat for the treatment of chronic thromboembolic pulmonary hypertension. *The New England journal of medicine* **369,** 319–329; 10.1056/NEJMoa1209657 (2013).

88. Ghofrani, H.-A. *et al.* Riociguat for the treatment of pulmonary arterial hypertension. *The New England journal of medicine* **369,** 330–340; 10.1056/NEJMoa1209655 (2013).

89. Follmann, M. *et al.* Discovery of the Soluble Guanylate Cyclase Stimulator Vericiguat (BAY 1021189) for the Treatment of Chronic Heart Failure. *Journal of medicinal chemistry* **60,** 5146–5161; 10.1021/acs.jmedchem.7b00449 (2017).

90. Boettcher, M. *et al.* Metabolism and Pharmacokinetic Drug-Drug Interaction Profile of Vericiguat, A Soluble Guanylate Cyclase Stimulator: Results From Preclinical and Phase I Healthy Volunteer Studies. *Clinical pharmacokinetics* **59,** 1407–1418; 10.1007/s40262-020-00895-x (2020).

91. Boettcher, M., Loewen, S., Gerrits, M. & Becker, C. Pharmacodynamic and Pharmacokinetic Interaction Profile of Vericiguat: Results from Three Randomized Phase I Studies in Healthy Volunteers. *Clinical pharmacokinetics* **60,** 337–351; 10.1007/s40262-020-00935-6 (2021).

92. Boettcher, M. *et al.* Safety, pharmacodynamic, and pharmacokinetic characterization of vericiguat: results from six phase I studies in healthy subjects. *European journal of clinical pharmacology* **77,** 527–537; 10.1007/s00228-020-03023-7 (2021).

93. Gheorghiade, M. *et al.* Effect of Vericiguat, a Soluble Guanylate Cyclase Stimulator, on Natriuretic Peptide Levels in Patients With Worsening Chronic Heart Failure and Reduced Ejection Fraction: The SOCRATES-REDUCED Randomized Trial. *JAMA* **314,** 2251–2262; 10.1001/jama.2015.15734 (2015).

94. Armstrong, P. W. *et al.* Vericiguat in Patients with Heart Failure and Reduced Ejection Fraction. *The New England journal of medicine* **382,** 1883–1893; 10.1056/NEJMoa1915928 (2020).

95. Markham A., D. S. Vericiguat: First Approval. Drugs., 721-726.; 10.1007/s40265-021-01496-z. (2021).

96. Pieske, B. *et al.* Vericiguat in patients with worsening chronic heart failure and preserved ejection fraction: results of the SOluble guanylate Cyclase stimulatoR in heArT failurE patientS with PRESERVED EF (SOCRATES-PRESERVED) study. *European heart journal* **38,** 1119–1127; 10.1093/eurheartj/ehw593 (2017).

97. Armstrong, P. W. *et al.* Effect of Vericiguat vs Placebo on Quality of Life in Patients With Heart Failure and Preserved Ejection Fraction: The VITALITY-HFpEF Randomized Clinical Trial. *JAMA* **324,** 1512–1521; 10.1001/jama.2020.15922 (2020).

98. Butler, J. *et al.* Rationale and Design of the VITALITY-HFpEF Trial. *Circulation. Heart failure* **12,** e005998; 10.1161/CIRCHEARTFAILURE.119.005998 (2019).

99. Haase, N., Kedziora, S. M., Müller, D. N. & Dechend, R. Lösliche Guanylatzyklase(sGC)-Stimulation mit Vericiguat. *Kardiologie* **16,** 466–478; 10.1007/s12181-022-00576-y (2022).

100. Conceição, G., Heinonen, I., Lourenço, A. P., Duncker, D. J. & Falcão-Pires, I. Animal models of heart failure with preserved ejection fraction. *Netherlands heart journal : monthly journal of the Netherlands Society of Cardiology and the Netherlands Heart Foundation* **24,** 275–286; 10.1007/s12471-016-0815-9 (2016).

101. Riehle, C. & Bauersachs, J. Small animal models of heart failure. *Cardiovascular research* **115,** 1838–1849; 10.1093/cvr/cvz161 (2019).

102. Okamoto, K. & Aoki, K. Development of a strain of spontaneously hypertensive rats. *Japanese circulation journal* **27,** 282–293; 10.1253/jcj.27.282 (1963).

103. Conrad, C. H., Brooks, W. W., Robinson, K. G. & Bing, O. H. Impaired myocardial function in spontaneously hypertensive rats with heart failure. *The American journal of physiology* **260,** H136-45; 10.1152/ajpheart.1991.260.1.H136 (1991).

104.   Doi, R. *et al.* Development of different phenotypes of hypertensive heart failure: systolic versus diastolic failure in Dahl salt-sensitive rats. *Journal of hypertension* **18,** 111–120; 10.1097/00004872-200018010-00016 (2000).

105.   Grobe, J. L., Mecca, A. P., Mao, H. & Katovich, M. J. Chronic angiotensin-(1-7) prevents cardiac fibrosis in DOCA-salt model of hypertension. *American journal of physiology. Heart and circulatory physiology* **290,** H2417-23; 10.1152/ajpheart.01170.2005 (2006).

106.   Rockman, H. A. *et al.* Segregation of atrial-specific and inducible expression of an atrial natriuretic factor transgene in an in vivo murine model of cardiac hypertrophy. *Proceedings of the National Academy of Sciences of the United States of America* **88,** 8277–8281; 10.1073/pnas.88.18.8277 (1991).

107.   Valero-Muñoz, M., Backman, W. & Sam, F. Murine Models of Heart Failure with Preserved Ejection Fraction: a "Fishing Expedition". *JACC. Basic to translational science* **2,** 770–789; 10.1016/j.jacbts.2017.07.013 (2017).

108.   Li, H. *et al.* Mimicking Metabolic Disturbance in Establishing Animal Models of Heart Failure With Preserved Ejection Fraction. *Frontiers in physiology* **13,** 879214; 10.3389/fphys.2022.879214 (2022).

109.   Tofovic, S. P., Kusaka, H., Kost, C. K. & Bastacky, S. Renal function and structure in diabetic, hypertensive, obese ZDFxSHHF-hybrid rats. *Renal failure* **22,** 387–406; 10.1081/jdi-100100882 (2000).

110.   Schiattarella, G. G. *et al.* Nitrosative stress drives heart failure with preserved ejection fraction. *Nature* **568,** 351–356; 10.1038/s41586-019-1100-z (2019).

111.   Ananthram, M. G. & Gottlieb, S. S. Renal Dysfunction and Heart Failure with Preserved Ejection Fraction. *Heart failure clinics* **17,** 357–367; 10.1016/j.hfc.2021.03.005 (2021).

112.   Adam, R. J., Williams, A. C. & Kriegel, A. J. Comparison of the surgical resection and infarct 5/6 nephrectomy rat models of chronic kidney disease. *American journal of physiology. Renal physiology* **322,** F639-F654; 10.1152/ajprenal.00398.2021 (2022).

113.   Patel, S., Rauf, A., Khan, H. & Abu-Izneid, T. Renin-angiotensin-aldosterone (RAAS): The ubiquitous system for homeostasis and pathologies. *Biomedicine & pharmacotherapy = Biomedecine & pharmacotherapie* **94,** 317–325; 10.1016/j.biopha.2017.07.091 (2017).

114.   Carey, R. M. & Padia, S. H. Physiology and Regulation of the Renin–Angiotensin–Aldosterone System. In *Textbook of Nephro-Endocrinology* (Elsevier2018), pp. 1–25.

115.   Murphy, T. J., Alexander, R. W., Griendling, K. K., Runge, M. S. & Bernstein, K. E. Isolation of a cDNA encoding the vascular type-1 angiotensin II receptor. *Nature* **351,** 233–236; 10.1038/351233a0 (1991).

116.   Ranjit, A., Khajehpour, S. & Aghazadeh-Habashi, A. Update on Angiotensin II Subtype 2 Receptor: Focus on Peptide and Nonpeptide Agonists. *Molecular pharmacology* **99,** 469–487; 10.1124/molpharm.121.000236 (2021).

117.   Silbernagl, S., Despopoulos, A. & Draguhn, A. (ed.). *Taschenatlas Physiologie.* 9th ed. (Georg Thieme Verlag, Stuttgart, New York, 2018).

118.   Feher, J. Regulation of Fluid and Electrolyte Balance. In *Quantitative Human Physiology* (Elsevier2017), pp. 740–751.

119.   Mullins, J. J., Peters, J. & Ganten, D. Fulminant hypertension in transgenic rats harbouring the mouse Ren-2 gene. *Nature* **344,** 541–544; 10.1038/344541a0 (1990).

120.   Pinto-Sietsma, S. J. & Paul, M. Transgenic rats as models for hypertension. *Journal of human hypertension* **11,** 577–581; 10.1038/sj.jhh.1000506 (1997).

121.   Ganten, D. *et al.* Species specificity of renin kinetics in transgenic rats harboring the human renin and angiotensinogen genes. *Proceedings of the National Academy of Sciences of the United States of America* **89,** 7806–7810; 10.1073/pnas.89.16.7806 (1992).

122.   Fukamizu, A. *et al.* Tissue-specific expression of the human renin gene in transgenic mice. *Biochemical and biophysical research communications* **165,** 826–832; 10.1016/s0006-291x(89)80040-3 (1989).

123.   Bohlender, J., Ménard, J., Wagner, J., Luft, F. C. & Ganten, D. Human renin-dependent hypertension in rats transgenic for human angiotensinogen. *Hypertension (Dallas, Tex. : 1979)* **27,** 535–540; 10.1161/01.HYP.27.3.535 (1996).

124.   Müller, D. N. *et al.* Effects of human renin in the vasculature of rats transgenic for human angiotensinogen. *Hypertension (Dallas, Tex. : 1979)* **26,** 272–278; 10.1161/01.HYP.26.2.272 (1995).

125.   Bohlender, J. *et al.* High human renin hypertension in transgenic rats. *Hypertension (Dallas, Tex. : 1979)* **29,** 428–434; 10.1161/01.hyp.29.1.428 (1997).

126.   Müller, D. N. *et al.* Angiotensin II (AT(1)) receptor blockade reduces vascular tissue factor in angiotensin II-induced cardiac vasculopathy. *The American journal of pathology* **157,** 111–122; 10.1016/S0002-9440(10)64523-3 (2000).

127.   Luft, F. C. *et al.* Hypertension-Induced End-Organ Damage. A New Transgenic Approach to an Old Problem. *Hypertension (Dallas, Tex. : 1979)* **33,** 212–218 (1999).

128.   Muller, D. N. *et al.* Immunosuppressive treatment protects against angiotensin II-induced renal damage. *The American journal of pathology* **161,** 1679–1693; 10.1016/S0002-9440(10)64445-8 (2002).

129.   Fischer, R. *et al.* Angiotensin II-induced sudden arrhythmic death and electrical remodeling. *American journal of physiology. Heart and circulatory physiology* **293,** H1242-53; 10.1152/ajpheart.01400.2006. (2007).

130.   Bartel, S., Hoch, B., Vetter, D. & Krause, E.-G. Expression of human angiotensinogen-renin in rat: effects on transcription and heart function. *Hypertension (Dallas, Tex. : 1979)* **39,** 219–223; 10.1161/hy0202.103275 (2002).

131.   Wellner, M. *et al.* Cardiac gene expression profile in rats with terminal heart failure and cachexia. *Physiological genomics* **20,** 256–267; 10.1152/physiolgenomics.00165.2004. (2005).

132.   Shagdarsuren, E. *et al.* Complement activation in angiotensin II-induced organ damage. *Circulation research* **97,** 716–724; 10.1161/01.RES.0000182677.89816.38 (2005).

133.   Wilck, N. *et al.* Nitric oxide-sensitive guanylyl cyclase stimulation improves experimental heart failure with preserved ejection fraction. *JCI insight* **3**; 10.1172/jci.insight.96006 (2018).

134.   Haase, N. *et al.* Relaxin does not improve Angiotensin II-induced target-organ damage. *PloS one* **9,** e93743; 10.1371/journal.pone.0093743 (2014).

135.   Mervaala, E. *et al.* Metabolomics in angiotensin II-induced cardiac hypertrophy. *Hypertension (Dallas, Tex. : 1979)* **55,** 508–515; 10.1161/HYPERTENSIONAHA.109.145490 (2010).

136.   Mervaala, E. M. *et al.* Endothelial dysfunction and xanthine oxidoreductase activity in rats with human renin and angiotensinogen genes. *Hypertension (Dallas, Tex. : 1979)* **37,** 414–418; 10.1161/01.hyp.37.2.414 (2001).

137.   Devereux, R. B. *et al.* Echocardiographic assessment of left ventricular hypertrophy: Comparison to necropsy findings. *The American journal of cardiology* **57,** 450–458; 10.1016/0002-9149(86)90771-x (1986).

138.   Troy, B. L., Pombo, J. & Rackley, C. E. Measurement of left ventricular wall thickness and mass by echocardiography. *Circulation* **45,** 602–611; 10.1161/01.cir.45.3.602 (1972).

139. Serri, K. *et al.* Global and regional myocardial function quantification by two-dimensional strain: application in hypertrophic cardiomyopathy. *Journal of the American College of Cardiology* **47,** 1175–1181; 10.1016/j.jacc.2005.10.061 (2006).

140. Leitman, M. *et al.* Two-dimensional strain-a novel software for real-time quantitative echocardiographic assessment of myocardial function. *Journal of the American Society of Echocardiography : official publication of the American Society of Echocardiography* **17,** 1021–1029; 10.1016/j.echo.2004.06.019 (2004).

141. Bansal, M. & Kasliwal, R. R. How do I do it? Speckle-tracking echocardiography. *Indian heart journal* **65,** 117–123; 10.1016/j.ihj.2012.12.004 (2013).

142. Stanton, T., Leano, R. & Marwick, T. H. Prediction of all-cause mortality from global longitudinal speckle strain: comparison with ejection fraction and wall motion scoring. *Circulation. Cardiovascular imaging* **2,** 356–364; 10.1161/CIRCIMAGING.109.862334 (2009).

143. Ponikowski, P. *et al.* 2016 ESC Guidelines for the diagnosis and treatment of acute and chronic heart failure: The Task Force for the diagnosis and treatment of acute and chronic heart failure of the European Society of Cardiology (ESC). Developed with the special contribution of the Heart Failure Association (HFA) of the ESC. *European journal of heart failure* **18,** 891–975; 10.1002/ejhf.592 (2016).

144. Mor-Avi, V. *et al.* Current and evolving echocardiographic techniques for the quantitative evaluation of cardiac mechanics: ASE/EAE consensus statement on methodology and indications endorsed by the Japanese Society of Echocardiography. *Journal of the American Society of Echocardiography : official publication of the American Society of Echocardiography* **24,** 277–313; 10.1016/j.echo.2011.01.015 (2011).

145. Ram, R., Mickelsen, D. M., Theodoropoulos, C. & Blaxall, B. C. New approaches in small animal echocardiography: imaging the sounds of silence. *American journal of physiology. Heart and circulatory physiology* **301,** H1765-80; 10.1152/ajpheart.00559.2011 (2011).

146. Cerqueira, M. D. *et al.* Standardized myocardial segmentation and nomenclature for tomographic imaging of the heart. A statement for healthcare professionals from the Cardiac Imaging Committee of the Council on Clinical Cardiology of the American Heart Association. *Circulation* **105,** 539–542; 10.1161/hc0402.102975 (2002).

147. Bénardeau, A. *et al.* Runcaciguat, a novel soluble guanylate cyclase activator, shows renoprotection in hypertensive, diabetic, and metabolic preclinical models of chronic kidney disease. *Naunyn-Schmiedeberg's archives of pharmacology* **394,** 2363–2379; 10.1007/s00210-021-02149-4 (2021).

148. Sangaralingham, S. J. *et al.* Cardiac micro-computed tomography imaging of the aging coronary vasculature. *Circulation. Cardiovascular imaging* **5,** 518–524; 10.1161/CIRCIMAGING.112.973057 (2012).

149. Ackers-Johnson, M. *et al.* A Simplified, Langendorff-Free Method for Concomitant Isolation of Viable Cardiac Myocytes and Nonmyocytes From the Adult Mouse Heart. *Circulation research* **119,** 909–920; 10.1161/CIRCRESAHA.116.309202 (2016).

150. Tian, X. *et al.* Protocol for Isolation of Viable Adult Rat Cardiomyocytes with High Yield. *STAR protocols* **1,** 100045; 10.1016/j.xpro.2020.100045 (2020).

151. Hall, A. R. & Hausenloy, D. J. Mitochondrial respiratory inhibition by 2,3-butanedione monoxime (BDM): implications for culturing isolated mouse ventricular cardiomyocytes. *Physiological reports* **4**; 10.14814/phy2.12606 (2016).

152. Gündüz, D., Hamm, C. W. & Aslam, M. Simultaneous Isolation of High Quality Cardiomyocytes, Endothelial Cells, and Fibroblasts from an Adult Rat Heart. *Journal of visualized experiments : JoVE*; 10.3791/55601 (2017).

153. Brattelid, T. *et al.* Reference gene alternatives to Gapdh in rodent and human heart failure gene expression studies. *BMC molecular biology* **11,** 22; 10.1186/1471-2199-11-22 (2010).

154. Ren, J., Zhang, N., Li, X., Sun, X. & Song, J. Identification of reference genes for gene expression studies among different developmental stages of murine hearts. *BMC developmental biology* **21,** 13; 10.1186/s12861-021-00244-6 (2021).

155. Quiros, P. M., Goyal, A., Jha, P. & Auwerx, J. Analysis of mtDNA/nDNA Ratio in Mice. *Current protocols in mouse biology* **7,** 47–54; 10.1002/cpmo.21. (2017).

156. Damoiseaux, J. G. *et al.* Rat macrophage lysosomal membrane antigen recognized by monoclonal antibody ED1. *Immunology* **83,** 140–147 (1994).

157. Vigolo, E. *et al.* Canonical BMP signaling in tubular cells mediates recovery after acute kidney injury. *Kidney international* **95,** 108–122; 10.1016/j.kint.2018.08.028 (2019).

158. Abdelaziz Mohamed, I., Gadeau, A.-P., Hasan, A., Abdulrahman, N. & Mraiche, F. Osteopontin: A Promising Therapeutic Target in Cardiac Fibrosis. *Cells* **8**; 10.3390/cells8121558 (2019).

159. Gupta, M. P. Factors controlling cardiac myosin-isoform shift during hypertrophy and heart failure. *Journal of molecular and cellular cardiology* **43,** 388–403; 10.1016/j.yjmcc.2007.07.045 (2007).

160. Wynn, T. A. & Ramalingam, T. R. Mechanisms of fibrosis: therapeutic translation for fibrotic disease. *Nature medicine* **18,** 1028–1040; 10.1038/nm.2807 (2012).

161. Sanjabi, S., Zenewicz, L. A., Kamanaka, M. & Flavell, R. A. Anti-inflammatory and pro-inflammatory roles of TGF-beta, IL-10, and IL-22 in immunity and autoimmunity. *Current opinion in pharmacology* **9,** 447–453; 10.1016/j.coph.2009.04.008 (2009).

162. Louch, W. E., Sheehan, K. A. & Wolska, B. M. Methods in cardiomyocyte isolation, culture, and gene transfer. *Journal of molecular and cellular cardiology* **51,** 288–298; 10.1016/j.yjmcc.2011.06.012 (2011).

163. Chen, Y. *et al.* NCF1/2/4 Are Prognostic Biomarkers Related to the Immune Infiltration of Kidney Renal Clear Cell Carcinoma. *BioMed research international* **2021,** 5954036; 10.1155/2021/5954036 (2021).

164. Kim, M. K. *et al.* Associations of Variability in Blood Pressure, Glucose and Cholesterol Concentrations, and Body Mass Index With Mortality and Cardiovascular Outcomes in the General Population. *Circulation* **138,** 2627–2637; 10.1161/CIRCULATIONAHA.118.034978 (2018).

165. Németh, B. T. *et al.* Cinaciguat prevents the development of pathologic hypertrophy in a rat model of left ventricular pressure overload. *Scientific reports* **6,** 37166; 10.1038/srep37166 (2016).

166. Hiebert, J. B., Vacek, J., Shah, Z., Rahman, F. & Pierce, J. D. Use of speckle tracking to assess heart failure with preserved ejection fraction. *Journal of cardiology* **74,** 397–402; 10.1016/j.jjcc.2019.06.004 (2019).

167. Beyhoff, N. *et al.* Application of Speckle-Tracking Echocardiography in an Experimental Model of Isolated Subendocardial Damage. *Journal of the American Society of Echocardiography : official publication of the American Society of Echocardiography* **30,** 1239-1250.e2; 10.1016/j.echo.2017.08.006 (2017).

168. Kim, H. Y. *et al.* Comparison of global and regional myocardial strains in patients with heart failure with a preserved ejection fraction vs hypertension vs age-matched control. *Cardiovascular ultrasound* **18,** 44; 10.1186/s12947-020-00223-0 (2020).

169. Andrade, J. *et al.* Control of endothelial quiescence by FOXO-regulated metabolites. *Nature cell biology* **23,** 413–423; 10.1038/s41556-021-00637-6 (2021).

170. Cai, Y., Zhang, B., Shalamu, A., Gao, T. & Ge, J. Soluble guanylate cyclase (sGC) stimulator vericiguat alleviates myocardial ischemia-reperfusion injury by improving microcirculation. *Annals of translational medicine* **10,** 662; 10.21037/atm-22-2583 (2022).

171. Romano, E. *et al.* Soluble guanylate cyclase stimulation fosters angiogenesis and blunts myofibroblast-like features of systemic sclerosis endothelial cells. *Rheumatology (Oxford, England)*; 10.1093/rheumatology/keac433 (2022).

172. Guo, Y. *et al.* iNOS contributes to heart failure with preserved ejection fraction through mitochondrial dysfunction and Akt S-nitrosylation. *Journal of advanced research* **43,** 175–186; 10.1016/j.jare.2022.03.003 (2023).

173. Fox, B. M. *et al.* Metabolomics assessment reveals oxidative stress and altered energy production in the heart after ischemic acute kidney injury in mice. *Kidney international* **95,** 590–610; 10.1016/j.kint.2018.10.020 (2019).

174. Guo, F. *et al.* Crosstalk between cardiomyocytes and noncardiomyocytes is essential to prevent cardiomyocyte apoptosis induced by proteasome inhibition. *Cell death & disease* **11,** 783; 10.1038/s41419-020-03005-8 (2020).

175. Zhang, Y. *et al.* Phenotypic characterization of primary cardiac fibroblasts from patients with HFpEF. *PloS one* **17,** e0262479; 10.1371/journal.pone.0262479 (2022).

176. Gibb, A. A., Lazaropoulos, M. P. & Elrod, J. W. Myofibroblasts and Fibrosis: Mitochondrial and Metabolic Control of Cellular Differentiation. *Circulation research* **127,** 427–447; 10.1161/CIRCRESAHA.120.316958 (2020).

177. Flores-Vergara, R. *et al.* Communication Between Cardiomyocytes and Fibroblasts During Cardiac Ischemia/Reperfusion and Remodeling: Roles of TGF-β, CTGF, the Renin Angiotensin Axis, and Non-coding RNA Molecules. *Frontiers in physiology* **12,** 716721; 10.3389/fphys.2021.716721 (2021).

178. LaFramboise, W. A. *et al.* Cardiac fibroblasts influence cardiomyocyte phenotype in vitro. *American journal of physiology. Cell physiology* **292,** C1799-808; 10.1152/ajpcell.00166.2006 (2007).

179. Zhang, N. *et al.* CXCR4-dependent macrophage-to-fibroblast signaling contributes to cardiac diastolic dysfunction in heart failure with preserved ejection fraction. *International journal of biological sciences* **18,** 1271–1287; 10.7150/ijbs.65802 (2022).

180. Litviňuková, M. *et al.* Cells of the adult human heart. *Nature* **588,** 466–472; 10.1038/s41586-020-2797-4 (2020).

181. Nicolás-Ávila, J. A. *et al.* A Network of Macrophages Supports Mitochondrial Homeostasis in the Heart. *Cell* **183,** 94-109.e23; 10.1016/j.cell.2020.08.031 (2020).

182. Ren, Z. *et al.* Single-Cell Reconstruction of Progression Trajectory Reveals Intervention Principles in Pathological Cardiac Hypertrophy. *Circulation* **141,** 1704–1719; 10.1161/CIRCULATIONAHA.119.043053 (2020).

183. Ritterhoff, J. *et al.* Metabolic Remodeling Promotes Cardiac Hypertrophy by Directing Glucose to Aspartate Biosynthesis. *Circulation research* **126,** 182–196; 10.1161/CIRCRESAHA.119.315483 (2020).

184. Hill, B. G. *et al.* Integration of cellular bioenergetics with mitochondrial quality control and autophagy. *Biological chemistry* **393,** 1485–1512; 10.1515/hsz-2012-0198 (2012).

185. Li, C. *et al.* Metabolic remodeling of cardiomyocytes identified in phosphoinositide-dependent kinase 1-deficient mice. *The Biochemical journal* **476,** 1943–1954; 10.1042/BCJ20190105 (2019).

186. Gizak, A., McCubrey, J. A. & Rakus, D. Cell-to-cell lactate shuttle operates in heart and is important in age-related heart failure. *Aging* **12,** 3388–3406; 10.18632/aging.102818 (2020).

187. Fillmore, N. *et al.* Uncoupling of glycolysis from glucose oxidation accompanies the development of heart failure with preserved ejection fraction. *Molecular medicine (Cambridge, Mass.)* **24,** 3; 10.1186/s10020-018-0005-x (2018).

188.   Murashige, D. *et al.* Comprehensive quantification of fuel use by the failing and nonfailing human heart. *Science (New York, N.Y.)* **370,** 364–368; 10.1126/science.abc8861 (2020).

189.   Schiattarella, G. G. *et al.* Xbp1s-FoxO1 axis governs lipid accumulation and contractile performance in heart failure with preserved ejection fraction. *Nature communications* **12,** 1684; 10.1038/s41467-021-21931-9 (2021).

190.   McCommis, K. S. *et al.* Nutritional modulation of heart failure in mitochondrial pyruvate carrier-deficient mice. *Nature metabolism* **2,** 1232–1247; 10.1038/s42255-020-00296-1 (2020).

191.   Deng, Y. *et al.* Targeting Mitochondria-Inflammation Circuit by β-Hydroxybutyrate Mitigates HFpEF. *Circulation research* **128,** 232–245; 10.1161/CIRCRESAHA.120.317933 (2021).

192.   Carley, A. N. *et al.* Short-Chain Fatty Acids Outpace Ketone Oxidation in the Failing Heart. *Circulation* **143,** 1797–1808; 10.1161/CIRCULATIONAHA.120.052671 (2021).

193.   Irvine, J. C. *et al.* The soluble guanylyl cyclase activator bay 58-2667 selectively limits cardiomyocyte hypertrophy. *PloS one* **7,** e44481; 10.1371/journal.pone.0044481 (2012).

194.   Masuyama, H. *et al.* Soluble guanylate cyclase stimulation on cardiovascular remodeling in angiotensin II-induced hypertensive rats. *Hypertension (Dallas, Tex. : 1979)* **48,** 972–978; 10.1161/01.HYP.0000241087.12492.47 (2006).

195.   Masuyama, H. *et al.* Pressure-independent effects of pharmacological stimulation of soluble guanylate cyclase on fibrosis in pressure-overloaded rat heart. *Hypertension research : official journal of the Japanese Society of Hypertension* **32,** 597–603; 10.1038/hr.2009.64 (2009).

196.   Abdelaziz, N., Colombo, F., Mercier, I. & Calderone, A. Nitric oxide attenuates the expression of transforming growth factor-beta(3) mRNA in rat cardiac fibroblasts via destabilization. *Hypertension (Dallas, Tex. : 1979)* **38,** 261–266; 10.1161/01.HYP.38.2.261 (2001).

197.   Ünlü, S. *et al.* Impact of apical foreshortening on deformation measurements: a report from the EACVI-ASE Strain Standardization Task Force. *European heart journal. Cardiovascular Imaging* **21,** 337–343; 10.1093/ehjci/jez189 (2020).

198.   Scott, S. R., Singh, K., Yu, Q., Sen, C. K. & Wang, M. Sex as Biological Variable in Cardiac Mitochondrial Bioenergetic Responses to Acute Stress. *International journal of molecular sciences* **23**; 10.3390/ ijms23169312 (2022).

199.   Cao, Y. *et al.* Sex differences in heart mitochondria regulate diastolic dysfunction. *Nature communications* **13,** 3850; 10.1038/s41467-022-31544-5 (2022).

200.   Withaar, C., Lam, C. S. P., Schiattarella, G. G., Boer, R. A. de & Meems, L. M. G. Heart failure with preserved ejection fraction in humans and mice: embracing clinical complexity in mouse models. *European heart journal* **42,** 4420–4430; 10.1093/eurheartj/ehab389 (2021).

Publications

Kedziora SM, Obermayer B, Sugulle M, Herse F, Kräker K, Haase N, Langmia IM, Müller DN, Staff AC, Beule D, Dechend R. **Placental Transcriptome Profiling in Subtypes of Diabetic Pregnancies Is Strongly Confounded by Fetal Sex.** Int J Mol Sci. 2022 Dec 6;23(23):15388. doi: 10.3390/ijms232315388. PMID: 36499721; PMCID: PMC9740420.

Kedziora SM, Kräker K, Markó L, Binder J, Sugulle M, Gauster M, Müller DN, Dechend R, Haase N, Herse F. **Kidney Injury Caused by Preeclamptic Pregnancy Recovers Postpartum in a Transgenic Rat Model.** Int J Mol Sci. 2021 Apr 5;22(7):3762. doi: 10.3390/ijms22073762. PMID: 33916404; PMCID: PMC8038582.

Schütte T, **Kedziora SM**, Haase N, Herse F, Alenina N, Müller DN, Bader M, Schupp M, Dechend R, Golic M, Kräker K. **Diabetic pregnancy as a novel risk factor for cardiac dysfunction in the offspring-the heart as a target for fetal programming in rats.** Diabetologia. 2021 Dec;64(12):2829-2842. doi: 10.1007/s00125-021-05566-5. Epub 2021 Sep 18. PMID: 34537857; PMCID: PMC8563640.

Schütte T, **Kedziora SM,** Haase N, Herse F, Busjahn A, Birukov A, Alenina N, Müller DN, Bader M, Schupp M, Dechend R, Kräker K, Golic M. **Intrauterine Exposure to Diabetic Milieu Does Not Induce Diabetes and Obesity in Male Adulthood in a Novel Rat Model. Hypertension.** 2021 Jan;77(1):202-215. doi: 10.1161/HYPERTENSIONAHA.120.16360. Epub 2020 Nov 30. PMID: 33249866.

Fedders R, Muenzner M, Weber P, Sommerfeld M, Knauer M, **Kedziora SM,** Kast N, Heidenreich S, Raila J, Weger S, Henze A, Schupp M**. Liver-secreted RBP4 does not impair glucose homeostasis in mice.** J Biol Chem. 2018 Sep 28;293(39):15269-15276. doi: 10.1074/jbc.RA118.004294. Epub 2018 Aug 20. PMID: 30126844; PMCID: PMC6166712.

Nonn O, Debnath O, Valdes DS, Sallinger K, Secener AK, Haider S, Fischer C, Tiesmeyer S, Nimo J, Kuenzer T, Maxian T, Knöfler M, Karau P, Bartolomaeus H, Kroneis T, Frolova A, Neuper L, Haase N, Kräker K, **Kedziora SM,** Forstner D, Verlohren S, Stern C, Coscia F,

Sugulle M, Jones S, Tilaganathan B, Eils R, Huppertz B, El-Heliebi A, Staff AC, Müller DN, Dechend R, Gauster M, Ishaque N, Herse F. **Disturbed trophoblast transition links preeclampsia progression from placenta to the maternal syndrome.** bioRxiv 2022.10.10.511539; doi: https://doi.org/10.1101/2022.10.10.511539

– preprint publication

Samuelsson AM, Bartolomaeus TUP, Anandakumar H, Thowsen I, Nikpey E, Han J, Marko L, Finne K, Tenstad O, Eckstein J, Berndt N, Kühne T, **Kedziora SM,** Sultan I, Skogstrand T, Karlsen TV, Nurmi H, Forslund SK, Bollano E, Alitalo K, Muller DN, Wiig H. **VEGF-B hypertrophy predisposes to transition from diastolic to systolic heart failure in hypertensive rats.** Cardiovascular Research.

– accepted

Kräker K, Napieczynska H, **Kedziora SM**, Haase N, Schelenz S, Müller DN, Heuser A, Dechend R. **High-resolution 3D microvascular fingerprint and multi-organ imaging in rodents – novel insights into the (cardio) vascular long-term risk after preeclamptic pregnancy**.

– under submission

Curriculum vitae

For data protection reasons, the CV is not included in the online version.

Aus Gründen des Datenschutzes ist der Lebenslauf in der Online-Version nicht enthalten.

For data protection reasons, the CV is not included in the online version.

Aus Gründen des Datenschutzes ist der Lebenslauf in der Online-Version nicht enthalten.